

NUMERICAL STUDY OF TRANSITIONS IN TAYLOR-COUETTE FLOW

THÈSE N° 1934 (1999)

PRÉSENTÉE AU DÉPARTEMENT DE GÉNIE MÉCANIQUE

ÉCOLE POLYTECHNIQUE FÉDÉRALE DE LAUSANNE

POUR L'OBTENTION DU GRADE DE DOCTEUR ÈS SCIENCES

PAR

Eric MAGÈRE

Ingénieur de l'Ecole Nationale Supérieure de Mécanique et d'Aérotechnique, Poitiers, France
de nationalité française

acceptée sur proposition du jury:

Prof. M. Deville, directeur de thèse
Prof. G. Labrosse, rapporteur
Prof. P.A. Monkewitz, rapporteur
Prof. E. Mund, rapporteur
Prof. A. Quarteroni, rapporteur
Dr B. Smith, rapporteur

Lausanne, EPFL
1999

Remerciements

Je remercie mon directeur de thèse, M. Deville, pour avoir été disponible tout au long de ma thèse pour me conseiller. Je remercie aussi S. Gavrilakis pour l'aide qu'il m'a apportée lors de la validation de mon code, ainsi que G. Labrosse, E. Mund, A. Quarteroni, P. Monkewitz et B. Smith pour les remarques intéressantes qu'ils m'ont faites.

Ensuite, il y a tous ces amis qui m'ont permis de travailler dans une ambiance sympathique, Alexander, Tiana, Natacha, Philippe, Olivier, les deux Nathalie, Jung-Eung, Jan, Yan, Pénélope, Frédéric, Alain, Léonor, et j'en oublie bien d'autres. Merci encore à Florence pour ses conseils. Et surtout merci à ma femme pour avoir su me soutenir dans les moments difficiles.

Abstract

This thesis is divided into two parts. In the first one the creation of a complete numerical tool, from the mesh generation to the data treatment, is presented. However time consuming this part has been, this is not the most important one. The second and more important part is concerned with the description and physical interpretation of the results obtained with the numerical tool previously developed.

- The numerical tool, which exists in its quasi-final version since mid-1997, fully satisfies the following requirements. It is specifically designed to study the flow in the annular space between coaxial, differentially-rotating cylinders of finite length. The spectral element method is used for the space discretization. The study of transition requires the high accuracy warranted by this type of method. The numerical scheme has also to be efficient. This requirement is satisfied, due to the fully-explicit time scheme adopted, where both diffusive and non-linear terms of the Navier-Stokes equations are treated explicitly, and the direct inversion of the pseudo-Laplacian matrix applied to the pressure. This inversion is performed in the most efficient way with a fast diagonalization technique. In the Reynolds numbers range we are interested in, the time-step limitation due to the linear viscous term is only slightly more stringent than the one due to the non-linear term. The last requirement that has been fulfilled has been to design as simple a code as possible.

The entire code is constructed from a number of well-known algorithms, fitted together to enhance efficiency. However, the way we regularize the boundary conditions is new. It represents the physics more precisely than Tavener *et al.* [65]. There is a second original feature in our code, which is linked to the time scheme. We derived our time discretization from the scheme of Gavrilakis *et al.* [31]. Their scheme cannot be applied to cylindrical coordinates as it is. We thus had to modify it.

- The second part of the thesis consists of the numerical study of the first transitions of the Taylor-Couette flow in a finite-length geometry. The aspect ratio between the length of the cylinders and the gap between them has been chosen equal to twelve; this is small enough for the effects of the upper and lower boundaries of the flow to be significant. It is believed that these end-effects play a non-negligible role in the transition of the flow. On the other hand, the aspect ratio is large enough to make qualitative comparisons with the infinite-length case, which has been studied extensively both theoretically and numerically. The transition process depends on a relatively large number of parameters. Our investigation focuses on the case where the cylinders rotate in opposite directions. The study of counter-rotating Taylor-Couette flow for a large but finite aspect ratio is the main originality of this thesis. Furthermore, the physical mechanism of the appearance

of the second bifurcation in classical Taylor-Couette flow, where only the inner cylinder is rotating, is described in the light of the non-linear interaction between velocity and vorticity.

Résumé

Ce travail de thèse est constitué de deux parties. La première a consisté à développer un outil numérique dans son intégralité, de la génération du maillage jusqu'au traitement des données. Cette partie a beau avoir pris plus de la moitié du temps imparti, ce n'est pas la plus importante. L'accent est mis sur la seconde partie de la thèse, qui concerne la description et l'interprétation physique des résultats obtenus avec l'outil numérique précédemment développé.

- L'outil numérique, qui existe dans sa version quasi définitive depuis mi-1997, répond entièrement aux exigences suivantes. Il est adapté à la géométrie du domaine fluide étudié, l'espace annulaire entre deux cylindres coaxiaux de longueur finie. Il permet d'étudier les délicats phénomènes de transition grâce à la discrétisation spatiale choisie, les éléments spectraux, qui garantit une grande précision. Il est efficace. Cette exigence est remplie grâce au choix d'un schéma temporel entièrement explicite, à la fois sur le terme non-linéaire et sur le terme diffusif, et à l'utilisation d'un solveur direct de diagonalisation rapide, réalisant avec un maximum d'efficacité l'inversion du pseudo-Laplacien sur la pression. Pour les nombres de Reynolds considérés dans cette étude, la limitation du pas de temps due au terme linéaire visqueux est à peine plus contraignante que celle due au terme non linéaire. En dernier lieu, le code est relativement simple.

Le code complet peut être décrit comme l'amalgame d'algorithmes pour la plupart déjà décrits dans la littérature, assemblés de manière à ce que le programme au complet soit le plus performant possible. Parmi les divers ingrédients constitutifs du code, deux ont un caractère original. Le premier est lié au traitement des conditions aux limites singulières entre le cylindre et les parois horizontales qui tournent à des vitesses différentes. Notre implémentation est dans la lignée de celle de Tavener *et al.* [65], mais elle représente encore plus précisément la physique. Le deuxième trait original de l'outil numérique tient au schéma d'intégration temporel. Celui-ci est basé sur un schéma développé par Gavrilakis *et al.* [31]. Ce schéma, initialement prévu pour une géométrie cartésienne, n'étant pas correct si l'on souhaite l'appliquer tel quel à une géométrie cylindrique, nous l'avons modifié de manière à ce qu'il soit valable dans le cas de notre géométrie.

- L'étude numérique des premières transitions de l'écoulement de Taylor-Couette en géométrie confinée constitue la seconde partie de la thèse. Le rapport entre la longueur des cylindres et la distance de l'entrefer choisi dans cette étude est douze. Cet rapport d'aspect est suffisamment petit pour que l'effet des bords supérieur et inférieur se fasse sentir, et suffisamment grand pour pouvoir faire des comparaisons, d'ordre qualitatif, avec les nombreux résultats théoriques et numériques obtenus dans le cas de cylindres infinis. La transition de cet écoulement dépend

d'un relativement grand nombre de paramètres. Nous nous sommes essentiellement intéressés au cas où les deux cylindres tournent en sens opposés. L'étude de l'écoulement de Taylor-Couette contra-rotatif dans un espace annulaire de grande hauteur, mais de hauteur finie, constitue la principale originalité de cette thèse. Par ailleurs, le mécanisme d'apparition de la deuxième bifurcation dans la configuration de Taylor-Couette classique, où seul le cylindre intérieur tourne, est décrit à la lumière de l'interaction non linéaire entre les champs de vitesse et de vorticité.

Contents

1	Introduction	1
1.1	State-of-the-art	9
1.1.1	Experimental results	9
1.1.2	Numerical results	11
1.2	Choice of the parameters	14
1.2.1	Geometric parameters	15
1.2.2	Dynamic parameters	17
1.2.3	History parameter	18
1.3	Aims of the thesis	18
1.4	Organization of the chapters	19
I	Numerical tools	21
2	Introduction to the spectral element method	23
2.1	<i>p</i> -type weighted residual methods	24
2.2	Spectral approximation	25
2.3	Pseudo-spectral approximation	27
2.4	A one-dimensional model equation	27
3	3D Navier-Stokes solver	33
3.1	Continuous formulation of the equations	34
3.2	Weak formulation of the equations	35
3.3	Spatial discretization	36
3.4	Time discretization	46
3.4.1	Fully-explicit scheme	46
3.4.2	RK2 scheme	48
3.5	Pressure solver	50
3.6	Boundary conditions	51
3.7	Linearized problem	54
3.7.1	Linearization of the equations in the vicinity of the base flow	54
3.7.2	Spatial discretization	54
3.7.3	Time discretization	56

4	Validation and performance	57
4.1	Validation	57
4.1.1	Analytical test cases	57
4.1.2	Comparison with experiments and other simulations	64
4.2	Performance	74
4.2.1	Performance of the algorithms	74
4.2.2	Performance of the code	77
II	Analysis of the transition	81
5	Linear stability analysis	83
5.1	Objective	83
5.2	Analysis method	83
6	Classical Taylor-Couette flow	91
6.1	Couette flow	91
6.1.1	Ghost cells	91
6.1.2	Ekman cells	92
6.2	First transition	93
6.2.1	Critical wavenumber	93
6.2.2	Critical Reynolds number	95
6.3	Supercritical Taylor vortex flow	96
6.3.1	Reynolds number dependence of the flow	96
6.3.2	Pressure distribution	97
6.4	Wavy Taylor vortex flow	97
6.4.1	Wavy Taylor vortex flow as a perturbation to the axisymmetric flow	98
6.4.2	Relationship between velocity and vorticity	99
7	Counter-rotating Taylor-Couette flow	117
7.1	Axisymmetric simulations of the first transition	117
7.2	Transition to bouncing vortices	128
8	Conclusions and perspectives	133
8.1	Conclusions	133
8.2	Perspectives	135
A	Useful formulae in cylindrical polar coordinates	137
A.1	Viscous shear stress tensor	137
A.2	Vorticity	137
A.3	Stream function in the axisymmetric case	137

B Spectral element method	139
B.1 Spectral approximation of functions	139
B.1.1 Singular Sturm-Liouville problem	139
B.1.2 Legendre polynomials	139
B.1.3 Gauss-Lobatto-Legendre weights and points	140
B.1.4 Lagrange-Legendre interpolants	140
B.1.5 Lagrange-Legendre interpolants derivatives	140
B.2 Tensor product	141
B.2.1 Definition	141
B.2.2 Properties	141
B.3 Operation count for a matrix vector multiplication	141
C Navier-Stokes solver in hourglass geometry	143
C.1 Mapping of the hourglass geometry	143
C.2 Spatial discretization	144
C.3 Time discretization	148

Notation

Numerical symbols

A^r	Stiffness matrix in radial direction, in velocity space
A^z	Stiffness matrix in axial direction, in velocity space
\widetilde{B}^r	Rectangular mass matrix in radial direction, from pressure to velocity space
\widetilde{B}^z	Rectangular mass matrix in axial direction, from pressure to velocity space
$\frac{B^r}{r}$	Radial mass matrix, in velocity space
rB^r	Radial mass matrix, in velocity space
B^z	Axial mass matrix, in velocity space
CSD	Diffusive stability constraint
CSN	Non linear stability constraint
\widetilde{G}^r	Rectangular radial gradient matrix, from pressure to velocity space
\widetilde{G}^z	Rectangular axial gradient matrix, from pressure to velocity space
g^e	Width of element Υ^{el}
h^l	Height of element Υ^{el}
h_i	Lagrange-Legendre interpolant based on the i -th GLL point
\tilde{h}_i	Lagrange-Legendre interpolant based on the i -th inner GLL point
I	Number of elements in radial direction
J	Number of elements in axial direction
$\widetilde{\mathcal{M}}_k^r$	Pseudo-Laplacian matrix in radial direction for azimuthal mode k
$\widetilde{\mathcal{M}}^z$	Pseudo-Laplacian matrix in axial direction
N_r	Polynomial degree for discretization in radial direction
N_θ	Number of azimuthal planes
N_z	Polynomial degree for discretization in axial direction
\mathcal{N}	Number of mesh points
$\mathcal{P}_{N,E}(\Upsilon)$	$\{\phi \in C^0(\Upsilon), \forall e \in \{1, 2, \dots, N\}, \phi _{\Upsilon^e} \in \mathcal{P}_N(\Upsilon^e)\}$, where $\overline{\Upsilon} = \cup_e \overline{\Upsilon^e}$
\widetilde{Q}_k^r	Eigenvectors of the pseudo-Laplacian matrix in radial direction for mode k
$\widetilde{Q}_k^r{}^{-1}$	Inverse of the eigenvectors matrix \widetilde{Q}_k^r
\widetilde{Q}^z	Eigenvectors of the pseudo-Laplacian matrix in axial direction
$\widetilde{Q}^z{}^{-1}$	Inverse of the eigenvectors matrix \widetilde{Q}^z
$\mathcal{H}^1(\Upsilon)$	Sobolev space of functions $\phi \in \mathcal{L}^2(\Upsilon)$ such that its first derivative $\in \mathcal{L}^2(\Upsilon)$
$\mathcal{H}_0^1(\Upsilon)$	$\{\phi \in \mathcal{H}^1(\Upsilon), \phi _{\partial\Upsilon} = 0\}$
X	$X = \mathcal{H}^1(\Upsilon) \cap \mathcal{P}_{N,E}(\Upsilon)$

X_0	$X_0 = \mathcal{H}_0^1(\Upsilon) \cap \mathcal{P}_{N,E}(\Upsilon)$
$\mathcal{L}^2(\Upsilon)$	Lebesgue space of square integrable functions on Υ
$\mathcal{L}_0^2(\Upsilon)$	$\{\phi \in \mathcal{L}^2(\Upsilon), \phi _{\partial\Upsilon} = 0\}$
Y	$Y = \mathcal{L}^2(\Upsilon) \cap \mathcal{P}_{N-2,E}(\Upsilon)$
Y_0	$Y_0 = \mathcal{L}_0^2(\Upsilon) \cap \mathcal{P}_{N-2,E}(\Upsilon)$
$\widetilde{\Lambda}_k^r$	Eigenvalues of the pseudo-Laplacian matrix in radial direction for mode k
Λ^z	Eigenvalues of the pseudo-Laplacian matrix in axial direction
Υ_d	Grid made of all the Gauss-Lobatto-Legendre points of all the elements
$\overset{\circ}{\Upsilon}_d$	Grid made of all the points of Υ_d except the boundary points
$\tilde{\Upsilon}_d$	Grid made of all the inner Gauss-Lobatto-Legendre points of all the elements
Υ_e	Open sub-domain of the open domain Υ
Π^p	Pressure test function on the whole domain D
Π^v	Velocity test function on the whole domain D
ϕ	Velocity test function on the meridian cross-section Υ
ψ	Pressure test function on the meridian cross-section Υ

Physical symbols

A		$A = \frac{R_2^2 \Omega_2 - R_1^2 \Omega_1}{R_2^2 - R_1^2}$
B		$B = R_1^2 R_2^2 \frac{\Omega_1 - \Omega_2}{R_2^2 - R_1^2}$
d	Gap between the two cylinders	$d = R_2 - R_1$
D	Domain (volume)	
L	Length of the cylinders	$L = H_2 - H_1$
P	Pressure characteristic scale	
R_1	Radius of the inner cylinder	
R_2	Radius of the outer cylinder	
Re	Reynolds number	$Re = \frac{d V}{\nu}$
Re_c	First critical Reynolds number	
Re_w	Second critical Reynolds number	
Re_m	Third critical Reynolds number	
Re_1	Inner cylinder Reynolds number	$Re_1 = \frac{d R_1 \Omega_1}{\nu}$
Re_2	Outer cylinder Reynolds number	$Re_2 = \frac{d R_2 \Omega_2}{\nu}$
Ta	Taylor number	$Ta = (R_1^2 \Omega_1 - R_2^2 \Omega_2) \frac{\Omega_1 d^3}{R_1 \nu^2}$
V	Velocity characteristic scale	
$\mathbf{v}_c(r)$	Azimuthal velocity for Couette flow	$\mathbf{v}_c = (0, v_c, 0), v_c(r) = A r + \frac{B}{r}$
z_1	Bottom plate height	$z_1 = H_1$
z_2	Top plate height	$z_2 = H_2$
α	Axial wavenumber	$\alpha = \frac{2\pi}{\lambda}$
η	Radii ratio	$\eta = \frac{R_1}{R_2}$
Γ	Aspect ratio	$\Gamma = \frac{L}{d}$

λ	Axial wavelength
$\Omega_c(\tau)$	Angular velocity for Couette flow
τ	Characteristic time scale
τ_D	Diffusive time scale
τ_C	Advection time scale
Υ	Meridian cross-section
\mathcal{U}	Rotation ratio

$$\Omega_c(\tau) = A + \frac{B}{\tau^2}$$

$$\tau = \tau_C$$

$$\tau_D = \frac{d^2}{\nu}$$

$$\tau_C = \frac{d}{\bar{v}}$$

$$\Upsilon =]R_1, R_2[\times]z_1, z_2[$$

$$\mathcal{U} = \frac{\Omega_2}{\Omega_1}$$

“Si on s’occupe des moyens, tôt ou tard on atteint la fin. Une fois qu’on a saisi ce point, la victoire finale ne saurait faire de doute. Quelles que soient les difficultés que nous rencontrons, quelles que soient nos apparentes défaites, il n’est pas question de renoncer à la recherche de la Vérité qui seule est, n’étant autre que Dieu lui-même. ”

Gandhi in “Tous les hommes sont frères”.

Chapter 1

Introduction

Taylor-Couette flow is that which develops in the annular space between two coaxial cylinders which are in relative motion. The fluid considered in most cases is Newtonian. However simple this flow may seem, it exhibits a rich variety of instability patterns depending, among other parameters, on the cylinders speeds [4, 40]. Although studied extensively since the end of the last century, this flow has not yet revealed all its secrets, and remains one of the fundamental problems in fluid mechanics. It is a paradigm for experimental, numerical and theoretical studies of hydrodynamic stability and transition. Further, the existing direct numerical simulations (DNS) [6, 26, 37, 48, 61] enable it to be used as a benchmark for turbulence modelling. Additionally, there are direct industrial applications:

- as a rotating filter separator used for the separation of plasma from blood, and for oily emulsions or particulates from combustion gases. A rotating filter separator consists of a porous inner cylinder rotating within an outer cylindrical shell. As a suspension travels axially in the annulus, the filtrate is withdrawn through the inner cylinder, leaving an increasingly concentrated suspension in the annulus. The unique advantage of rotating filtration is that plugging of the pores of the filter with particles is greatly reduced compared to standard filtration techniques.
- in nuclear engineering, a Taylor-Couette device is used at CEA-Marcoule to reprocess spent nuclear fuel [7]. Taylor-Couette flow has interesting stirring properties at high Reynolds numbers which makes it an alternative to already existing techniques used for spent nuclear fuel reprocessing. The purpose of the Taylor-Couette facility is to provide an intimate contact of two non-miscible fluids (aqueous and organic liquids) in order to allow interphase diffusion of certain components. Because of their lower density, organic droplets accumulate in the regions where the pressure is low. At high Reynolds numbers, the turbulent Taylor vortices produce enough shear deformation to generate an emulsion, thus enhancing the mass transfer. An efficient control of the residence time in the reactor is obtained by superimposing an axial flow.

Taylor-Couette flow depends on the following geometric and dynamic parameters. The geometric parameters are the aspect ratio, $\Gamma = \frac{L}{d}$, with L the length of the cylinders and d the gap width between the cylinders (see figure 1.1), and the radii ratio, $\eta = \frac{R_1}{R_2}$, where R_1 and R_2 are the inner and outer radii, respectively. Both the geometry and the dynamics of the boundary conditions at the top and bottom of the annular space influence the flow. The horizontal end plates are either fixed to the inner cylinder or to the outer one; we do not consider the more general case in which the end plates rotate independently. The dynamic parameters are the inner and outer Reynolds numbers: $Re_1 = \frac{R_1 \Omega_1 d}{\nu}$ and $Re_2 = \frac{R_2 \Omega_2 d}{\nu}$, respectively. When the cylinders are rotating in the same direction, Re_1 and Re_2 are both positive, as Reynolds numbers are supposed to be, but when they are rotating in opposite directions, Re_1 is chosen positive and Re_2 negative by convention. Another frequent choice of dynamic parameters is the rotation ratio, $\mathcal{U} = \frac{\Omega_2}{\Omega_1}$, and the Taylor number, defined as: $Ta = (R_1^2 \Omega_1 - R_2^2 \Omega_2) \frac{\Omega_1 d^3}{R_1 \nu^2}$, or the square root of this expression. Ta is always positive in the parameter range we are interested in, which is defined by: $\Omega_1 > 0$ and $\Omega_2 \leq 0$. Finally, another dynamic parameter, which is usually not considered, is the acceleration rate or, equivalently, the path followed in parameter space from one state, defined by (Re_1, Re_2) , to another. The acceleration history between two successive flow states is indeed important for determining the final flow state, as has been demonstrated by Burkhalter and Koschmieder [12].

Base flow

When the cylinders are of infinite length, there exists an analytical solution at low Reynolds numbers [55] called *Couette flow*. The base flow velocity is $\mathbf{v}_c = (0, v_c, 0)$ in cylindrical coordinates (r, θ, z) , with

$$v_c(r) = Ar + \frac{B}{r}, \text{ where, } A = \frac{R_2^2 \Omega_2 - R_1^2 \Omega_1}{R_2^2 - R_1^2} \text{ and } B = (\Omega_1 - \Omega_2) \frac{R_1^2 R_2^2}{R_2^2 - R_1^2}. \quad (1.1)$$

The base flow pressure is defined by:

$$\frac{\partial p_c}{\partial r}(r) = \frac{v_c^2}{r}.$$

In dimensionless form,

- for $\mathcal{U} < 0$, the characteristic velocity is $V = -R_2 \Omega_2$, therefore,

$$A = \frac{\eta^2 - \mathcal{U}}{\mathcal{U}(1 + \eta)} \text{ and } B = \frac{1}{1 + \eta} \left(\frac{\eta}{1 - \eta} \right)^2 \frac{\mathcal{U} - 1}{\mathcal{U}}.$$

- for $\mathcal{U} \geq 0$, the characteristic velocity is $V = R_1 \Omega_1$, hence,

$$A = \frac{\mathcal{U} - \eta^2}{\eta(1 + \eta)} \text{ and } B = \left(\frac{1}{1 - \eta} \right)^2 \frac{\eta}{1 + \eta} (1 - \mathcal{U}).$$

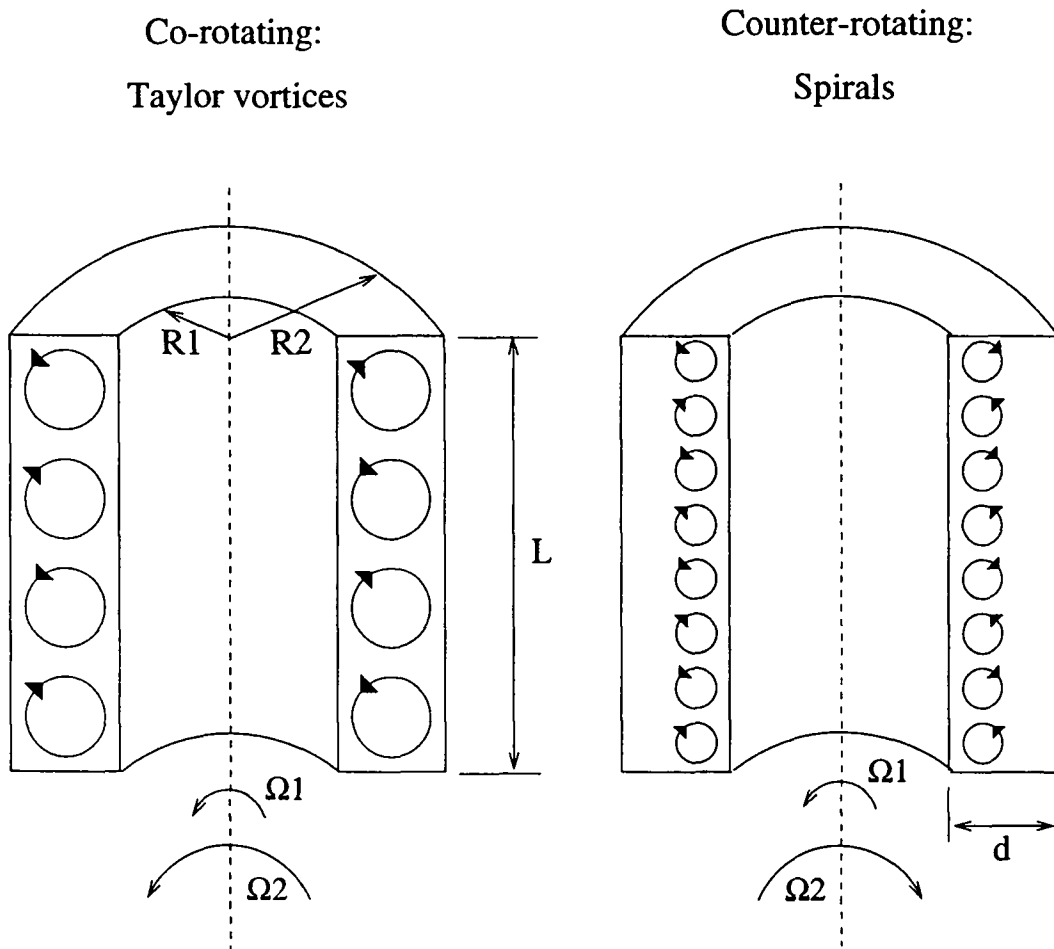


Figure 1.1: Taylor-Couette apparatus and flow patterns after the first bifurcation.

First bifurcation

The stability of Taylor-Couette flow was first studied by Rayleigh [55]. Assuming the cylinders to be of infinite length, the fluid to be inviscid, and the perturbations to be axisymmetric, he found that the flow is stable if the square of the circulation does not decrease with r . This condition is now known as *Rayleigh's circulation criterion*. Its mathematical expression,

$$\frac{d}{dr}[(2\pi r v_c)^2] > 0 ,$$

can be simplified to,

$$A v_c(r) > 0$$

- In the co-rotating case, for $\mathcal{U} \geq 0$, v_c is positive so that the sign of $A v_c(r)$ depends only on A . The radial derivative of the square of the circulation is therefore positive, and the flow hence stable, if $\mathcal{U} > \eta^2$.
- In the counter-rotating case, i.e. for $\mathcal{U} < 0$, we have $A < 0$ and $B > 0$, hence, the base velocity evolves monotonously with r from a positive value, $R_1\Omega_1$, to a negative value, $R_2\Omega_2$. Consequently, the square of the circulation first decreases from a positive value to zero, and increases afterwards. Rayleigh's circulation criterion indicates therefore that this flow is unstable. More precisely, we can say that the region of the fluid near the inner cylinder is unstable, while the zone near the outer cylinder is stable. The cylindrical surface separating these two regions is called the *nodal surface*.

Synge [63] gave a mathematical proof of Rayleigh's criterion in 1933. He later showed that in a viscous fluid the condition $\mathcal{U} > \eta^2$ was sufficient, but not necessary, for stability, according to linear theory [64].

In 1890, Couette [20] designed a viscometer based on the flow between cylinders. Only the outer cylinder was rotating in his experiment. He observed that the torque transmitted by the flow on the inner cylinder varied linearly with the speed of the rotating cylinder until a critical value of the velocity was reached. Thereafter, the torque increased at a greater rate than the velocity, denoting a change in flow regime. Hence, the flow is unstable at high Reynolds numbers, even though Rayleigh's inviscid stability criterion is satisfied.

Mallock [47] repeated Couette's experiments in 1896, first with the outer cylinder rotating and the inner one fixed, and later with the inner cylinder rotating and the outer one fixed. In the first case, his experiments yielded the same results as Couette's. But, he found no linear dependence of the torque on the velocity in the second case.

Transition to Taylor vortices It became clear from the work of Taylor [66] in 1923 that none of the second set of Mallock's experiments corresponded to laminar, azimuthal

flows. Taylor calculated analytically the stability limit of the flow to axisymmetric disturbances in the infinite-length case, considering this time a viscous fluid. Here, we will only present his most important results, albeit using more up-to-date methods. Let (\mathbf{v}_T, p_T) , be a slight deviation of the base Couette flow and also a solution of the Navier-Stokes equations. We write $\mathbf{v}_T = \mathbf{v} + \mathbf{v}_c$ and $p_T = p + p_c$, with: $\|\mathbf{v}\| \ll \|\mathbf{v}_c\|$ and $|p| \ll |p_c|$. The Navier-Stokes equations are then linearized in the vicinity of this base flow. The linearized Navier-Stokes equations are further simplified taking the axisymmetry hypothesis into account. The resulting dimensionless equations are expressed as follows in cylindrical coordinates:

$$\left\{ \begin{array}{l} \left(\frac{\partial}{\partial t} - \nabla^2 + \frac{1}{r^2} \right) u - 2C(r) v = -\frac{\partial p}{\partial r} \quad , \\ \left(\frac{\partial}{\partial t} - \nabla^2 + \frac{1}{r^2} \right) v + 2A Re u = 0 \quad , \\ \left(\frac{\partial}{\partial t} - \nabla^2 \right) w = -\frac{\partial p}{\partial z} \quad , \\ 0 = \left(\frac{\partial}{\partial r} + \frac{1}{r} \right) u + \frac{\partial w}{\partial z} \quad , \end{array} \right. \quad (1.2)$$

with: (u, v, w) the components of the perturbed velocity, \mathbf{v} , and $C(r) = Re \frac{v_c(r)}{r} = Re \left(A + \frac{B}{r^2} \right)$. The Reynolds number is $Re = \frac{dV}{\nu}$, with V , the characteristic velocity. And,

$$\nabla^2 = \frac{\partial^2}{\partial r^2} + \frac{1}{r} \frac{\partial}{\partial r} + \frac{\partial^2}{\partial z^2} .$$

Eliminating the pressure disturbance p and the perturbed axial velocity w , one is left with a system of two equations for the two unknowns, the radial component of the velocity, u , and the azimuthal velocity, v :

$$\left\{ \begin{array}{l} \frac{\partial^2}{\partial z^2} \left[\left(\frac{\partial}{\partial t} - \nabla^2 + \frac{1}{r^2} \right) u - 2C(r) v \right] + \frac{\partial}{\partial r} \left(\frac{\partial}{\partial t} - \nabla^2 \right) \left(\frac{\partial}{\partial r} + \frac{1}{r} \right) u = 0 \quad , \\ \left(\frac{\partial}{\partial t} - \nabla^2 + \frac{1}{r^2} \right) v + 2A Re u = 0 \quad . \end{array} \right. \quad (1.3)$$

Taylor's early experiments showed that instability led to a steady, secondary flow in the form of toroidal vortices, regularly spaced along the axis of the cylinders. The equations can again be simplified by analyzing the disturbance into normal modes, that is, let $(u, v) = (u_n, v_n) \exp(\sigma t + i\kappa z)$, where κ is the axial wavenumber, σ is the growth rate of the perturbation, and (u_n, v_n) only depend on r . We obtain:

$$\left\{ \begin{array}{l} (DD_* - \kappa^2 - \sigma)(DD_* - \kappa^2)u_n = 2\kappa^2 C(r) v_n \quad , \\ (DD_* - \kappa^2 - \sigma)v_n = 2A Re u_n \quad , \end{array} \right. \quad (1.4)$$

where D represents $\frac{d}{dr}$ and $D_* = \frac{d}{dr} + \frac{1}{r}$.

The equations (1.4) define an eigenvalue problem of the form, $\mathcal{F}(\eta, \mathcal{U}, Ta, \kappa, \sigma) = 0$. The solution of this problem is simplified considerably by the so-called principle of exchange of stabilities, which states that when the real part of σ , $\Re(\sigma)$ is zero, then its imaginary part is also. Therefore, the *neutral curve* is given by $\sigma = 0$. The neutral curve is the set of points in the (κ, Ta) plane for which $\Re(\sigma) = 0$. Above this curve

the flow is unstable, and below it stable. The analysis we have made so far reproduces the main lines of Taylor's theory. We proceed with the analysis using the much simpler method developed by Chandrasekhar [14] to solve this problem. Expanding v_n in a set of Fourier components that vanish on the boundary, he found an eigenvalue relation in the form of a determinant of infinite order. Retaining only the first term of the Fourier expansion, and using the *narrow-gap hypothesis*, which states that $\eta \rightarrow 1$, we obtain the following result:

$$T = (1 + \mathcal{U})Ta = \frac{(\pi^2 + \alpha^2)^3}{\alpha^2[1 - \{16\pi^2\alpha \cosh^2(\frac{\alpha}{2})\}/\{(\pi^2 + \alpha^2)^2(\sinh(\alpha) + \alpha)\}]} \quad (1.5)$$

Here, $\alpha = \kappa d$ is the nondimensional axial wavenumber. The modified Taylor number, T , reaches a critical value, $T_c = 1715$, when the expression (1.5) is minimized. The advantage of using T instead of Ta is that the critical value does not then vary with \mathcal{U} . The corresponding critical wavenumber is $\alpha_c = 3.12$. The critical value of T , derived by Taylor is $T_c = 1706$, not far from more recent, and also more precise estimates: $T_c = 1708$ for $\alpha_c = 3.12$. Expression (1.5) is presented in figure 1.2.

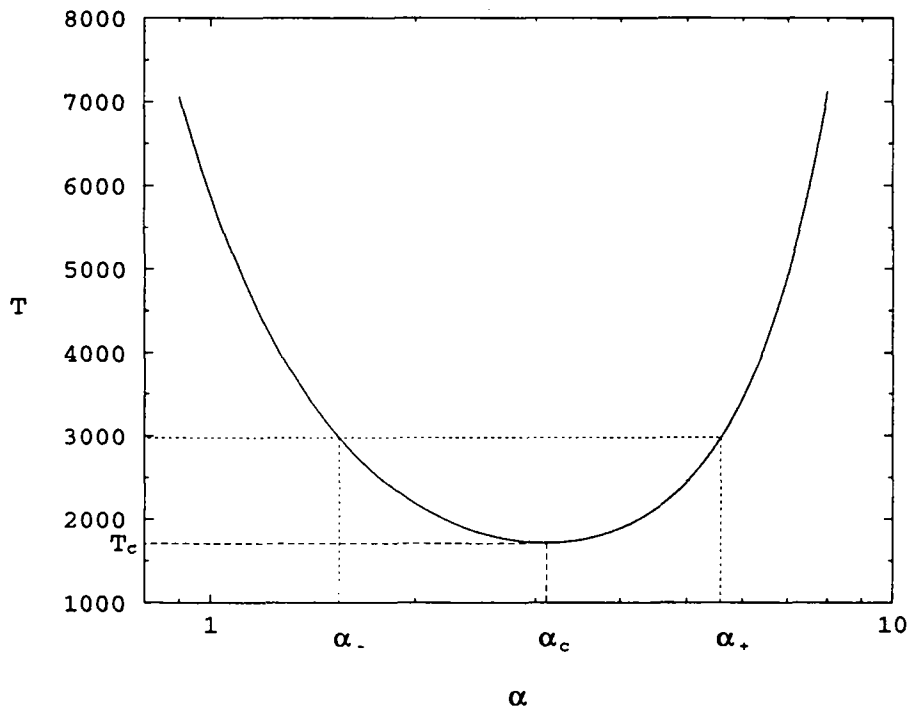


Figure 1.2: *Neutral stability curve in the narrow-gap case. Above the critical Taylor number, T_c , the axial wave number is no longer unique, but belongs to a finite interval, $[\alpha_-, \alpha_+]$.*

The first transition is mathematically described as a super-critical, steady bifurcation, also called the pitchfork bifurcation, from Couette flow to Taylor vortex flow.

Transition to spirals Krueger *et al.* [41] considered the linear problem for cylinders rotating in opposite directions, and found that in the narrow-gap approximation, when

\mathcal{U} is less than -0.78 , the most unstable disturbance is no longer axisymmetric. As \mathcal{U} decreases, the most unstable mode has first an azimuthal wavenumber $k = 1$, but then takes higher values in rapid succession. At the lowest value considered for \mathcal{U} , namely -1.25 , it appears that the most unstable mode is $k = 5$. Krueger *et al.* confirmed these theoretical results qualitatively for the particular cases: $\eta = 0.95$ and $\mathcal{U} = 0$, and $\eta = 0.95$ and $\mathcal{U} = -1$. The counter-rotating problem was treated theoretically by Chossat and Iooss [17] for the two cases: $\eta = 0.75$ and $\eta = 0.95$. They found the first *codimension-2 points*.

Let us first define the *codimension of a bifurcation*. According to Mullin [15], “the codimension of a bifurcation may be defined to be the smallest dimension of parameter space which contains the bifurcation in a persistent way”. In our case, once the geometric parameters are fixed, the flow is characterized by the two dynamic parameters Re_1 and Re_2 . In this two-dimensional parameter space only *codimension-1* and *codimension-2* bifurcations are expected. The *codimension-1* bifurcations are obtained by varying one parameter and holding the other. The *codimension-2* bifurcations are theoretically obtained by varying at the same time Re_1 and Re_2 . In practice a *codimension-2* bifurcation point is found at the intersection between two *codimension-1* bifurcation curves. In this thesis, we are primarily concerned with a special kind of *codimension-2* point that we call *codimension-2 point $k|k+1$* , and we will focus on those observed in the counter-rotating case. Such points belong to two different bifurcation curves, one indicating the transition from the azimuthal Couette flow to a spiral regime with k azimuthal modes, and the other one separating Couette flow from a spiral regime with $k+1$ azimuthal modes. Such kinds of *codimension-2* points are present in figure 5.4.

The findings of Chossat and Iooss [17] are summarized in the following tables.

codimension-2 point	0 1	1 2	2 3
\mathcal{U}	-0.572	-0.698	-1.149

Table 1.1: *codimension-2 points $k|k+1$ for $\eta = 0.75$.*

codimension-2 point	0 1	1 2	2 3	3 4	4 5
\mathcal{U}	-0.731	-0.763	-0.794	-0.875	-1.041

Table 1.2: *codimension-2 points $k|k+1$ for $\eta = 0.95$.*

The first transition curve, to spirals or Taylor vortices, can be found in Esser and Grossmann [29].

Second bifurcation Davey *et al.* [24] showed that, for $Re_2 = 0$, with increasing Re_1 , a second critical Reynolds number, Re_w , which depends on η , is reached. At Re_w , the Taylor vortex flow becomes unstable, the instability leading to a wavy vortex flow.

The wavy vortices have a definite frequency and move with a definite wave velocity in the azimuthal direction. Mathematically, this second instability is a time-periodic, super-critical bifurcation from Taylor vortex flow to wavy vortex flow. It is also called a Hopf bifurcation. The transition to wavy Taylor vortex flow has been studied experimentally by Coles [19]. One of the important observations of his experiments is the non-uniqueness of the spatial structure: different axial and azimuthal wavenumbers are observed at the same final Reynolds number, Re_1 . These different final states, at the same value of $Re_1 > Re_w$, are functions of the initial conditions and the path followed in parameter space.

The transition from Taylor vortex flow to wavy Taylor vortex flow is also the rule for any $Re_2 > Re_{min}$, with $Re_{min} = -155 \pm 10$, according to the stability diagram obtained experimentally by Andereck *et al.* [4] for $\eta = 0.883$. However, when counter-rotation takes place for higher absolute values of Re_2 , the first transitions are time-periodic bifurcations from a Couette flow to a spirals flow, and from this regime to interpenetrating spirals. Strikingly, at even higher counter-rotating (absolute) values of Re_2 , the flow first undergoes a transition from Couette flow to interpenetrating spirals and then directly to spiral turbulence. No path to chaos is available yet to explain such behaviour.

The portion of the flow regimes diagram obtained experimentally by Andereck *et al.* for $\eta = 0.883$ [4], that we have investigated, is reproduced in figure 1.3. The different flow patterns observed in this region are:

- azimuthal laminar flow with weak Ekman cells, denoted by AZI,
- Taylor vortices (TV): doughnut-like, counter-rotating vortices stacked on top of each other in the axial direction,
- spiral vortices (SPI): time-periodic, non-axisymmetric, helical vortices with one azimuthal frequency and a correlated axial frequency,
- wavy vortices (WV): time-periodic, non-axisymmetric, Taylor vortices with one azimuthal frequency,
- interpenetrating spirals (IPS): superposition of two spiral vortices travelling in opposite directions,
- wavy interpenetrating spirals (WIS): superposition of wavy spiral vortices, travelling in opposite directions,
- modulated wavy vortices (MWV): non-axisymmetric, Taylor vortices with two azimuthal frequencies.

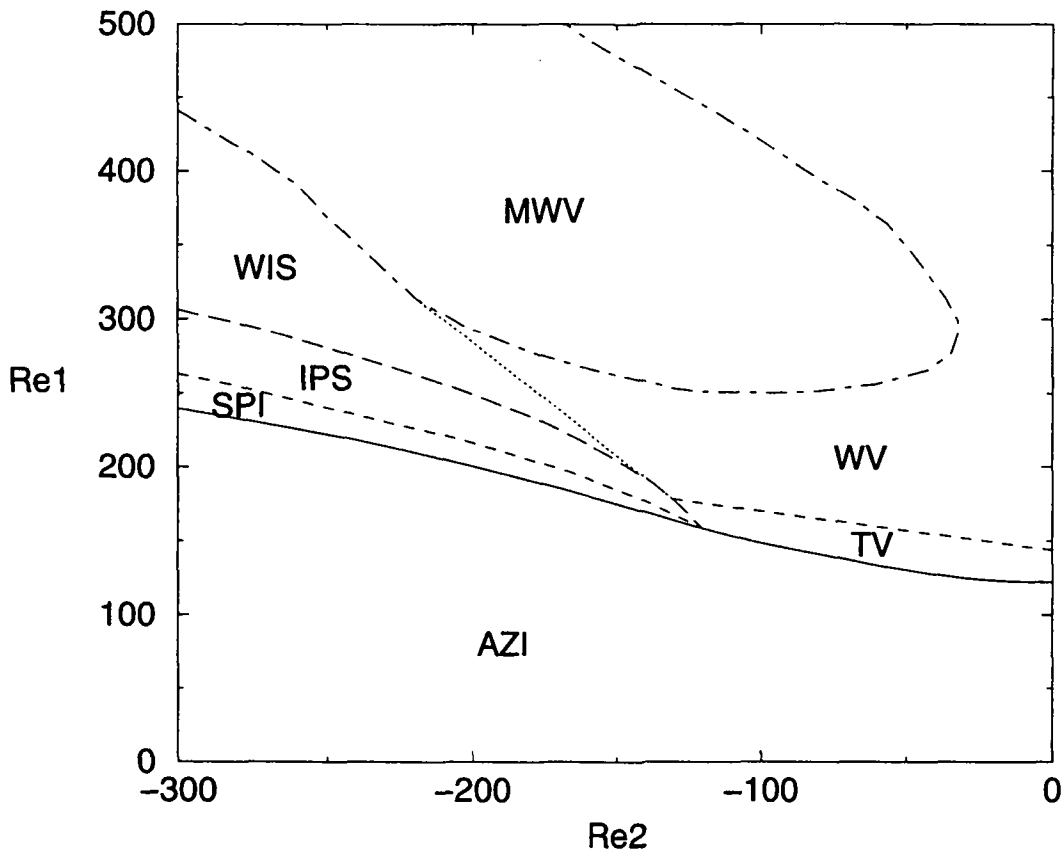


Figure 1.3: Reproduced here is the flow-regimes diagram of Andereck et al. [4], for $\eta = 0.883$ and $\Gamma = 30$. AZI refers to the azimuthal laminar flow with Ekman vortices, TV to the Taylor vortex flow, SPI to the spiral vortices flow, WV to the wavy vortices flow, IPS to the interpenetrating spirals flow, WIS to the wavy interpenetrating spirals flow, and MWV to the modulated wavy vortices according to their notations.

1.1 State-of-the-art

1.1.1 Experimental results

We are primarily interested in experiments that can be qualitatively compared to our simulations; that is, experiments with geometric and dynamic parameters close to ours, and, more particularly among these, the few experiments showing 2D flow fields. We therefore only report here the work of Wereley and Lueptow [68] and Litschke and Roesner [42].

Wereley and Lueptow [68] measured azimuthal velocity profiles for the Taylor vortex, wavy vortex, modulated wavy vortex and turbulent Taylor vortex flows using laser

Doppler velocimetry. In their experiment, the inner cylinder rotates while the outer cylinder, together with the horizontal end plates, are fixed. The radii ratio is $\eta = 0.844$ and the aspect ratio $\Gamma = 37.5$. These values are close to those of our classical Taylor-Couette flow simulations: $\eta = 0.875$ and $\Gamma = 30$. The ramp rate they used to increase the Reynolds number between successive flow states was $\frac{dRe}{dt} \approx 80$, where the time t is made dimensionless using the characteristic diffusion time $\frac{Ld}{\nu}$. The azimuthal velocity was measured at about 400 points per vortex pair, with typically ten points in the radial direction and between 35 and 45 in the axial direction. For the time-dependent flows: wavy vortex, modulated wavy vortex and turbulent Taylor vortex flow, Wereley and Lueptow averaged in time the velocity at each measurement point to obtain a full-field velocity profile. The total time needed to obtain one of these profiles was between four and six hours. For the turbulent Taylor vortex flow, the number of radial points was reduced to four while the number of axial points was kept at 40, in order that the overall measurement time remained the same. The experimental results they obtained were the first to confirm Davey's analytical prediction of the velocity field for super-critical Taylor vortex flow [23]. Their results also compared favorably with Marcus' results [48]. Apart from this, the other point they wished to clarify concerned the Reynolds number dependence of the flow pattern. The azimuthal velocity fields they measured indicate two predominant effects with increasing Reynolds number:

- the magnitude of the radial gradient of azimuthal velocity near both cylinders increases, characterizing boundary layers, while the velocity in the middle portion of the annular gap tends to become uniform, due to turbulent mixing, and
- the radial outflow region between pairs of vortices becomes increasingly jet-like.

Litschke and Roesner [42] investigated the road to turbulence in Taylor-Couette flow. They focused their study on the role of turbulence spots of intermittent character on the onset of turbulence. They observed that the spots moved in the same direction as the outer cylinder, while the interpenetrating spirals moved in the opposite direction. The interpenetrating spirals pattern are present at lower Reynolds numbers than necessary for turbulence spots, but remain when these spots appear. By varying the gap width they also found that the phenomenon of spiral turbulence, which represents a spirally shaped ribbon of turbulent flow in the annulus, could only be detected in geometries with a small gap size, i.e. a radii ratio $\eta \approx 1$. They investigated the growth of turbulent spirals for $\eta = 0.895$ and $\Gamma = 68.5$ under two different boundary conditions:

- when the top and bottom plates of the cylinders are rotating with the outer cylinder, they observed that, for a given outer Reynolds number, $Re_2 = -2737$, an abrupt start of the rotation of the inner cylinder to $Re_1 = 784$ produced different successive regimes. Spiral vortex structures begin to grow in the mid-plane region, they later begin to interpenetrate, then the first turbulent spot breaks up at mid-height. Finally, growing from midplane, turbulent regions start to build up the regular spiral ribbon.

- The behaviour changes dramatically if the end plates are connected with the inner cylinder. For an outer Reynolds number of -1598 and an inner one of 586 , again reached by a sudden start, the first structures, spiral vortices as well as turbulent spots and ribbons, can be observed near the end plates.

Litschke and Roesner's experiment is relevant to our simulations for two main reasons. Firstly, they studied the counter-rotating case, and secondly they used the two boundary conditions we are interested in for the end plates: that is, fixed to the inner cylinder or to the outer one.

1.1.2 Numerical results

We focus here on results obtained with accurate schemes and, more particularly, those obtained with spectral methods, and on simulations taking into account the finite-length effects in a realistic way.

Moser *et al.* [49] used a spectral method to study the classical Taylor-Couette flow, where only the inner cylinder is rotating. Periodicity is assumed in both axial and azimuthal directions. Fourier transforms are then used in those two directions. In the radial direction, their method employs an expansion in vector functions based on Chebyshev polynomials, which inherently satisfy the boundary conditions and the continuity equation. This has the advantage of treating the boundary and continuity constraints exactly and reducing the number of variables per spectral mode.

Fasel and Booz [30] used an implicit finite-difference method to study super-critical Taylor vortex flow. Their numerical scheme has fourth-order accuracy with respect to space dimensions and second-order accuracy with respect to time. Although this method is not extremely accurate, they showed their results were independent of the mesh size, thus indicating sufficient spatial resolution. Their study pertains to axisymmetric and axially-periodic flows. They investigated the wide gap case, for $\eta = 0.5$, and for Reynolds numbers, Re , varying from slightly super-critical to Re ten times the critical Reynolds number. When only the dynamic parameter Re is mentioned, it refers to the inner cylinder, and it is assumed that $Re_2 = 0$. The evolution of the torque with Re they present clearly shows the departure from Couette flow to Taylor vortex flow at $Re_c = 68.2$. The meridian cross-sections of the three velocity components, as well as the streamlines, the pressure and vorticity contours, reveal that, as Re is increased:

- outgoing jet-like structures tend to form,
- boundary layers form while the core region tends to move as a solid-body, and
- a much larger number of harmonics is necessary to describe the flow correctly.

Lücke *et al.* [43] investigated the classical Taylor-Couette flow both numerically and experimentally for $\Gamma = 1.05$ and $\eta = 0.5066$. Only the inner cylinder is rotating, while the outer one and the end plates are held fixed. Increasing the Reynolds number, they observed a transition from a symmetric, two-cell flow to an asymmetric flow which asymptotically tends to a one-cell flow. They made a quantitative comparison between numerics and experiment of the breaking of the mirror symmetry. The results agree well except near the transition threshold, in the corner regions, where the inner rotating cylinder touches the fixed end plates. This difference is presumably due to the treatment of the boundary conditions at the inner corners. A small gap separates the inner cylinder from the end plates in the experiment while this is not represented in the simulation. One of the purposes of the numerical method proposed in chapter 3 of this thesis is to alleviate this problem by introducing more realistic boundary conditions.

Neitzel [51] performed computations of time-dependent Taylor vortex flows in finite-length geometries. The motion is initiated by an impulsive start of the inner cylinder from a state of rest of the entire system. The rigid end plates are attached to the inner cylinder and therefore begin to rotate at $t = 0$. The flow is supposed to be axisymmetric. The unknowns considered are the stream-function, the circulation in the azimuthal direction, and the θ -component of the vorticity. Neitzel reduced the size of the computational domain by assuming the flow to be symmetric about the midplane. He considered two different aspect ratios, $\Gamma = 22$ and $\Gamma = 23.35$ and a unique radii ratio, $\eta = 0.727$. The case ($\Gamma = 23.35, \eta = 0.727$) was chosen to match the smallest experimental configuration of Burkhalter and Koschmieder [12]. Neitzel made simulations for different ratios: $\frac{Re}{Re_c} = 1.03, 2, 3, 4$ and 6 . Here, $Re = \frac{\Omega_1 d^2}{\nu}$ denotes the Reynolds number and Re_c the critical Reynolds number from linear-stability theory for infinite cylinders. For each of the simulations, he presents:

- the evolution of the end cell size with the Taylor to critical Taylor number ratio, $\frac{Ta}{Ta_c} = \left(\frac{Re}{Re_c}\right)^2$,
- the interior cell wavelength versus $\frac{Ta}{Ta_c}$,
- the amplitude histories, indicating the development of the Taylor-vortex structure, and
- the vortex front velocity evolution with $\frac{Re}{Re_c}$.

His results show a non-linear increase of the end cell size with the Taylor number, Ta , and a decrease of the interior cell wavelength with Ta . The latter result is in contradiction with the cusped-like behaviour found by Burkhalter and Koschmieder. The amplitude histories Neitzel obtained clearly show that no steady state was reached for $\frac{Re}{Re_c} = 1.03$ and $\frac{Re}{Re_c} = 6$. He also reported that the onset-time decreases with $\frac{Re}{Re_c}$. And, as $\frac{Re}{Re_c} \rightarrow 1$, the onset-time of the Taylor vortices tends to infinity. Neitzel's explanation concerning the wrong number of vortices he found for Reynolds ratios above 4 has to

be discarded. According to him, the fact that his simulations are axisymmetric could be responsible for the inaccurate number of vortices obtained. We have ourselves performed impulsive start simulations, also considering the axisymmetric case, and we have found the correct number of vortices, as predicted by the linear stability theory together with the quantization condition. However, we chose different boundary conditions. In our case, the end plates are attached to the stationary outer cylinder, and we do not make the mirror-symmetry hypothesis. In our opinion, the too short integration time Neitzel used accounts for the discrepancies between his simulations and Burkhalter and Koschmieder's experiments. Furthermore, Neitzel observed not only the propagation of vortices from the end plate into the interior but also the development of cells near the midplane at the same time. This puzzling result might either be due to his choice of symmetric boundary conditions at the midplane, which might have introduced a local perturbation of sufficient intensity to generate Taylor vortices, or be due to the fact that the end plates are rotating together with the inner cylinder in his case. This choice of boundary condition is rarely found in the literature and so no comparison could be made.

King *et al.* [38] conducted both laboratory experiments and numerical simulations to determine the speed of travelling azimuthal waves on Taylor vortices in a circular Couette system with the inner cylinder rotating and the outer at rest. The dependence of the wave speed on the Reynolds number, Re , the radii ratio, η , the average axial wavelength, and the number of azimuthal waves, was investigated both experimentally and numerically. They found that the wave speed was weakly dependent on Reynolds number, aspect ratio, axial wavelength and number of waves. However, at large Reynolds numbers, the wave speed depends primarily only on η , increasing monotonically threefold in the range studied, i.e. $0.63 \leq \eta \leq 0.95$. King *et al.* also performed an approximate stability analysis which predicts that the wave speed at large Reynolds numbers in the small gap limit, $\eta \rightarrow 1$, approaches the value $0.563\Omega_1$, where Ω_1 is the angular velocity of the inner cylinder. Their measurements of the wave speed compare remarkably well to this predicted value.

Marcus [48] assumes periodicity in the axial direction which enables him to use Fourier polynomials in that direction. The azimuthal direction also is discretized using Fourier expansions, while Chebyshev polynomials are chosen for the radial direction. He imposes what he calls "shif-and-reflect" symmetry, that requires a p -azimuthal-waves flow to satisfy:

$$\begin{cases} u(r, \theta, z, t) = u(r, \theta + \frac{\pi}{p}, -z, t) , \\ v(r, \theta, z, t) = v(r, \theta + \frac{\pi}{p}, -z, t) , \\ w(r, \theta, z, t) = -w(r, \theta + \frac{\pi}{p}, -z, t) , \end{cases} \quad (1.6)$$

with t , the time. Time discretization is performed with a time-splitting method, and the resulting splitting errors are removed by special Green functions. The diffusion term is

treated implicitly and the non-linear one explicitly. He shows several 2-dimensional projections of the velocity field, and conjectures that the travelling waves are a secondary instability caused by the strong radial motion in the outflow boundaries of the Taylor vortices and are not shear instabilities associated with inflection points of the azimuthal flow. He also demonstrates that, at the critical Reynolds number where Taylor vortex flow becomes unstable to wavy-vortex flow, the speed of the travelling wave is equal to the azimuthal angular velocity of the fluid at the centre of the Taylor vortices. His results constitute a landmark in the study of wavy vortex flow.

Streett and Hussaini [61, 62] propose two spectral collocation algorithms that do not rely on the infinite cylinders hypothesis. Hence, they use Gauss-Lobatto-Chebyshev points in both the radial and the axial directions. The azimuthal direction is discretized using Fourier expansions. A multi-domain technique is used in the axial direction. In the first algorithm, they perform time discretization with a time-splitting method and reduce the resulting slip velocity to a small value (varying between about 10^{-8} and 10^{-10}). The second algorithm employs a staggered-mesh discretization, combined with a multi-grid/conjugate-gradient technique. It is the most accurate of the two algorithms, but it pertains only to the axisymmetric case. In a classical way, both algorithms treat the diffusion term implicitly and the non-linear one explicitly. We have made comparisons with their results in chapter 4.

Coughlin and Marcus [21] performed a mathematical analysis of the transition from temporally periodic rotating waves to quasi-periodic modulated waves in rotating flows with circularly symmetric boundary conditions and applied it to the flow between concentric rotating cylinders. They used Floquet theory to deduce the functional form of instabilities of the rotating wave, and from this derived the form of modulated wave solution to the Navier-Stokes equations. They used the pseudo-spectral, initial-value code of Marcus [48] to compute solutions to the Navier-Stokes equations for both rotating waves and two branches of modulated waves, those discussed by Gorman and Swinney [34, 35], and those discovered by Zhang and Swinney [70]. The first flow, referred to as GS, is a two-travelling wave flow, while the second, referred to as ZS, is a non-travelling modulation. They argue that the centrifugal instability beyond the primary transition to Taylor vortex flow is important only in maintaining the basic vortical structure. They describe this structure as adequate to neutralize the centrifugal instability and suggest that the subsequent transitions to WV and MWV are due to the instability of the outflow jet.

1.2 Choice of the parameters

The parameters characterizing Taylor-Couette flow are of two types: geometric and dynamic. Belonging to the first class are the radii ratio, η , and the aspect ratio, Γ . The

way the horizontal end plates are fixed, to the inner cylinder or to the outer one, or even rotating independently from the cylinders, can be considered as both a geometric and a dynamic parameter. The two dynamic parameters used by Andereck *et al.* [4] are the inner and outer Reynolds numbers, Re_1 and Re_2 , respectively. To these two classical dynamic parameters, we add the acceleration rate between two Reynolds pairs, (Re_1, Re_2) , or more generally, the path followed in parameter space.

Authors	η	$\mathcal{U} = \frac{\Omega_2}{\Omega_1}$	Γ	Fixation
Couette	0.98	∞	32	to R_1
Taylor	0.73 0.74 0.88 0.94	-2.3 to 0.65	81 87 186 383	
Coles	0.874		28	
Andereck <i>et al.</i>	0.883		30	to R_2
King <i>et al.</i>	0.50 0.88 0.95	-2 to 0.2	80	

Table 1.3: *Parameter range studied by different authors.*

1.2.1 Geometric parameters

Aspect ratio: Most simulations consider infinite aspect ratios, and most experiments use large aspect ratios. Indeed, the aspect ratios in Taylor's experiments varied between 81 and 383 (see table 1.3 for more detail). There are two advantages in using an infinite aspect ratio for the simulations. The first one is that the base flow is known analytically in that case. The second one is that, considering only transitions to axially periodic flows like TV, WV or MWV, one can use periodic boundary conditions together with Fourier series to discretize in the axial direction. But, according to some recent work [15], the finite length of the apparatus has an indisputable influence on the transition process. The finite case was therefore chosen in this thesis.

In choosing an aspect ratio, two guidelines were followed. The first one was to treat a case already investigated experimentally to compare against and thereby validate our results. Among the numerous experiments, we can cite Couette's apparatus, which had an aspect ratio of 32, King *et al.*'s with an aspect ratio of 80, Coles' with an aspect ratio of 28 and Andereck *et al.*'s aspect ratio of 30. In order to simulate the physics correctly, one has to use a number of spectral elements, E , proportional to the aspect ratio. The calculation cost involved in the simulation grows as E^2 . And, the time for the flow to settle is proportional to the diffusion time in the axial direction, which itself is proportional to Γ^2 . Hence, one is quickly limited to low values of Γ . The maximum Γ attainable for simulating an unsteady flow is about 30 (to 40) for our code. The second guideline is in contradiction with the first. It is indeed the aim of any research to produce original results. We therefore decided to treat the case of an aspect ratio, Γ , not found in the literature, or more precisely a couple (η, Γ) never studied before. Most of the simulations and experiments performed for finite aspect ratios, in the range 0 to

40, are low aspect ratios. Streett and Hussaini [61, 62] produced numerical results for $\Gamma \simeq 1$. Mullin [50] and Pfister *et al.* [54] studied a larger range, from 0.3 to 12.4. The experimentalists rarely investigated Taylor-Couette flow for aspect ratios smaller than about 30, except in the work of Benjamin and Mullin [10] and in that of Pfister *et al.* [54], who made comparisons with Mullin's numerical results. The intermediate aspect ratio we have chosen, $\Gamma = 12$, is large enough to produce a more interesting path to chaos than the now well-known period doubling route, and small enough for the flow regimes to be distinguished if sufficient precision can be reached with the numerical discretization.

Radii ratio: Because of the simplifications it allows, the small-gap case is often chosen in theoretical work. It is therefore very much studied experimentally and numerically for comparison purposes. The small-gap case is also interesting because it can have applications in mechanical engineering for slide bearings. However, it is too difficult to make accurate measurements in a small gap, when dealing with aspect ratios below 12. Pfister [53] therefore uses $\eta = 0.5$. We chose the radii ratio, $\eta = 0.875$, to compare with Marcus' results. The case, $\eta = 0.875$ and $\Gamma = 12$, we study is original, the closest configurations being that of Mullin, $\eta = 0.5$ and $\Gamma = 12$, and the one of Marcus, $\eta = 0.875$ and $\Gamma = \infty$. The geometric parameters and the reasons for these choices are summarized in table 1.4

Γ	12	20	30
η	Original	Original	Comparison [48]

Table 1.4: *Choice of the geometrical parameters.*

End plates fixation: The end plates are most often attached to the outer cylinder. This is what we call the classical fixation configuration. When the inner cylinder is set into motion, and only this cylinder, the bifurcation to Taylor vortices is imperfect due to the end conditions. Vortices first start growing from the Ekman cells at the top and bottom. The growth rate is small at the beginning but then Taylor vortices appear suddenly in the remaining Couette-flow central region. Alziary de Roquefort and Grillaud [3] observed that at low subcritical Reynolds numbers only two counter-rotating Ekman cells, connected at midplane, were present in the flow. Weak ghost cells then appear in pairs until $N - 2$ cells (Ekman cells+ghost cells) finally occupy the whole annulus length at a slightly subcritical Reynolds number. Once Re_c is exceeded, $N - 2$ Taylor vortices replace $N - 4$ ghost cells, the 2 Ekman cells still remaining. The total number of cells evolves then from $N - 2$ to N when the transition curve is passed. Couette [20], and later Mullin [15], used a different configuration in which the end plates were rotating together with the inner cylinder, while the outer one was fixed.

In his short-length, Taylor-Couette geometry, Mullin found that the rotating ends case also produced axisymmetry-breaking bifurcations, but curiously in a wider range of the parameter space than in the classical case.

Our finding is that, in the counter-rotating case, the classical fixation forces the instability to appear first in the midplane region, in the form of a pair of azimuthally-partially-developed, counter-rotating vortices which are deflected, the upper, azimuthally-unclosed vortex towards the upper wall and the lower, unclosed vortex towards the lower wall, so that an arrowhead spiral pattern starts to develop. The experiment of Litschke and Roesner [42] confirms our observation. The presence of the end plates, and the way they are fixed to the outer cylinder, may explain why the spiral patterns start forming in the middle (see chapter 7).

According to the work of Chossat and Iooss [17], the end plates fixation configuration is not the most important feature to determine whether the flow will bifurcate from the Couette regime to Taylor vortices, or from Couette flow to spirals. They investigated the first transition in the counter-rotating case for cylinders of infinite length. Bearing in mind the results of Rayleigh [55] concerning the position of the nodal surface, Chossat and Iooss' findings tend to prove that the change from Taylor vortices to spirals is correlated to the nodal surface position. As the rate of counter-rotation, denoted by $|\mathcal{U}| = \left| \frac{\Omega_1}{\Omega_2} \right|$, increases, the nodal surface moves from the outer cylinder towards the inner cylinder. Our own interpretation (see chapter 7) is that the super-critical flow is no longer the Taylor vortex flow but the spirals flow, when the corrected nodal surface leaves the outer cylinder. This correction means that we take into account the diffusivity by adding a buffer layer to the non-viscous unstable layer. This increases slightly the value of the inviscid nodal radius.

1.2.2 Dynamic parameters

The counter rotating case, $(Re_1 \geq 0, Re_2 \leq 0)$, is the least studied. The most complete contribution is that of Andereck *et al.* who systematically explored the parameters range $(0 \leq Re_1 \leq 960, -4000 \leq Re_2 \leq 1200)$. In the range, $(0 \leq Re_1 \leq 960, -4000 \leq Re_2 \leq 0)$, the different flow patterns they observed were:

- azimuthal laminar flow,
- Taylor vortices,
- spiral vortices,
- wavy vortices,
- interpenetrating spirals,
- wavy, interpenetrating spirals,
- modulated, wavy vortices,

- intermittent turbulent spots,
- spiral turbulence, and
- featureless turbulence.

We decided to study the first transition in the counter-rotating case where some theoretical knowledge is also available. The theoretical investigations of Chossat and Iooss [17], concerned with an infinite aspect ratio and two radii ratios: $\eta = 0.75$ and $\eta = 0.95$, were a good starting point for our own study. A linear stability analysis is first needed to extend their results to the case we chose, $\eta = 0.875$. Chossat and Iooss studied the succession of transitions to spirals with k azimuthal modes, k ranging from 0 to 2, for $\eta = 0.75$ (see table 1.1), and from 0 to 4, for $\eta = 0.95$ (see table 1.2). They found the marginal stability curves for each k , as well as the codimension-2 points where the super-critical regime jumps from a k spirals pattern to a $k + 1$ spirals pattern. Chossat [16] postulates that the interpenetrating spirals observed in the Andereck *et al.* experiments could result from the superposition of the k and $k + 1$ spiral modes, travelling in opposite directions.

1.2.3 History parameter

The flow regime does not only depend on the geometric and dynamic parameters but also on the path followed in parameter space to reach a given set of parameters. The parameters we call history parameters are those that could be varied with time in a real experiment. They thus comprise \dot{Re}_1 , \dot{Re}_2 and $\dot{\Gamma}$, where $\dot{}$ stands for time derivative. We discard $\dot{\eta}$ from the history parameters because it is not possible to make an experiment where η varies continuously, while keeping low eccentricity, surface deformation, etc.

In the case where only the inner cylinder is rotating, Burkhalter and Koschmieder [12] produced Taylor vortices whose wavelength, λ , is different from the critical wavelength, λ_c . They obtained $\lambda < \lambda_c$ through “sudden-start” experiments and $\lambda > \lambda_c$ through “filling” experiments, i.e. in which Γ varies continuously with time.

According to Coles [19], the path followed by Re_1 , for $Re_2 = 0$, also produces different final states when dealing with super-critical flows. For instance, he obtained different flow regimes when decreasing or increasing the Reynolds number to a final Reynolds number $Re > Re_c$.

Andereck *et al.* state that, when \dot{Re} stays below what they call the adiabatic growth rate, the same final state is observed whichever path is followed.

1.3 Aims of the thesis

Our first goal is to find a physical explanation to the second bifurcation of the classical Taylor-Couette flow. Because, according to Marcus [48]: “Analytic finite-amplitude

and linearized or truncated numerical studies have given us many mathematical details of wavy-vortex flow, and the experimental studies have supplied us with stability diagrams, wave speed measurements and torque-Reynolds-number relations, but surprisingly little *physical* understanding of Taylor-Couette flow has been gained since Rayleigh [56] explained the inviscid centrifugal instability that governs the formation of Taylor vortices”.

One of the facts we were most puzzled about at the beginning of this thesis work was that, depending on Re_2 , the first transition may either form Taylor vortices or spirals. But, the cause for the appearance of these two different patterns is the same. The centrifugal instability gives rise to these structures when a critical value of the Reynolds number is exceeded. Above Re_c the diffusion can no longer resist the latent centrifugal instability. Hence, our second goal is to find out the mechanism responsible for the appearance of spirals in the counter-rotating case.

1.4 Organization of the chapters

Apart from the introduction chapter (chapter 1), this thesis has two main parts. In the first part, the numerical tools are set up and validated. This part is divided into an introductory chapter, chapter 2, devoted to a description of the general features of the spectral element method. Then, chapter 3 describes the assembling of the numerical algorithms that constitute the whole DNS program. The last section of this chapter treats a subset of the DNS code, dealing with the linearized Navier-Stokes equations and periodic, axial boundary conditions. Chapter 4 addresses the validation of the code and its performance on different computers. The validation is first concerned with numerical tests and then by physical tests, i.e. comparison with published experiments and simulations.

The second part of the thesis is concerned with the description and interpretation of the results of the simulations performed with the two numerical tools described in the first part. The first chapter of the second part, chapter 5, is devoted to the analysis of the results obtained with the linear stability code. Then, chapter 6 deals with the classical Taylor-Couette flow, that is when only the inner cylinder is rotating, and chapter 7 treats the counter-rotating case. Finally, conclusions and perspectives are drawn in chapter 8.

Part I

Numerical tools

Chapter 2

Introduction to the spectral element method

The spectral element technique is an extension of spectral methods. The comprehensive book by Canuto *et al.* [13] describes the spectral methods. Patera later devised from these the spectral element method [52]. More recent overviews of the method are given by Rønquist [58] and by Maday and Patera [45]. Shorter, and also good, introductions can be found in Timmermans [67] and Couzy [22]. Spectral element methods have the geometric flexibility of other decomposition methods, such as the h -type finite element method [32]. The spectral element technique is similar to the p -type finite element method proposed by Babuška *et al.* [9].

The spectral element technique and, more generally, spectral methods are characterized by the property that for problems with a sufficiently smooth solution, exponential convergence of the approximation to the solution is obtained by expanding the solution in a series of special functions, solutions of singular Sturm-Liouville problems. The expansion functions classically used in spectral element methods are Fourier expansions, Chebyshev and Legendre polynomials.

In the spectral element approximation, the domain is divided into non-overlapping, conforming elements. The discretization process is based on a variational formulation of the partial differential equations. The main effect of the variational approach is to lower the continuity requirements at the element boundaries. The integral equations appearing in the variational formulation are integrated by high-order Gauss-Lobatto-Legendre quadrature. The variables in each element are expanded in a series of high order polynomial basis functions. For reasons of efficiency, a tensorial basis is used. The discrete matrix-vector system is generated in the standard Galerkin way, leading to a block-banded system.

In the following sections, the fundamentals of spectral elements are described and a one-dimensional, linear, elliptic model equation is given as an example.

2.1 p -type weighted residual methods

In this section the concept of p -convergence of a numerical approximation method is discussed from a general point of view. The following partial differential equation is taken as a starting point.

$$\mathcal{L}s = f \text{ in } \Upsilon, \quad (2.1)$$

with Υ an open bounded domain. Here, $\mathcal{L}: U \subset H \rightarrow H$ is a continuous positive-definite differential operator with its domain being the linear vector space U , a subspace of a Hilbert space H , and $f \in C^0(\Upsilon)$.

V

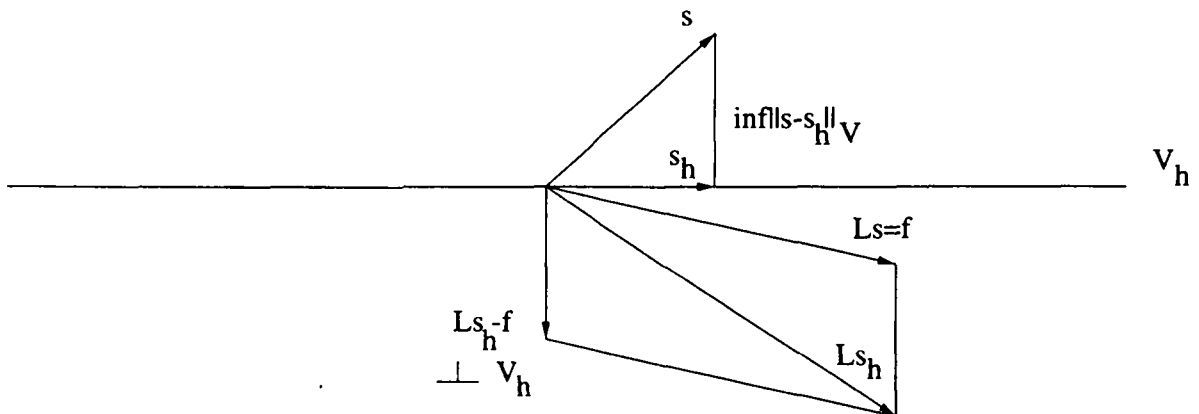


Figure 2.1: Galerkin weighted residual approximation method. Galerkin “best approximation result”.

The class of p -type weighted residual techniques can be divided into global methods, such as spectral methods, and methods that use any form of domain decomposition, such as the spectral element method. The main advantage of domain decomposition techniques is that they are able to handle complex geometries. Another consequence is that the system matrix is block-banded, which results in less computing time and memory storage compared to global methods. Moreover, these techniques provide a very useful application for parallel computing, since many operations can be performed at elemental level [22].

If a Galerkin domain decomposition method is used, the basis for the numerical scheme is the variational or weak formulation of equation (2.1),

find an $s \in U \subset V$ such that

$$a(s, v) = (f, v)_H \quad \forall v \in V, \quad (2.2)$$

where the functions $v \in V$ are the trial functions, $(f, v)_H$ is the natural inner product in V , and $a(u, v) = (\mathcal{L}u, v)_H$ is a bilinear form. If the bilinear form, $a(\cdot, \cdot)$, is continuous and coercive, application of the Lax-Milgram lemma [18] states that problem (2.2) has a unique solution $s \in V$. Further approximation of V by the $(N + 1)$ -dimensional subspace V_h with basis $(\psi_i)_{i \in \{0, 1, \dots, N\}}$ gives the discrete problem:

Find an $s_h \in V_h$ such that

$$a(s_h, v_h) = (f, v_h)_H \quad \forall v_h \in V_h, \quad (2.3)$$

or equivalently, find an $s_h \in V_h$ such that

$$a(s_h, \psi_i) = (f, \psi_i)_H \quad \forall i \in \{0, 1, \dots, N\}. \quad (2.4)$$

An important result of the variational Galerkin formulation is the following lemma of Céa [18], also known as the “best approximation result”:

$$\|s - s_h\|_V \leq C \|s - v_h\|_V \quad \forall v_h \in V_h, \quad (2.5)$$

where $\|\cdot\|_V$ denotes the norm of the space V , and C is a constant. The lemma states that the error $\|s - s_h\|_V$, called approximation error, is bounded by the smallest distance $\|s - v_h\|_V$. In other words, the approximation s_h is as accurate as the best approximation for the exact solution s in the space V_h . This result is illustrated in figure 2.1.

For practical reasons, V_h is chosen as a space of polynomials of degree $\leq N$. The idea behind p -type methods is to obtain a more accurate solution by decreasing the distance $\inf \|s - v_h\|_V$. This is done by increasing N , the polynomial degree. This approach is called p -convergence. Before describing the spectral element discretization, we first analyse how accurately a function s can be approximated by increasing the degree of its approximation.

2.2 Spectral approximation

In a weighted residual approximation method, the approximate solution to the ordinary differential equation is expanded in a truncated series of expansion functions:

$$S_N s(x) = \sum_{i=0}^N s_i \phi_i(x), \quad (2.6)$$

with s_i , the expansion coefficients and ϕ_i , the expansion functions. In p -type methods, convergence is achieved by letting $N \rightarrow \infty$, i.e. by increasing the degree of the expansion.

The essential point behind spectral methods is that the expansion functions are chosen such that the expansion (2.6) has the property of exponential convergence if the approximated function is sufficiently smooth. The convergence rate is therefore determined by the smoothness of that function. In order to establish this, let us consider the expansion of an analytical function, s , in terms of an infinite sequence of orthogonal functions, ϕ_i :

$$s(x) = \sum_{i=0}^{\infty} s_i \phi_i(x) . \quad (2.7)$$

If the system of orthogonal functions is complete in a suitable Hilbert space, the relation (2.7) can be inverted. Thus, the function s can be described both through its values in physical space and through its coefficients, s_i , in spectral space.

In the case of periodic functions, the obvious expansions are Fourier expansions. A well-known result of Fourier theory states that if a function s is periodic and analytical with periodic derivatives, the i th coefficient of its Fourier series decays faster than any inverse power of i , that is,

$$\forall n > 0, \exists i_0, \forall i > i_0, |s_i| < i^{-n} . \quad (2.8)$$

The exponential (or spectral) rate of convergence can also be obtained for expansions of non-periodic functions. If the function s is expanded in a series of eigenfunctions of singular Sturm-Liouville problems, the i th coefficient of the expansion decays faster than any inverse power of the eigenvalue, λ_i , of the associated Sturm-Liouville problem, that is,

$$\forall n > 0, \exists i_0, \forall i > i_0, |s_i| < \lambda_i^{-n} . \quad (2.9)$$

In Appendix B, more results on Sturm-Liouville expansions are given. In particular, polynomial expansions are of importance for reasons of computational efficiency. In Canuto *et al.* [13], it is shown that the only polynomial solutions to singular Sturm-Liouville problems on $[-1, 1]$ are encompassed in the class of Jacobi polynomials. The two most common applications in this class are the Chebyshev and Legendre polynomials. For a detailed survey of properties of these polynomials see Abramovitz and Stegun [1]. Since Legendre-type expansions are typically used in the spectral element method, some properties of Legendre polynomials and Legendre expansions are given in Appendix B as well.

2.3 Pseudo-spectral approximation

The approximation (2.6) defines a continuous transform between physical space and spectral space. In general, the spectral expansion coefficients s_i are not computed exactly, since they depend on all values of the function in physical space. In pseudo-spectral methods, a set of approximate coefficients, \hat{s}_i , is calculated using the values of s at a finite number of interpolation points. The finite series defined by the discrete coefficients \hat{s}_i is then the interpolating polynomial of s at the interpolation points. It is given by:

$$\mathcal{I}_N s(x) = \sum_{i=0}^N \hat{s}_i \phi_i(x) . \quad (2.10)$$

The interpolating polynomial satisfies:

$$\mathcal{I}_N s(x_i) = s(x_i) , \quad \forall i \in \{0, 1, \dots, N\} , \quad (2.11)$$

where the x_i are the interpolation points. Equation (2.11) gives the discrete transform between the values $s(x_i)$ and the set of its discrete coefficients, \hat{s}_i .

In Canuto *et al.* [13], it is shown that if the interpolation points are Gauss-type quadrature points, the spectral accuracy is retained in replacing the continuous transform with the discrete transform. However, doing this adds another cause of error, called integration error. In practice, the interpolating polynomial is often written as:

$$\mathcal{I}_N s(x) = \sum_{i=0}^N s_i \varphi_i(x) , \quad (2.12)$$

with $s_i = s(x_i)$ and φ_i the Lagrangian interpolant in the Gauss-type quadrature points. Explicit values for φ_i and its derivatives in the collocation points, x_i , are given for Legendre interpolation in Appendix B.

2.4 A one-dimensional model equation

In order to establish the fundamentals of the spectral element technique, the following linear, symmetric, elliptic boundary value problem in one dimension is considered:

$$\begin{cases} -\frac{d}{dx} \left(a(x) \frac{ds}{dx} \right) + b(x)s = 0 & \text{in } \Upsilon =]x_1, x_2[, \\ s(x_1) = s(x_2) = 0 . \end{cases} \quad (2.13)$$

Let us define α , β and γ such that a and b satisfy:

$$0 < \alpha < a(x) < \beta \quad \text{and} \quad 0 < b(x) < \gamma, \quad (2.14)$$

where a and b belong to $C^0(\bar{\Upsilon})$, $C^0(\bar{\Upsilon})$ being the space of continuous functions in $\bar{\Upsilon}$. Let us also introduce $f \in \mathcal{L}^2(\Upsilon)$ with the Lebesgue space $\mathcal{L}^2(\Upsilon)$ defined by:

$$\mathcal{L}^2(\Upsilon) = \left\{ v \mid \int_{\Upsilon} v^2 dx < \infty \right\}. \quad (2.15)$$

The natural inner product in this space is defined as:

$$(u, v) = \int_{\Upsilon} u(x)v(x)dx, \quad \forall u, v \in \mathcal{L}^2(\Upsilon), \quad (2.16)$$

with the induced norm, $\|v\|^2 = (v, v)$. The basis for the numerical scheme is the variational equivalent to problem (2.13). The space of acceptable solutions is the Sobolev space $\mathcal{H}_0^1(\Upsilon)$ given by:

$$\mathcal{H}_0^1(\Upsilon) = \left\{ v \in \mathcal{L}^2(\Upsilon) \mid \frac{dv}{dx} \in \mathcal{L}^2(\Upsilon), v(x_1) = v(x_2) = 0 \right\}. \quad (2.17)$$

The variational equivalent to problem (2.13) can be written as:

Find an $s \in \mathcal{H}_0^1(\Upsilon)$ such that

$$a(s, v) = (f, v), \quad \forall v \in \mathcal{H}_0^1(\Upsilon), \quad (2.18)$$

where the bilinear continuous form $a(., .)$ is defined by:

$$a(u, v) = \int_{\Upsilon} a \frac{du}{dx} \frac{dv}{dx} dx + \int_{\Upsilon} bu(x)v(x)dx, \quad \forall u, v \in \mathcal{H}_0^1(\Upsilon). \quad (2.19)$$

The bilinear form $a(., .)$ is continuous and coercive. Application of the Lax-Milgram lemma to problem (2.18) therefore leads to a unique solution $s \in \mathcal{H}_0^1(\Upsilon)$.

The first step in the spectral element discretization is to break up the domain Υ into E non-overlapping elements Υ^e .

$$\bar{\Upsilon} = \cup_{e=1}^E \bar{\Upsilon}^e = \cup_{e=1}^E [x_0^e, x_0^e + l^e], \quad (2.20)$$

where the length and origin of each macro-element, Υ^e , are respectively l^e and x_0^e .

The next step is to discretize the space of acceptable solutions $\mathcal{H}_0^1(\Upsilon)$. The space of approximation for the solution s is taken to be the $(N + 1)$ -dimensional subspace X_0 of $\mathcal{H}_0^1(\Upsilon)$ defined as:

$$X_0 = \mathcal{H}_0^1(\Upsilon) \cap \mathcal{P}_{N,E}(\Upsilon), \quad (2.21)$$

where $\mathcal{P}_{N,E}(\Upsilon) = \{\phi \in C^0(\Upsilon), \forall e \in \{1, 2, \dots, N\}, \phi|_{\Upsilon^e} \in \mathcal{P}_N(\Upsilon^e)\}$, $\mathcal{P}_N(\Upsilon^e)$ denoting the space of polynomials in Υ^e of degree less than N . The discrete variational problem can now be written as: find $s_h \in X_0$ such that

$$\sum_{e=1}^E a(s_h, v_h)_{\Upsilon^e} = \sum_{e=1}^E (f, v_h)_{\Upsilon^e}, \quad \forall v_h \in X_0, \quad (2.22)$$

where the subscript Υ^e denotes the restriction to element Υ^e . In general, equation (2.22) can not be implemented without numerical quadrature. The choice of quadrature corresponds to the choice of a discrete inner product. The high-order discretization suggests a Gauss-type quadrature formula. Therefore, a Legendre-type quadrature is chosen, since it has a natural weight function equal to one. For reasons to be explained at the end of this section, Gauss-Lobatto integration is chosen. This quadrature is defined by:

$$\int_{-1}^1 f(\zeta) d\zeta = \sum_{k=0}^N f(\zeta_k) \rho_k, \quad \forall f \in \mathcal{P}_N([-1, 1]), \quad (2.23)$$

where the ζ_k are the Gauss-Lobatto-Legendre points and the ρ_k , the Gauss-Lobatto-Legendre weights. In order to be able to apply the quadrature, an affine transformation is used to map each element Υ^e to the standard, or parent, element $\hat{\Upsilon} =]-1, 1[$, $x \in \Upsilon^e \rightarrow \zeta \in \hat{\Upsilon}$. Due to this transformation, the terms in equation (2.22) can be written as:

$$a(s_h, v_h)_{\Upsilon^e} = \int_{\hat{\Upsilon}} a \frac{ds_h}{d\zeta} \frac{dv_h}{d\zeta} J^{-1} d\zeta + \int_{\hat{\Upsilon}} b s_h(\zeta) v_h(\zeta) J d\zeta, \quad (2.24)$$

$$(f, v_h)_{\Upsilon^e} = \int_{\hat{\Upsilon}} f v_h(\zeta) J d\zeta. \quad (2.25)$$

The transformation Jacobian, J , is given by:

$$J = \frac{dx}{d\zeta}. \quad (2.26)$$

Applying the Gauss-Lobatto-Legendre quadrature to the system (2.22) yields the following fully discrete problem: find $s_h \in X_0$ such that

$$\sum_{e=1}^E a(s_h, v_h)_{GLL} = \sum_{e=1}^E (f, v_h)_{GLL}, \quad \forall v_h \in X_0. \quad (2.27)$$

The corresponding discrete inner product $(\cdot, \cdot)_{GLL}$ with induced norm $\|\cdot\|_{GLL}$ is given by:

$$(u, v)_{GLL} = \sum_{k=0}^N J_k u(\zeta_k) v(\zeta_k) \rho_k, \quad \forall u, v \in C^0(\hat{\Upsilon}), \quad (2.28)$$

where $J_k = J(\zeta_k)$. Furthermore, the discrete bilinear form $a(\cdot, \cdot)_{GLL}$ is given by:

$$a(u, v)_{GLL} = \sum_{k=0}^N [a(x_k) \frac{du}{d\zeta}(\zeta_k) \frac{dv}{d\zeta}(\zeta_k) J_k^{-1} + b(x_k) u(\zeta_k) v(\zeta_k) J_k] \rho_k, \quad \forall u, v \in C^1(\hat{\Upsilon}). \quad (2.29)$$

Here, the x_k are the global points corresponding to the local Gauss-Lobatto points ζ_k . Equation (2.27) can be seen as the complete spectral element discretization of the original differential equation (2.13). Again, application of the Lax-Milgram lemma shows that the problem (2.27) has a unique solution $s_h \in X_0$.

In order to implement the discrete system (2.27), it is necessary to choose a basis for the approximation space X_0 . The choice of basis affects the form and conditioning of the discrete equations. Moreover, it is important with respect to the inter-elemental coupling. Therefore, a Gauss-Lobatto-Legendre Lagrangian interpolant basis is chosen to represent a function in X_0 , since the Lobatto points include the boundary points of the reference element $\hat{\Upsilon}$. The basis functions, $(\phi_i(\zeta))_{i \in \{0, 1, \dots, N\}}$ satisfy:

$$\begin{cases} \phi_i \in \mathcal{P}_N & , \quad 0 \leq i \leq N, \\ \phi_i(\zeta_j) = \delta_{ij} & , \quad 0 \leq i, j \leq N, \end{cases} \quad (2.30)$$

where δ_{ij} is the Kronecker symbol: its value is one when $i = j$ and zero otherwise. The approximate solution s_h in each element Υ^e can be written as:

$$s_h(x)|_{\Upsilon^e} = s_h^e(x) = \sum_{i=0}^N s_i^e \phi_i(\zeta), \quad (2.31)$$

where $s_i^e = s_h^e(x_i)$. The approximate solution is continuous over element boundaries since $s_h \in \mathcal{H}_0^1(\Upsilon)$. As a consequence, the coefficients satisfy:

$$s_N|_{\Upsilon^{e-1}} = s_0|_{\Upsilon^e}, \quad \forall e \in \{2, \dots, E\}. \quad (2.32)$$

Moreover, s_h must satisfy the homogeneous Dirichlet boundary conditions:

$$s_0|_{\Upsilon^1} = s_N|_{\Upsilon^e} = 0. \quad (2.33)$$

It is convenient to represent the source term f in terms of the basis in X_0 . Substitution of s_h , f_h and the test function v_h into equation (2.27) in the standard Galerkin way yields the discrete block-banded matrix system:

$$(\mathcal{A} + b\mathcal{B})\mathbf{s} = \mathcal{B}\mathbf{f} , \quad (2.34)$$

or equivalently:

$$\sum_{e=1}^E \sum_{i=0}^N (A_{ji}^e + bB_{ji}^e) s_i^e = \sum_{e=1}^E \sum_{i=0}^N B_{ji}^e f_i^e , \quad \forall j \in \{0, 1, \dots, N\} . \quad (2.35)$$

In equation (2.34), the calligraphic font adopted to denote the matrices, \mathcal{A} , $b\mathcal{B}$ and \mathcal{B} , implies that direct stiffness has been performed. By this, we mean that the contributions of corresponding global element boundary points are summed to ensure condition (2.32), and the Dirichlet boundary conditions (2.33) are taken into account by eliminating from the system the rows and columns corresponding to the boundary points. The elemental matrices are given by:

$$\begin{cases} A_{ji}^e &= \sum_{k=0}^N a(x_k) \frac{d\phi_i}{d\zeta}(\zeta_k) \frac{d\phi_j}{d\zeta}(\zeta_k) J_k^{-1} \rho_k , \quad \forall 0 \leq i, j \leq N , \\ bB_{ji}^e &= b(x_i) J_i \rho_i \delta_{ij} , \quad \forall 0 \leq i, j \leq N , \\ B_{ji}^e &= J_i \rho_i \delta_{ij} , \quad \forall 0 \leq i, j \leq N . \end{cases} \quad (2.36)$$

A detailed error analysis for linear elliptic problems is given by Maday and Patera [45]. One of their results states that if the solution and data are C^∞ , exponential convergence to the exact solution s is obtained for s_h if $N \rightarrow \infty$.

A remark should be made about the matrix system. As already mentioned, elements only couple at boundary nodes because of the Gauss-Lobatto interpolation. The choice of Gauss-Lobatto numerical integration ensures an exact evaluation of the stiffness, or diffusion, matrix \mathcal{A} in the case of a constant coefficient a . The mass matrices $b\mathcal{B}$ and \mathcal{B} are not computed exactly. However, the use of Gauss-Lobatto integration has two advantages. Firstly, it enables an efficient use of tensor product basis functions in higher dimensions. Moreover, it results in diagonal mass matrices $b\mathcal{B}$ and \mathcal{B} , a property that is very useful when approximating time-dependent problems with an explicit time-integration.

Chapter 3

3D Navier-Stokes solver

We have used known methods to build an efficient code. The original features of our numerical algorithm are the following. The way we regularize the boundary conditions is new. We present a fully-explicit algorithm for the time-marching scheme as a good alternative to the classical implicit/explicit splitting of the diffusion and non-linear terms, respectively. In that process, a second original feature arises. We derived our time discretization from the scheme of Gavrilakis *et al.* [31], though they used the standard fourth-order Runge-Kutta scheme, while we use the standard second-order Runge-Kutta scheme. The only change we made in their algorithm is the following. In our case, that is for cylindrical coordinates, the gradient and the divergence operators do not commute, the continuity equation has then to be enforced at each intermediate time step of our explicit, second-order Runge-Kutta scheme.

The primitive variables, pressure and velocity, are represented by Fourier series in the circumferential direction and by spectral elements in the radial and axial directions. By Fourier transforming the governing equations, one obtains a two-dimensional problem (r, z) for each Fourier mode. Then, one resorts to the weak formulation of the two-dimensional problem with the velocity components in a polynomial space of degree N and the pressure field in a space of degree $N - 2$. This procedure avoids the presence of spurious pressure modes. For simplicity, we choose the same grid points for the velocity and pressure expansion, i.e. the $N + 1$ Gauss-Lobatto-Legendre (GLL) points for the velocity and the $N - 1$ inner GLL points for the pressure, as Azaïez *et al.* proposed in [8]. Using a tensor product formulation, we build operators separately in each direction (r, z) , and we use the fast-diagonalization technique of Lynch *et al.* [44] to recover the pressure from the direct inversion of a pseudo-Poisson operator. This method is equivalent to inverting matrices depending on one direction only and then inverting one diagonal matrix depending on both radial and axial directions. The inversion of the pressure operator is the core of our solver and is performed very rapidly due to this technique.

3.1 Continuous formulation of the equations

The fluid is considered to be viscous, Newtonian, incompressible and isothermal. Hence, the incompressible Navier-Stokes equations can be used to describe the flow.

Navier-Stokes equations These equations express the conservation of mass (3.1) and of momentum (3.2). The continuity equation reads:

$$\nabla \cdot \mathbf{v} = 0 \quad \forall(\mathbf{r}, t) \in D \times [0, +\infty[\quad , \quad (3.1)$$

where $\mathbf{v} = \mathbf{v}(\mathbf{r}, t)$, $\mathbf{r} = (r, \theta, z)$ are the cylindrical coordinates, defined on the domain $D =]R_1, R_2[\times]0, 2\pi[\times]z_1, z_2[$ and t is the time.

The momentum equation reads:

$$\frac{\partial \mathbf{v}}{\partial t} + (\mathbf{v} \cdot \nabla) \mathbf{v} = -\frac{1}{\rho} \nabla p + \nu \nabla^2 \mathbf{v} \quad \forall(\mathbf{r}, t) \in D \times [0, +\infty[\quad . \quad (3.2)$$

Here ρ is the density of the fluid and ν its kinematic viscosity. The scalar $p = p(\mathbf{r}, t)$ contains both the pressure and the gravity potential, $-\rho g z$. We will call, p , the pressure from now on.

Non-Dimensionalization We make the following choice for the characteristic scales:

- $d = R_2 - R_1$, the gap between the two cylinders, is the length scale. R_1 , is the radius of the inner cylinder, and R_2 , the radius of the outer cylinder.
- $V = |R_1 \Omega_1|$, or $|R_2 \Omega_2|$, is the velocity scale. Here Ω_1 is the angular velocity of the inner cylinder and Ω_2 that for the outer cylinder.
 - In the case where only the inner cylinder is rotating, $V = |R_1 \Omega_1|$.
 - In the counter-rotating case, $V = |R_2 \Omega_2|$.
- $\tau = \tau_C = \frac{d}{V}$, is the time scale. It is the characteristic advection time.
- $P = \rho V^2$, is the pressure scale. It corresponds to the centrifugal force acting on the flow.

The dimensionless continuity equation is unchanged, while the momentum equation becomes:

$$\frac{\partial \mathbf{v}}{\partial t} + (\mathbf{v} \cdot \nabla) \mathbf{v} = -\nabla p + \frac{1}{Re} \nabla^2 \mathbf{v} \quad \forall(\mathbf{r}, t) \in D \times [0, +\infty[\quad , \quad (3.3)$$

where $Re = \frac{dV}{\nu}$ is the Reynolds number and the physical quantities, space, time, velocity and pressure, are scaled with respect to d , τ , V and P respectively.

Complete set of equations Taking the boundary and initial conditions into account, the complete set of equations is:

$$\left\{ \begin{array}{l} \frac{\partial \mathbf{v}}{\partial t} + (\mathbf{v} \cdot \nabla) \mathbf{v} = -\nabla p + \frac{1}{Re} \nabla^2 \mathbf{v} \quad \forall (\mathbf{r}, t) \in D \times [0, +\infty[\quad , \\ \nabla \cdot \mathbf{v} = 0 \quad \forall (\mathbf{r}, t) \in D \times [0, +\infty[\quad , \\ \mathbf{v} = \mathbf{v}_b \quad \forall (\mathbf{r}, t) \in \partial D \times]0, +\infty[\quad , \\ \mathbf{v} = \mathbf{v}_i \quad \forall (\mathbf{r}, t) \in D \times \{0\} \quad , \end{array} \right. \quad (3.4)$$

where the velocity at the boundaries, ∂D , is denoted by \mathbf{v}_b and the initial velocity field by \mathbf{v}_i .

3.2 Weak formulation of the equations

θ discrete (r, z, t) continuous equations The azimuthal direction being periodic, we first approximate the velocity \mathbf{v} and the pressure p by finite Fourier series:

$$\mathbf{v}(\mathbf{r}, t) = \sum_{k=-N_\theta/2}^{N_\theta/2} \mathbf{v}_k(r, z, t) \exp(\mathbf{i} k \theta) \quad , \quad p(\mathbf{r}, t) = \sum_{k=-N_\theta/2}^{N_\theta/2} p_k(r, z, t) \exp(\mathbf{i} k \theta) \quad ,$$

with k , the azimuthal wavenumber, N_θ the cut-off and \mathbf{i} the square root of -1 .

We define the test functions Π^v and Π^p as products of Fourier bases by continuous functions of the Sobolev space $\mathcal{H}_0^1(\Upsilon)$, ϕ , and of the Lebesgue space $\mathcal{L}_0^2(\Upsilon)$, ψ , respectively, where $\Upsilon =]R_1, R_2[\times]z_1, z_2[$ and $\mathcal{L}_0^2(\Upsilon) = \{\psi \in \mathcal{L}^2(\Upsilon), \psi|_{\partial\Upsilon} = 0\}$. These test functions are expressed by the relations:

$$\left\{ \begin{array}{l} \Pi^v(\mathbf{r}) = \phi(r, z) \exp(\mathbf{i} k \theta) \quad , \\ \Pi^p(\mathbf{r}) = \psi(r, z) \exp(\mathbf{i} k \theta) \quad . \end{array} \right.$$

We define the following scalar product of unit weight: $\langle f, g \rangle = \int_D f \bar{g}$, where \bar{g} denotes the complex conjugate of g .

Using a Galerkin projection, we obtain a two-dimensional problem for each of the Fourier modes, k ,

$$\left\{ \begin{array}{l} \int_{\Upsilon} \left[\frac{\partial \mathbf{v}_k}{\partial t} + [(\mathbf{v} \cdot \nabla) \mathbf{v}]_k \right] \phi r dr dz = \int_{\Upsilon} \left[-\nabla p_k + \frac{1}{Re} \nabla^2 \mathbf{v}_k \right] \phi r dr dz \quad , \\ - \int_{\Upsilon} [\nabla \cdot \mathbf{v}_k] \psi r dr dz = 0 \quad . \end{array} \right. \quad (3.5)$$

We take here the opposite of the divergence equation to later have a pseudo-Laplacian matrix that is positive.

Divergence theorem If we apply the divergence theorem to the product, $\phi \nabla u$, ϕ and u being scalar functions of (r, z) , we obtain the following equation:

$$\int_{\Upsilon} \nabla \cdot (\phi \nabla u) d\Upsilon = \int_{\Upsilon} \phi \nabla^2 u d\Upsilon + \int_{\Upsilon} \nabla \phi \cdot \nabla u d\Upsilon = \int_{\partial\Upsilon} \phi \nabla u \cdot \mathbf{n} d\gamma \quad ,$$

where \mathbf{n} is the unit outward normal vector on $\partial\Upsilon$ and $d\gamma$ the linear measure on $\partial\Upsilon$. We use this result to reduce the order of differentiation of the three Laplacian components: $\nabla^2 u_k$, $\nabla^2 v_k$ and $\nabla^2 w_k$. Thus, we replace the second-order derivatives on one term by two first-order derivatives on two terms. Considering ϕ to be a test function belonging to X_0 , we have $\phi = 0$ on $\partial\Upsilon$. The divergence theorem can therefore be simplified to:

$$\int_{\Upsilon} \phi \nabla^2 u \, d\Upsilon = - \int_{\Upsilon} \nabla \phi \cdot \nabla u \, d\Upsilon .$$

Formula for the pressure Another useful formula is:

$$\int_{\Upsilon} \nabla f \, d\Upsilon = \int_{\partial\Upsilon} f \mathbf{n} \, d\gamma .$$

Applying this formula to the scalar $f = \phi p$ for any test function, ϕ , of X_0 and bearing in mind that $\nabla(\phi p) = \phi \nabla p + p \nabla \phi$, we obtain :

$$\int_{\Upsilon} \phi \nabla p \, d\Upsilon = - \int_{\Upsilon} p \nabla \phi \, d\Upsilon .$$

Weak formulation of the Navier-Stokes equations Using these two formulas, the weak formulation of the Navier-Stokes equations can be simplified to:

$$\begin{cases} \int_{\Upsilon} \left[\frac{\partial \mathbf{v}_k}{\partial t} + [(\mathbf{v} \cdot \nabla) \mathbf{v}]_k \right] \phi \, r \, dr \, dz & = \int_{\Upsilon} p_k \nabla \phi \, r \, dr \, dz - \frac{1}{Re} \int_{\Upsilon} \nabla \mathbf{v}_k \cdot \nabla \phi \, r \, dr \, dz \\ - \int_{\Upsilon} [\nabla \cdot \mathbf{v}_k] \psi \, r \, dr \, dz & = 0 \end{cases} , \quad (3.6)$$

3.3 Spatial discretization

The section Υ is further decomposed in $E = I \times J$ rectangular elements: $\bar{\Upsilon} = \cup_{(e,l) \in \{1,2,\dots,I\} \times \{1,2,\dots,J\}} \bar{\Upsilon}^{el}$ (see figure 3.1). The integral over Υ can then be expressed as:

$$\int_{\Upsilon} F \, r \, dr \, dz = \sum_{e=1}^I \sum_{l=1}^J \int_{\Upsilon^{el}} F \, r \, dr \, dz , \quad (3.7)$$

and

$$\int_{\Upsilon^{el}} F(r, z) \, r \, dr \, dz = \int_{-1}^1 dx \int_{-1}^1 dy F[r(x), z(y)] r(x) \frac{g^e h^l}{2} . \quad (3.8)$$

Here, $(r(x), z(y))$ represents the affine mapping from $] -1, 1[\times] -1, 1[$ to $\Upsilon^{el} =]r_0^e, r_0^e + g^e[\times]z_0^l, z_0^l + h^l[$.

$$\begin{cases} r(x) & = r_0^e + \frac{g^e}{2}(x+1) \\ z(y) & = z_0^l + \frac{h^l}{2}(y+1) \end{cases} , \quad (3.9)$$

and

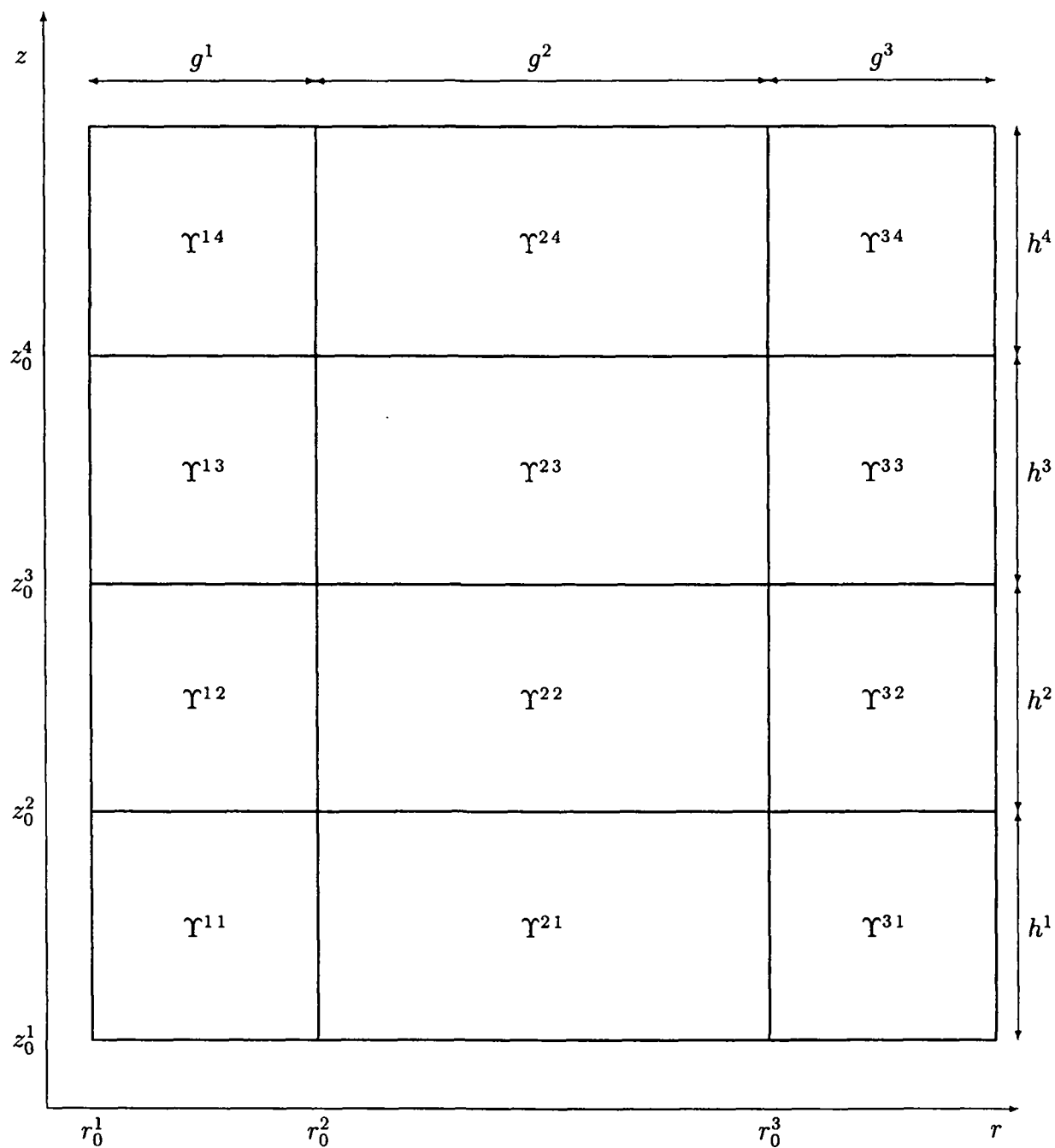


Figure 3.1: $\Upsilon^{el} =]r_0^e, r_0^e + g^e[\times]z_0^l, z_0^l + h^l[.$

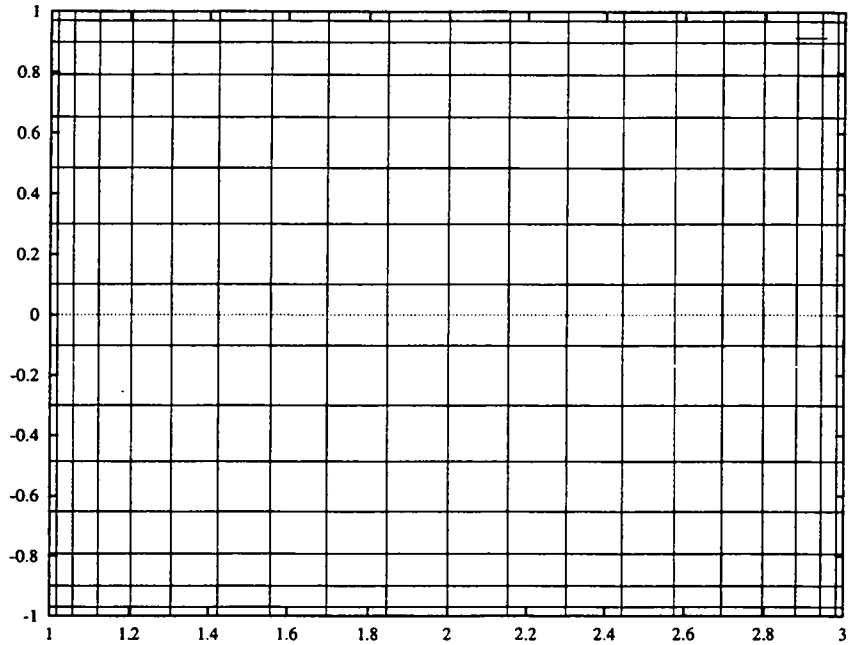


Figure 3.2: Grid of 21×16 GLL points, local to an element.

$$\begin{cases} r_0^e = R_1 + \sum_{i=1}^{e-1} g^i & \forall e \geq 2, \\ z_0^l = z_1 + \sum_{i=1}^{l-1} h^i & \forall l \geq 2. \end{cases}$$

We set $r_0^1 = R_1$ and $z_0^1 = z_1$.

A Lagrange-Legendre interpolation is applied to the Fourier modes:

$$\mathbf{v}_k(r, z, t)|_{\Upsilon^{el}} = \sum_{i=0}^{N_r} \sum_{j=0}^{N_z} \mathbf{v}_{ijk}^{el}(t) \phi_{ij}^{el}(r, z), \quad (3.10)$$

where ϕ_{ij}^{el} belongs to $X = \mathcal{H}^1(\Upsilon) \cap \mathcal{P}_{N,E}(\Upsilon)$. Here, $\mathcal{P}_{N,E}(\Upsilon)$ is the space of piecewise test functions $\phi = \phi_{ij}^{el}$ defined on Υ as $\phi_{ij}^{el} = h_i[x(r)]h_j[y(z)]$ on Υ^{el} and zero on all the other elements $\Upsilon^{\alpha\beta}$. The polynomial $h_i h_j$ is of degree $N = N_r \times N_z$. The basis h_i (respectively h_j) is the Lagrange interpolant of degree N_r (respectively N_z) associated with the i -th (respectively j -th) Gauss-Lobatto-Legendre point of $]-1, 1[$ (see Appendix B and figure 3.2).

In order to eliminate spurious pressure modes, two methods can be used. In a (P_N/P_N) formulation, which uses the same grid for both velocity and pressure, the inherent

spurious pressure modes are filtered. In a (P_N/P_{N-2}) formulation on a staggered mesh, typically on Gauss points for the pressure and Gauss-Lobatto points for the velocity [45], the spurious pressure modes are simply not created. We use the (P_N/P_{N-2}) formulation, but instead of taking the pressure at the Gauss-Legendre points and the velocity at the Gauss-Lobatto-Legendre points, we apply the modified version of Azaïez *et al.* [8] which requires using the inner GLL points for the pressure. This method has the advantages of the two former methods, it needs no filtering and also no extrapolation from the pressure grid to the velocity grid, with the exception of the points lying on the element interfaces. The pressure is then expanded as follows:

$$p_k(r, z, t)|_{\Upsilon^{el}} = \sum_{i=1}^{N_r-1} \sum_{j=1}^{N_z-1} p_{ijk}^{el}(t) \psi_{ij}^{el}(r, z), \quad (3.11)$$

where ψ_{ij}^{el} belongs to $Y = \mathcal{L}^2(\Upsilon) \cap \mathcal{P}_{N-2,E}(\Upsilon)$. Furthermore, we have $\psi_{ij}^{el}[r(x), z(y)] = \tilde{h}_i(x) \tilde{h}_j(y)$ on Υ^{el} , and $\psi_{ij}^{el} = 0$ elsewhere; \tilde{h}_i (respectively \tilde{h}_j) is the Lagrange interpolant of degree $N_r - 2$ (respectively $N_z - 2$) associated to the i -th (respectively j -th) inner GLL point (see Appendix B for the formula).

We use a unique discrete inner product defined on each element by the Gauss-Lobatto-Legendre quadrature rule, which uses the same nodes as the interpolation technique,

$$\int_{-1}^1 dx \int_{-1}^1 dy f(x, y) g(x, y) r(x) = \sum_{i=0}^{N_r} \sum_{j=0}^{N_z} f_{ij}^{el} g_{ij}^{el} r_i^e \rho_i \rho_j. \quad (3.12)$$

In the former relation, $r_i^e = r(x_i)$, r belonging to Υ^{el} and ρ_i and ρ_j represent the GLL weights, defined in Appendix B. The pressure is therefore extrapolated on the interfaces of the elements to obtain the pressure gradient on the velocity grid.

The test functions are chosen in the subspace of trial functions that verify the boundary conditions as in [58]. Let $\phi = \phi_{ij}^{el} = h_i(x) h_j(y)$, $(i, j) \in \{0, \dots, N_r\} \times \{0, \dots, N_z\}$, be the test function for the momentum equation. It belongs to $X_0 = \mathcal{H}_0^1(\Upsilon) \cap \mathcal{P}_{N,E}(\Upsilon)$.

Let $\psi = \psi_{ij}^{el} = \tilde{h}_i[x(r)] \tilde{h}_j[y(z)]$ be the test function for the continuity equation. We have $\psi \in Y_0$, with: $Y_0 = \mathcal{L}_0^2(\Upsilon) \cap \mathcal{P}_{N-2,E}(\Upsilon)$. This choice of different test functions results in rectangular gradient and divergence matrices.

Weak formulation of the equations in cylindrical coordinates The weak formulation of the Navier-Stokes equations in cylindrical coordinates can be expressed as follows:

$$\left\{ \begin{array}{l} \int_{\Upsilon} \left[\frac{\partial u_k}{\partial t} + n l_k^r \right] \phi r dr dz = \int_{\Upsilon} \left[-\frac{\partial p_k}{\partial r} + \frac{1}{Re} (\nabla^2 u_k - \frac{u_k}{r^2} - 2ik \frac{v_k}{r^2}) \right] \phi r dr dz, \\ \int_{\Upsilon} \left[\frac{\partial v_k}{\partial t} + n l_k^\theta \right] \phi r dr dz = \int_{\Upsilon} \left[-ik \frac{p_k}{r} + \frac{1}{Re} (\nabla^2 v_k - \frac{v_k}{r^2} + 2ik \frac{u_k}{r^2}) \right] \phi r dr dz, \\ \int_{\Upsilon} \left[\frac{\partial w_k}{\partial t} + n l_k^z \right] \phi r dr dz = \int_{\Upsilon} \left[-\frac{\partial p_k}{\partial z} + \frac{1}{Re} \nabla^2 w_k \right] \phi r dr dz, \\ - \int_{\Upsilon} \left[\frac{1}{r} \frac{\partial}{\partial r} (r u_k) + \frac{ik}{r} v_k + \frac{\partial w_k}{\partial z} \right] \psi r dr dz = 0, \end{array} \right. \quad (3.13)$$

where the semi-discrete Laplacian of the k -th mode of f , f_k is:

$$\nabla^2 f_k = \frac{1}{r} \frac{\partial}{\partial r} \left(r \frac{\partial f_k}{\partial r} \right) - \frac{k^2}{r^2} f_k + \frac{\partial^2 f_k}{\partial z^2}.$$

The notations nl_k^r , nl_k^θ and nl_k^z represent the three components of the non-linear term $(\mathbf{v} \cdot \nabla)\mathbf{v}_k$. The form and discretization of this term will be discussed later. In equation (3.13), $\mathbf{v}_k = (u_k, v_k, w_k)$, and u_k , v_k and w_k are the radial, azimuthal and axial velocity components. We now consider precisely each different constituent part of the Navier-Stokes equations.

Individual terms in the Navier-Stokes equations The time derivative, for example, yields:

$$\begin{aligned} \int_{\Upsilon} \frac{\partial u_k}{\partial t} \phi r dr dz &= \int_{\Upsilon} \frac{\partial u_k}{\partial t} \phi_{ij}^{el} r dr dz = \\ &= \sum_{s=1}^I \sum_{o=1}^J \sum_{m=0}^{N_r} \sum_{n=0}^{N_z} \sum_{p=0}^{N_r} \sum_{q=0}^{N_z} \frac{du_{pqk}^{so}}{dt} h_p(x_m) h_q(y_n) h_i(x_m) h_j(y_n) \delta_{(e,l)(s,o)} \frac{g^s}{2} \frac{h^o}{2} r_m^s \rho_m \rho_n \\ &= \sum_{m=0}^{N_r} \sum_{n=0}^{N_z} \sum_{p=0}^{N_r} \sum_{q=0}^{N_z} \frac{du_{pqk}^{el}}{dt} h_p(x_m) h_q(y_n) h_i(x_m) h_j(y_n) \frac{g^e}{2} \frac{h^l}{2} r_m^e \rho_m \rho_n \\ &= \sum_{m=0}^{N_r} \sum_{n=0}^{N_z} (rB^r \otimes B^z)_{imjn} \frac{du_{mnk}^{el}}{dt}. \quad (3.14) \end{aligned}$$

The notation δ is the Kronecker symbol, so that $\delta_{(e,l)(s,o)} = 1$ when the doublets (e, l) and (s, o) are the same, and $\delta_{(e,l)(s,o)} = 0$ otherwise. We introduce the following mass matrices, defined locally for each Υ^{el} : $(rB^r)_{ij} = \rho_j r_j^e \delta_{ij} \frac{g^e}{2}$, $B_{ij}^z = \rho_j \delta_{ij} \frac{h^l}{2}$, where g^e is the width of the element Υ^{el} and h^l , its height. For simplicity we do not add an upper index, e or l , on these matrices to denote the element. The definition of the tensor product \otimes , and its main properties are found in Appendix B.

Another mass matrix is introduced due to terms of the form:

$$\begin{aligned} \int_{\Upsilon} \frac{u_k}{r^2} \phi r dr dz &= \\ &= \sum_{s=1}^I \sum_{o=1}^J \sum_{m=0}^{N_r} \sum_{n=0}^{N_z} \sum_{p=0}^{N_r} \sum_{q=0}^{N_z} u_{pqk}^{so} \frac{1}{r_m^s} \delta_{pm} \delta_{im} \rho_m \frac{g^s}{2} \delta_{qn} \delta_{jn} \rho_n \frac{h^o}{2} \delta_{(e,l)(s,o)} \\ &= \sum_{m=0}^{N_r} \sum_{n=0}^{N_z} \sum_{p=0}^{N_r} \sum_{q=0}^{N_z} u_{pqk}^{el} \frac{1}{r_m^e} \delta_{pm} \delta_{im} \rho_m \frac{g^e}{2} \delta_{qn} \delta_{jn} \rho_n \frac{h^l}{2} \\ &= \sum_{m=0}^{N_r} \sum_{n=0}^{N_z} \left(\frac{B^r}{r} \otimes B^z \right)_{imjn} u_{mnk}^{el}, \end{aligned}$$

with $\left(\frac{B^r}{r} \right)_{ij} = \frac{1}{r_j^e} \rho_j \delta_{ij} \frac{g^e}{2}$.

Concerning the non-linear term, we do not perform a convolution because of the huge number of operations it would involve, of the order of N_θ^2 for a vector of length

N_θ . Instead, we transform the velocity components and their derivatives into physical space with a fast Fourier transform (FFT), whose operational count is proportional to $N_\theta \log N_\theta$ for a vector of length N_θ , and multiply the velocity by its gradient before transforming the result back to Fourier space. The radial and axial derivatives are obtained by multiplying the velocity vector defined on Υ^{el} by the derivative matrices local to that element, $D_{ij}^r = \frac{2}{g^e} d_{ij}$ and $D_{ij}^z = \frac{2}{h^l} d_{ij}$, respectively. The parent derivative matrix is given by: $d_{ij} = \frac{dh_i}{dx}(\eta_i)$, where η_i is a GLL point of the parent element $[-1, 1] \times [-1, 1]$. The azimuthal derivative of u_k is simply iku_k .

The first relevant part of the pressure gradient is the radial derivative:

$$\begin{aligned}
- \int_{\Upsilon} p_k \frac{\partial(\phi r)}{\partial r} dr dz &= - \sum_{s=1}^I \sum_{o=1}^J \sum_{m=0}^{N_r} \sum_{n=0}^{N_z} \sum_{u=1}^{N_r-1} \sum_{q=1}^{N_z-1} p_{uqk}^{so} \\
&\quad \tilde{h}_u(x_m) \tilde{h}_q(y_n) \left(\frac{2}{g^s} \frac{dh_i}{dx}(x_m) r_m^s + h_i(x_m) \right) h_j(y_n) \delta_{(e,l)(s,o)} \frac{g^s h^o}{4} \rho_m \rho_n \\
&= - \sum_{m=0}^{N_r} \sum_{n=0}^{N_z} \sum_{u=1}^{N_r-1} \sum_{q=1}^{N_z-1} p_{uqk}^{el} \tilde{h}_u(x_m) \tilde{h}_q(y_n) \left(\frac{2}{g^e} \frac{dh_i}{dx}(x_m) r_m^e + h_i(x_m) \right) h_j(y_n) \frac{g^e h^l}{4} \rho_m \rho_n \\
&= \sum_{u=1}^{N_r-1} \sum_{q=1}^{N_z-1} (\widetilde{G}^r \otimes \widetilde{B}^z)_{iujq} p_{uqk}^{el} \cdot \quad (3.15)
\end{aligned}$$

In equation (3.15), we use the following matrices defined as: $\widetilde{G}^r = -D^{rT} \widetilde{rB}^r - \widetilde{B}^r$, $\widetilde{rB}^r_{ij} = \rho_i r_i^e \tilde{h}_j(x_i) \frac{g^e}{2}$, $\widetilde{B}^r_{ij} = \rho_i \tilde{h}_j(x_i) \frac{g^e}{2}$ and $\widetilde{B}^z_{ij} = \rho_i \tilde{h}_j(y_i) \frac{h^l}{2}$.

The second relevant part of the pressure gradient is the axial derivative:

$$\begin{aligned}
- \int_{\Upsilon} p_k \frac{\partial \phi}{\partial z} r dr dz &= \\
- \sum_{s=1}^I \sum_{o=1}^J \sum_{m=0}^{N_r} \sum_{n=0}^{N_z} \sum_{u=1}^{N_r-1} \sum_{q=1}^{N_z-1} p_{uqk}^{so} \tilde{h}_u(x_m) \tilde{h}_q(y_n) h_i(x_m) \frac{2}{h^o} \frac{dh_j}{dy}(y_n) \delta_{(e,l)(s,o)} r_m^s \frac{g^s h^o}{4} \rho_m \rho_n \\
&= - \sum_{m=0}^{N_r} \sum_{n=0}^{N_z} \sum_{u=1}^{N_r-1} \sum_{q=1}^{N_z-1} p_{uqk}^{el} \tilde{h}_u(x_m) \tilde{h}_q(y_n) h_i(x_m) \frac{2}{h^l} \frac{dh_j}{dy}(y_n) r_m^e \frac{g^e h^l}{4} \rho_m \rho_n \\
&= \sum_{u=1}^{N_r-1} \sum_{q=1}^{N_z-1} (\widetilde{rB}^r \otimes \widetilde{G}^z)_{iujq} p_{uqk}^{el} \cdot \quad (3.16)
\end{aligned}$$

Here $\widetilde{G}^z = -D^{zT} \widetilde{B}^z$.

The transpose of the radial, azimuthal and axial gradient matrices can be recognized in the continuity equation:

$$\begin{aligned}
& - \int_{\Upsilon} \left[\frac{1}{r} \frac{\partial}{\partial r} (ru_k) + \frac{ik}{r} v_k + \frac{\partial w_k}{\partial z} \right] \psi r dr dz = \\
& - \sum_{s=1}^I \sum_{o=1}^J \sum_{m=0}^{N_r} \sum_{n=0}^{N_z} \sum_{p=0}^{N_r} \sum_{q=0}^{N_z} [u_{pqk}^{so} (\delta_{pm} \tilde{h}_i(x_m) \delta_{qn} \tilde{h}_j(y_n)) \\
& + \frac{2}{g^s} \frac{dh_p}{dx}(x_m) \tilde{h}_i(x_m) r_m^s \delta_{qn} \tilde{h}_j(y_n) \rho_m \frac{g^s}{2} \rho_n \frac{h^o}{2} \delta_{(e,l)(s,o)} \\
& + ikv_{pqk}^{so} \delta_{pm} \tilde{h}_i(x_m) \rho_m \frac{g^s}{2} \delta_{qn} \tilde{h}_j(y_n) \rho_n \frac{h^o}{2} \delta_{(e,l)(s,o)} \\
& + w_{pqk}^{so} \delta_{pm} \tilde{h}_i(x_m) r_m^s \rho_m \frac{g^s}{2} \frac{dh_q}{dy}(y_n) \tilde{h}_j(y_n) \rho_n \delta_{(e,l)(s,o)}] \\
& = - \sum_{p=0}^{N_r} \sum_{q=0}^{N_z} u_{pqk}^{el} \tilde{h}_i(x_p) \tilde{h}_j(y_q) \rho_p \frac{g^e}{2} \rho_q \frac{h^l}{2} \\
& - \sum_{m=0}^{N_r} \sum_{p=0}^{N_r} \sum_{q=0}^{N_z} u_{pqk}^{el} \frac{dh_p}{dx}(x_m) \tilde{h}_i(x_m) r_m^e \tilde{h}_j(y_q) \rho_m \rho_q \frac{h^l}{2} \\
& - \sum_{p=0}^{N_r} \sum_{q=0}^{N_z} ikv_{pqk}^{el} \tilde{h}_i(x_p) \rho_p \frac{g^e}{2} \tilde{h}_j(y_q) \rho_q \frac{h^l}{2} \\
& - \sum_{n=0}^{N_z} \sum_{p=0}^{N_r} \sum_{q=0}^{N_z} w_{pqk}^{el} \tilde{h}_i(x_p) r_p^e \rho_p \frac{g^e}{2} \frac{dh_q}{dy}(y_n) \tilde{h}_j(y_n) \rho_n \\
& = \sum_{p=0}^{N_r} \sum_{q=0}^{N_z} \left[(\tilde{G}^r \otimes \tilde{B}^z)^T_{ipjq} u_{pqk}^{el} - ik(\tilde{B}^r \otimes \tilde{B}^z)^T_{ipjq} v_{pqk}^{el} + (\tilde{r} \tilde{B}^r \otimes \tilde{G}^z)^T_{ipjq} w_{pqk}^{el} \right]. \quad (3.17)
\end{aligned}$$

The first distinct part of the diffusion term is the second-order radial derivative:

$$\begin{aligned}
& - \int_{\Upsilon} \frac{\partial u_k}{\partial r} \frac{\partial \phi}{\partial r} r dr dz = \\
& - \sum_{s=1}^I \sum_{o=1}^J \sum_{m=0}^{N_r} \sum_{n=0}^{N_z} \sum_{p=0}^{N_r} \sum_{q=0}^{N_z} u_{pqk}^{so} \frac{2}{g^s} \frac{dh_p}{dx}(x_m) h_q(y_n) \frac{2}{g^s} \frac{dh_i}{dx}(x_m) h_j(y_n) r_m^s \frac{g^s h^o}{4} \rho_m \rho_n \delta_{(e,l)(s,o)} \\
& = - \sum_{m=0}^{N_r} \sum_{n=0}^{N_z} \sum_{p=0}^{N_r} \sum_{q=0}^{N_z} u_{pqk}^{el} \frac{2}{g^e} \frac{dh_p}{dx}(x_m) h_q(y_n) \frac{2}{g^e} \frac{dh_i}{dx}(x_m) h_j(y_n) r_m^e \frac{g^e h^l}{4} \rho_m \rho_n \\
& = \sum_{p=0}^{N_r} \sum_{q=0}^{N_z} (A^r \otimes B^z)_{ipjq} u_{pqk}^{el}, \quad (3.18)
\end{aligned}$$

where the second-order radial derivative matrix is:

$$A_{ij}^r = -\frac{2}{g^e} \sum_{k=0}^{N_r} r_k^e \rho_k d_{ki} d_{kj}.$$

$$s_k^z = -nl_k^z + \frac{1}{Re} (r\mathcal{B}^r)^{-1} \otimes (\mathcal{B}^z)^{-1} \left[\mathcal{A}^r \otimes \mathcal{B}^z - k^2 \frac{\mathcal{B}^r}{r} \otimes \mathcal{B}^z + r\mathcal{B}^r \otimes \mathcal{A}^z \right] w_k. \quad (3.23)$$

We now define:

$$\tilde{\mathcal{G}} = \begin{pmatrix} \tilde{\mathcal{G}}^r \otimes \tilde{\mathcal{B}}^z \\ ik\tilde{\mathcal{B}}^r \otimes \tilde{\mathcal{B}}^z \\ r\tilde{\mathcal{B}}^r \otimes \tilde{\mathcal{G}}^z \end{pmatrix} \quad \text{and} \quad \mathcal{B} = \begin{pmatrix} r\mathcal{B}^r \otimes \mathcal{B}^z \\ r\mathcal{B}^r \otimes \mathcal{B}^z \\ r\mathcal{B}^r \otimes \mathcal{B}^z \end{pmatrix}.$$

In compact matrix form, the discrete equations are now:

$$\begin{cases} \mathcal{B} \frac{d\mathbf{v}_k}{dt} + \tilde{\mathcal{G}} p_k - \mathcal{B} \mathbf{s}_k = \mathbf{0} \\ -\tilde{\mathcal{D}} \mathbf{v}_k = \mathbf{0} \end{cases} \quad (3.24)$$

In (3.24), $\mathbf{v}_k = (u_k, v_k, w_k)$. The three components of the source term \mathbf{s}_k are $(s_k^r, s_k^\theta, s_k^z)$. The divergence operator is $\tilde{\mathcal{D}} = (\tilde{\mathcal{G}}^{rT} \otimes \tilde{\mathcal{B}}^{zT}, -ik\tilde{\mathcal{B}}^{rT} \otimes \tilde{\mathcal{B}}^{zT}, r\tilde{\mathcal{B}}^{rT} \otimes \tilde{\mathcal{G}}^{zT})$. The gradient matrix, $\tilde{\mathcal{G}}$, and the divergence matrix, $\tilde{\mathcal{D}}$, verify $\tilde{\mathcal{D}} = \tilde{\mathcal{G}}^T$.

The non-linear term This term can be expressed in different forms: the rotation form, $\omega \wedge \mathbf{v} + \frac{1}{2} \nabla(v^2)$, where $\omega = \nabla \wedge \mathbf{v}$ is the vorticity, the convective form, $(\mathbf{v} \cdot \nabla) \mathbf{v}$, the conservative or divergence form, $\nabla \cdot (\mathbf{v} \otimes \mathbf{v})$, and the skew-symmetric form, $\frac{1}{2} (\mathbf{v} \cdot \nabla) \mathbf{v} + \frac{1}{2} \nabla \cdot (\mathbf{v} \otimes \mathbf{v})$. The rotation form is the least expensive because only six derivatives need to be evaluated, while nine derivatives are needed for both the convective and conservative forms, and eighteen for the skew-symmetric form. Although the four continuous expressions do not differ for a solenoidal velocity field, they are slightly different when they are expressed in discrete form. We use the skew-symmetric form, in any event, because it is the only one that remains stable for long integration times for a chaotic or turbulent flow. In the process of evaluating the non-linear term, we use FFT transforms of length N_θ , creating thus an aliasing error, that is non-negligible from modes $(N_\theta/2)$ till N_θ . To prevent aliasing errors, the 3/2 rule could be used. This consists of applying FFT transforms of length $3N_\theta$ to a modified velocity field which is a vector of length $3N_\theta$, whose first N_θ modes are those of the original field and the other $2N_\theta$ modes are set to zero. However, as the cost of the evaluation of the non-linear term is not negligible in our case, we do not use the 3/2 rule. Another way to reduce the cost of the calculation of the non-linear term would be to use the alternating form instead of the skew-symmetric form. This form consists in using alternately the convective and divergence forms. This procedure is stable for long integration times for a turbulent flow according to Zang [69]. The advantage of this form over the one we use is that only nine derivatives need to be obtained.

3.4 Time discretization

3.4.1 Fully-explicit scheme

In order to keep the high accuracy achieved spatially by the spectral element method, one has to use at least a second-order scheme for the time integration. Among the classical explicit schemes, we have considered the Adams-Bashforth scheme and the Runge-Kutta scheme. The stability region of the second-order Adams-Bashforth scheme (AB2) is about half as small as that of the second-order Runge-Kutta scheme (RK2); however, the operational cost for the RK2 is twice that of the AB2. So there is no clear advantage in choosing one rather than the other. The RK2 scheme only requires one time step for the initialization, while two are needed for the AB2. Two velocity fields, with three components each, and one pressure field have to be stored to be able to restart a simulation in the case of the AB2 scheme, while only one velocity field has to be stored before restarting a simulation in the case of the RK2 scheme. The amount of memory needed by a DNS is such that we have chosen the least memory consuming of the two methods, i.e. the RK2 scheme. A fully-explicit treatment of $\mathbf{s}_k(\mathbf{v}) = -Re \mathbf{nl}_k(\mathbf{v}) + \mathcal{B}^{-1} \mathcal{A} \mathbf{v}_k$ is chosen instead of the classical implicit linear viscous/explicit non-linear decomposition. Here, \mathcal{A} denotes the Laplacian operator and \mathbf{nl}_k , the three components of mode k of the non-linear term, nl_k^r , nl_k^θ and nl_k^z . Normally, an Uzawa operator for the pressure has to be inverted. Inversion can be performed directly or iteratively. The most efficient method to perform a direct inversion is the fast-diagonalization technique. As will be seen later on, in our case it is even more efficient than any iterative method. This technique requires the matrix to be inverted be separable. To fulfil this requirement, the matrix first has to be derived from the discretization of a set of separate partial differential equations. Let us consider the set of n separate partial differential equations, $L\mathbf{v} = \mathbf{s}$, in a discretized form. We introduce the following definition:

The n -dimensional matrix L is separable if it can be expressed as follows

$$\begin{aligned}
 L &= L_1 \otimes \dots \otimes I \otimes I \\
 &+ I \otimes L_2 \otimes I \otimes \dots \otimes I \\
 &\quad \quad \quad \quad \quad \quad \quad \quad \quad \quad \quad + \dots \\
 &+ I \otimes \dots \otimes I \otimes L_i \otimes I \otimes \dots \otimes I \\
 &\quad \quad \quad \quad \quad \quad \quad \quad \quad \quad \quad + I \otimes \dots \otimes I \otimes L_n .
 \end{aligned}$$

In this relation, L_i corresponds to the one-dimensional matrix in the i -th direction, and I to the one-dimensional identity matrix. Unfortunately, the Uzawa matrix can not be expressed in a separate form, because it involves rectangular matrices together with a full inverse matrix, \mathcal{H}^{-1} . Hence, the fast-diagonalization technique [44, 36] can not be applied. An iterative method would then be needed. For a three-dimensional problem with one periodic direction, each matrix-vector multiplication involved in the algorithm requires $2M^4$ operations (1 addition and 1 multiplication counts for one operation), with M^3 the total number of grid points (see Appendix B). The detailed

evaluation of the operations count is postponed until chapter 4. Each iteration step can be achieved within approximately 10 matrix-vector multiplications. In the case of the totally explicit choice, the pseudo-Laplacian operator for the pressure, $\tilde{\mathcal{D}}\mathcal{B}^{-1}\tilde{\mathcal{G}}$, can be inverted with the fast-diagonalization method and requires therefore $6M^4$ operations (see chapter 4). The solver in itself is therefore more efficient in the fully-explicit case than in the implicit/explicit one. However, the time-step requirements are more stringent for the former. Indeed, if an explicit treatment of the discrete Navier-Stokes equations is chosen, two stability constraints have to be enforced on the time step Δt . The first condition is imposed on the diffusion part of the operator,

$$\Delta t \leq \text{CSD} [(\Delta r^{-2} + (r\Delta\theta)^{-2} + \Delta z^{-2})^{-1}]_{\min} , \text{CSD} < \text{CSD}_{\max} , \quad (3.25)$$

where $(\Delta r, \Delta\theta, \Delta z)$ is the local mesh size at one grid point. The limiting value CSD_{\max} can be obtained from simulations where the diffusion constraint is the most stringent. We found $\text{CSD}_{\max} = 0.36$ through numerous tests: we increased the time step until a numerical instability occurred and approached afterwards the limit by a bisection method with a precision of 0.5%. The second condition comes from the non-linear term and is known as the CFL condition,

$$\Delta t \leq \frac{\text{CSN}}{Re} \left[\left(\frac{|u|}{\Delta r} + \frac{|v|}{r\Delta\theta} + \frac{|w|}{\Delta z} \right)^{-1} \right]_{\min} , \text{CSN} < \text{CSN}_{\max} , \quad (3.26)$$

where (u, v, w) are the velocity components at a given grid point. The limiting value CSN_{\max} is also obtained from numerical experiments. This limit is more problem dependent than the limit on the diffusion term. The limiting value for CSN, $\text{CSN}_{\max} = 0.2$, has been obtained with a precision of the order of 10% for the few simulations we made where the diffusion constraint was less stringent than the non-linear constraint. A more restrictive expression of conditions (3.25) and (3.26) is:

$$\begin{cases} \Delta t \leq \text{CSD} [\Delta r_{\min}^{-2} + (r_{\min}\Delta\theta)^{-2} + \Delta z_{\min}^{-2}]^{-1} , \\ \Delta t \leq \frac{\text{CSN}}{Re} \left(\frac{|u|_{\max}}{\Delta r_{\min}} + \frac{|v|_{\max}}{r_{\min}\Delta\theta} + \frac{|w|_{\max}}{\Delta z_{\min}} \right)^{-1} . \end{cases}$$

Let us consider the case where $\Delta r_{\min} \sim \Delta z_{\min} \ll (r\Delta\theta)_{\min}$. Such a grid is well adapted for simulations of Taylor vortex or wavy Taylor vortex flows. The first problem is axisymmetric and the second one requires only a few azimuthal modes. In a square element discretized in $(N+1) \times (N+1)$ GLL points, we have $\Delta r_{\min} \sim \frac{1}{N^2}$, so that the diffusion constraint allows a maximum time step $\Delta t_{\max} \propto \frac{1}{N^4}$. In our flow simulations, $|u|_{\max} \sim |w|_{\max} < |v|_{\max} = 1$, so that the non-linear constraint simplifies to $\Delta t_{\max} \propto \frac{1}{Re N^2}$. From these rough estimates, we can expect the two stability constraints to approach a similar value at a high enough Reynolds number (~ 100) for a polynomial of degree $N = 10$. These estimates are qualitatively correct, as can be seen in figure 3.3. Here we present the ratio of the maximum time step allowed by the CFL constraint to the maximum time step imposed by the CSD constraint. It decreases with Re , the inner

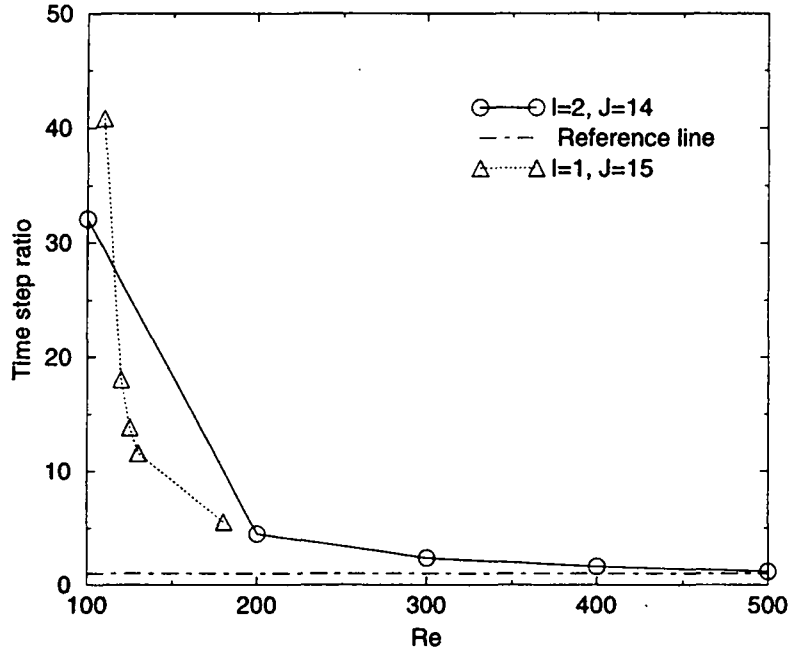


Figure 3.3: Ratio of the maximum time step allowed by the CFL constraint to the maximum time step imposed by the CSD constraint for different simulations. The simulations for $\Gamma = 12$, $I = 2$, and $J = 14$ are represented by circles, and those for $\Gamma = 30$, $I = 1$, and $J = 15$ by triangles. In both cases $\eta = 0.875$ and $N = 12$. The Reynolds number is $Re = Re_1$.

cylinder Reynolds number. In these simulations, only the inner cylinder is rotating. At $Re = 500$, the maximum time step allowed by the diffusion constraint is only 1.2 times smaller than the time step determined by the CFL constraint alone.

3.4.2 RK2 scheme

RK2 for a model equation

Considering the model equation:

$$\frac{dv}{dt} = f(t, v), \quad (3.27)$$

the classical, explicit second-order Runge-Kutta scheme (RK2) reads:

$$v^{n+1} = v^n + \Delta t f\left[t^n + \frac{\Delta t}{2}, v^n + \frac{\Delta t}{2} f(t^n, v^n)\right]. \quad (3.28)$$

RK2 scheme for the Navier-Stokes equations

Dropping the indices k of the Fourier modes for the sake of simplicity, the semi-discrete Navier-Stokes equations (3.24) give rise to the set of ordinary differential equations:

$$\begin{cases} \frac{d\mathbf{v}}{dt} = -\mathcal{B}^{-1}\tilde{\mathcal{G}}p + \mathbf{s}(\mathbf{v}) , \\ -\tilde{\mathcal{D}}\mathbf{v} = 0 . \end{cases} \quad (3.29)$$

The RK2 scheme reads then as follows:

$$\begin{cases} \mathbf{v}^{n+1} = \mathbf{v}^n + \Delta t[-\mathcal{B}^{-1}\tilde{\mathcal{G}}p^{n+\frac{1}{2}} + \mathbf{s}^{n+\frac{1}{2}}] , \\ -\tilde{\mathcal{D}}\mathbf{v}^{n+1} = 0 , \end{cases} \quad (3.30)$$

with $p^{n+\frac{1}{2}} = p(t^n + \frac{\Delta t}{2})$, $\mathbf{v}^{n+\frac{1}{2}} = \mathbf{v}(t^n + \frac{\Delta t}{2})$, and $\mathbf{s}^{n+\frac{1}{2}} = \mathbf{s}(\mathbf{v}^{n+\frac{1}{2}})$.

- We first obtain $\mathbf{v}^{n+\frac{1}{2}}$ from \mathbf{v}^n . This first step proceeds like an Euler scheme of time step $\frac{\Delta t}{2}$. The resulting equations can be rewritten as follows:

$$\begin{pmatrix} \mathcal{B} & \tilde{\mathcal{G}} \\ -\tilde{\mathcal{D}} & 0 \end{pmatrix} \begin{pmatrix} \mathbf{v}^{n+\frac{1}{2}} \\ \frac{\Delta t}{2}p^n \end{pmatrix} = \begin{pmatrix} \mathcal{B}\mathbf{f}^n \\ 0 \end{pmatrix} , \quad (3.31)$$

where $\mathbf{f}^n = \mathbf{v}^n + \frac{\Delta t}{2}\mathbf{s}^n$ is known. Using the generalized block LU decomposition, equation (3.31) can further be decomposed:

$$\begin{pmatrix} \mathcal{B} & 0 \\ -\tilde{\mathcal{D}} & \tilde{\mathcal{D}}\mathcal{B}^{-1}\tilde{\mathcal{G}} \end{pmatrix} \begin{pmatrix} \mathbf{v}^* \\ \frac{\Delta t}{2}p^n \end{pmatrix} = \begin{pmatrix} \mathcal{B}\mathbf{f}^n \\ 0 \end{pmatrix} , \quad (3.32)$$

and

$$\begin{pmatrix} \mathcal{I} & \mathcal{B}^{-1}\tilde{\mathcal{G}} \\ 0 & \mathcal{I} \end{pmatrix} \begin{pmatrix} \mathbf{v}^{n+\frac{1}{2}} \\ \frac{\Delta t}{2}p^n \end{pmatrix} = \begin{pmatrix} \mathbf{v}^* \\ \frac{\Delta t}{2}p^n \end{pmatrix} . \quad (3.33)$$

The boundary conditions on the velocity are implicitly included when the divergence matrix is applied. To be more precise,

$$\tilde{\mathcal{D}}\mathbf{v}^* = \tilde{\mathcal{D}} \begin{pmatrix} \overset{\circ}{\mathbf{v}} \\ \mathbf{v}_b^{n+1} \end{pmatrix} ,$$

where $\overset{\circ}{\mathbf{v}}$ is the intermediate velocity field \mathbf{v}^* , restricted to $\overset{\circ}{\Upsilon}_d$, and \mathbf{v}_b is the given velocity on the boundary, $\Gamma_d = \Upsilon_d - \overset{\circ}{\Upsilon}_d$.

- We then obtain \mathbf{v}^{n+1} from $\mathbf{v}^{n+\frac{1}{2}}$ as follows:

$$\begin{pmatrix} \mathcal{B} & \tilde{\mathcal{G}} \\ -\tilde{\mathcal{D}} & 0 \end{pmatrix} \begin{pmatrix} \mathbf{v}^{n+1} \\ \Delta t p^{n+\frac{1}{2}} \end{pmatrix} = \begin{pmatrix} \mathcal{B}\mathbf{f}^{n+\frac{1}{2}} \\ 0 \end{pmatrix}, \quad (3.34)$$

where $\mathbf{f}^{n+\frac{1}{2}} = \mathbf{v}^n + \Delta t \mathbf{s}^{n+\frac{1}{2}}$ is known. Using again the generalized block LU decomposition, equation (3.34) can further be decomposed into

$$\begin{pmatrix} \mathcal{B} & 0 \\ -\tilde{\mathcal{D}} & \tilde{\mathcal{D}}\mathcal{B}^{-1}\tilde{\mathcal{G}} \end{pmatrix} \begin{pmatrix} \mathbf{v}^* \\ \Delta t p^{n+\frac{1}{2}} \end{pmatrix} = \begin{pmatrix} \mathcal{B}\mathbf{f}^{n+\frac{1}{2}} \\ 0 \end{pmatrix}, \quad (3.35)$$

and

$$\begin{pmatrix} \mathcal{I} & \mathcal{B}^{-1}\tilde{\mathcal{G}} \\ 0 & \mathcal{I} \end{pmatrix} \begin{pmatrix} \mathbf{v}^{n+1} \\ \Delta t p^{n+\frac{1}{2}} \end{pmatrix} = \begin{pmatrix} \mathbf{v}^* \\ \Delta t p^{n+\frac{1}{2}} \end{pmatrix}. \quad (3.36)$$

3.5 Pressure solver

The pressure is obtained from the direct inversion of the pseudo-Laplacian operator $\tilde{\mathcal{D}}\mathcal{B}^{-1}\tilde{\mathcal{G}}$. For solving for the pressure, we use the fast-diagonalization technique of Lynch *et al.* [44]. Let us reintroduce the indices k to denote Fourier modes, and drop the upper indices indicating the time level. We write the pressure equation, obtained via equation (3.35), term by term so that we obtain:

$$\begin{aligned} \tilde{\mathcal{D}}\mathcal{B}^{-1}\tilde{\mathcal{G}} p_k &= \\ & \left\{ \left[\tilde{\mathcal{G}}^r{}^T (r\mathcal{B}^r)^{-1} \tilde{\mathcal{G}}^r + k^2 \tilde{\mathcal{B}}^r{}^T (r\mathcal{B}^r)^{-1} \tilde{\mathcal{B}}^r \right] \otimes \left[\tilde{\mathcal{B}}^z{}^T (\mathcal{B}^z)^{-1} \tilde{\mathcal{B}}^z \right] \right. \\ & \left. + \left[r\tilde{\mathcal{B}}^r{}^T (r\mathcal{B}^r)^{-1} r\tilde{\mathcal{B}}^r \right] \otimes \left[\tilde{\mathcal{G}}^z{}^T (\mathcal{B}^z)^{-1} \tilde{\mathcal{G}}^z \right] \right\} p_k \\ &= \frac{1}{\Delta t} \tilde{\mathcal{D}}\mathbf{v}^*. \end{aligned} \quad (3.37)$$

Here again, $\mathbf{v}^* = \begin{pmatrix} \mathring{\mathbf{v}}_k \\ \mathbf{v}_b^{n+1} \end{pmatrix}$, so that velocity boundary conditions are included in equation (3.37).

Multiplying this equation by $\left[r\tilde{\mathcal{B}}^r{}^T (r\mathcal{B}^r)^{-1} r\tilde{\mathcal{B}}^r \right]^{-1} \otimes \left[\tilde{\mathcal{B}}^z{}^T (\mathcal{B}^z)^{-1} \tilde{\mathcal{B}}^z \right]^{-1}$ one obtains the separable equation:

$$[\tilde{\mathcal{M}}_k^r \otimes \tilde{\mathcal{I}}^z + \tilde{\mathcal{I}}^r \otimes \tilde{\mathcal{M}}^z] p_k = f_k, \quad (3.38)$$

where:

- $\tilde{\mathcal{M}}_k^r = \left[r\tilde{\mathcal{B}}^r{}^T (r\mathcal{B}^r)^{-1} r\tilde{\mathcal{B}}^r \right]^{-1} \left[\tilde{\mathcal{G}}^r{}^T (r\mathcal{B}^r)^{-1} \tilde{\mathcal{G}}^r + k^2 \tilde{\mathcal{B}}^r{}^T (r\mathcal{B}^r)^{-1} \tilde{\mathcal{B}}^r \right]$ and

$$\bullet \quad \widetilde{\mathcal{M}}^z = \left[\widetilde{\mathcal{B}}^z{}^T (\mathcal{B}^z)^{-1} \widetilde{\mathcal{B}}^z \right]^{-1} \left[\widetilde{\mathcal{G}}^z{}^T (\mathcal{B}^z)^{-1} \widetilde{\mathcal{G}}^z \right].$$

The right-hand side of equation (3.38) is given by:

$$f_k = \left[{}_r\widetilde{\mathcal{B}}^r{}^T ({}_r\mathcal{B}^r)^{-1} {}_r\widetilde{\mathcal{B}}^r \right]^{-1} \otimes \left[\widetilde{\mathcal{B}}^z{}^T (\mathcal{B}^z)^{-1} \widetilde{\mathcal{B}}^z \right]^{-1} \frac{1}{\Delta t} \widetilde{\mathcal{D}}\mathbf{v}^*.$$

The matrices $\widetilde{\mathcal{I}}^r$ and $\widetilde{\mathcal{I}}^z$ are the pressure identity matrices in the radial and axial directions, respectively. We decompose the matrices $\widetilde{\mathcal{M}}_k^r$ and $\widetilde{\mathcal{M}}^z$ in their respective eigenspaces:

$$\begin{cases} \widetilde{\mathcal{M}}_k^r &= \widetilde{\mathcal{Q}}_k^r \widetilde{\Lambda}_k^r \widetilde{\mathcal{Q}}_k^r{}^{-1} \\ \widetilde{\mathcal{M}}^z &= \widetilde{\mathcal{Q}}^z \widetilde{\Lambda}^z \widetilde{\mathcal{Q}}^z{}^{-1} \end{cases}.$$

Here, $\widetilde{\mathcal{Q}}_k^r$ is the matrix of the eigenvectors of $\widetilde{\mathcal{M}}_k^r$, and $\widetilde{\mathcal{Q}}^z$ the matrix of the eigenvectors of $\widetilde{\mathcal{M}}^z$, while $\widetilde{\Lambda}_k^r$ and $\widetilde{\Lambda}^z$ denote the eigenvalues matrices of $\widetilde{\mathcal{M}}^r$ and $\widetilde{\mathcal{M}}^z$, respectively. Consequently, for each mode k we obtain:

$$p_k = (\widetilde{\mathcal{Q}}_k^r \otimes \widetilde{\mathcal{Q}}^z) [\widetilde{\Lambda}_k^r \otimes \widetilde{\mathcal{I}}^z + \widetilde{\mathcal{I}}^r \otimes \widetilde{\Lambda}^z]^{-1} (\widetilde{\mathcal{Q}}_k^r{}^{-1} \otimes \widetilde{\mathcal{Q}}^z{}^{-1}) f_k. \quad (3.39)$$

The inversion of the pressure operator is the core of our solver, and is performed very rapidly due to this technique. The pressure appears in equations (3.5) only as a gradient, hence the pressure is defined modulo a constant. Once the equation for p is expressed in the pressure eigenvector space, this constant mode is easily identified as the unique eigenvector corresponding to the zero eigenvalue. An easy way to regularize the eigenvalues matrix, $\widetilde{\Lambda}_0^r \otimes \widetilde{\mathcal{I}}^z + \widetilde{\mathcal{I}}^r \otimes \widetilde{\Lambda}^z$, which we want to invert, is to replace the inverse of the zero eigenvalue by zero. This corresponds to fixing the mean pressure value over the whole domain to be zero. This is better than to impose the value of the pressure at one single point, because in that case nothing will prevent the mean pressure value from changing with time.

3.6 Boundary conditions

We impose no-slip boundary conditions on the four walls, i.e., on the two cylinders and the bottom and top end plates. Two cases have been considered, each involving a singularity of the velocity. The difficulty is that spectral methods generally can not deal easily with singularities. The property of exponential convergence of the expansion to the exact solution is indeed lost in the neighbourhood of the singularity. The error pollutes the whole domain in the case of any classical spectral method. In a spectral element method the solution is also poorly resolved in any macro-element containing a singularity, but it is less harmful for the other elements. This is one of the reasons why the spectral element formulation was chosen for this work.

- In the first case, the end plates are fixed to the outer cylinder. A singularity occurs on the two circles joining the end plates to the inner cylinder, that is at $(r, z) = (R_1, z_1)$ and $(r, z) = (R_1, z_2)$, the azimuthal velocity being different on the horizontal boundaries and on the inner cylinder. However, there is no singularity of the velocity in the corner regions of the experimental set-up. This is prevented by the small construction gap that exists between the inner cylinder, rotating at angular speed Ω_1 , and the top and bottom end plates, rotating at angular speed Ω_2 . Thus, the same gap between the inner cylinder and the two end walls is modelled in our simulation. The flow in this gap of size $\varepsilon \ll d$ is supposed to be mostly azimuthal and to evolve smoothly from the laminar, azimuthal Couette regime near the inner cylinder to the solid-body rotation of the top and bottom end plates.

We therefore replace the rotation velocity of the end plates, Ω_2 , by $\Omega(r)$ on $[R_1, R_1 + \varepsilon]$ where $\Omega(r) = \Omega_C(r)f_1(r) + \Omega_2f_2(r)$, with f_1 and f_2 two C^∞ functions defined so that Ω evolves smoothly from Ω_C to Ω_2 on $[R_1, R_1 + \varepsilon]$ (see figure 3.4). Ω_C is the rotation velocity of the circular Couette flow occurring between two cylinders of radii R_1 and $R_1 + \varepsilon$ rotating at angular velocities Ω_1 and Ω_2 , respectively:

$$\begin{aligned} - \Omega_C(r) &= a + \frac{b}{r^2}, \\ - a &= \frac{(R_1 + \varepsilon)^2 \Omega_2 - R_1^2 \Omega_1}{(R_1 + \varepsilon)^2 - R_1^2}, \text{ and} \\ - b &= \frac{(\Omega_1 - \Omega_2) R_1^2 (R_1 + \varepsilon)^2}{(R_1 + \varepsilon)^2 - R_1^2}. \end{aligned}$$

We impose both the angular velocity and its first derivative on the gap boundaries:

$$\begin{aligned} - \Omega(R_1) &= \Omega_C(R_1) = \Omega_1, \\ - \frac{d\Omega}{dr}(R_1) &= \frac{d\Omega_C}{dr}(R_1), \\ - \Omega(R_1 + \varepsilon) &= \Omega_2, \text{ and} \\ - \frac{d\Omega}{dr}(R_1 + \varepsilon) &= 0. \end{aligned}$$

We choose f_1 and f_2 to be sinusoidal functions:

$$\begin{aligned} - f_1(r) &= A_1 \sin\left(\frac{\pi}{2} \frac{R_1 + \varepsilon - r}{\varepsilon}\right) + B_1 \cos\left(\frac{\pi}{2} \frac{R_1 + \varepsilon - r}{\varepsilon}\right) \text{ and} \\ - f_2(r) &= A_2 \sin\left(\frac{\pi}{2} \frac{R_1 + \varepsilon - r}{\varepsilon}\right) + B_2 \cos\left(\frac{\pi}{2} \frac{R_1 + \varepsilon - r}{\varepsilon}\right). \end{aligned}$$

The four constraints determine the constants A_1 , A_2 , B_1 and B_2 .

- In the second case, the singularities are found at $(r, z) = (R_2, z_1)$ and $(r, z) = (R_2, z_2)$. The same regularization procedure is applied, but in $[R_2 - \varepsilon, R_2]$ this time. We replace the rotation velocity of the end plates, Ω_1 , by $\Omega(r) = \Omega_1 f_1(r) + \Omega_C(r) f_2(r)$ in the breach, with $f_i(r) = A_i \sin\left(\frac{\pi}{2} \frac{R_2 - r}{\varepsilon}\right) + B_i \cos\left(\frac{\pi}{2} \frac{R_2 - r}{\varepsilon}\right)$ and $i \in \{1, 2\}$. The velocity $\Omega_C(r) = a + \frac{b}{r^2}$ is the rotation velocity of the circular Couette

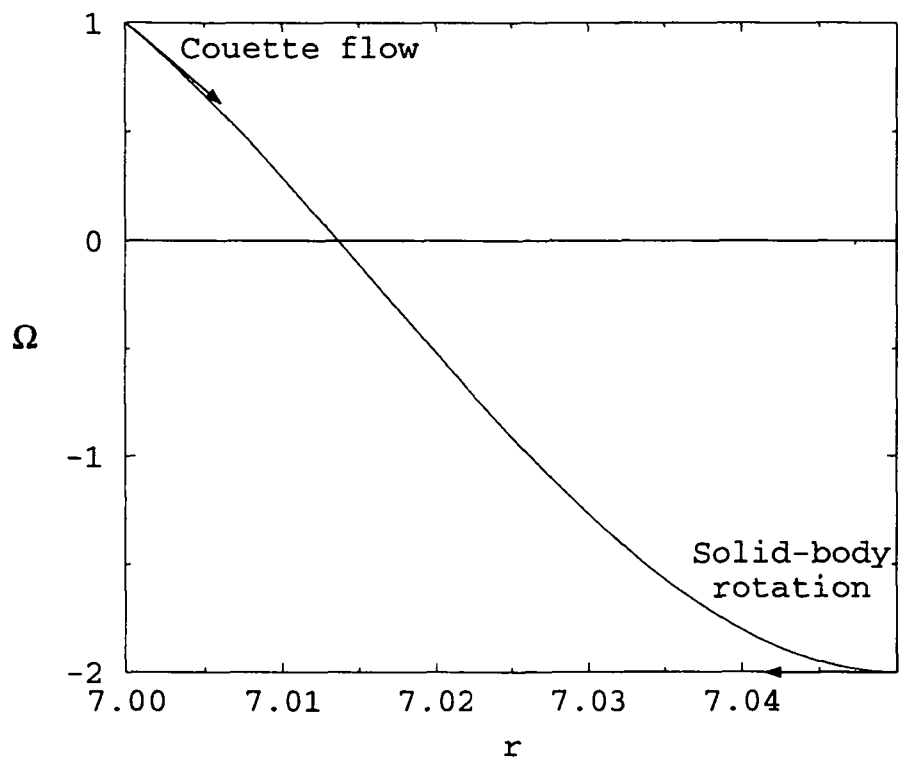


Figure 3.4: Angular velocity imposed in the clearance between the inner cylinder and the end plates to prevent a singularity. The angular velocity of the inner cylinder is $\Omega_1 = 1$; that of the outer cylinder is $\Omega_2 = -2$. The inner radius is $R_1 = 7$, the gap width $d = 1$ and the clearance $\epsilon = 0.05d$.

flow occurring between two cylinders of radii $R_2 - \varepsilon$ and R_2 . The coefficients are then:

$$\begin{aligned} - a &= \frac{R_2^2 \Omega_2 - (R_2 - \varepsilon)^2 \Omega_1}{R_2^2 - (R_2 - \varepsilon)^2} \text{ and} \\ - b &= \frac{(\Omega_1 - \Omega_2)(R_2 - \varepsilon)^2 R_2^2}{R_2^2 - (R_2 - \varepsilon)^2}. \end{aligned}$$

We impose

$$\begin{aligned} - \Omega(R_2) &= \Omega_C(R_2) = \Omega_2, \\ - \frac{d\Omega}{dr}(R_2) &= \frac{d\Omega_C}{dr}(R_2), \\ - \Omega(R_2 - \varepsilon) &= \Omega_1 \text{ and} \\ - \frac{d\Omega}{dr}(R_2 - \varepsilon) &= 0 \end{aligned}$$

to determine A_1 , A_2 , B_1 and B_2 .

3.7 Linearized problem

We consider the case of two infinite cylinders rotating around their common axis.

3.7.1 Linearization of the equations in the vicinity of the base flow

Let (\mathbf{v}_T, p_T) , be a slight disturbance of the base flow and also a solution of the Navier-Stokes equations. We write $\mathbf{v}_T = \mathbf{v} + \mathbf{v}_c$ and $p_T = p + p_c$, with: $\|\mathbf{v}\| \ll \|\mathbf{v}_c\|$ and $|p| \ll |p_c|$. We only keep the first-order perturbation terms in the equations. We then get the dimensionless linearized Navier-Stokes equations, expressed as follows in cylindrical coordinates:

$$\begin{cases} \frac{\partial u}{\partial t} = \nabla^2 u - \frac{u}{r^2} - \frac{2}{r^2} \frac{\partial v}{\partial \theta} - \frac{\partial p}{\partial r} + 2C(r) v - C(r) \frac{\partial u}{\partial \theta} & , \\ \frac{\partial v}{\partial t} = \nabla^2 v - \frac{v}{r^2} + \frac{2}{r^2} \frac{\partial u}{\partial \theta} - \frac{1}{r} \frac{\partial p}{\partial \theta} - 2A Re u - C(r) \frac{\partial v}{\partial \theta} & , \\ \frac{\partial w}{\partial t} = \nabla^2 w - \frac{\partial p}{\partial z} - C(r) \frac{\partial w}{\partial \theta} & , \\ 0 = \frac{\partial u}{\partial r} + \frac{1}{r} u + \frac{1}{r} \frac{\partial v}{\partial \theta} + \frac{\partial w}{\partial z} & , \end{cases} \quad (3.40)$$

with $C(r) = Re \frac{v_c(r)}{r} = Re \left(A + \frac{B}{r^2} \right)$. As in the first section of this chapter, the Reynolds number is $Re = \frac{dV}{\nu}$.

Because Couette flow satisfies the boundary conditions, the perturbation has homogeneous Dirichlet boundary conditions.

3.7.2 Spatial discretization

Choice of the basis We express u , v , w , and p in a tensor basis made of Lagrange-Legendre interpolants in the radial direction and Fourier expansions in both azimuthal

and axial directions. The azimuthal direction is periodic by definition. And, we know from numerous previous studies with infinite cylinders, that the flow regime following the base Couette flow is periodic in the axial direction. Both Taylor-vortex flow and spiral flow are indeed axially periodic.

Expansion in Fourier directions The velocity is expanded as follows:

$$\mathbf{v}(r, \theta, z, t) = \sum_{k=0}^{N^\theta-1} \sum_{o=0}^{N^z-1} \mathbf{v}_{ko}(r, t) \exp(\mathbf{i} k \theta) \exp(\mathbf{i} o Z) \quad (3.41)$$

The same expression applies for any of the velocity components and for the pressure. We introduce $Z = \frac{2\pi}{\lambda} z$, λ being the axial period.

Equations in Fourier space The equations (3.40) being linear, there are $N^\theta \times N^z$ independent equations to solve for each pair of Fourier modes (k, o) . Each of these has the following form:

$$\begin{cases} \dot{u}_{ko} = u''_{ko} + \frac{1}{r} u'_{ko} - \left[\frac{1+k^2}{r^2} + \bar{o}^2 + \mathbf{i} k C(r) \right] u_{ko} + 2 [C(r) - \mathbf{i} \frac{k}{r^2}] v_{ko} - p'_{ko} & , \\ \dot{v}_{ko} = v''_{ko} + \frac{1}{r} v'_{ko} - \left[\frac{1+k^2}{r^2} + \bar{o}^2 + \mathbf{i} k C(r) \right] v_{ko} + 2 [-A Re + \mathbf{i} \frac{k}{r^2}] u_{ko} - \mathbf{i} \frac{k}{r} p_{ko} & , \\ \dot{w}_{ko} = w''_{ko} + \frac{1}{r} w'_{ko} - \left[\frac{k^2}{r^2} + \bar{o}^2 + \mathbf{i} k C(r) \right] w_{ko} - \mathbf{i} \bar{o} p_{ko} & , \\ 0 = u'_{ko} + \frac{1}{r} u_{ko} + \mathbf{i} \frac{k}{r} v_{ko} + \mathbf{i} \bar{o} w_{ko} & . \end{cases}$$

The radial derivative is denoted by a prime: $\frac{\partial u}{\partial r} = u'$, and the time derivative by a dot: $\frac{\partial u}{\partial t} = \dot{u}$. We also introduce the notation $\bar{o} = \frac{2\pi}{\lambda} o$.

Expansion in the radial direction We decompose the radial domain $[R_1, R_2]$ in E subintervals $[r_0^e, r_0^e + g^e]$, $e \in \{1, 2, \dots, E\}$. The radial expansion of the velocity in the interval $[r_0^e, r_0^e + g^e]$ is:

$$\mathbf{v}_{ko}(r, t)|_{[r_0^e, r_0^e + g^e]} = \sum_{n=0}^{N_r} \mathbf{v}_{nko}^e(t) \phi_n^e(r) . \quad (3.42)$$

The test function ϕ_n^e is zero in any element except $[r_0^e, r_0^e + g^e]$ where we have: $\phi_n^e[r(x)] = h_n(x)$. There, $r(x) = r_0^e + \frac{g^e}{2}(x+1)$ is the affine mapping from the parent element $[-1, 1]$ to the e -th radial element, $[r_0^e, r_0^e + g^e]$. As in the third section of this chapter, h_n denotes the Lagrange interpolant based on the n -th Gauss-Lobatto-Legendre point, $0 \leq n \leq N_r$.

On $[r_0^e, r_0^e + g^e]$, the expansion for the pressure is:

$$p_{ko}(r, t)|_{[r_0^e, r_0^e + g^e]} = \sum_{n=1}^{N_r-1} p_{nko}^e(t) \psi_n^e(r) \quad (3.43)$$

The test function ψ_n^e is zero in any element except on $[r_0^e, r_0^e + g^e]$, where it is defined by $\psi_n^e[r(x)] = \tilde{h}_n(x)$. The function \tilde{h}_n , is defined in the third section of this chapter as the Lagrange interpolant at the n -th inner GLL point, $1 \leq n \leq N_r - 1$.

Ordinary Differential Equations The same steps as in the fourth section of this chapter are taken, so that we obtain the following semi-discrete equations:

$$\begin{cases} \mathcal{B} \dot{u}_{ko} = \mathcal{A} u_{ko} - \mathcal{B} \left[\frac{1+k^2}{r^2} + \tilde{\sigma}^2 + \mathbf{i}kC(r) \right] u_{ko} + 2\mathcal{B} \left[C(r) - \mathbf{i}\frac{k}{r^2} \right] v_{ko} - \tilde{\mathcal{G}} p_{ko} & , \\ \mathcal{B} \dot{v}_{ko} = \mathcal{A} v_{ko} - \mathcal{B} \left[\frac{1+k^2}{r^2} + \tilde{\sigma}^2 + \mathbf{i}kC(r) \right] v_{ko} + 2\mathcal{B} \left[D + \mathbf{i}\frac{k}{r^2} \right] u_{ko} - \mathbf{i}k\tilde{\mathcal{B}} p_{ko} & , \\ \mathcal{B} \dot{w}_{ko} = \mathcal{A} w_{ko} - \mathcal{B} \left[\frac{k^2}{r^2} + \tilde{\sigma}^2 + \mathbf{i}kC(r) \right] w_{ko} - \mathbf{i}\tilde{\sigma} \tilde{r}\tilde{\mathcal{B}} p_{ko} & , \\ \mathbf{0} = -\tilde{\mathcal{G}}^T u_{ko} + \mathbf{i}k\tilde{\mathcal{B}}^T v_{ko} + \mathbf{i}\tilde{\sigma} \tilde{r}\tilde{\mathcal{B}}^T w_{ko} & . \end{cases} \quad (3.44)$$

The terms u_{ko} , v_{ko} , w_{ko} and p_{ko} now represent vectors in the discrete space: $\mathbf{v}_{ko} = (\mathbf{v}_{nko}^e)_{\substack{1 \leq e \leq I \\ 0 \leq n \leq N_r}}$, and $p_{ko} = (p_{nko}^e)_{\substack{1 \leq e \leq I \\ 1 \leq n \leq N_r - 1}}$.

3.7.3 Time discretization

We choose the same time stepping scheme as for the 3D Navier-Stokes solver.

Chapter 4

Validation and performance

4.1 Validation

4.1.1 Analytical test cases

The key steps of the validation are presented here (see also the internal report [46]). The validation preceded by testing each subroutine separately first, and meaningful groups of subroutines next, and then still larger groups, until there were only three main subparts to represent the code: creation of the source term, inversion and time marching.

Elementary parts

We consider velocity and pressure fields as given data and compare separately each term in the Navier-Stokes equations calculated analytically with the same term evaluated numerically.

The velocity field we have chosen for these comparisons is divergence free and is expressed as follows:

$$\begin{cases} u(r, \theta, z) = \frac{1}{r} \sin(\theta) \cos(\pi z), \\ v(r, \theta, z) = \pi r \sin(\pi r) \cos(\theta) \cos(\pi z), \\ w(r, \theta, z) = \sin(\pi r) \sin(\theta) \sin(\pi z). \end{cases} \quad (4.1)$$

The pressure field is:

$$p(r, \theta, z) = \sin(\pi r) \sin(\theta) \sin(\pi z). \quad (4.2)$$

We performed the validation by verifying the spectral convergence of the non-linear (both in convective and skew-symmetric forms), diffusive, pressure gradient and weak divergence terms to the exact solution. The number of elements in each direction and the size of the macro-elements were varied for each term. We report in figure 4.1 the convergence diagrams obtained with 2 elements in the radial direction and 3 in the axial direction. The sizes of the elements are 1 in the radial direction and 0.67 in the axial

direction. The polynomial degree in the azimuthal direction is 4. For low values of the polynomial degree, N , in both radial and axial directions, the numerical convergence curve for the divergence corresponds very closely to the theoretical convergence curve varying as N^{-N} . But, above $N = N_c = 12$ (N_c varies from 12 to 18 depending on the term of the equation considered), the error for the discrete divergence starts increasing. This increase is slow compared with the exponential decrease. The exact representation of the sinusoidal test functions in a Lagrange polynomial basis requires the whole set of basis functions, $\sin(x) = \sum_0^\infty a_n h_n(\zeta(x))$, for $x = \pi r$ or πz , $\zeta \in [-1, 1]$. The coefficients, a_n , of this expansion decrease exponentially with n . When the theoretical value of a_n falls below the round-off error, ϵ , of the machine (around 10^{-16} in single precision on the CRAY YMPM94), the calculated coefficient stays at a plateau of level ϵ . Furthermore, the application of the derivation matrix to a vector is equivalent to multiplying its higher coefficients by the square of the polynomial degree, N^2 . Hence, once N exceeds N_c , the most significant error term is no longer the truncation error, decreasing as N^{-N} , but the error linked to the round-off error of the computer, increasing as ϵN^2 . Once the theoretical convergence curve is corrected likewise, we call it practical convergence curve (see 4.1).

Pseudo-Poisson

The inversion of the pseudo-Laplacian, being the core of our code, we validated it carefully.

Characterization of the pseudo-Poisson operator The pseudo-Poisson matrix, involved in the determination of the pressure, is compared with its continuous counterpart, the Laplacian operator. The eigenvectors of the continuous operator and of the matrix are presented in figures 4.2 and 4.3. The eigenfunctions of the radial part of the continuous Laplacian, $\frac{1}{r} \frac{\partial}{\partial r} (r \frac{\partial}{\partial r})$, are Bessel functions, while those of the axial part, $\frac{\partial^2}{\partial z^2}$, are sine and cosine functions. The discrete and continuous eigenvectors match well if the mesh is sufficiently fine. Typically, a single sine period is resolved correctly if the polynomial degree is higher than 8 in one element. Due to the clustering of the GLL points near the element boundaries (the distance between successive points evolves there as $1/N^2$), modes close to the N^2 mode can also be captured in addition to the expected first N modes.

All the eigenvalues ($\widetilde{\Lambda}_k^r$ and $\widetilde{\Lambda}^z$) of the pseudo-Poisson matrix are real and strictly negative except the one corresponding to the constant pressure mode, which lies in the kernel. Figure 4.4 presents the eigenvalues of $\widetilde{\mathcal{M}}_k^r$ for $k = 0$ and $k = 1$. In figure 4.5 are shown the eigenvalues of the axial matrix $\widetilde{\mathcal{M}}^z$. The first 70% of both curves behaves like N^2 , with $N = N_r$ for the first figure and $N = N_z$ for the second figure, while the remaining eigenvalues evolve as N^4 .

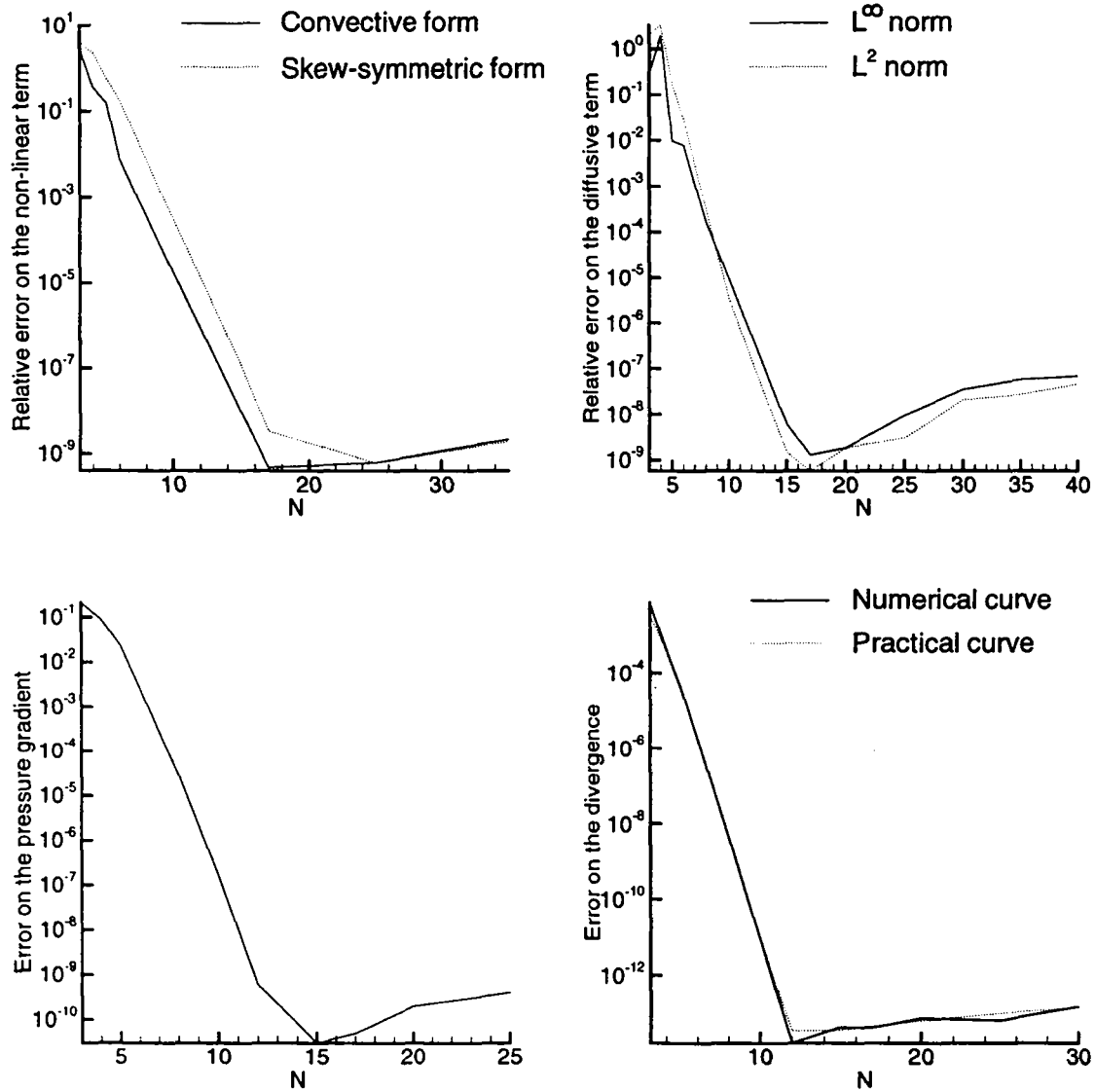


Figure 4.1: Spectral convergence curves of the radial non-linear term, the radial Laplacian, the radial pressure gradient and the weak divergence. In each case, $N = N_r = N_z$ is the polynomial degree of the expansion. For the non-linear term, whose non-zero modes are 0 and 2, $N_\theta = 8$, and in all other three cases, where only the mode 1 is present, $N_\theta = 4$. The domain is discretized with $I = 2$ elements in the radial direction and $J = 3$ elements in the axial direction. If not mentioned, the norm chosen is the norm of the maximum, L^∞ .

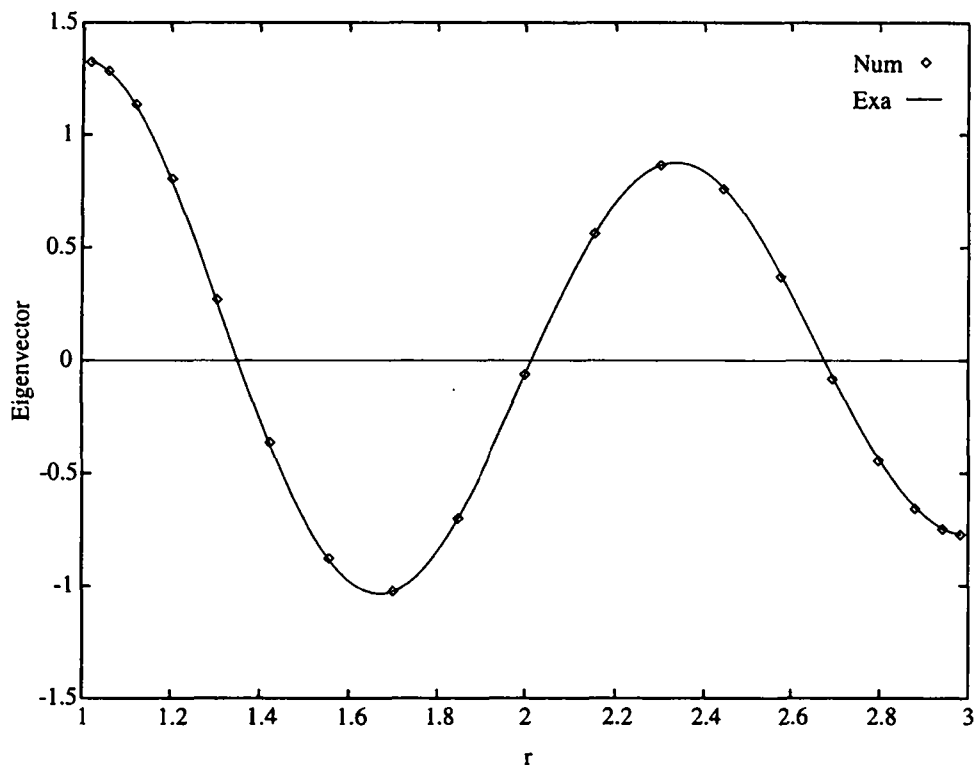


Figure 4.2: *Fourth eigenfunction of the matrix \tilde{Q}_0^r of the Laplacian in the radial direction. $I = 1$, and $N_r = 20$. The line of equation $-9.9 [Y_1(4.7381) \cdot J_0(4.7381 x) - J_1(4.7381) \cdot Y_0(4.7381 x)]$ is the continuous eigenfunction, where J_0 and J_1 are the Bessel functions of the first kind of order 0 and 1, and Y_0 and Y_1 the Bessel functions of the second kind of order 0 and 1. The points are the discrete counterpart.*

Inversion of the pseudo-Laplacian We verify here the spectral accuracy of the numerical solution of equation:

$$\nabla^2 p = f . \quad (4.3)$$

To better understand the difference between a Laplacian and a pseudo-Laplacian, we decompose equation (4.3) in two relations:

$$\begin{cases} -\nabla p = \mathbf{s} , \\ -\nabla \cdot \mathbf{s} = f . \end{cases} \quad (4.4)$$

The equivalent matrix form is:

$$\begin{cases} -\mathcal{B}^{-1} \tilde{\mathcal{G}} p = \mathbf{s} , \\ -\tilde{\mathcal{D}} \mathbf{S} = f . \end{cases} \quad (4.5)$$

with $\mathbf{S} = \begin{pmatrix} \mathbf{s} \\ \mathbf{s}_b \end{pmatrix}$, \mathbf{s} being defined in $\mathring{\Upsilon}_d$ and \mathbf{s}_b in Γ_d .

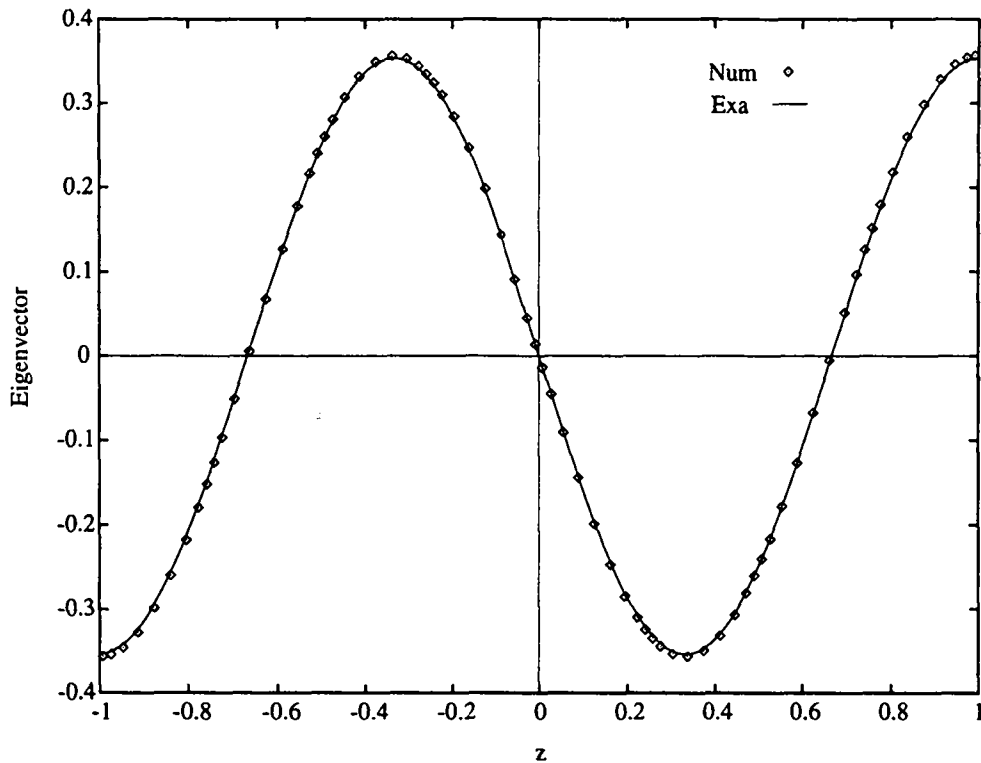


Figure 4.3: Fourth eigenfunction of the Laplacian in the axial direction. $J = 8$ and $N_z = 10$. The line of equation $-\frac{1}{2\sqrt{2}} \sin(\frac{3\pi}{2} x)$ is the axial eigenvector of eigenfunctions matrix \tilde{Q}^z . The points are the discrete counterpart.

The resulting equation on the pressure is:

$$\tilde{D}B^{-1}\tilde{G}p = f - \tilde{D} \begin{pmatrix} 0 \\ s_b \end{pmatrix}, \quad (4.6)$$

Therefore, the test on this part of the code can be performed in two different ways. Either we choose a pressure field, p , such that its gradient is zero on the boundary, which results in having $s_b = 0$, and then form the source term f as the analytical expression $\nabla^2 p$, or we take a pressure field without any condition on the boundary, but replace the pressure gradient by zero on the domain boundary, therefore imposing again $s_b = 0$, and apply the divergence matrix to this analytical expression to create the source term f . We simply look for spectral convergence of the numerical solution of equation (4.3) towards the given pressure field. In our validation, we performed both tests with the pressure:

$$p(r, \theta, z) = \sin(\pi r) \sin(\theta) \sin(\pi z), \quad (4.7)$$

in two different domains:

- $[0.5, 2.5] \times [0, 2\pi] \times [-0.5, 1.5]$, where the normal pressure gradient cancels on the domain boundary and

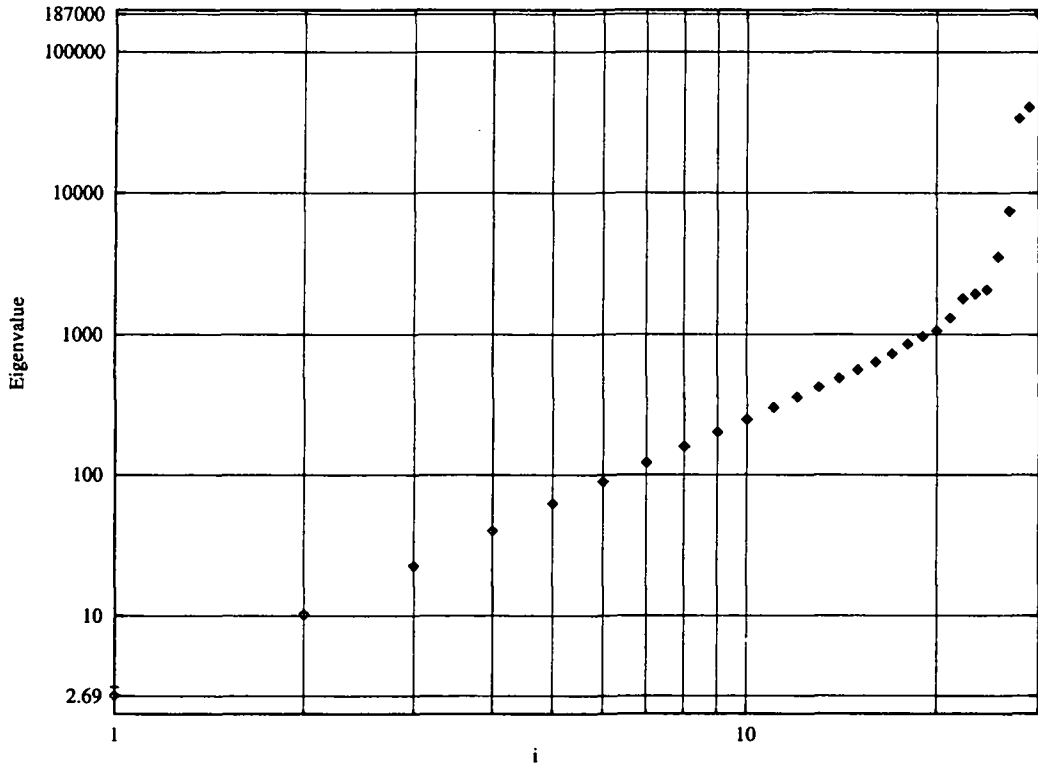


Figure 4.4: Absolute value of the eigenvalues of the Laplacian in the radial direction $|\tilde{\Lambda}_{k \in \{0,1\}}^r(i)|$. $I = 2$ and $N_r = 16$. The eigenvalue index is i . The symbols \diamond represents $\tilde{\Lambda}_0^r$ and $+$ represents $\tilde{\Lambda}_1^r$.

- $[1, 3] \times [0, 2\pi] \times [-1, 1.1]$, where, ∇p does not cancel on the domain boundary.

Only the results of the second test are presented here, in figure 4.6, because this test is more drastic on the pressure boundary conditions.

Time-marching scheme

We have tested the validity of the time-marching scheme for two different pressure and velocity fields defined as the product of the analytical steady fields of equations (4.1) and (4.2) by the time functions $f(t) = \exp(-t)$ or $f(t) = \sin(\pi t)$.

$$\begin{cases} u(r, \theta, z) = \frac{1}{r} \sin(\theta) \cos(\pi z) f(t), \\ v(r, \theta, z) = \pi r \sin(\pi r) \cos(\theta) \cos(\pi z) f(t), \\ w(r, \theta, z) = \sin(\pi r) \sin(\theta) \sin(\pi z) f(t), \\ p(r, \theta, z) = \sin(\pi r) \sin(\theta) \sin(\pi z) f(t). \end{cases} \quad (4.8)$$

We carried out three different tests starting from the simple Darcy equations to finally treat the whole Navier-Stokes equations. The domain is the same in all three cases: $\tilde{\Upsilon} = [1, 3] \times [0, 2\pi] \times [-1, 1.1]$.

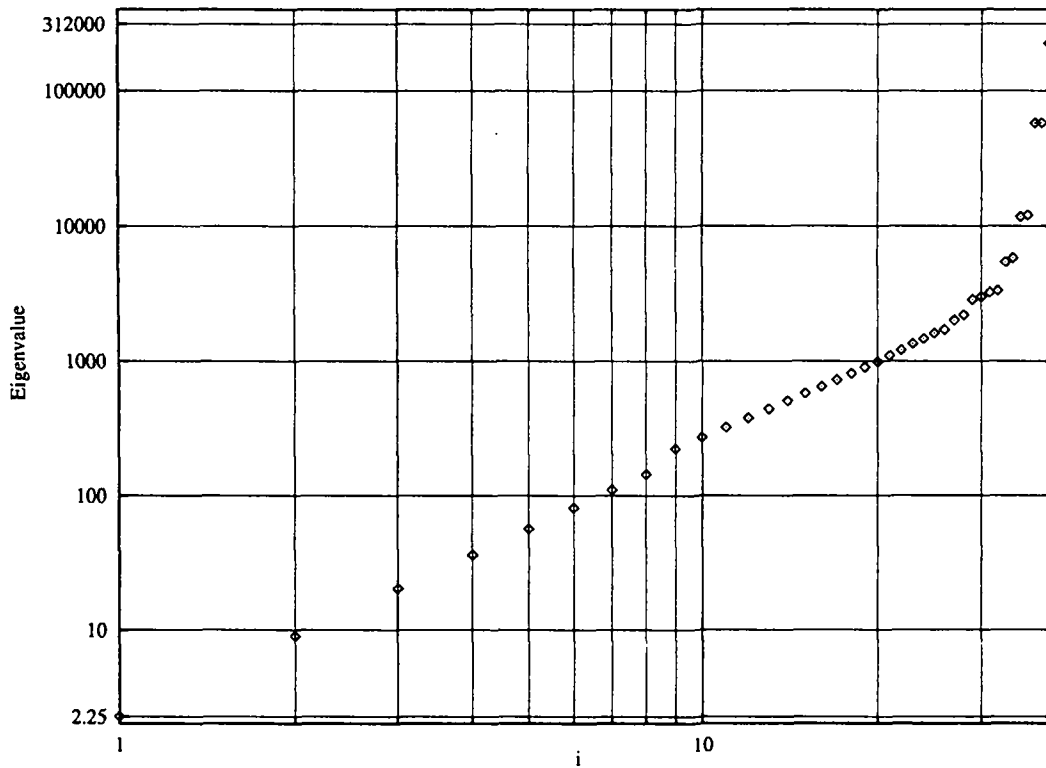


Figure 4.5: Absolute value of the eigenvalues of the Laplacian in the axial direction $|\tilde{\Lambda}^z(i)|$. $J = 3$ and $N_z = 15$.

“Unsteady Darcy” equations The model equations are:

$$\begin{cases} \frac{\partial \mathbf{v}}{\partial t} = -\nabla p + \mathbf{f} & \text{in } \Upsilon, \\ \nabla \cdot \mathbf{v} = 0 & \text{in } \tilde{\Upsilon}. \end{cases} \quad (4.9)$$

Unsteady Stokes equations The model equations are:

$$\begin{cases} \frac{\partial \mathbf{v}}{\partial t} = \Delta \mathbf{v} - \nabla p + \mathbf{f} & \text{in } \Upsilon, \\ \nabla \cdot \mathbf{v} = 0 & \text{in } \tilde{\Upsilon}. \end{cases} \quad (4.10)$$

Unsteady Navier-Stokes equations The model equations are:

$$\begin{cases} \frac{\partial \mathbf{v}}{\partial t} = -\mathbf{n}l(\mathbf{v}) + \Delta \mathbf{v} - \nabla p + \mathbf{f} & \text{in } \Upsilon, \\ \nabla \cdot \mathbf{v} = 0 & \text{in } \tilde{\Upsilon}. \end{cases} \quad (4.11)$$

We only present here the results of the first test. The others have the same general behaviour. We have verified that the numerical velocity and pressure fields followed accurately the exact solution with respect to time. We have also compared the order of the scheme we have obtained to the order we expected, i.e. second-order time accuracy. Figures 4.7 and 4.8 present the time evolution of the error ($\|\cdot\|_\infty$) between the calculated and the exact velocity. We see in the first figure that when the time step ratio is ten, the corresponding error ratio is a hundred. In the same way, when the time step ratio is

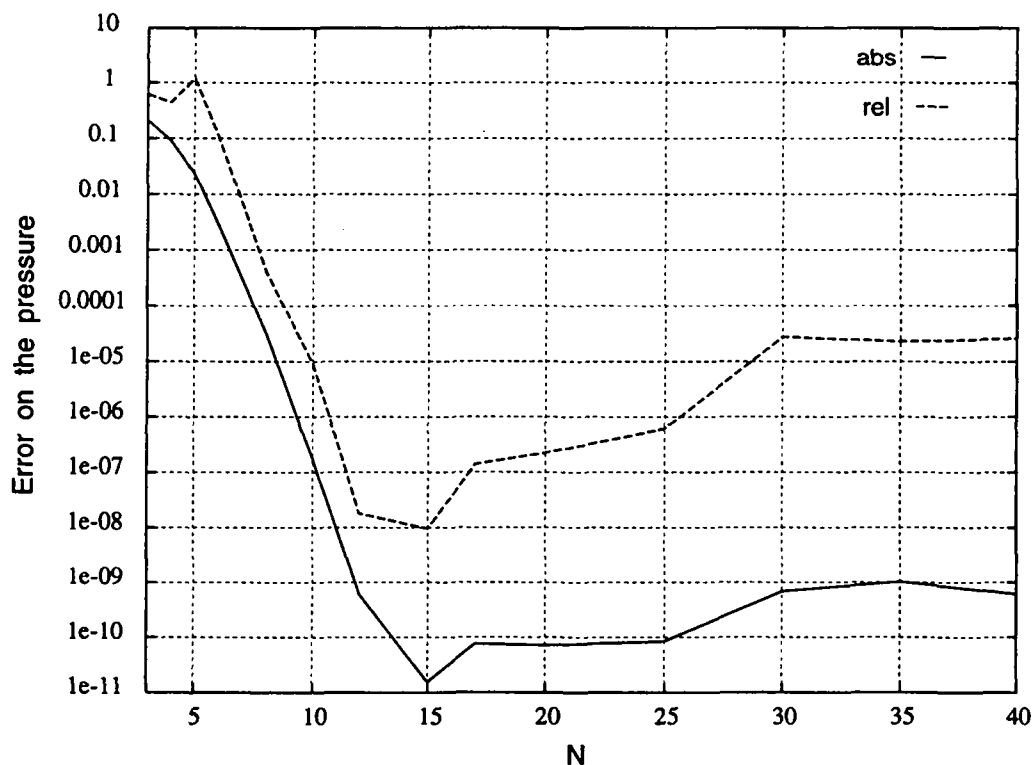


Figure 4.6: L^∞ Norm of the absolute and relative error made on the pressure obtained by inversion of the pseudo-Laplacian.

Time step Δt_1	Time step Δt_2	Time step ratio $\frac{\Delta t_1}{\Delta t_2}$	Error ratio		
			Time 0.2	Time 0.5	Time 1
10^{-1}	10^{-2}	10	99.97	99.97	99.97
10^{-2}	10^{-3}	10	99.99	99.99	99.99

Table 4.1: Error ratio compared with time step ratio, for w and $f(t) = \exp(-t)$.

two, in (4.8), the error ratio is four. This result is shown in a more qualitative fashion in the following tables (4.1 and 4.2).

4.1.2 Comparison with experiments and other simulations

The purpose is to validate the full algorithm by comparing numerical results with existing experimental data. Among the many existing results, we chose the two following experiments because they enabled us to validate separately the regularization of the boundary conditions we had chosen on one hand and the time-stepping scheme on the other hand. The first experiment deals with a steady flow and necessitates a regularization of the boundary conditions, while the second one deals with an unsteady flow where no regularization is needed.

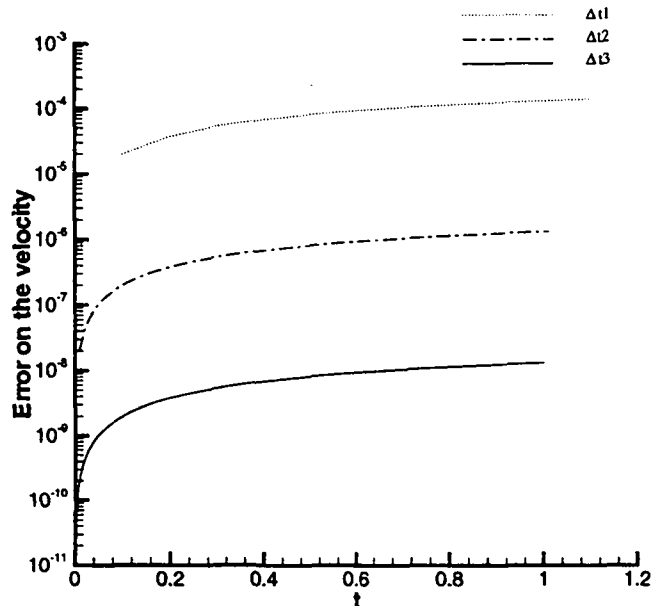


Figure 4.7: Time history of the L_∞ error on the azimuthal velocity for three different time steps: $\Delta t_1 = 10^{-1}$, $\Delta t_2 = 10^{-2}$, $\Delta t_3 = 10^{-3}$. Time dependence is given by $f(t) = e^{-t}$. The order of the scheme is 2 as expected because $\frac{\|V_{num}(\Delta t_1) - V_{exa}(\Delta t_1)\|_\infty}{\|V_{num}(\Delta t_2) - V_{exa}(\Delta t_2)\|_\infty} = \left(\frac{\Delta t_1}{\Delta t_2}\right)^2$.

Time step	Time step	Time step	Error ratio		
Δt_1	Δt_2	ratio $\frac{\Delta t_1}{\Delta t_2}$	Time 0.1	Time 0.5	Time 0.9
10^{-2}	$5 \cdot 10^{-3}$	2	4.0001	4.0001	4.0001
$5 \cdot 10^{-3}$	$2.5 \cdot 10^{-3}$	2	4.00002	4.00002	4.00003

Table 4.2: Error ratio compared with time step ratio, for v and $f(t) = \sin(t)$.

Validation of the regularization of the boundary conditions

We have compared our results to those obtained numerically by Streett and Hussaini [61, 62] and also those obtained experimentally by Aitta *et al.* [2] for the same geometry and the same dynamic parameters. They studied the transition occurring in Taylor-Couette flow for a radii ratio $\eta = 0.5$ and very short aspect ratios, such that there is only one vortex pair. If the speed of the inner cylinder is smaller than a critical value, the vortices are symmetric, but above that speed, one vortex starts to grow at the expense of the other. Depending on the aspect ratio, this transition can be supercritical, for $\Gamma \leq 1.255$, or subcritical, $\Gamma \geq 1.255$, according to [2]. The subcritical behaviour is observed for aspect ratios between 1.267 and 1.304 in [54]. In the supercritical case the symmetry is broken smoothly, while in the subcritical case the bifurcation is abrupt. Whereas most numericists have simulated Taylor-Couette flow in the case of infinite-length cylinders, such an assumption is not possible in the case of the transition

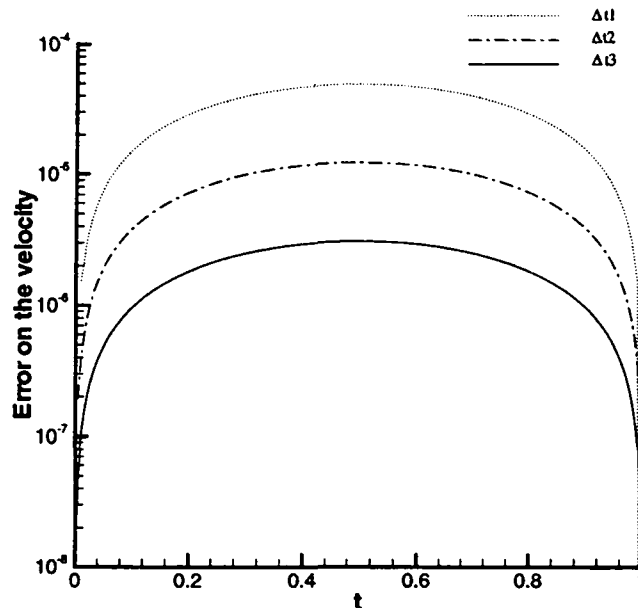


Figure 4.8: Time history of the L_∞ error on the azimuthal velocity for three different time steps: $\Delta t_1 = 2.5 \cdot 10^{-3}$, $\Delta t_2 = 5 \cdot 10^{-3}$, $\Delta t_3 = 10^{-2}$. Time dependence is given by $f(t) = \sin(\pi t)$.

we want to study here because Ekman cells, whose characteristic velocity (between 1% and 10% of the maximum azimuthal velocity) is small but not negligible compared with the main flow, appear due to the presence of the end plates. We have therefore chosen to use no slip boundary conditions on the horizontal ends. In the present case the end plates are fixed to the outer cylinder. These three parts are motionless while the inner cylinder is rotating. This creates a singularity of the azimuthal velocity at the circle lines joining the end plates and the inner cylinder. We compared our simulations with those of Streett *et al.*. But, the way we treat the singularity is different from theirs.

Streett *et al.* used high-order, weighted-residual techniques of the spectral kind in the radial and axial directions and Fourier expansions in the azimuthal direction to perform a direct numerical simulation of the flow. They split the velocity field in a first part, \mathbf{v}_b , which satisfies both the boundary conditions and a Poisson equation inside the domain, and a second part, \mathbf{v}_c , which satisfies simple homogeneous Dirichlet boundary conditions as well as modified Navier-Stokes equations. This modification consists of adding a source term, resulting from the splitting of the original velocity: $\mathbf{v} = \mathbf{v}_b + \mathbf{v}_c$. The problem of the singularity remains on the velocity field; \mathbf{v}_b , in this case.

We then decided to turn to another treatment of the boundary conditions, that presented in chapter 3. We introduce a small gap between the inner cylinder and the two end plates in the simulation. The flow in this gap is supposed to evolve smoothly, following a function $F(r)$, from the laminar azimuthal Couette regime, near the inner

cylinder, to the solid body rotation of the top and bottom end plates. The exact form of F is unknown. But, according to Tavener *et al.* [65], who did a similar study, “provided ϵ is sufficiently small (< 0.02), the effect of the form of F on the flow patterns away from the immediate vicinity of the corners is negligibly small”. We demonstrate briefly here that the radial and axial velocities that one could expect are negligibly small. The radial velocity in the gap is supposed to be affected by the radial velocity in the Ekman boundary layer present at the end plates, while the axial velocity is itself under the influence of the Stewartson boundary layer developing on the inner cylinder. Considering mass conservation, both in the gap and in the main region, we are able to scale the maximum radial velocity in the breach as: $\sqrt{E_k} \frac{\epsilon}{d} V$, and the maximum axial velocity in the breach as: $\sqrt{E_k} \frac{d}{L} V$, V being the characteristic magnitude of the azimuthal velocity in the main region. The Ekman number characterizing the ratio of diffusion to inertia on a disk of characteristic radius R_1 moving at a differential angular speed Ω_1 compared with the surrounding fluid, is: $E_k = \frac{\nu}{\Omega_1 R_1^2}$.

We observed a transition from a symmetric flow made of two equal Ekman cells to an asymmetric one made of two cells of different sizes, as can be seen in figure 4.9. Here is presented the time evolution of the stream function in the meridian plane, the flow being axisymmetric. The first picture, at the upper left of figure 4.9, is taken at the initial time. At $t = 0$, a perturbation is introduced in which the intensity (characterized by the stream function) of the upper Ekman cell is multiplied by a factor 1.001. The Reynolds number of this unsteady simulation is $Re_1 = 165$. The initial symmetric flow is unstable for this Reynolds number so that the upper Ekman cell starts to increase until the flow reaches steady-state. The asymmetry of the final flow is characterized by the so-called asymmetry parameter, Ψ , first proposed by Aitta *et al.* [2] and also used by Streett *et al.* [61, 62]:

$$\Psi = \frac{\int_0^L w(r = R_1 + 0.14d, z) dz}{\int_0^L |w(r = R_1 + 0.14d, z)| dz}.$$

The final steady-state asymmetry is $\Psi = 0.82$.

We repeated this study for different Reynolds numbers, from $Re_1 = 142$ to 170, and from $Re_1 = 170$ back to $Re_1 = 142$. These simulations are summarized in figure 4.10. Increasing the Reynolds number (the initial state is symmetric), we find that the flow becomes asymmetric for $Re_1 = 148$. But, when decreasing the Reynolds number (the initial state is asymmetric this time) the flow returns to symmetry for $Re_1 = 145$. Hysteresis is observed, which is characteristic of a subcritical transition.

Our results compare very well to the simulations of Streett *et al.* and well also to the experiments of Aitta *et al.*, but less so. The difference between the experimental results and the numerical ones may be due to a small difference in the radius for which the asymmetry is measured, as is conjectured by Streett *et al.*, or to the finite clearance existing between the rotating inner cylinder and the fixed end plates in the experiment. In figure 4.11 is shown the variation of the asymmetry parameter, Ψ , with the clearance

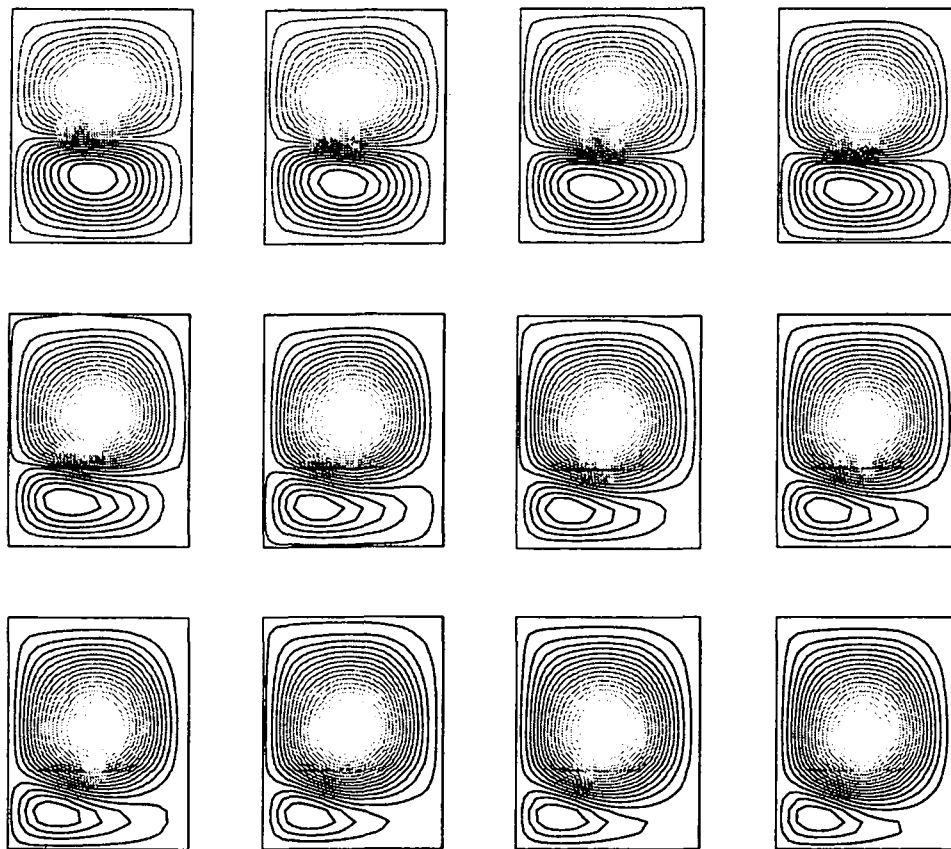


Figure 4.9: *Streamlines in the meridian plane. The Reynolds number is: 165, and $\Gamma = 1.281$. Here are shown 12 successive times starting from the unstable symmetric flow and continuing until the final asymmetric flow, characterized by $\Psi = 0.82$. The increment, $\Delta\Psi$, is 0.1 between each picture.*

we impose numerically. From this, it appears that the larger the clearance is, the closer the experimental and the numerical results become.

Comparison with the pulsed Taylor-Couette flow experiment

The pulsed Taylor-Couette flow is that of a fluid confined between two coaxial cylinders, fastened together, that rotate with angular speed: $\Omega(t) = \Omega_m + \Omega_0 \cos \omega t$. This flow undergoes a periodic destabilization when the rotational speed, Ω_0 , is increased. The primary flow, consisting of two Stokes layers developing from each of the cylindrical walls, bifurcates to periodically appearing Taylor vortices.

The relevant non-dimensional parameters are:

- the modulation frequency, $\sigma = \frac{\omega d^2}{\nu} = \frac{\tau_D}{\tau_p}$, τ_D being the diffusive time-scale and $\tau_p = \frac{1}{\omega}$ the characteristic pulsation time,
- $\gamma = \sqrt{\frac{\sigma}{2}}$, which also represents the modulation and can be expressed as the ratio

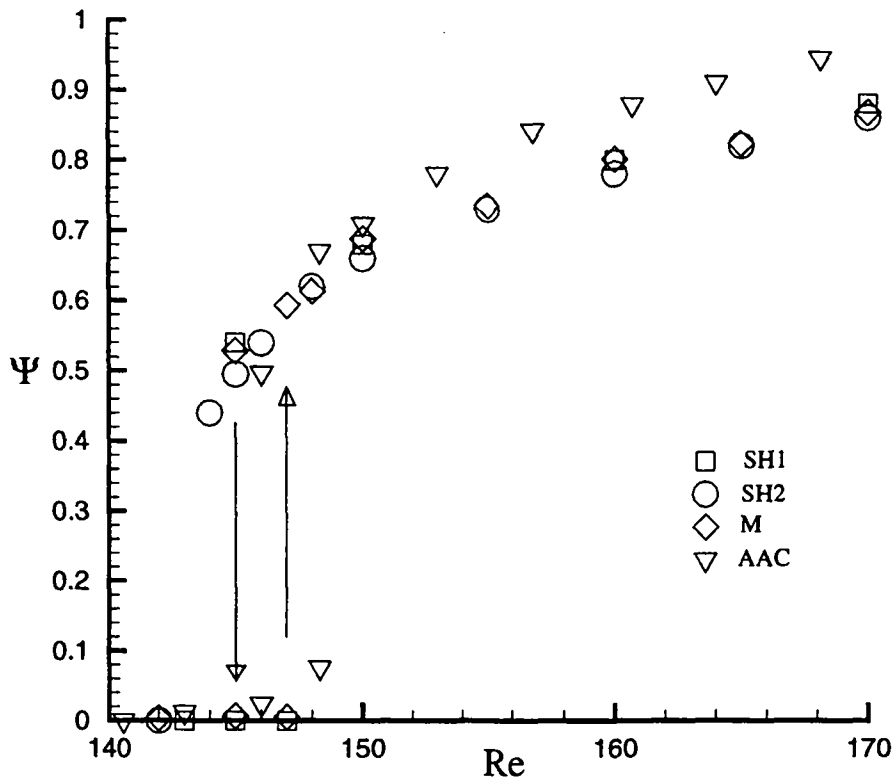


Figure 4.10: Comparison between the the experiments of Aitta, Ahlers and Cannel, ∇ ; the steady, \circ , and time-dependent, \square , simulations of Streett and Hussaini; and ours, \diamond .

of two length scales: $\gamma = \frac{d}{\delta}$, where $\delta = \sqrt{\frac{2\nu}{\omega}}$ is the Stokes layer thickness of an oscillating flat plate with pulsation ω .

- The Taylor number, $Ta = \frac{\Omega_0 \sqrt{R_1 d^3}}{\nu}$, or equivalently,
- the Reynolds number: $Re = \frac{R_1 \Omega_0 d}{\nu}$, and
- the rotation number: $r_o = \frac{d}{R_1} \frac{\Omega_m}{\Omega_0}$. This dynamic parameter is more specific to pulsed Taylor-Couette flow.

We performed a simulation at the same geometrical and dynamical parameters as those of Ern [27], i.e. $\Gamma = 39.4$, $\eta = 0.90$. We only treat the case $\Omega_m = 0$.

Primary flow The primary flow consists of two Stokes layers developing from each of the cylindrical walls. In the case of infinitely long cylinders, the base flow is solely azimuthal; the velocity field, \mathbf{v} , being $(0, v_b, 0)$ in cylindrical coordinates (r, θ, z) . The

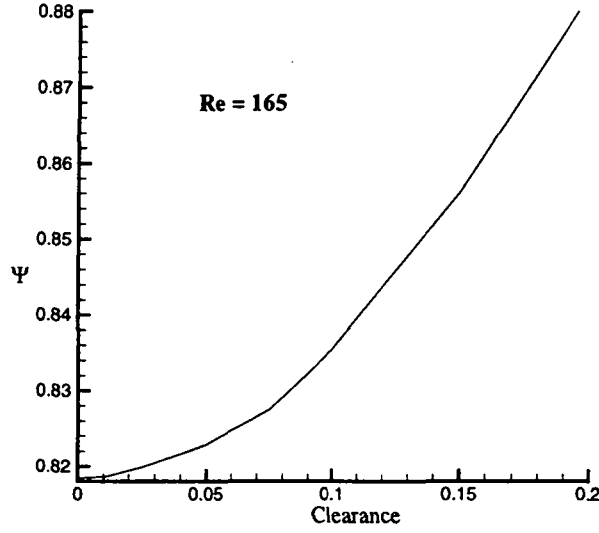


Figure 4.11: At $Re = 165$, Ψ changes by about 10% when the clearance goes from 0 to 20% of the gapwidth.

velocity is defined by the following equation:

$$\frac{\partial v_b}{\partial t} = \nu \frac{\partial}{\partial r} \left(\frac{1}{r} \frac{\partial (rv_b)}{\partial r} \right) . \quad (4.12)$$

If the radius ratio, η , is close to one, the primary flow has a simple analytical expression [5]:

$$v_b(x, t) = v_1(x) \cos(\sigma t) + v_2(x) \sin(\sigma t) ,$$

where:

$$x = \frac{r - R_1}{R_2 - R_1} ,$$

$$v_1(x) = \frac{\cos(\gamma x) \cosh(\gamma(1-x)) + \cosh(\gamma x) \cos(\gamma(1-x))}{\cosh(\gamma) + \cos(\gamma)} ,$$

and

$$v_2(x) = \frac{\sin(\gamma x) \sinh(\gamma(1-x)) + \sinh(\gamma x) \sin(\gamma(1-x))}{\sinh(\gamma) + \sin(\gamma)} .$$

In figure 4.12 is given the time evolution of the analytical solution in the narrow-gap approximation, i.e. for η close to one, during one period. At this high value, $\sigma = 24$, Stokes layers can be seen near each cylinder. Their motion is forced by that of the

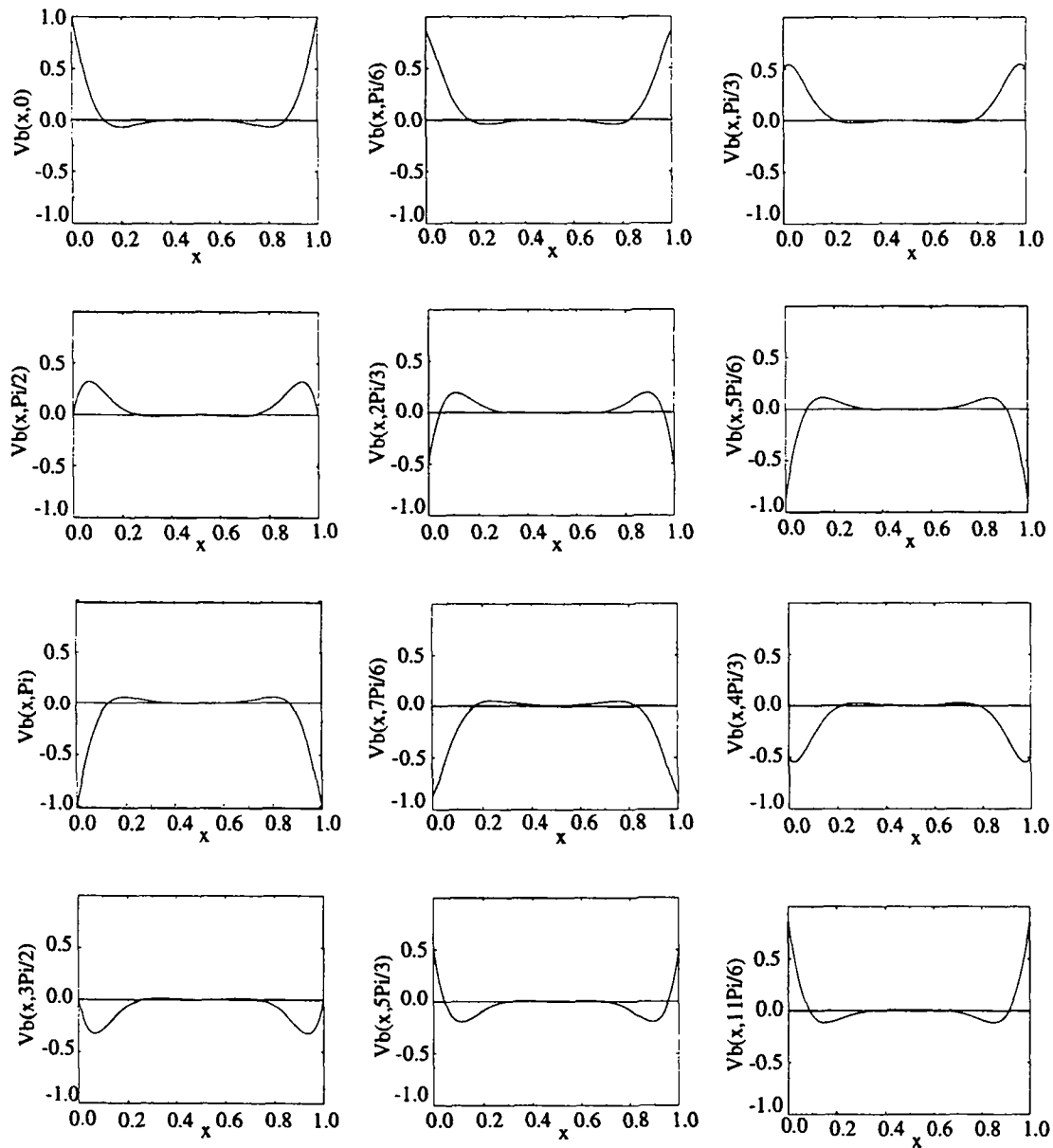


Figure 4.12: Time evolution of the analytical solution of the unsteady laminar flow. The forcing at the boundaries is given by: $\Omega(t) = \Omega_m + \Omega_0 \cos(\omega t)$. $Re = 1050$, and $\sigma = 24$.

boundaries. The core of the fluid is relatively motionless, while the motion of the intermediate regions between the middle radius and the boundaries is both damped and phase shifted.

The primary flow is stable at low Taylor numbers. Above $Ta = 206$, the flow undergoes a periodic destabilization. Transient, axially-periodic, counter-rotating Taylor vortices then appear.

Secondary flow Considering that the characteristic time-scale for the growth of the perturbations is negligible compared with the time of the pulsation, a quasi-steady, linear analysis of the flow can be performed. Another hypothesis is made concerning the wavelength: Ern considered it small compared with the gap width, which is arguable, the wavelength of the vortices being of the order of two gap widths. She obtained the curve given in figure 4.13 showing the evolution of the critical Taylor number with time. The destabilization will first appear if the Taylor number exceeds the minimum of these curves.

One should not search for an exact match between figure 4.14, obtained in the simulation, and figure 4.15, obtained in the experiment, because they do not represent exactly the same velocity. In fact, figure 4.14 represents the history of $\langle w(t) \rangle = \sqrt{\langle w^2(t) \rangle}$, while figure 4.15 represents the history of $\langle w_{rms}(t) \rangle = \sqrt{\langle w_{rms}^2(t) \rangle}$, where:

$$\langle w^2(t) \rangle = \int_{z_5}^{z_{10}} w^2(r_{\frac{3}{4}}, \theta_0, z, t) dz, \quad (4.13)$$

$$\langle w_{rms}^2(t) \rangle = \int_{z_5}^{z_{10}} w_m^2(z, t) dz, \quad (4.14)$$

and

$$\begin{aligned} w_m^2(z, t) &= \int_{\delta S} w^2(r, \theta, z, t) ds \\ &= \int_{\delta r} \int_{\delta \theta} w^2(r, \theta, z, t) r dr d\theta. \end{aligned} \quad (4.15)$$

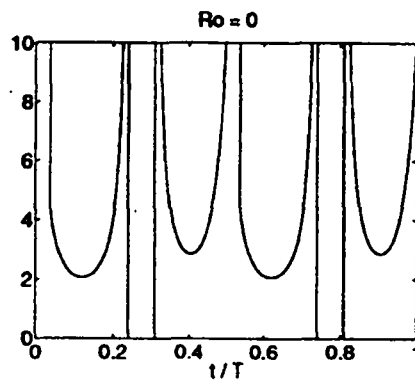
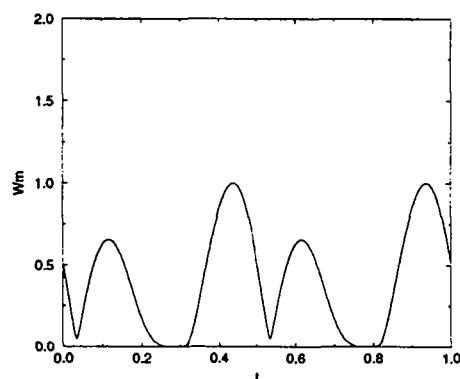
The measurements of the axial velocity $w_m(z, t)$ as a function of the axial position z and the time t presented here were obtained with an ultrasound Doppler velocimeter (UDV). The relative error on the velocity measurement varies between 1.5% and 3% depending on the ratio of the maximum velocity to the measurement scale. This apparatus does not measure the velocity at one point (r, θ, z) , but in a small circular section, δS , centered in the middle of the gap, and of diameter about two thirds of the gap. This velocity profile is then integrated along a vertical line going from top to bottom. The top third of the overall length is measured because the UDV is placed on the top of the apparatus. Half of the measurements, those corresponding to the upper Ekman cell and its close neighbourhood, are discarded. The rest are used to produce $\langle w_{rms}^2(t) \rangle$. The history of the numerical velocity profile $w(r_{\frac{3}{4}}, \theta_0, z, t)$ is obtained at the radius $r_{\frac{3}{4}} = R_1 + \frac{3}{4}d$. The axial velocity is not to be measured in the middle of the gap because its value is

Times	Stability analysis	Simulation	Experiment
τ_1	0.108	0.117	0.11
τ_2	0.450	0.435	0.44

Table 4.3: *Times of appearance of the Taylor vortices.*

close to zero for all times there. The azimuthal position θ_0 has no importance, the flow being axisymmetric.

The times of appearance of the destabilization of the primary flow to transient Taylor vortices is nearly the same according to the quasi-steady linear analysis, the simulation and the experiment, as can be seen in table 4.3 and figures 4.13 to 4.15.

Figure 4.13: *Evolution of the critical Taylor number during one period, T .*Figure 4.14: *Oscillations of $W_m = \langle w(t) \rangle$ during one forcing period. The time $t = 1$ corresponds to one pulsation period. $\gamma = 1$, $Ta = 350$.*

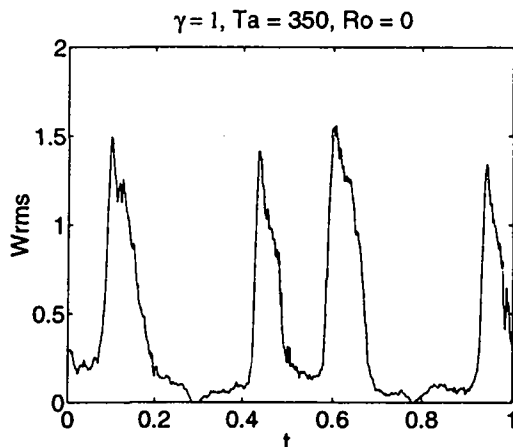


Figure 4.15: Oscillations of $\langle w_{rms}(t) \rangle$ during one forcing period.

4.2 Performance

4.2.1 Performance of the algorithms

Operations cost

We estimate here the operations count for the most time-consuming parts of the code. Let us consider a grid made of N_θ Fourier planes in the azimuthal direction and $I \times J$ elements in the meridian cross-section, i.e. the (r, z) plane. In each element, we have $(N_r + 1) \times (N_z + 1)$ points. The total number of velocity mesh points is then: $\mathcal{N}_v = (IN_r + 1) (JN_z + 1) N_\theta \simeq IN_r JN_z N_\theta$. We recall here that the grid points on the interfaces between the elements are unique, although they belong to more than one element. The number of pressure points is: $\mathcal{N}_p = I(N_r - 1) J(N_z - 1) N_\theta \simeq IN_r JN_z N_\theta$. From now on, we approximate the number of mesh points, whether it be for the pressure or the velocity, by $\mathcal{N} = IN_r JN_z N_\theta$.

Cost of the elementary operations The elementary operations we consider are derivatives with respect to spatial directions, and Fast Fourier Transforms (FFTs). Each differentiation is performed locally on an element, Υ^{el} . The operations count is hence the product of a local matrix (defined on Υ^{el}) by a global vector of \mathcal{N} components.

- The radial derivative costs $N_r \mathcal{N}$ operations in floating-point arithmetic. By operation, we mean one multiplication and one addition; additions and multiplications can be performed at the same processing speed by modern processors.
- The axial derivative costs $N_z \mathcal{N}$ operations.
- The azimuthal derivative costs \mathcal{N} operations. It is simply the multiplication of each mode k by ik .
- According to [13], the Fast Fourier Transform in the direction θ costs $(5p+3q+4r+\frac{39}{5}s+\frac{13}{3}t-6) \mathcal{N}$ operations, if N_θ can be factorized in products: $N_\theta = 2^p 3^q 4^r 5^s 6^t$.

For $N_\theta = 2^p$, we have then $[5 \log_2(N_\theta) - 6] \mathcal{N}$ operations for a FFT of $\frac{\mathcal{N}}{N_\theta}$ vectors of length N_θ .

Inversion cost To write the pressure equation (3.38) in a separable form, one first has to multiply the source term $\frac{1}{\Delta t} \tilde{\mathcal{D}}\mathbf{V}^*$ by the (globally-defined) matrices $\left[\widetilde{r\mathcal{B}^r}^T (r\mathcal{B}^r)^{-1} r\widetilde{\mathcal{B}^r} \right]^{-1}$ and $\left[\widetilde{\mathcal{B}^z}^T (\mathcal{B}^z)^{-1} \widetilde{\mathcal{B}^z} \right]^{-1}$. Although matrices $\widetilde{r\mathcal{B}^r}^T (r\mathcal{B}^r)^{-1} r\widetilde{\mathcal{B}^r}$ and $\widetilde{\mathcal{B}^z}^T (\mathcal{B}^z)^{-1} \widetilde{\mathcal{B}^z}$ are defined locally to each element, their inverse are not due to direct stiffness. The fast diagonalization method is equivalent to multiplying the source term, f_k , by four matrices which depend on one direction only, $(\widetilde{\mathcal{Q}^z})^{-1}$, $(\widetilde{\mathcal{Q}^r_k})^{-1}$, $\widetilde{\mathcal{Q}^z}$ and $\widetilde{\mathcal{Q}^r_k}$, and by the inverse of a diagonal matrix depending on both radial and axial directions, $\widetilde{\Lambda}_k^r \otimes \widetilde{\mathcal{I}^z} + \widetilde{\mathcal{I}^r} \otimes \widetilde{\Lambda}^z$. These five matrices are defined during a pre-processing stage.

- Matrix vector products of $\frac{1}{\Delta t} \tilde{\mathcal{D}}\mathbf{V}^*$ by $\left[\widetilde{r\mathcal{B}^r}^T (r\mathcal{B}^r)^{-1} r\widetilde{\mathcal{B}^r} \right]^{-1}$ and $\left[\widetilde{\mathcal{B}^z}^T (\mathcal{B}^z)^{-1} \widetilde{\mathcal{B}^z} \right]^{-1}$ cost $IN_r\mathcal{N}$ and $JN_z\mathcal{N}$ operations, respectively.
- The inversion itself, as expressed in equation (3.39), needs two global matrices for the multiplications in the radial and axial directions, costing $2(IN_r + JN_z)\mathcal{N}$ operations, and one multiplication by a diagonal matrix of \mathcal{N} components, $\widetilde{\Lambda}_k^r \otimes \widetilde{\mathcal{I}^z} + \widetilde{\mathcal{I}^r} \otimes \widetilde{\Lambda}^z$, needing \mathcal{N} operations.

The operations count for the inversion is then:

$$3(IN_r + JN_z)\mathcal{N} + \mathcal{O}(\mathcal{N}) .$$

Cost of the evaluation of the non-linear term The full expression of the skew-symmetric form of the non-linear term in cylindrical coordinates, (nl^r, nl^θ, nl^z) , is given by:

$$\begin{aligned} 2nl^r &= u \frac{\partial u}{\partial r} + \frac{\partial u^2}{\partial r} + \frac{v}{r} \frac{\partial u}{\partial \theta} + \frac{\partial}{\partial \theta} \left(\frac{uv}{r} \right) + w \frac{\partial u}{\partial z} + \frac{\partial uw}{\partial z} - \frac{2v^2}{r} + \frac{u^2}{r} , \\ 2nl^\theta &= u \frac{\partial v}{\partial r} + \frac{\partial uv}{\partial r} + \frac{v}{r} \frac{\partial v}{\partial \theta} + \frac{\partial}{\partial \theta} \left(\frac{v^2}{r} \right) + w \frac{\partial v}{\partial z} + \frac{\partial vw}{\partial z} + \frac{3uv}{r} , \\ 2nl^z &= u \frac{\partial w}{\partial r} + \frac{\partial uw}{\partial r} + \frac{v}{r} \frac{\partial w}{\partial \theta} + \frac{\partial}{\partial \theta} \left(\frac{vw}{r} \right) + w \frac{\partial w}{\partial z} + \frac{\partial w^2}{\partial z} + \frac{uw}{r} . \end{aligned} \quad (4.16)$$

The velocity components, u , v and w , expressed in Fourier space, are denoted by \hat{u} , \hat{v} and \hat{w} , respectively. All the variables are expressed in Fourier space everywhere in the code except in the subroutine which computes the non-linear term, where both physical and Fourier space expressions are needed.

- The number of FFTs is 12. The products $\frac{v}{r} \frac{\partial u}{\partial \theta}$, $\frac{v}{r} \frac{\partial v}{\partial \theta}$ and $\frac{v}{r} \frac{\partial w}{\partial \theta}$ are performed in physical space, therefore requiring 6 FFTs from Fourier to physical space, 3 to obtain u , v and w from \hat{u} , \hat{v} and \hat{w} , and 3 more to get $\frac{\partial u}{\partial \theta}$, $\frac{\partial v}{\partial \theta}$ and $\frac{\partial w}{\partial \theta}$ from $\frac{\partial \hat{u}}{\partial \theta}$, $\frac{\partial \hat{v}}{\partial \theta}$ and $\frac{\partial \hat{w}}{\partial \theta}$. These expressions are then again Fourier transformed, so that there are 3 more FFTs to do. The products $\frac{\partial}{\partial \theta} \left(\frac{uv}{r} \right)$, $\frac{\partial}{\partial \theta} \left(\frac{v^2}{r} \right)$ and $\frac{\partial}{\partial \theta} \left(\frac{vw}{r} \right)$ require 3

FFTs; these are needed to obtain \widehat{uv} , $\widehat{v^2}$ and \widehat{vw} from $\frac{uv}{r}$, $\frac{v^2}{r}$ and $\frac{vw}{r}$. Azimuthal differentiation of any component of the velocity is performed while this component is in Fourier space.

- The number of azimuthal derivatives is 6.
- The number of radial derivatives is 6.
- The number of axial derivatives is also 6.

The overall operations cost for the skew-symmetric form of the non-linear term is then:

$$6(N_r + N_z)\mathcal{N} + 60 \log_2(N_\theta)\mathcal{N} + \mathcal{O}(\mathcal{N}) .$$

Cost of the evaluation of the diffusion term The diffusion term is defined through equations (3.21) to (3.23). The mass matrices, $\frac{\mathcal{B}^r}{r}$, $r\mathcal{B}^r$ and \mathcal{B}^z , being diagonal, their product with a velocity component requires \mathcal{N} operations. The product by the rigidity matrices \mathcal{A}^r and \mathcal{A}^z is more costly, these matrices being full in each element.

- The number of matrix vector products in the radial direction is 3.
- The number of matrix vector products in the axial direction is also 3.
- The number of diagonal matrix vector products is 20.

The diffusion term operations cost is then:

$$3(N_r + N_z)\mathcal{N} + \mathcal{O}(\mathcal{N}) .$$

Operations cost for the divergence To evaluate the divergence from the operator, $\widetilde{\mathcal{D}} = \left(-\widetilde{\mathcal{G}}^r \otimes \widetilde{\mathcal{B}}^z, ik\widetilde{\mathcal{B}}^r \otimes \widetilde{\mathcal{B}}^z, r\widetilde{\mathcal{B}}^r \otimes -\widetilde{\mathcal{G}}^z \right)$,

- 3 local matrix-vector multiplications in the radial direction are needed.
- 3 local matrix-vector multiplications in the axial direction are also necessary.

Therefore, the total operations count for the divergence is:

$$3(N_r + N_z)\mathcal{N} + \mathcal{O}(\mathcal{N}) .$$

Total operations count Summing, the total operations count is then:

$$3(IN_r + JN_z)\mathcal{N} + 12(N_r + N_z)\mathcal{N} + 60 \log_2(N_\theta)\mathcal{N} + \mathcal{O}(\mathcal{N}) . \quad (4.17)$$

In the case where the number of grid points is the same in three directions, $M = IN_r = JN_z = N_\theta$, we can simplify (4.17). The leading order of the total operations cost is then: $6M^4$.

Memory requirements

We do not use dynamic memory allocation, although FORTRAN 90 provides that possibility. The reason is that we are more concerned by computational efficiency than by memory limitations. Operations on vectors are more easily vectorized if they are stored close to each other. Whereas in a classical declaration of variables, these are stored next to each other in the order they are needed, dynamic memory allocation does not prevent the variables from being spread out through the whole memory. For safety reasons, we also imposed the input arguments of the subroutines to be associated to different variables than the output arguments. To have an idea of the memory requirements, we look for the larger terms in the code, made of \mathcal{N} components. In the main program, we need at the same time:

- the three components of the non-linear term,
- the three diffusion terms,
- the three pressure gradients,
- the pressure,
- the source term for the pressure equation,
- the diagonal matrices $[\widetilde{\Lambda}_k^r \otimes \widetilde{\mathcal{I}}^z + \widetilde{\mathcal{I}}^r \otimes \widetilde{\Lambda}^z]^{-1}$, $k \in \{0, 1, \dots, N_\theta - 1\}$,
- the three components of the velocity at the current time step,
- the three components of the velocity at the previous time step, and
- the three components of the velocity in physical space.

The approximate memory requirement for the whole code is then $21\mathcal{N}$ words.

4.2.2 Performance of the code

We present here the CPU time needed for each time step, S_1 , in seconds, and the CPU time per time step and per mesh point, S_2 , in seconds also. The corresponding spatial discretization is indicated in tables 4.4 to 4.7, where we have assumed $N = N_r = N_z$. The maximum memory used is also written, in Mega Words (MW) on the CRAY machines and in Mega Bytes (MB) on the NEC (one word corresponds to 8 bytes). We also present in tables 4.5 to 4.7 the speed of the code and its more important subroutines in Mega Flops compared with the peak performance of the respective computers.

Computer	I	J	N	N_θ	\mathcal{N}	Memory	MFLOPS	Peak perf.	S_1	S_2
Cray YMP	2	14	12	4	$1.69 \cdot 10^4$	1.58 MW	111	333	0.690	$4.08 \cdot 10^{-5}$
Cray J90	2	14	12	4	$1.69 \cdot 10^4$	1.58 MW	85	200	0.911	$5.39 \cdot 10^{-5}$
NEC SX4	2	24	10	256	$1.3 \cdot 10^6$	63 MB	348	$2 \cdot 10^3$	71.7	$5.53 \cdot 10^{-5}$

Table 4.4: Performance on different computers.

Part	Percentage	MFLOPS
Non-linear	42	54
Inversion	23	183
Divergence	14	31
Diffusive	10	60
Pressure gradient	9	125

Table 4.5: Percentage of time spent in each part of the code and its own speed on the CRAY YMPM94. The peak performance of the CRAY YMP is 333 MFLOPS.

Part	Percentage	MFLOPS
Non-linear	38	44
Inversion	28	110
Divergence	13	22
Diffusive	10	44
Pressure gradient	8	100

Table 4.6: Percentage of time spent in each part of the code and its own speed on the CRAY J90SE. The peak performance of the CRAY J90 is 200 MFLOPS.

Part	Percentage	MFLOPS
Diffusive	29	240
Inversion	24	349
Divergence	20	244
Pressure gradient	20	332
Non-linear	6	367

Table 4.7: Percentage of time spent in each part of the code and its own speed on the NEC SX4. The peak performance of the NEC SX4 is 2 GFLOPS.

Simplicity of the codes

The DNS code, main program, together with the 16 subroutines, is made up of 4400 Fortran (Fortran 90) lines only. This is very small compared to the hundred thousand lines of some commercial codes.

The second code, for linear stability analysis, comprising 9 subroutines plus the main program, and it consists of 2000 Fortran lines.

Part II

Analysis of the transition

Chapter 5

Linear stability analysis

5.1 Objective

Our main aim is the study of transition of Taylor-Couette flow for the counter-rotating case. Before committing large amounts of CPU time to carry out a direct numerical simulation (DNS), we need to know where the first transition occurs. For this flow, theoretical results based on linear stability analysis are possible. We chose to perform this analysis for the simpler case of infinite cylinders because the first bifurcation of this flow is almost independent of the aspect ratio, Γ , as is reported in the literature [40]. This hypothesis of infinite length cylinders has two advantages:

- The first is that we can limit the axial extension of the domain to the characteristic wavelength, which is less than or equal to 2 non-dimensional units. In comparison, we have used three different heights for the cylinders for the DNS: 12, 20 and 30 characteristic length-scales.
- The second advantage is that we can use Fourier expansions instead of Lagrange-Legendre polynomials. The cost of calculating the derivatives increases as N in the case of Fourier expansions of degree N , while it increases as N^2 in the case of Lagrange expansions of degree N .

These two points make it easier to perform the analysis.

5.2 Analysis method

We only follow the first steps of the now classical linear stability analysis of Taylor-Couette flow. As explained for instance in Drazin and Reid [25], we first linearize the Navier-Stokes equations about the base flow which is known analytically for infinite length cylinders. Instead of performing a normal mode analysis and ending up with an eigenvalue relation [25, Page 94], we solve numerically the set of linear partial differential equations (3.40) for a given perturbation. The perturbation we introduce is made of

k pairs of spirals. The case $k = 0$ corresponds to an axisymmetric perturbation. The meridian cut of the spiral perturbation is:

$$\begin{cases} u[r(x), 0, z(y)] &= \frac{1}{r(x)} [\sin(\pi x)]^2 (16y^4 - 32y^3 + 16y^2 - \frac{8}{15}) , \\ v[r(x), 0, z(y)] &= 0 , \\ w[r(x), 0, z(y)] &= -\frac{\pi}{r(x)d} \sin(2\pi x) z(y) (\frac{16}{5}y^4 - 8y^3 + \frac{16}{3}y^2 - \frac{8}{15}) , \end{cases} \quad (5.1)$$

where the reduced coordinates x and y are given by:

$$\begin{cases} x &= \frac{r-R_1}{d} , \\ y &= \frac{z}{\lambda} . \end{cases} \quad (5.2)$$

This velocity field is solenoidal and such that $w(r, 0, 0) = w(r, 0, \lambda) = 0$. We also have $\int_0^\lambda ru(r, 0, z) dz = 0$.

The azimuthal dependence is given by:

$$\mathbf{v}(r, \theta, z) = \mathbf{v}(r, 0, z - k\frac{\lambda\theta}{2\pi}) \quad \forall \theta \in [0, \frac{2\pi}{k}] , \text{ and}$$

$$\mathbf{v}(r, \theta + \frac{2\pi}{k}, z) = \mathbf{v}(r, \theta, z) .$$

This is not the exact solution of the eigenvalue problem [25, Page 94], but an approximation, which reproduces the main features of the strongest perturbation, as can be seen in figure 5.1.

We chose the variation of \mathbf{v} to be sinusoidal in the radial direction, because the expansion of a sine, or cosine function has several non-zero components on a Lagrange-Legendre polynomial basis. The same way, the axial dependence of \mathbf{v} is chosen to be a polynomial because its expansion in a Fourier basis has many non-zero components. Therefore, although we do not introduce the most unstable perturbation at the beginning of our calculation, it is however contained in our initial perturbation. This perturbation will then evolve naturally with time towards the most unstable one.

We report in figure 5.2 the time evolution of the kinetic energy of the perturbation for $Re_1 = 210$, $Re_2 = -200$, $\lambda = 1.72$, $k = 1$ and $\eta = 0.875$. The radii ratio is the same for all the simulations made in this section. This value, $\eta = 0.875$, is also the one used for most of the DNS presented in the next chapter. At time $t = 0$, the perturbation introduced is such that $|u|_{max} \sim |w|_{max} \sim 10^{-3} V$, $V = R_2\Omega_2$ being the characteristic velocity of the base flow. Whatever supercritical Reynolds number we choose for the simulation, the behaviour of the kinetic energy is the same as in figure 5.2. We find an initial decrease of the energy, followed by a sharp increase and finally an exponential growth rate. The first phase (decrease) takes place because the initial perturbation has bigger stable components than unstable ones. After the stable perturbations have subsequently decayed, the increase due to the unstable modes is dominating. The growth rate we observe is the sum of all unstable perturbations. To explain this sharp

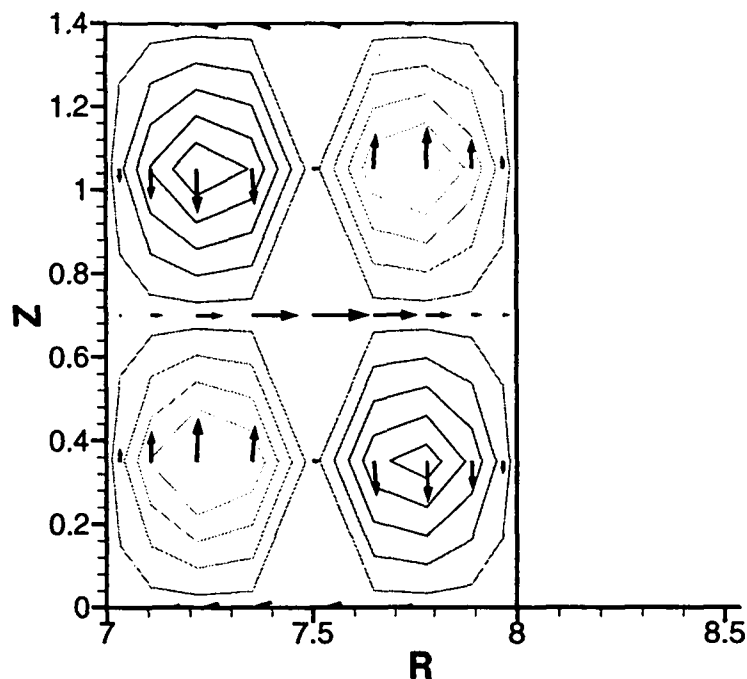


Figure 5.1: Meridian cross-section of the perturbation introduced at time 0. Here are shown the axial velocity contours together with the (r, z) vector field.

increase early on, we suppose that some of the unstable modes we introduced at time $t = 0$ had more energy than the most unstable one. The energy of the most destabilizing mode overwhelms all the other positive contributions in the third phase.

We know that the growth rate of the most unstable perturbation, the final one in our case, is proportional to $Re - Re_c$, the difference between the Reynolds number of the simulation and the critical one. In order to find the critical Reynolds number we therefore need to record at least two time evolutions of the kinetic energy at two different Reynolds numbers. We impose the outer Reynolds number and vary the inner one. The critical Reynolds number we find in this way depends on the wave number, α , we have chosen for the simulations. We then have to repeat these operations to obtain the wave number corresponding to the minimum $Re_c(\alpha)$. The pair of critical wave number, α_c , and critical Reynolds number, $Re_c(\alpha_c)$, is the one we present in figures 5.3 and 5.4, respectively. As observed by Chossat and Iooss [17], for different radii ratios, $\eta = 0.75$ (see table 5.1) and $\eta = 0.95$ (see table 5.3), we observe that the most unstable perturbation is first axisymmetric, $k = 0$, and then asymmetric, with a number of spiral pairs, k , increasing with the outer Reynolds number, $|Re_2|$ (see table 5.2). The results we present in table 5.2 are for an aspect ratio in between the values chosen by Chossat and Iooss. Our findings compare qualitatively well with theirs.

There is a sudden decrease of the wave number as we go from a k spiral pairs perturbation to a $k + 1$ spiral pairs perturbation. The type of perturbation we introduce, with

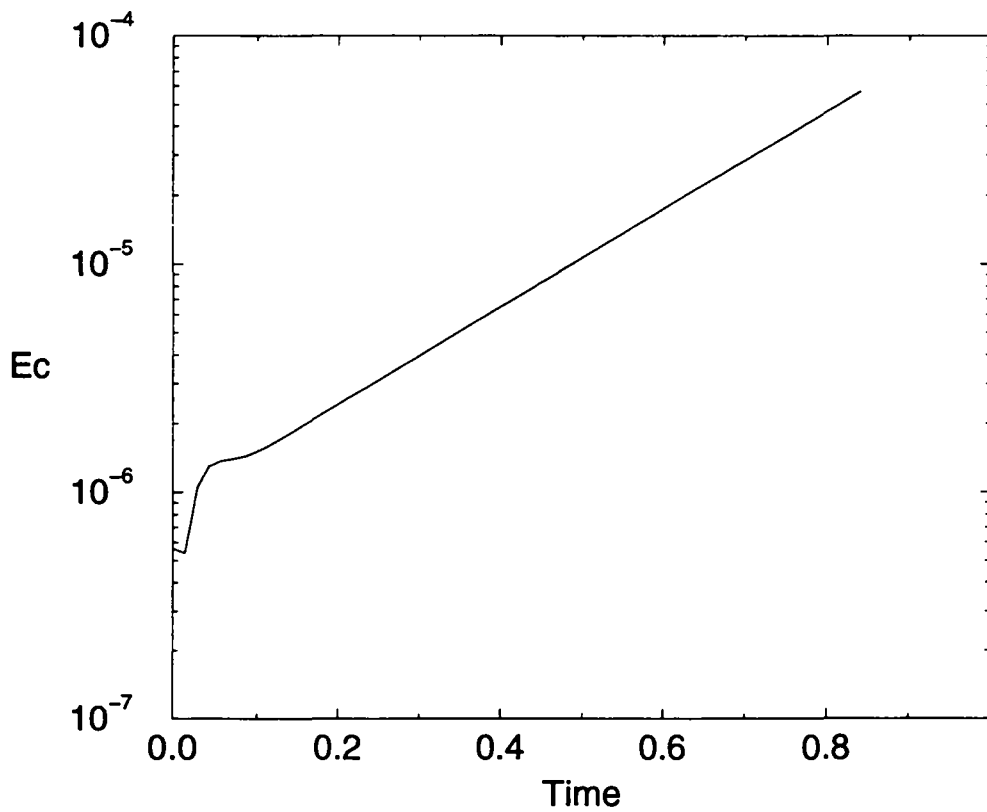


Figure 5.2: Time evolution of the kinetic energy of the perturbation, for $Re_1 = 210$, $Re_2 = -200$, $\lambda = 1.72$, $k = 1$ and $\eta = 0.875$. The intensity level of the initial perturbation is 10^{-3} compared to the base flow characteristic velocity.

only one vortex in the radial direction, does not seem to be adequate when k exceeds 4. This has also been noticed by Chossat *et al.* [17]. They could not find the strongest perturbation beyond $k = 3$ for $\eta = 0.75$, or beyond $k = 5$ for $\eta = 0.95$.

Codimension 2 point	0 1	1 2	2 3
\mathcal{U}	-0.572	-0.698	-1.149

Table 5.1: Codimension 2 points $k|k + 1$ found by Chossat and Iooss for $\eta = 0.75$.

Codimension 2 point	0 1	1 2	2 3	3 4
\mathcal{U}	-0.68	-0.72	-0.88	-1.29
Re_1	161.7	168.9	190.6	251.6
Re_2	-124.9	-139.6	-191.4	-369.9

Table 5.2: Codimension 2 points $k|k + 1$ for $\eta = 0.875$.

Codimension 2 point	0 1	1 2	2 3	3 4	4 5
\mathcal{U}	-0.731	-0.763	-0.794	-0.875	-1.041

Table 5.3: Codimension 2 points $k|k + 1$ found by Chossat and Iooss for $\eta = 0.95$.

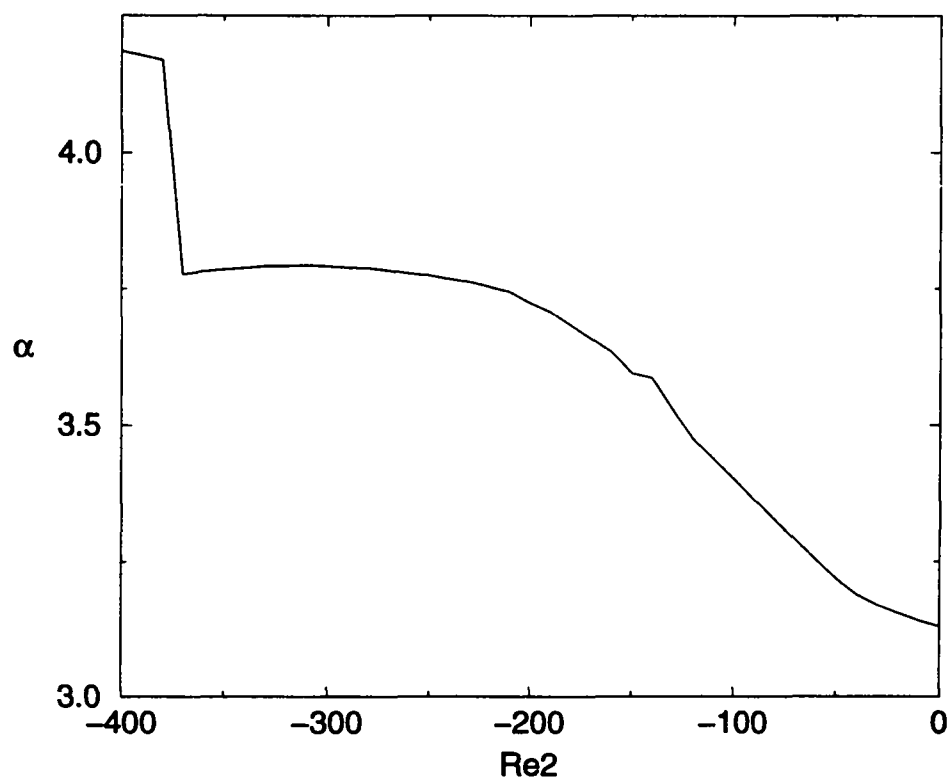


Figure 5.3: Critical axial wave numbers, α , as a function of the outer Reynolds number, Re_2 . The sharp increases correspond to the limit between a k mode solution and a $k+1$.

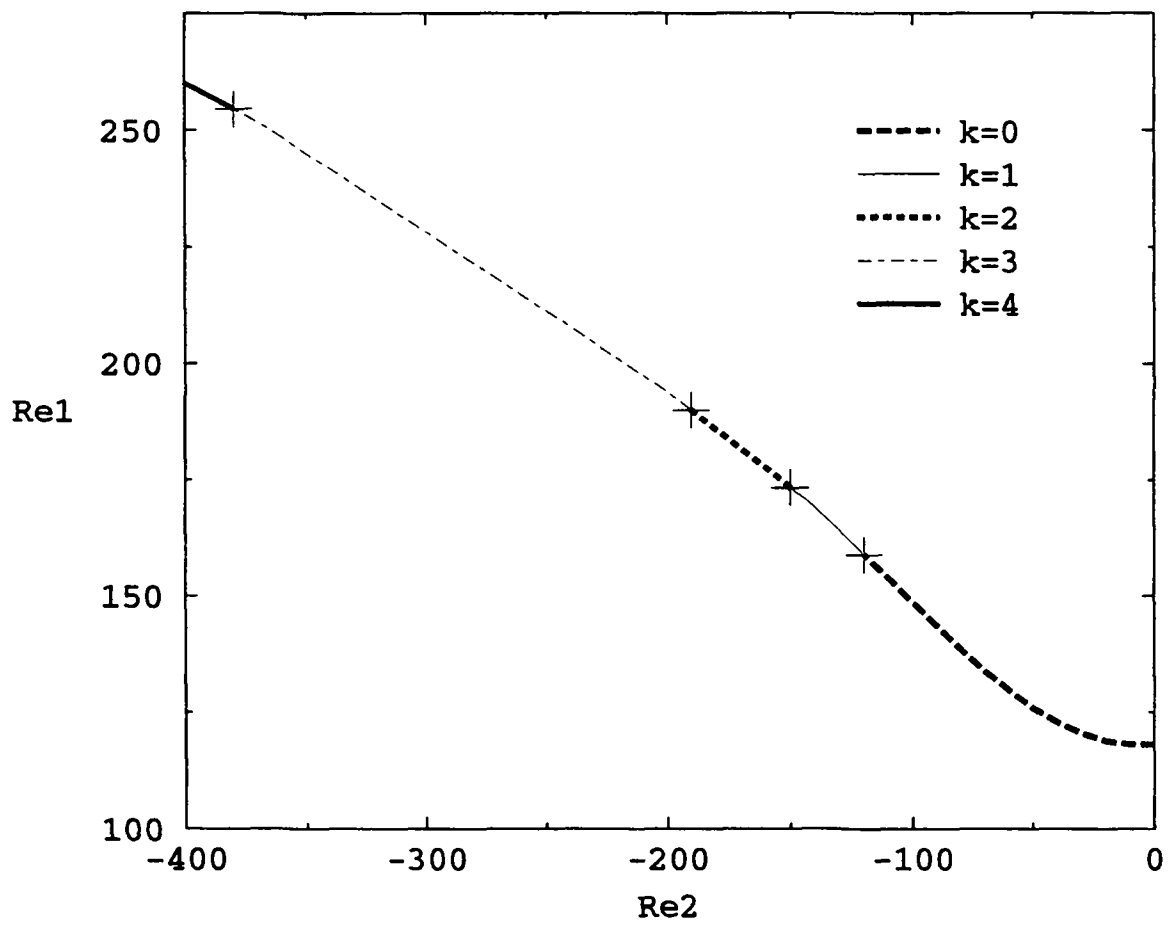


Figure 5.4: Critical inner Reynolds number, Re_1 , as a function of the outer Reynolds number, Re_2 . The preferred number of spiral pairs, k , is also indicated.

Chapter 6

Classical Taylor-Couette flow

We have obtained the first azimuthal laminar flows by starting the simulation from a zero initial velocity field, with non-zero boundary conditions corresponding to the final state. The Reynolds number jump from one simulation to another was decreased approaching a critical Reynolds number. The relative increase of Reynolds number for crossing a bifurcation was about 20% of the final Reynolds number. All of these simulations remain steady, once the transient due to this impulsive acceleration is complete. The typical time for the flow to establish within a reasonably small error is $\frac{L^2}{6\nu}$, a sixth of the diffusion time based on the total length of the cylinders.

We only consider here the case in which the inner cylinder is rotating and the end plates are fixed to the outer cylinder. In this case, the only dynamical parameter is the Reynolds number of the inner cylinder, Re_1 . It is then simply denoted by Re in this section.

6.1 Couette flow

6.1.1 Ghost cells

Below the critical Reynolds number of the first bifurcation, weak Taylor vortices can be seen developing slowly, by a diffusion process, from the top and bottom Ekman cells. For such Reynolds numbers, the Navier-Stokes equations have a unique analytical solution for cylinders of infinite length. In the case of finite cylinders, the horizontal ends modify the flow. The difference between these two solutions is most noticeable near the ends. Alziary de Roquefort and Grillaud [3] have made a detailed study of the subcritical behaviour of the Taylor-Couette flow, while varying the Reynolds number. Weak cells appear well below the first transition. The number of these cells and their intensity increase with Re . The cell intensity, represented by $|\psi|_{max}$, the maximum of the absolute value of the stream function, is vanishingly small away from the horizontal plates. At $Re = 110$ and $\Gamma = 30$, five cells can be distinguished near each end, as can be seen in figure 6.2. The intensity of the fifth one, counting from bottom to mid-height, is about 100 times smaller than the first cell intensity, as is reported in figure

6.1. Therefore, the cells that are away from the end plates are often called ghost cells. The two cells directly touching the top and bottom end plates are called Ekman cells.

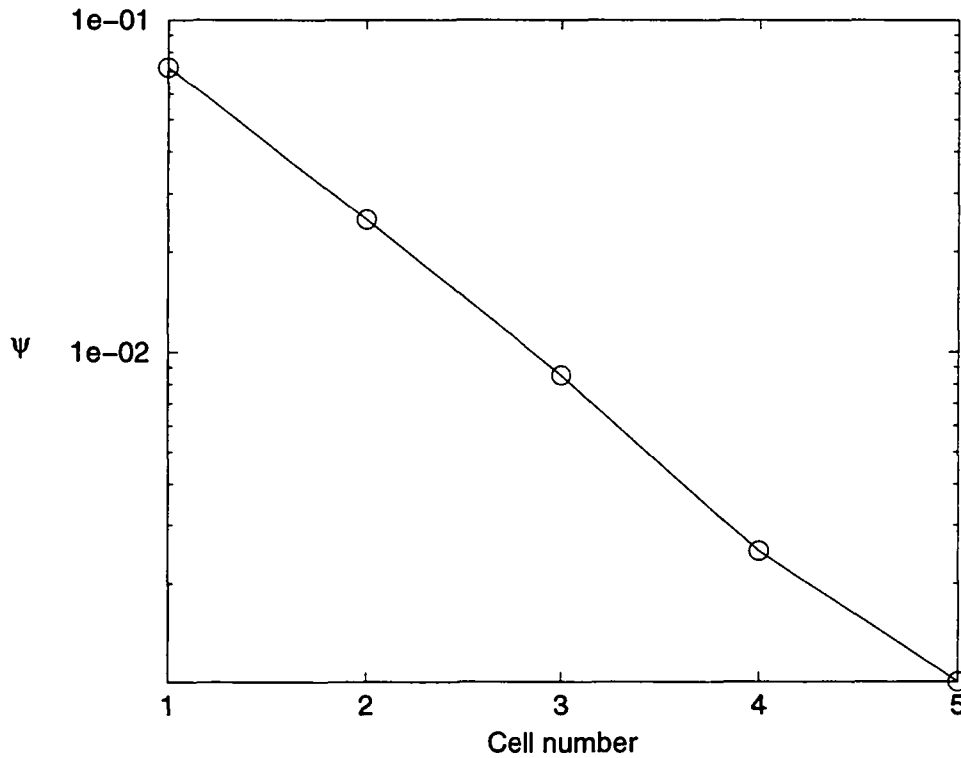


Figure 6.1: *Cell intensity of the six first cells. The bottom cell is the cell number 1. The intensity is denoted by ψ , the maximum of the absolute value of the stream function in the cell.*

6.1.2 Ekman cells

Ekman cells appear because of the imbalance between the pressure gradient, $\frac{\partial p}{\partial r}$, and the centrifugal force, $\frac{v^2}{r}$, in the boundary layer at each end. This imbalance itself is linked to the no-slip boundary conditions the flow must fulfil. The velocity decreases to zero as we move towards the stationary end plates, creating a relatively thick boundary layer. This is because the Reynolds numbers we deal with are small. The pressure is roughly constant across the boundary layer. The radial pressure gradient is therefore stronger than the centrifugal force in the boundary layer generating a flow from the outer cylinder towards the inner cylinder.

Re	$\frac{Re}{Re_c}$	λ_-	λ_+
120	1.016	1.85	2.20
125	1.059	1.71	2.37
130	1.101	1.62	2.48
200	1.694	1.26	2.80

Table 6.1: Accessible range of wavelengths. The three first rows are calculated according to the third order non-linear theory of Kogelman and Di Prima [39]. The last row is calculated according to Riecke and Paap's results [57]. The narrow-gap approximation is also made.

6.2 First transition

The first transition, from Couette to Taylor vortex flow, is characterized by its critical wavenumber and critical Reynolds number.

6.2.1 Critical wavenumber

There is a unique wavenumber accessible at the critical Reynolds number separating Couette and Taylor vortex flows. To reach this state starting from the laminar Couette flow requires infinite time [51]. Indeed, the evolution of the perturbation during the changeover is governed by an expression proportional to $\exp[\sigma(Re - Re_c)t]$. The simulations therefore have to be made above the critical Reynolds number, as given by the linear stability analysis. The axial wavenumbers, $\alpha = \frac{2\pi}{\lambda}$, accessible by the so-called supercritical Taylor vortex flow, belong to a continuous interval $[\alpha_-, \alpha_+]$ that grows with $Re - Re_c$. The interval predicted by non-linear stability theory is smaller than the one predicted by the linear theory. The accessible wavenumbers at the Reynolds numbers of our simulations are given in table 6.1. The first three intervals were calculated according to Kogelman and Di Prima's third-order, non-linear theory [39]. These early results agree within a few percents with those obtained later by Riecke and Paap [57], as long as the reduced Reynolds number, $\frac{Re - Re_c}{Re_c} < 1.1$. Riecke and Paap were the first to obtain quantitative agreement with existing experimental results, even far above the critical Reynolds number. The range of accessible wavenumbers is narrower compared to the non-linear theory if $\frac{Re - Re_c}{Re_c}$ is large. We therefore calculated the interval $[\lambda_-, \lambda_+]$ according to their theory, for $\frac{Re - Re_c}{Re_c} = 0.694$.

Acceleration ramp

The lower values of the wavelength, λ , have been attained by Burkhalter and Koschmieder [12] in their sudden-start experiments, and the higher values from filling experiments [12]. In our simulations, we go from subcritical to supercritical Reynolds number within one time step. These conditions are comparable to the sudden-start experiments of

Burkhalter and Koschmieder. It is worth noting here that the effective wavenumber can be kept at its critical value while increasing very slowly the Reynolds number, below the so-called quasi-steady speed [4]. This procedure is however too costly to be used in our simulations. For an initial Reynolds number 500, increasing the Reynolds number by $\Delta Re = 1$ would need $1.75 \cdot 10^5$ time steps at the quasi-steady speed. The mean wavelength we find at $Re = 120$ for aspect ratio $\Gamma = 30$ is $\lambda = 1.957$ in non-dimensional units. The mean wavelength is calculated taking all cells into account except the two end cells, as in [12]. For the aspect ratio $\Gamma = 20$ and at Reynolds number $Re = 200$, we find $\lambda = 1.953$, while we find $\lambda = 1.912$ for $\Gamma = 12$ at $Re = 200$. The critical wavelength given by linear theory is $\lambda_c = 2.008$ in the same non-dimensional units. For each of the aspect ratios considered here, the effective wavelength adopted by the flow in our “sudden-start” simulations is smaller than the critical wavelength, as expected.

Quantization phenomenon

The fact that our flow domain is finite in the axial direction has a strong influence on the flow patterns. It is referred to in the literature as the quantization problem [40]. It has two effects:

- The number of cells has first to be an integer.
- The two end cells impose this number to be even, provided Γ is an order of magnitude greater than one.

Depending on the length of the end cells and the total number of vortices, N_T , the inner vortices, those that do not touch the end walls, can have different lengths as summarized in tables 6.2 to 6.4.

$N_T - 2$	24	26	28	30	32
$\lambda_{Ek} = 1.2$	2.300	2.123	1.971	1.840	1.725
$\lambda_{Ek} = 1.3$	2.283	2.108	1.957	1.827	1.713
$\lambda_{Ek} = 1.4$	2.267	2.092	1.943	1.813	1.700

Table 6.2: Mean wavelength for $\Gamma = 30$.

When supercritical, the Taylor vortex flow chooses its wavelength inside the accessible range $[\lambda_-, \lambda_+]$, according to non-linear theory. The wavelength choice is further reduced according to the quantization principle explained above.

$N_T - 2$	14	16	18	20	22
$\lambda_{Ek} = 1.15$	2.529	2.213	1.967	1.770	1.609
$\lambda_{Ek} = 1.21$	2.511	2.198	1.953	1.758	1.598
$\lambda_{Ek} = 1.25$	2.500	2.188	1.944	1.750	1.591

Table 6.3: Mean wavelength for $\Gamma = 20$.

$N_T - 2$	8	10	12
$\lambda_{Ek} = 1.20$	2.400	1.920	1.600
$\lambda_{Ek} = 1.22$	2.390	1.912	1.593
$\lambda_{Ek} = 1.25$	2.375	1.900	1.583

Table 6.4: Mean wavelength for $\Gamma = 12$.

For the two simulations at $Re = 200$ ($\Gamma = 20$ and $\Gamma = 12$), far above the critical Reynolds number, $Re_c \simeq 120$, the range of accessible wavelengths is wide. The wavelength chosen by the flow is smaller than the critical one, as expected from the impulsive increase of the Reynolds number, as is deduced by figures 6.3 and 6.4, respectively. The wavenumber of the Taylor vortices is however very close to the critical wavenumber. This is in qualitative agreement with Snyder's findings [60]. However, no quantitative comparison can be made because the radius ratio of his experiment is $\eta = 0.5$.

6.2.2 Critical Reynolds number

We know from Davey [23] that the square of the equilibrium amplitude of the supercritical Taylor vortex flow scales with $Re - Re_c$. The amplitude we choose is the radial velocity at mid-height and mid-gap. We have performed three simulations, for $\Gamma = 30$, at $Re = 120$, $Re = 125$ and $Re = 130$, and have derived from these the critical Reynolds number precisely. The value we found, $Re_c = 118.24$, is above the critical value predicted by linear theory for $\eta = 0.875$. According to Roberts [59], the critical Reynolds number in the case of infinite cylinders, for $\alpha_c = 3.13$ and for the radii ratio $\eta = 0.875$, is $Re_c = 118.16$. This small discrepancy has two possible origins:

- The simulations we used to determine the critical Reynolds number are not exactly steady. However, the level of acceleration is so small, of the order of 10^{-7} in the azimuthal direction and an order of magnitude less in the other two directions, that we may neglect it.
- The second and most important cause of the difference is the dependence of the critical Reynolds number on the wavelength. The wavelength obtained in our calculations being different from the critical wavelength on the neutral curve, that is, just at the onset of the instability; the corresponding Reynolds number has to be slightly higher than the theoretical one. This effect can be taken into

account by looking at the critical Reynolds number corresponding to $\alpha = 3.074$ ($\lambda = 1.957$), instead of $\alpha_c = 3.13$, on the marginal curve (see figure 1.2). The critical Reynolds number found that way is the same as the one obtained from our simulations, within a tolerance of 10^{-4} .

As we have seen in the previous chapter, the influence of the wavenumber, α , on the critical Reynolds number, $Re_c(\alpha)$, is small. In our case, the relative difference between the theoretical critical wavelength and the calculated one is 2%, while the relative difference in Reynolds numbers is 0.1%.

Influence of the radii ratio on Re_c

In figure 6.5, leaving apart the end regions, the flow is still azimuthal at $Re = 150$. Indeed, we know from [59] that the critical Reynolds number of the first transition in the flow between infinite cylinders is $Re_c = 168.85$ for $\eta = 0.94$ and $\alpha_c = 3.13$ instead of $Re_c = 118.16$ in the case with $\eta = 0.875$ and $\alpha_c = 3.13$.

6.3 Supercritical Taylor vortex flow

6.3.1 Reynolds number dependence of the flow

We consider here a given geometry: $\Gamma = 12$ and $\eta = 0.875$. Moreover, we only take into account axisymmetric solutions of the Navier-Stokes equations, and we do not investigate whether they are stable or not. However, according to Brindley and Mobbs [11], the ratio of the critical Reynolds number for the second transition, Re_w , to the critical Reynolds number for the first transition, Re_c , increases significantly as Γ is reduced below 40. They report that for $\Gamma = 12$, $\eta = 0.79$ and $\lambda = 1.16$, $\frac{Re_w}{Re_c} \simeq 5.1$. Therefore, we can expect the flow to still be axisymmetric in our case, for $\Gamma = 12$, $\eta = 0.875$ and $\frac{Re}{Re_c} \leq \frac{400}{120}$. In any event, these axisymmetric solutions are good starting points for fully 3D computations. We studied three supercritical flows at $Re = 200$, $Re = 300$ and $Re = 400$, and compared these flows with the subcritical flow at $Re = 100$. For each of these simulations, we present the contours in the meridian cross-section of the stream function, ψ , the ratio of the azimuthal velocity squared to the radius, $\frac{v^2}{r}$, the radial pressure gradient, $p'_r = \frac{\partial p}{\partial r}$, the non-linear term in the radial direction, nl_r , the shear stress $\sigma_{\theta z}$, the radial vorticity, ω_r , and the azimuthal vorticity, ω_θ .

The stream function in figure 6.6, corresponding to the $Re = 100$ results, clearly shows the two Ekman cells, one touching the top plate and the other the bottom plate. The azimuthal vorticity contours shows that 8 ghost cells are present, while only 2 of them appear in the stream function figure. One would need an exponential distribution of the stream function levels, and not a linear one as is the case here, to recover the 8 ghost cells.

The pairs of counter-rotating Taylor vortices are squeezed together in the outflow regions, the more so as the Reynolds number is increased, as can be seen comparing

the streamlines of the three supercritical flows. This indicates that the outward radial transport of azimuthal momentum gets stronger and creates jet-like secondary flows with increasing Re/Re_c .

All of the three figures 6.6 to 6.8 show a close link between:

- ψ and ω_θ ,
- $\frac{v^2}{r}$, $\frac{\partial p}{\partial r}$ and nl_r , and
- $\sigma_{\theta z}$ and ω_r .

More precisely, we can deduce from these figures that the equilibrium between the radial pressure gradient and the centrifugal force is still valid if the Reynolds number is above critical. We indeed know that if the Reynolds number is below Re_c , the relation: $\frac{\partial p}{\partial r} = \frac{v^2}{r}$ is exact everywhere in the flow when the cylinders are infinite, and that this relation is approximately correct if the annular space is closed axially, the more so away from the endplates. When the flow is supercritical we also find that $\frac{\partial p}{\partial r} \simeq -nl_r \simeq \frac{v^2}{r}$. The supercritical Reynolds numbers of figures 6.2 and 6.3 are 1.1 and 1.7 times higher than the critical value, respectively. The deformation in the azimuthal velocity contours is therefore more important in figure 6.3 than in figure 6.2.

6.3.2 Pressure distribution

When the flow is above the first transition, Taylor vortices appear and inward and outward radial flows with them. The flow is called inward when going from outer to inner cylinder and outward when directed from the inner to the outer cylinder. Where these flows impact, whether on the inner or the outer cylinder, a higher pressure is observed and where they originate, a lower pressure. Because of the superimposed positive radial pressure gradient, and also because of the relative weakness of the inflow compared to the (centrifugally-unstable) outflow, the low pressure zones at the intersection of the inner cylinder with the outward flows are at a lower pressure than the corresponding zones at the intersection of the outer cylinder with the inward flows. This finding, together with the linked observation of the pinching of the vortices in the outflow region, may explain why the outflow has been called jet-like in the literature.

6.4 Wavy Taylor vortex flow

We present here the results of a simulation for $\eta = 0.875$, $\Gamma = 30$ and $Re = 180$. We know, from Brindley and Mobbs [11], that the critical Reynolds number for appearance of wavy vortex flow, denoted by Re_w , increases markedly as Γ decreases. Therefore, we chose a relatively large value $\Gamma = 30$. This particular value is interesting because it is often the one chosen by experimentalists, such as Andereck *et al.* [4] for instance. According to Edwards *et al.* [26], the critical Reynolds number for the second bifurcation, to wavy vortex flow, is $Re_w = 137.2$ for $\eta = 0.87$ and $Re_w = 135.7$ for $\eta = 0.89$.

Using linear interpolation, we estimate $Re_w = 136.7$ in our case, i.e. for $\eta = 0.875$. The next transition, to modulated wavy vortex flow, occurs at $Re_m = 791.2$ according to Coughlin and Marcus [21]. Our simulation at $Re = 180$ is therefore in the range where the flow exhibits a wavy vortex structure.

The wavy vortex flow is periodic in the azimuthal direction. Six azimuthal modes are present in our case. We therefore only show one 6-th of the circumference in figure 6.9. In this picture are shown 8 meridian cross-sections of the flow for θ ranging from 0 to $\frac{7\pi}{24}$. Two counter-rotating Taylor vortices are made visible by the vector field (u, w) . The position and relative strength of these two vortices oscillate with θ . The θ -dependent axial location of the outflow region between the outward jets corresponds to the axial position of the maximum azimuthal velocity, as can be deduced by comparing the peak of the velocity contour, $v = 0.5$, and the jet axial position. These jets are responsible for the transport of azimuthal momentum from the inner to the outer wall.

The strength of the upper cell first decreases, from $\theta = -\frac{2\pi}{24}$ to $\theta = \frac{2\pi}{24}$, and then increases, from $\theta = \frac{2\pi}{24}$ to $\theta = \frac{6\pi}{24}$. While its strength diminishes, the vortex moves downward. The downward, and later upward, motion of the two counter-rotating Taylor vortex cells is even more obvious in figure 6.10, which shows the azimuthal vorticity contours from $\theta = 0$ to $\frac{7\pi}{24}$. The minimum strength of the upper cell is between $\theta = \frac{\pi}{24}$ and $\theta = \frac{2\pi}{24}$. This corresponds to the maximum of the lower cell. For an axial origin correctly chosen (in the middle of an inward or outward jet), the flow pattern shows the shift-and-reflect symmetry described by Marcus [48], $(u(r, \theta, z), v(r, \theta, z), w(r, \theta, z)) = (u(r, \theta + \frac{4\pi}{24}, -z), v(r, \theta + \frac{4\pi}{24}, -z), -w(r, \theta + \frac{4\pi}{24}, -z))$, as can be seen clearly in figures 6.9, 6.10 and 6.14.

The minimum axial location of these cells is between $\theta = \frac{3\pi}{24}$ and $\theta = \frac{4\pi}{24}$; that is, shifted a fourth of a period compared to the azimuthal position corresponding to the minimum strength of the upper cell.

This wavy flow pattern rotates around the axis of the cylinders as a solid body. From figure 6.11, we obtain the wave speed $\frac{s}{\omega} = 2.63/6 = 0.438$. Hence, the period of the azimuthal wave is $T = 2.28 T_1$, where T_1 is the rotation period of the inner cylinder. The flow pattern, being periodic in azimuthal direction with period $k = 6$, the wave speed obtained directly from figure 6.11 has to be divided by six to determine the wave speed of the whole structure. The axial, periodic movement of the vortices is most important at mid-height and invisible near the end plates. The axial wavelength, based on all the vortices but the two touching the end plates, is $\lambda = 1.97$, in dimensionless units.

6.4.1 Wavy Taylor vortex flow as a perturbation to the axisymmetric flow

We are able to produce numerically a physically unstable solution of the Navier-Stokes equations at $Re = 180$. Because we use Fourier series in the azimuthal direction, we can erase all the Fourier modes except the zero mode. Therefore, we can impose that the

solution remains axisymmetric. The solution we obtain is thus the base flow that one would use to perform a perturbation analysis. We present in figure 6.12 the perturbed flow, that is, the difference of the wavy Taylor vortex solution and the Taylor vortex base flow. Here are shown the contours of $v - v_b$ and the vector field $(u - u_b, w - w_b)$. From $\theta = 0$ to $\frac{3\pi}{24}$, a vortex, rotating clockwise, travels from the outer to the inner cylinder, where it then disappears. Another vortex, rotating anti-clockwise this time, reappears at a lower vertical position near the outer cylinder and travels again at a constant height from the outer to the inner cylinder, where it vanishes. This vortex is located in the outflow region between the original wavy Taylor vortices, and is small in comparison. The counter-rotating vortex that is visible in the perturbed flow pattern is, in contrast, relatively large compared to the wavy Taylor vortex.

Comparing figures 6.9 and 6.12, we learn that both the highest and lowest axial positions of the outflow jet correspond to the disappearance of the small vortex in the perturbed solution, that is between $\theta = -\frac{\pi}{24}$ and 0, and between $\theta = \frac{3\pi}{24}$ and $\frac{4\pi}{24}$, respectively.

In figure 6.13, we plot the kinetic energy contours of the perturbed velocity field. The maxima of kinetic energy correspond clearly to the maximum and minimum of $v - v_b$. Most of the kinetic energy of the perturbation is due to the perturbed azimuthal velocity.

6.4.2 Relationship between velocity and vorticity

We observe in figure 6.14 a close relationship between the radial vorticity contours and the wavy vortex cells. The strong link between ω_r and the velocity can also be seen in figure 6.15, where the vector field $(u, v - 0.5)$ is plotted together with the radial vorticity contours. To better understand the correlation between the velocity and the vorticity fields, we write below the vorticity transport equation to identify the prevailing terms in it. This equations is:

$$\frac{\partial \omega}{\partial t} + \omega \cdot \nabla \mathbf{v} = \mathbf{v} \cdot \nabla \omega + \nabla^2 \omega . \quad (6.1)$$

In cylindrical coordinates:

$$\left\{ \begin{array}{l} \frac{\partial \omega_r}{\partial t} + C(\mathbf{v})\omega_r = C(\omega)u + \frac{1}{Re}(\nabla^2 \omega_r - \frac{\omega_r}{r^2} - \frac{2}{r^2} \frac{\partial \omega_\theta}{\partial \theta}) , \\ \frac{\partial \omega_\theta}{\partial t} + C(\mathbf{v})\omega_\theta + \frac{v\omega_r}{r} = C(\omega)v + \frac{\omega_\theta u}{r} + \frac{1}{Re}(\nabla^2 \omega_\theta - \frac{\omega_\theta}{r^2} + \frac{2}{r^2} \frac{\partial \omega_r}{\partial \theta}) , \\ \frac{\partial \omega_z}{\partial t} + C(\mathbf{v})\omega_z = C(\omega)w + \frac{1}{Re} \nabla^2 \omega_z , \end{array} \right. \quad (6.2)$$

with the advection operator, for \mathbf{v} , given by

$$C(\mathbf{v}) = u \frac{\partial}{\partial r} + \frac{v}{r} \frac{\partial}{\partial \theta} + w \frac{\partial}{\partial z} ,$$

and that for ω by

$$C(\omega) = \omega_r \frac{\partial}{\partial r} + \frac{\omega_\theta}{r} \frac{\partial}{\partial \theta} + \omega_z \frac{\partial}{\partial z} .$$

Finally, the Laplacian operator is given by

$$\nabla^2 = \frac{1}{r} \frac{\partial}{\partial r} \left(r \frac{\partial}{\partial r} \right) + \frac{1}{r^2} \frac{\partial^2}{\partial \theta^2} + \frac{\partial^2}{\partial z^2} .$$

As can be seen in figure 6.16, three of the six terms constituting the non-linear term in the radial direction are negligible. These are: $\frac{\omega_\theta}{r} \frac{\partial u}{\partial \theta}$, $u \frac{\partial \omega_r}{\partial r}$ and $\frac{v}{r} \frac{\partial \omega_r}{\partial \theta}$. Two of the remaining terms, $w \frac{\partial \omega_r}{\partial z}$ and $-\omega_r \frac{\partial u}{\partial r}$, have the same spatial behaviour, the first one being slightly smaller than the second one. The non-linear term balances the diffusion term in the whole cross-section. As can be seen in figure 6.17, four of the eight terms constituting the non-linear term in the azimuthal direction are negligible. These are: $\frac{\omega_\theta}{r} \frac{\partial v}{\partial \theta}$, $\frac{\omega_\theta u}{r}$, $\frac{v}{r} \frac{\partial \omega_\theta}{\partial \theta}$ and $w \frac{\partial \omega_\theta}{\partial z}$. The larger of the non-linear terms are $\omega_r \frac{\partial v}{\partial r}$ and $\omega_z \frac{\partial v}{\partial z}$, which are nearly opposite to each other. In fact, $\omega_r \frac{\partial v}{\partial r} + \omega_z \frac{\partial v}{\partial z}$ is of the same order of magnitude as $\frac{v}{r} \omega_r$ and $u \frac{\partial \omega_\theta}{\partial r}$. Furthermore, $\frac{v}{r} \omega_r$ and $\omega_r \frac{\partial v}{\partial r} + \omega_z \frac{\partial v}{\partial z}$ have the same qualitative behaviour. The diffusion term in the azimuthal direction balances the non-linear term, but not as well as in the radial direction, thus indicating that the unsteady term, $\frac{\partial \omega_\theta}{\partial t}$, is non negligible in portions of the meridian plane. In the axial direction, $\frac{\omega_\theta}{r} \frac{\partial w}{\partial \theta}$ is negligible and the sum $u \frac{\partial \omega_z}{\partial r} - \omega_z \frac{\partial w}{\partial z}$ also (see figure 6.18). The three remaining terms of the axial non-linear term are, in decreasing order, $\omega_r \frac{\partial w}{\partial r}$, $w \frac{\partial \omega_z}{\partial z}$ and $\frac{v}{r} \frac{\partial \omega_z}{\partial \theta}$. The Laplacian term in z , $\frac{1}{Re} \nabla^2 \omega_z$, and $\omega_r \frac{\partial w}{\partial r}$ dominate. Their distribution in space differs, so that the unsteady term, $\frac{\partial \omega_z}{\partial t}$, has the same order of magnitude as these two terms.

Among all the terms mentioned here, $\frac{\partial w}{\partial t}$, $\mathbf{v} \cdot \nabla \omega - \omega \cdot \nabla \mathbf{v}$ and $\nabla^2 \omega$, none varies markedly either with θ or time. Furthermore, we can point out the predominant role played by the terms $\omega_r \frac{\partial w}{\partial r}$ and $\nabla^2 \omega_z$ in the axial vorticity equation. The first term expresses the axial transport of the vortices (through their radial gradient of axial velocity) due to the radial vorticity. The second term is a diffusion term that diminishes this axial transport. As can be seen in figure 6.18, the axial transport is maximum in the middle of the original Taylor vortices and reaches a minimum between these centers. The diffusion maxima correspond to the transport minima, and vice versa. The term $\omega_r \frac{\partial w}{\partial r}$ is nearly θ independent although both ω_r and $\frac{\partial w}{\partial r}$ strongly depend on θ , as can be seen in figure 6.14. This means that any increase of ω_r (at the origin of the advection) is balanced by a proportional decrease of $\frac{\partial w}{\partial r}$, which expresses the strength of the vortex, and reciprocally.

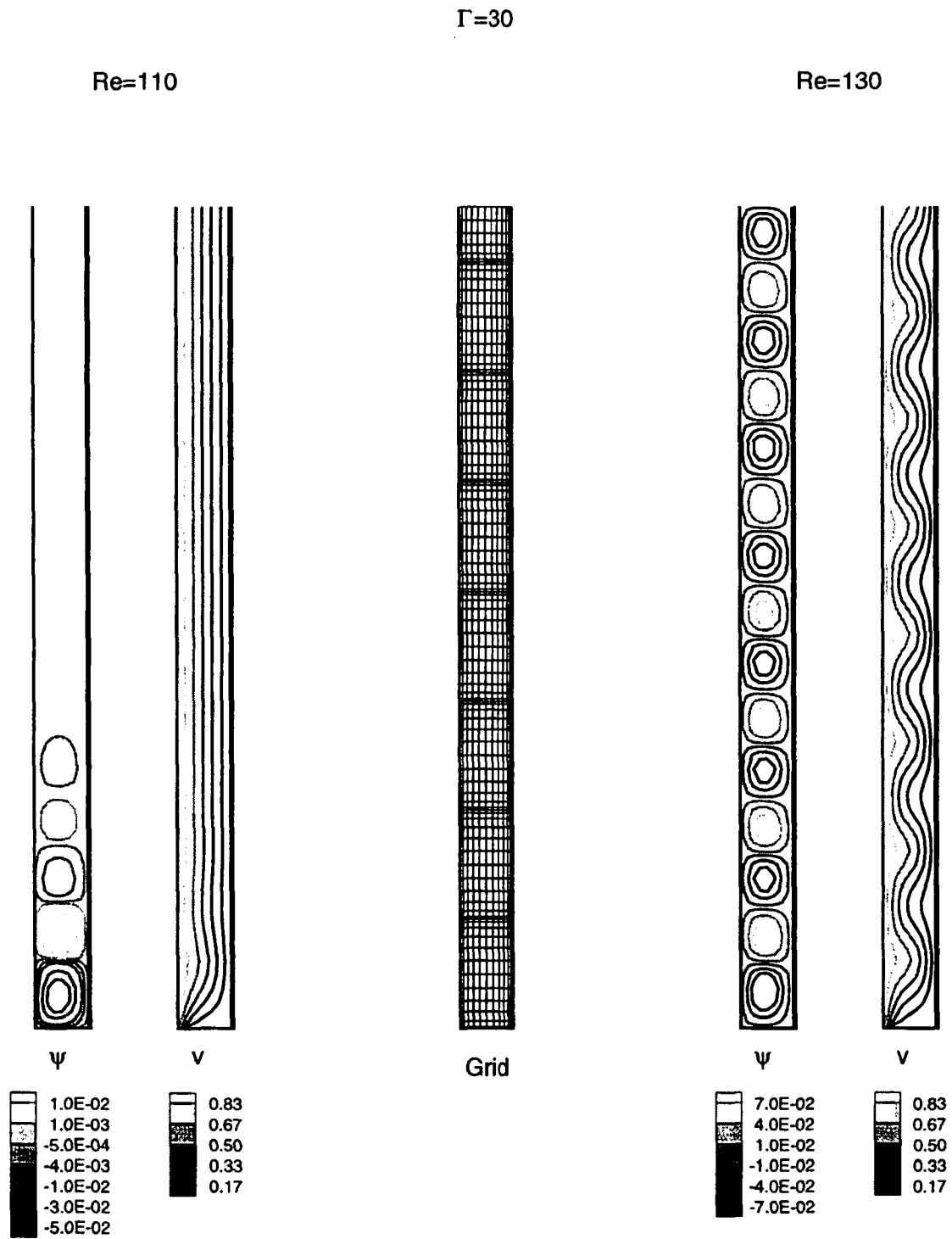


Figure 6.2: Contours in the meridian plane of the stream function ψ and the azimuthal velocity, v , from bottom to mid-height. The radii ratio is $\eta = 0.875$. Grid of 1×15 elements and 13×13 GLL points per element.

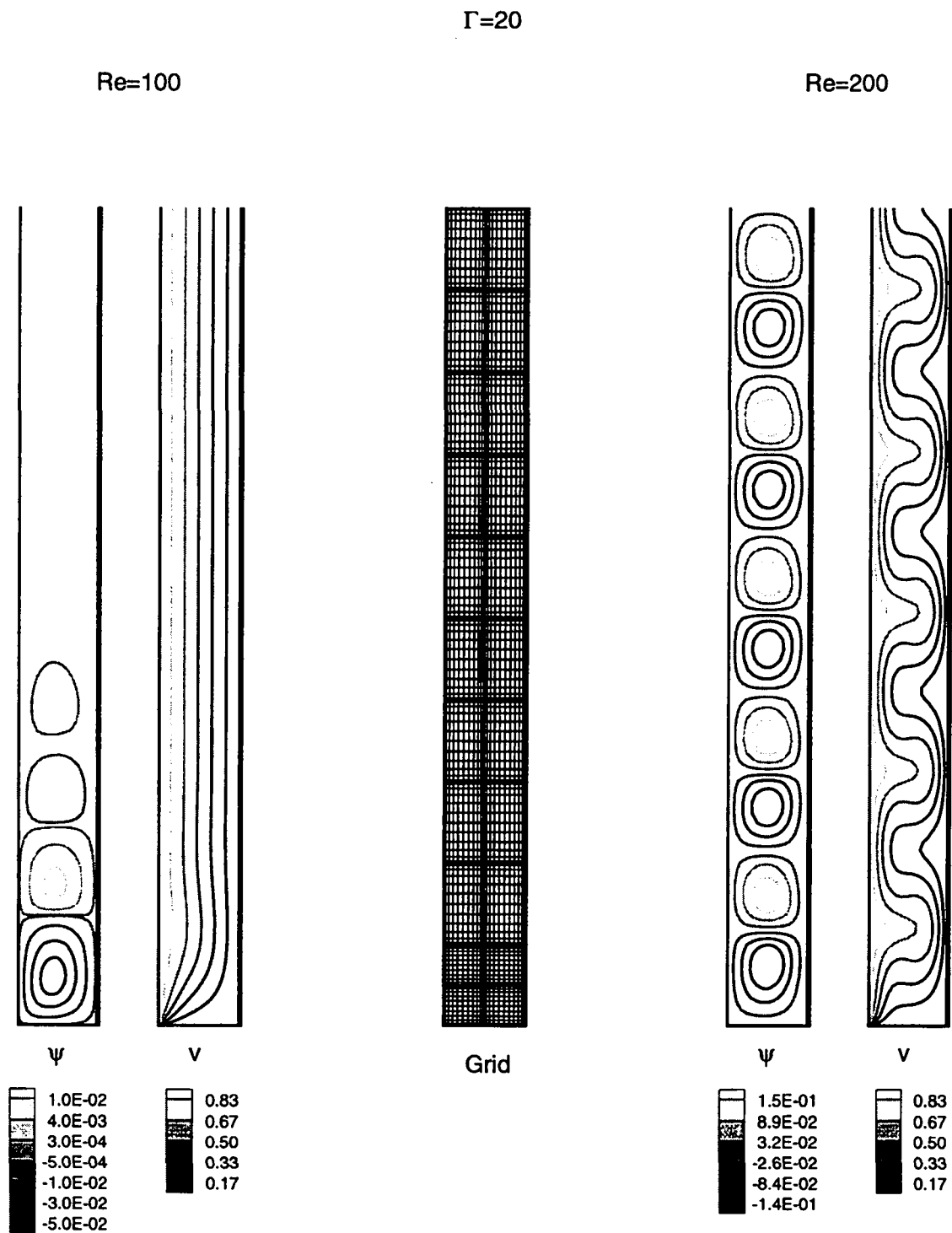


Figure 6.3: Contours in the meridian plane of the stream function ψ and the azimuthal velocity, v , from bottom to mid-height. The radii ratio is $\eta = 0.875$. Grid of 2×22 elements and 13×13 GLL points per element.

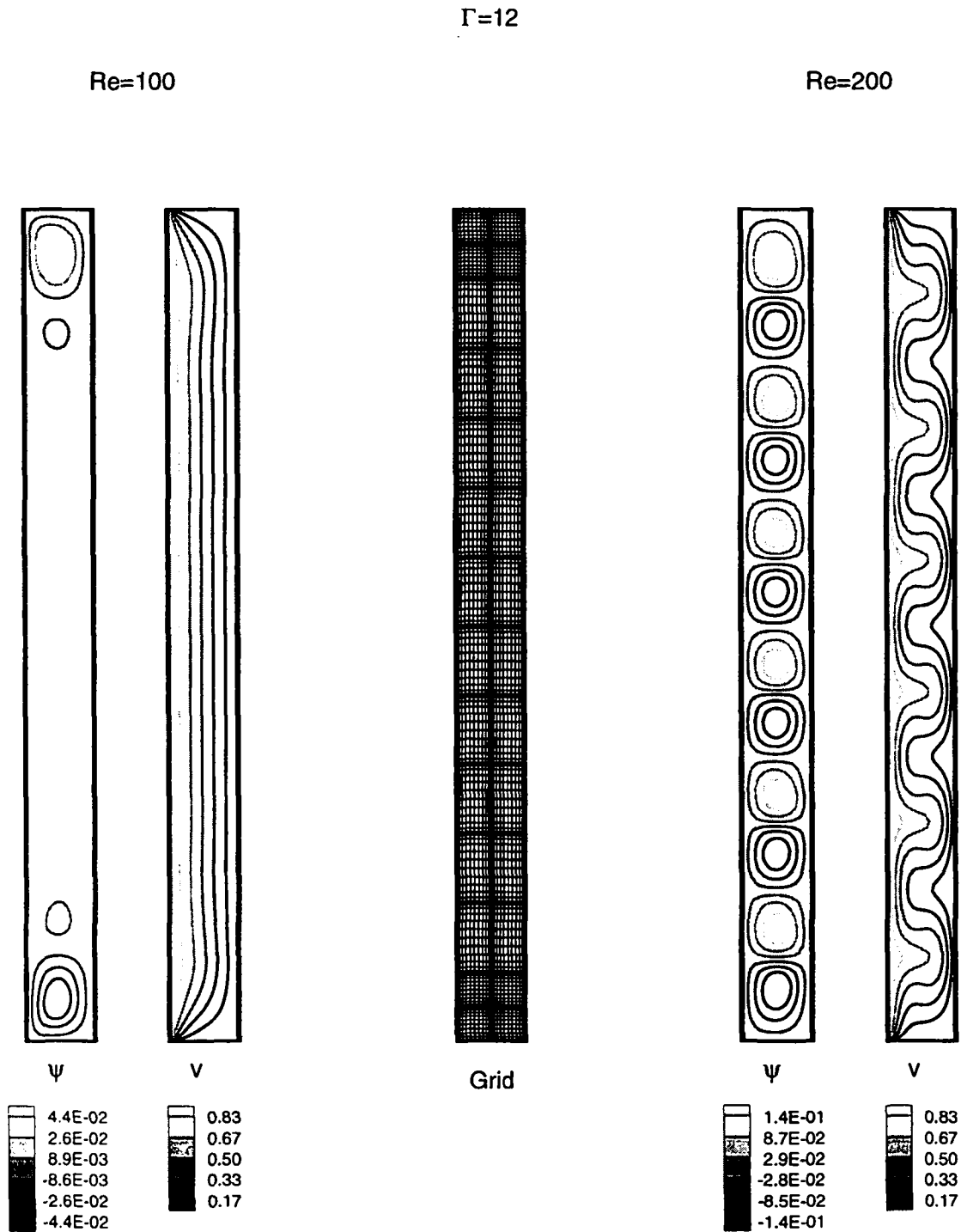


Figure 6.4: Contours in the meridian plane of the stream function ψ and the azimuthal velocity, v . The radii ratio is $\eta = 0.875$. Grid of 2×22 elements and 13×13 GLL points per element.

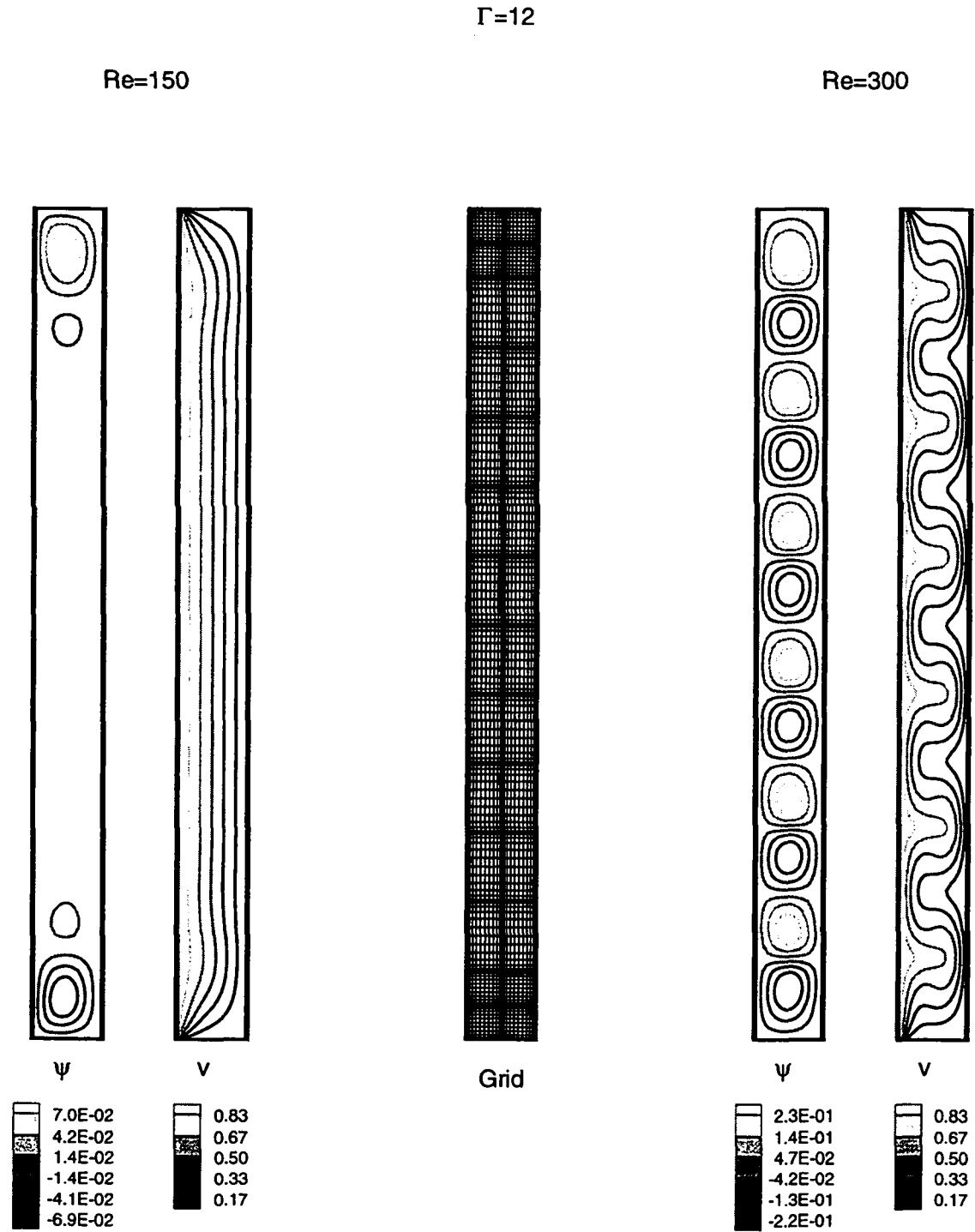


Figure 6.5: Contours in the meridian plane of the stream function ψ and the azimuthal velocity, v . The radii ratio is $\eta = 0.940$. Grid of 2×14 elements and 13×13 GLL points per element.

Re = 100

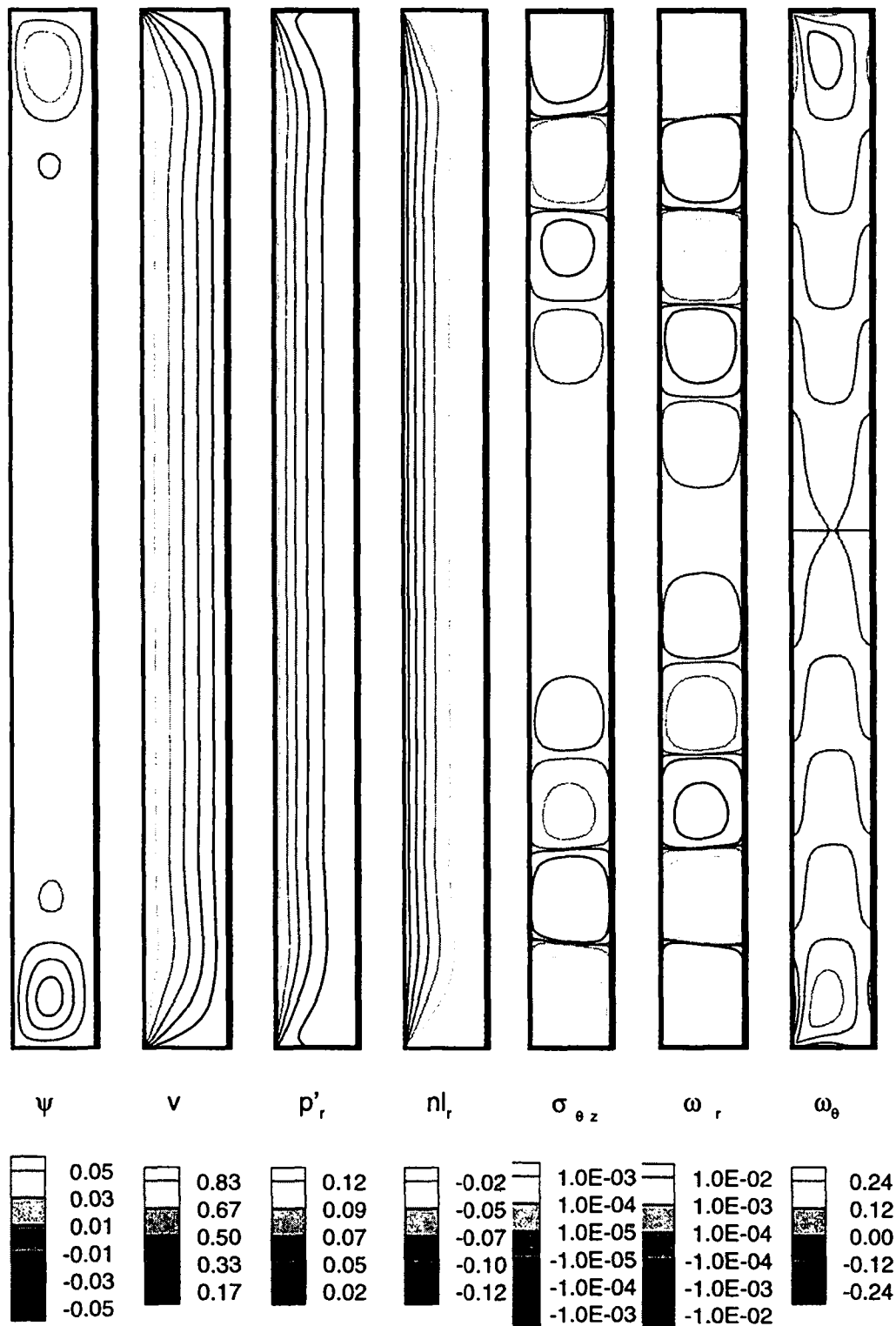


Figure 6.6: The aspect ratio is $\Gamma = 12$ and the radii ratio $\eta = 0.875$. Grid of 2×14 elements and 13×13 GLL points per element.

Re=200

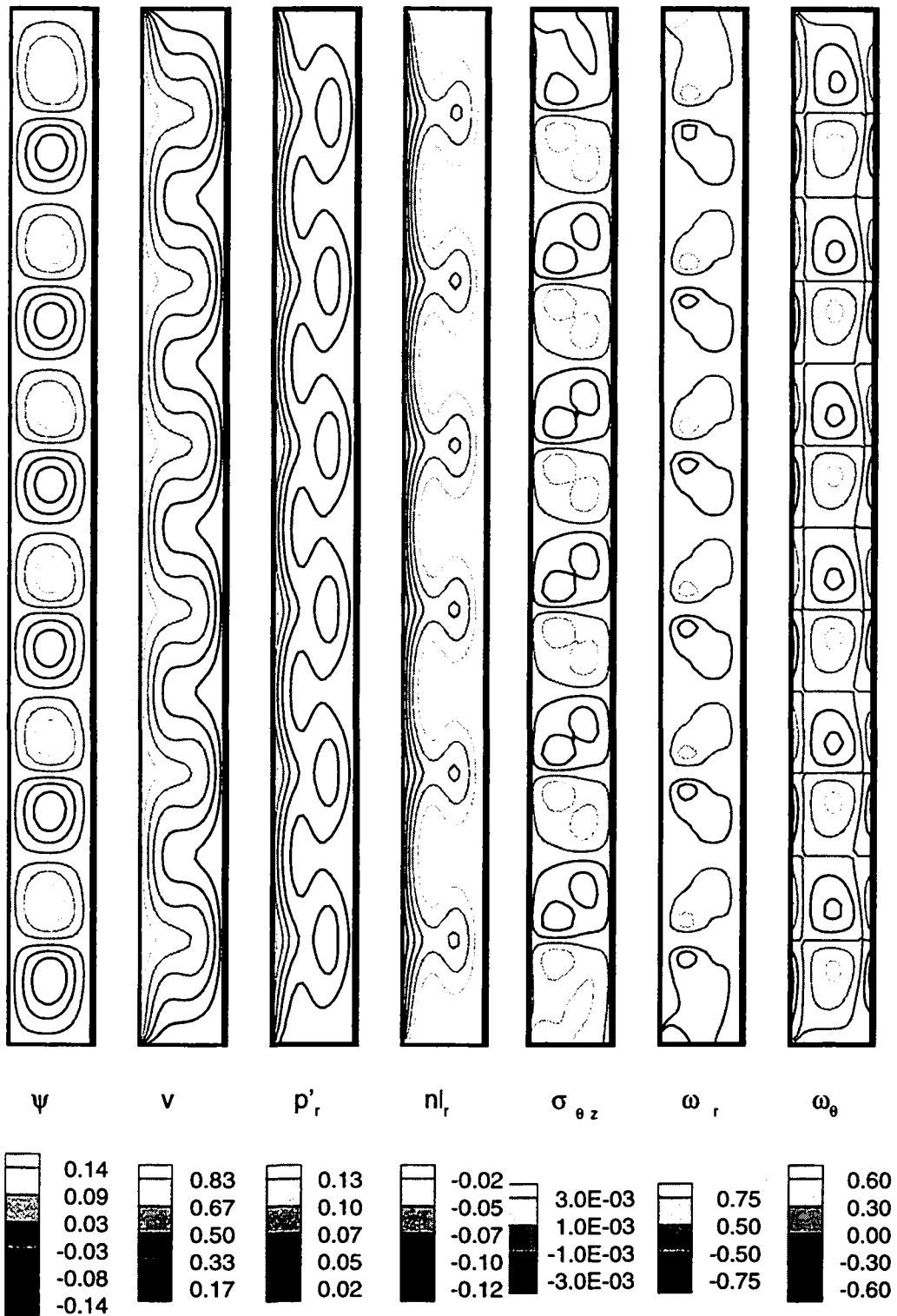


Figure 6.7: The aspect ratio is $\Gamma = 12$ and the radii ratio $\eta = 0.875$. Grid of 2×14 elements and 13×13 GLL points per element.

Re=400

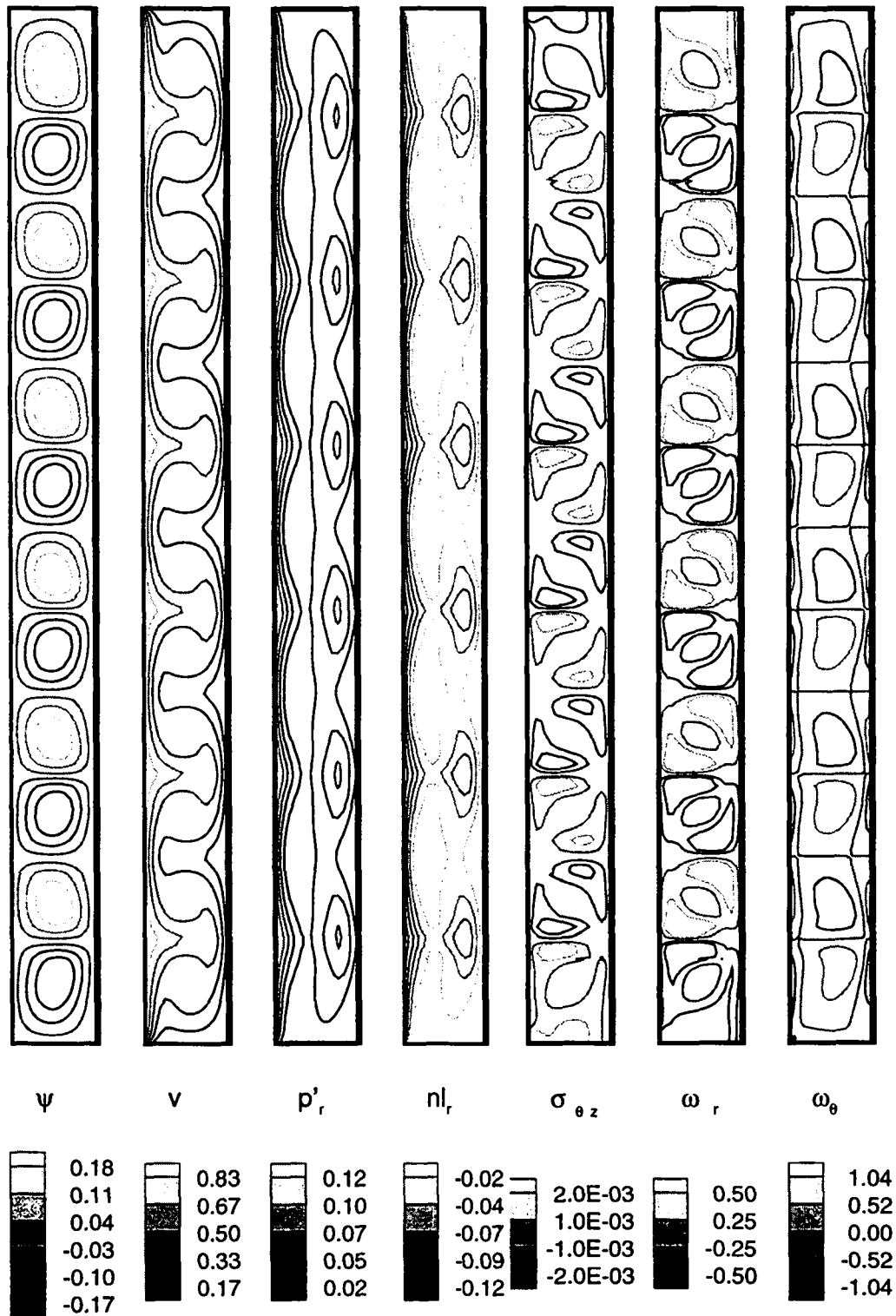


Figure 6.8: The aspect ratio is $\Gamma = 12$ and the radii ratio $\eta = 0.875$. Grid of 2×14 elements and 13×13 GLL points per element.

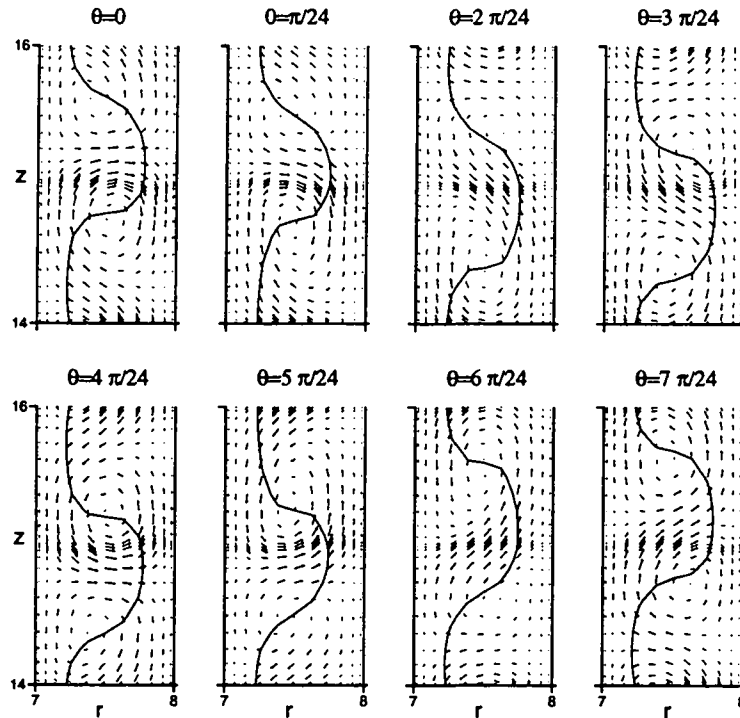


Figure 6.9: Vector field (u, w) and azimuthal velocity contour, $v = 0.5$, in successive meridional cross-sections at $Re = 180$.

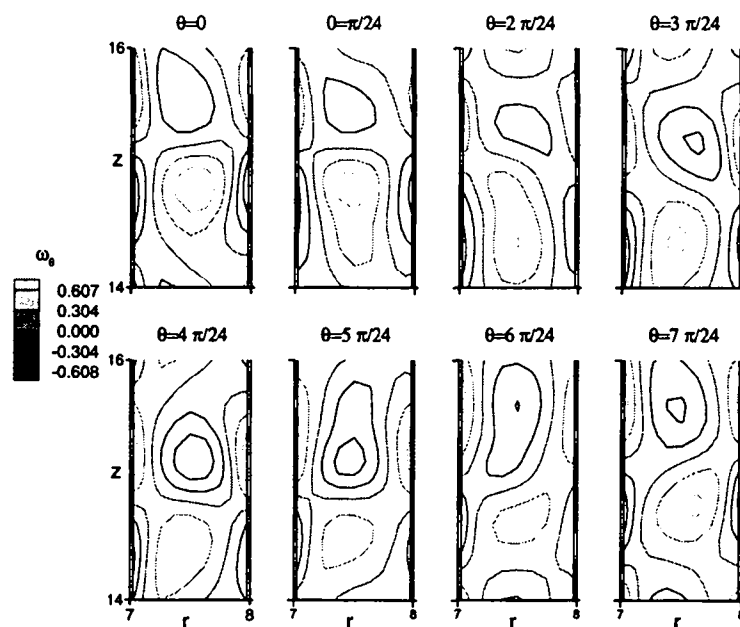


Figure 6.10: Azimuthal vorticity contours in successive meridional cross-sections at $Re = 180$.

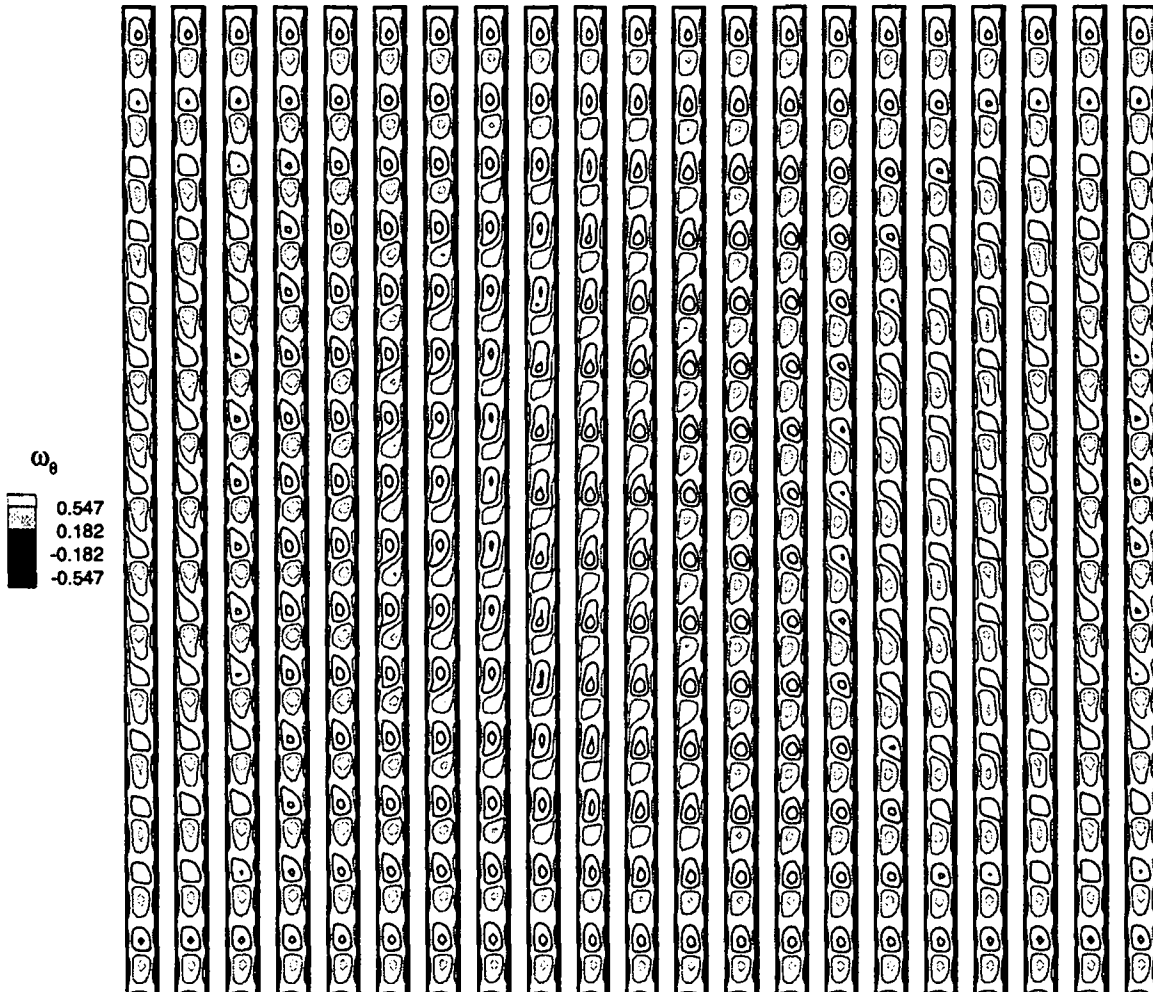


Figure 6.11: Time evolution of the azimuthal vorticity, ω_θ , at $Re = 180$. The time step between each cross-section is $50\Delta t$, with $\Delta t = 2.2 \cdot 10^{-3} \tau$ and $\tau = \frac{1}{\eta\Omega_1}$.

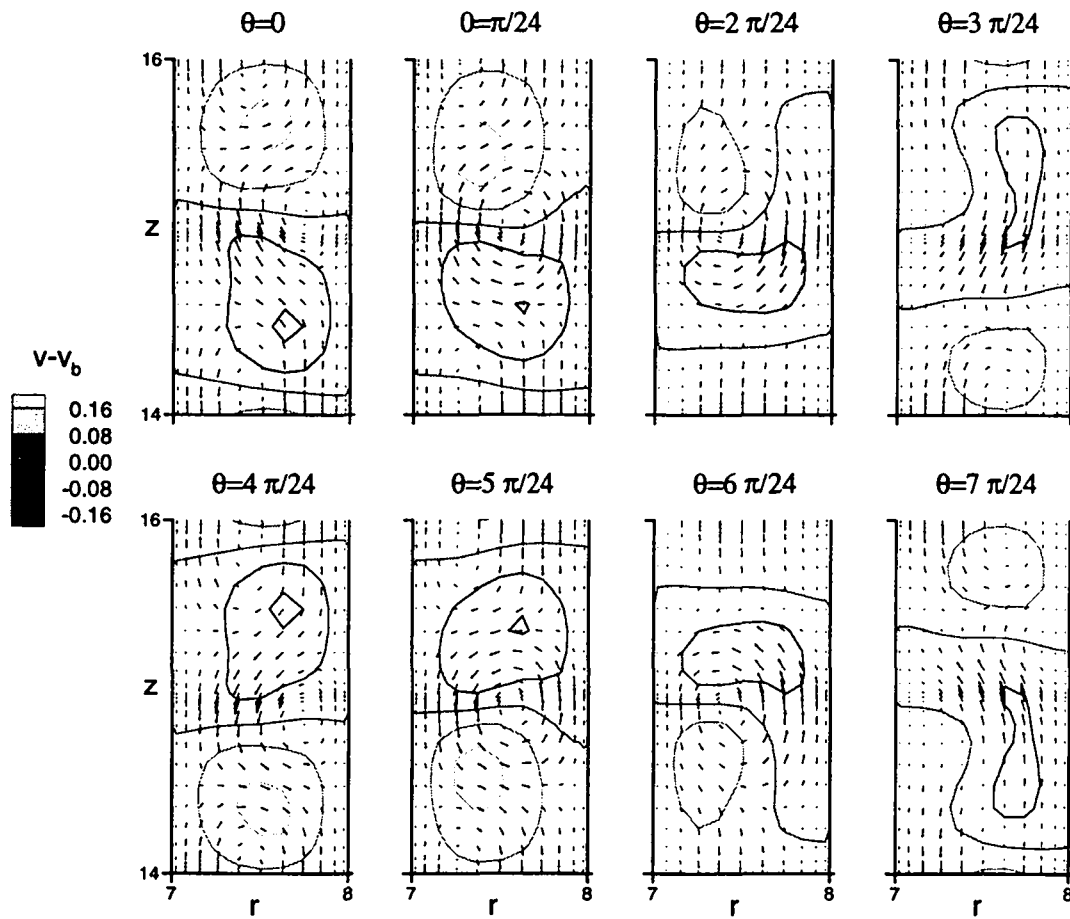


Figure 6.12: Contours of $v - v_b$ and vector field $(u - u_b, w - w_b)$ in successive meridional cross-sections at $Re = 180$.

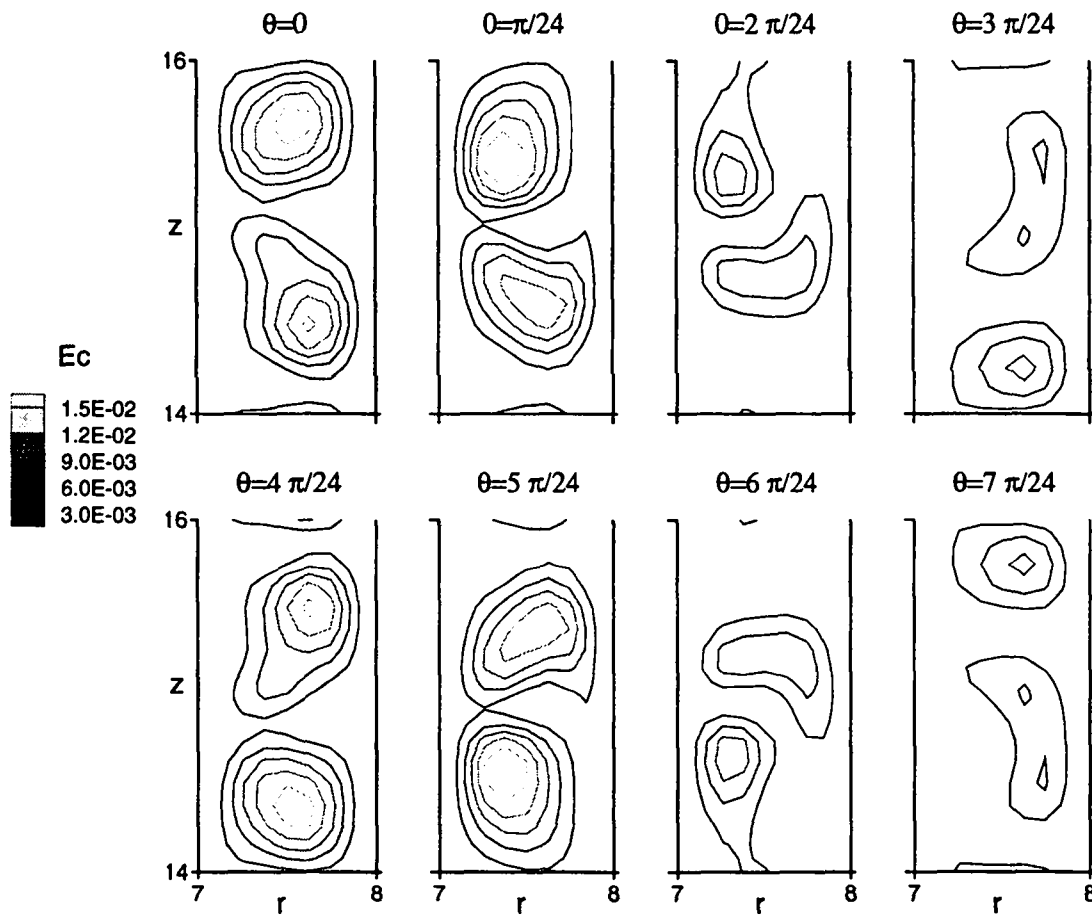


Figure 6.13: Contours of the kinetic energy of the perturbation, E_c , in successive meridional cross-sections at $Re = 180$.

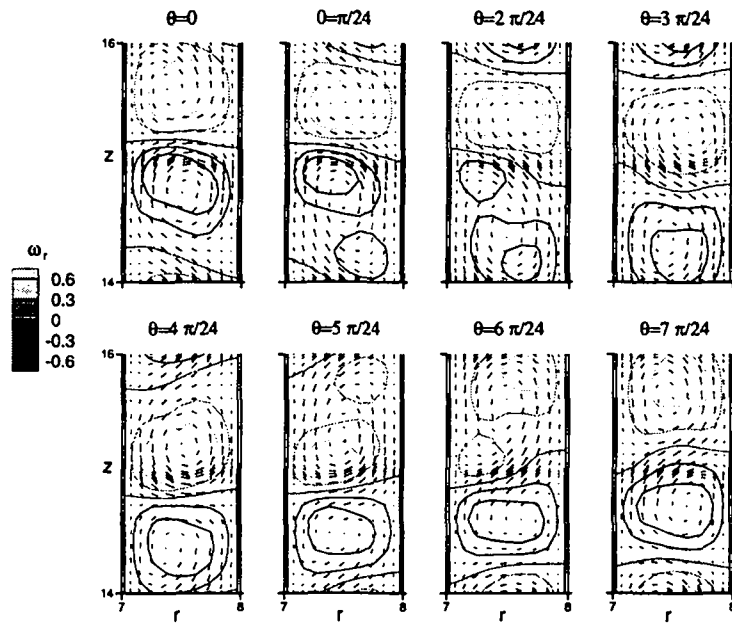


Figure 6.14: Vector field (u, w) and radial vorticity contours in successive meridional cross-sections at $Re = 180$.

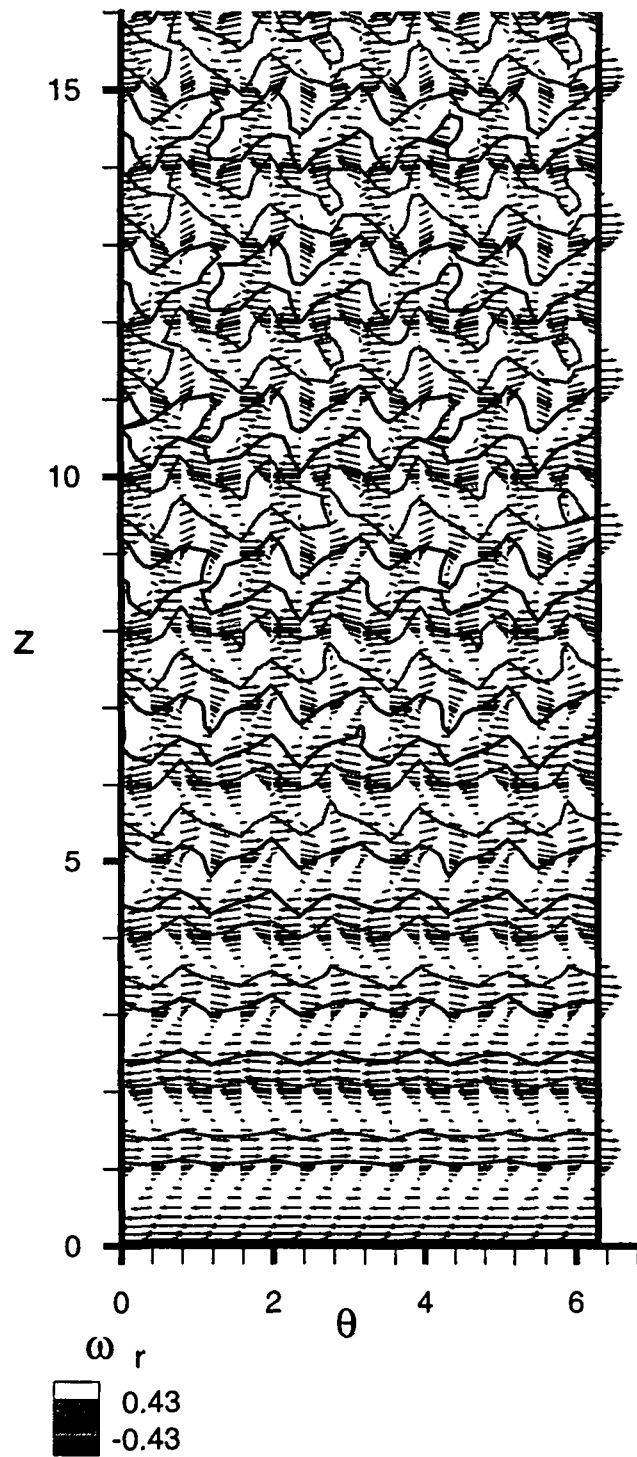


Figure 6.15: Vector field $(u, v - 0.5)$ and radial vorticity contours on the mid-radius cylindrical surface at $Re = 180$.

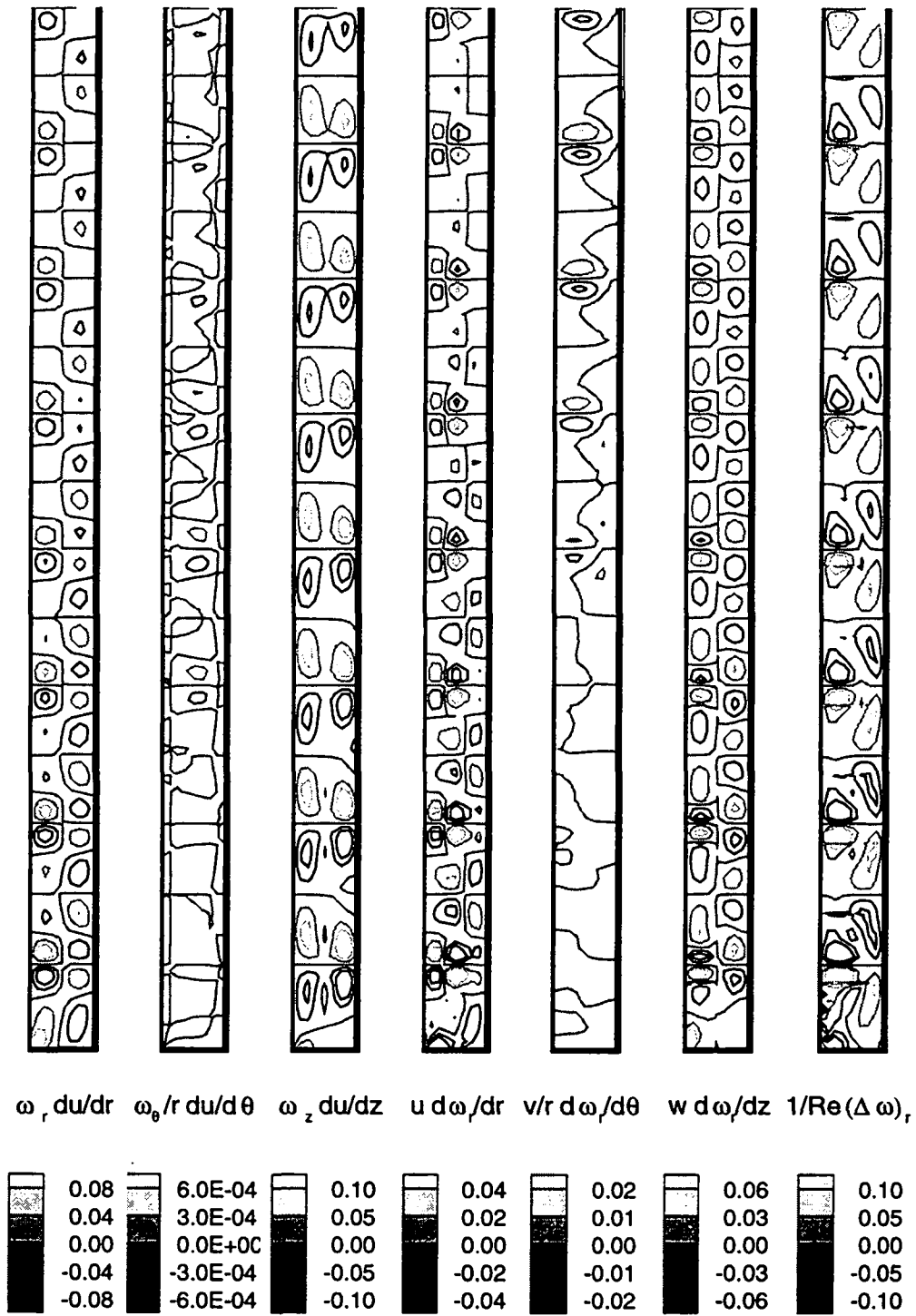


Figure 6.16: Meridian cross-sections of the different constituents of the radial vorticity equation at $Re = 180$.

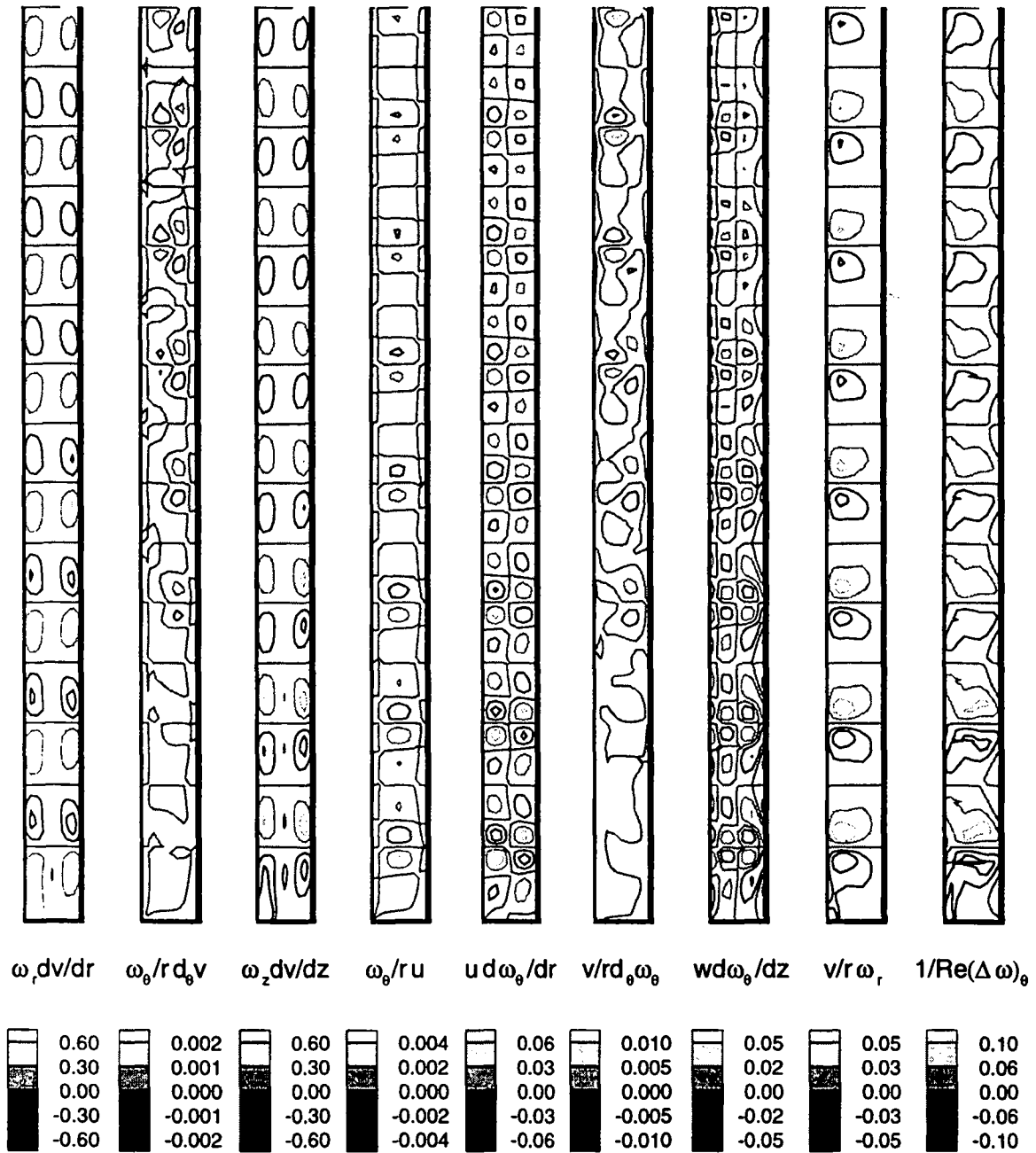


Figure 6.17: Meridian cross-sections of the different constituents of the azimuthal vorticity equation at $Re = 180$.

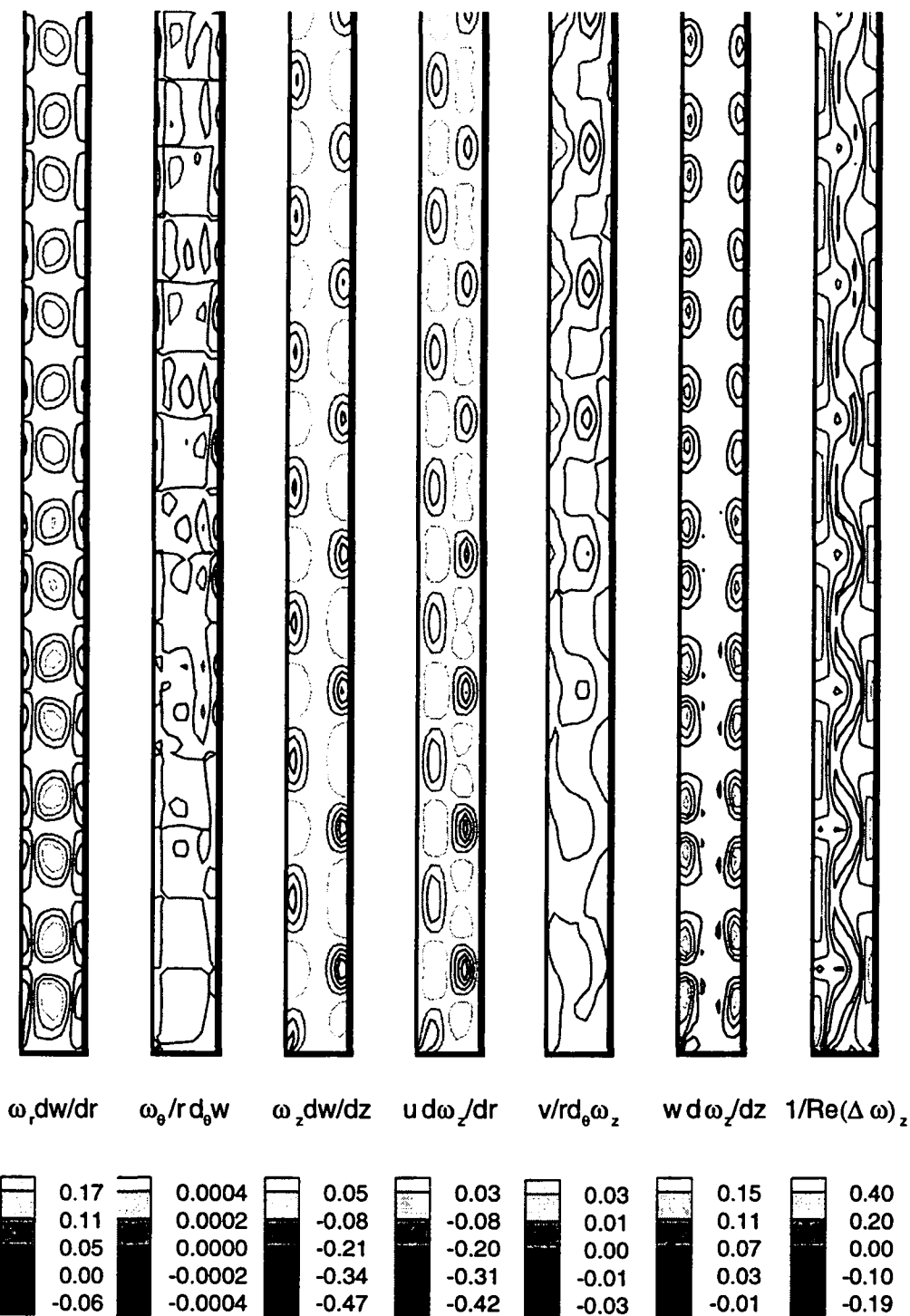


Figure 6.18: Meridian cross-sections of the different constituents of the axial vorticity equation at $Re = 180$.

Chapter 7

Counter-rotating Taylor-Couette flow

As in chapter 6, we begin our investigations with axisymmetric simulations, which are less computationally demanding than the complete 3D simulations and are therefore a good way to span a relatively large number of dynamical parameters, (Re_1, Re_2) , to find the most interesting cases. All of the simulations in chapter 7 are concerned with the finite-length case, and more precisely with the aspect ratio $\Gamma = 12$.

7.1 Axisymmetric simulations of the first transition

We investigate here the mechanism which defines the radial extent of the vortices that appear after the first bifurcation. Our hypothesis is that this mechanism is the same for both axisymmetric simulations and 3D simulations.

We have chosen four outer Reynolds numbers to investigate the first transition: -100 , -132 , -165 and -200 . According to chapter 5, above the first critical inner Reynolds number, the $Re_2 = -100$ simulations should show an axisymmetric flow, the $Re_2 = -132$ simulations a spiral regime with $k = 1$ azimuthal mode, the $Re_2 = -165$ simulations a spiral regime with $k = 2$ azimuthal modes and the last series of simulations, at $Re_2 = -200$, a spiral regime with $k = 3$ azimuthal modes. However, the cylinders being of finite length here, the predictions of chapter 5 are just rough indications of what we may find.

For all of the four series of simulations presented below, we have first performed a calculation at the outer Reynolds numbers -100 , -132 , -165 and -200 , and for $Re_1 = 0$, then a calculation at the same Re_2 , and for $0 < Re_1 < Re_c$. We finally have performed one supercritical calculation starting from the last of the two subcritical calculations.

As we have already noticed in chapter 6, all the following figures, from 7.1 to 7.8, show a close link between:

- ψ and ω_θ ,
- v , p and nl_r , and

- $\sigma_{\theta z}$ and ω_r .

We now describe the four series of simulations. In each of the following figures are presented successively the streamlines, ψ , and the contours of the azimuthal velocity, v , the pressure p , the radial, non-linear term, nl_r , the shear stress $\sigma_{\theta z}$, the radial vorticity, ω_r , and the azimuthal vorticity, ω_θ . For the four subcritical simulations of figures 7.1, 7.3, 7.5, and 7.7 four small cells touching the end plates have visible streamlines. Because they touch the end plates, we call these cells Ekman cells. Eight ghost cells can be seen in the ω_θ contours for the case (140, -100), six for the case (155, -132), but none for the last two subcritical cases, (170, -165), and (180, -200). Twelve Taylor vortices appear in figures 7.2 and 7.6, while there are ten in figures 7.4 and 7.8. These vortices are axially elongated compared to classical Taylor-Couette flow, as can be seen in table 7.1. As the rate of counter-rotation is increased, the vortices near the end are damped, while the Ekman cells increase in strength, and axial extent. In figure 7.8 the four extreme Taylor vortices are weakened, and only the mid-plane vortices seem unperturbed by the four Ekman cells. The table 7.1 indicates also a decrease of the radial extension of the vortices, this effect being linked to the diminishing *nodal radius*. The nodal radius is the radius for which the azimuthal vorticity of the base Couette flow is zero. The base Couette flow being given in equation (1.1), the nodal radius can be expressed by the following formula:

$$\left(\frac{R_n}{R_1}\right)^2 = \frac{Re_1 - \eta Re_2}{\eta^2 Re_1 - \eta Re_2}.$$

As $-Re_2$ becomes large, the ratio of critical Reynolds numbers, Re_1/Re_2 reaches a constant. The nodal radius therefore also tends to an asymptotic constant value that we call R_n^∞ .

Couette flow is known to be unstable in the *nodal region*, that is the annular zone $R_1 \leq r \leq R_n$, in the case of an inviscid fluid. Although the fluid considered here is viscous, the centrifugal instability, latent in the nodal region (see Rayleigh's criterion), remains the cause of destabilization. The roles of the viscosity are:

- first, to postpone the instability to non-zero values of the inner Reynolds number, considering counter-rotation,
- second, to extend the unstable zone beyond the nodal region by diffusion.

The second role of the viscosity may seem ambiguous because instead of damping the instability it actually enhances it.

Thus, summarizing, when the fluid is viscid, the zone of instability corresponds to the nodal zone plus a small diffusion layer, about 20% of $R_n - R_1$.

Influence of the attachment of the end plates to the cylinders

With the end plates fixed to the inner cylinder rather than the outer, the strength of the Ekman cells is stronger, and these occupy more space. The number of Taylor vortices is thus reduced from six pairs to five, as can be seen in figure 7.9.

$Re_2 = -100$

$Re_1 = 140$

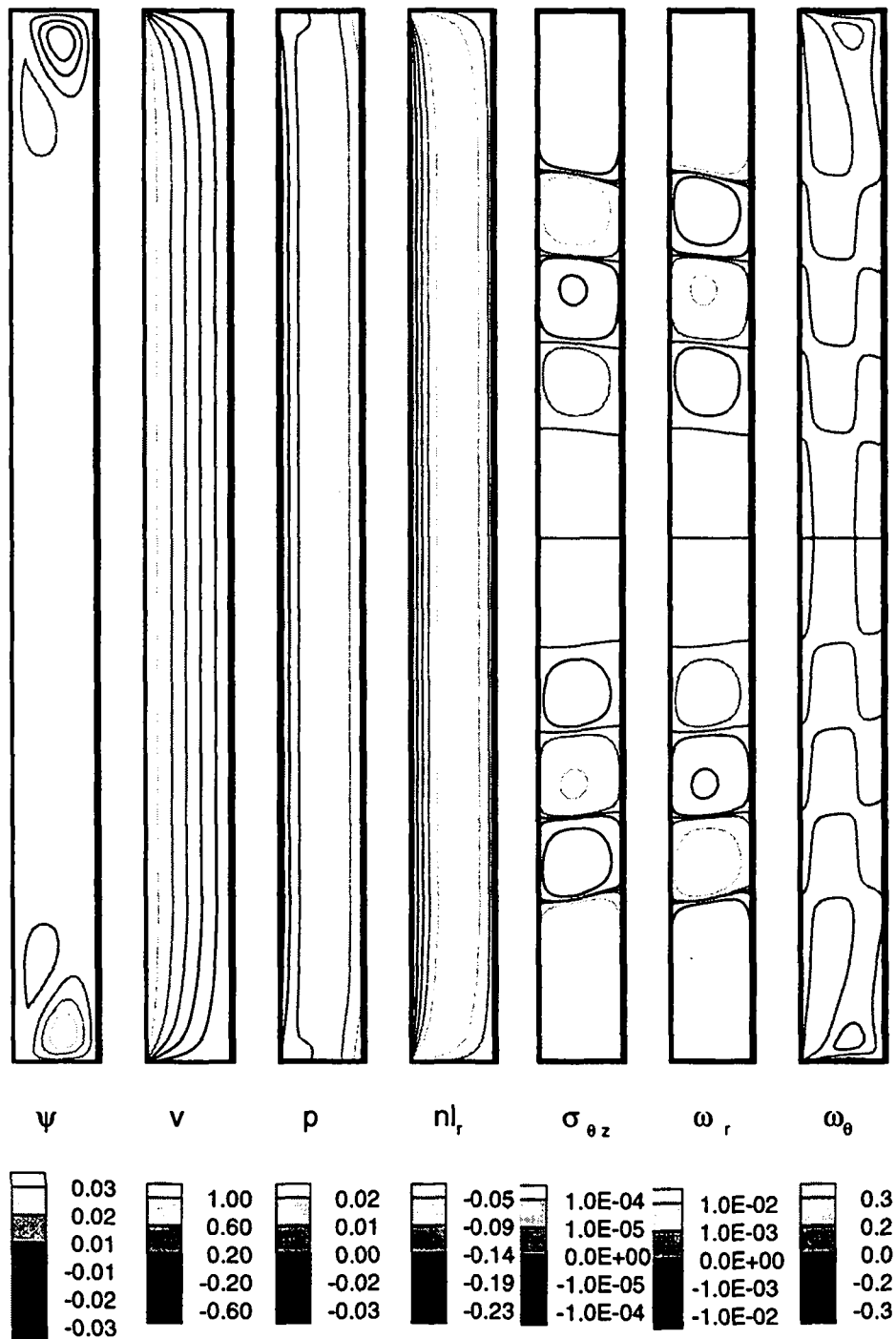


Figure 7.1: Couette flow with four Ekman cells and eight ghost cells.

$Re_2 = -100$

$Re_1 = 160$

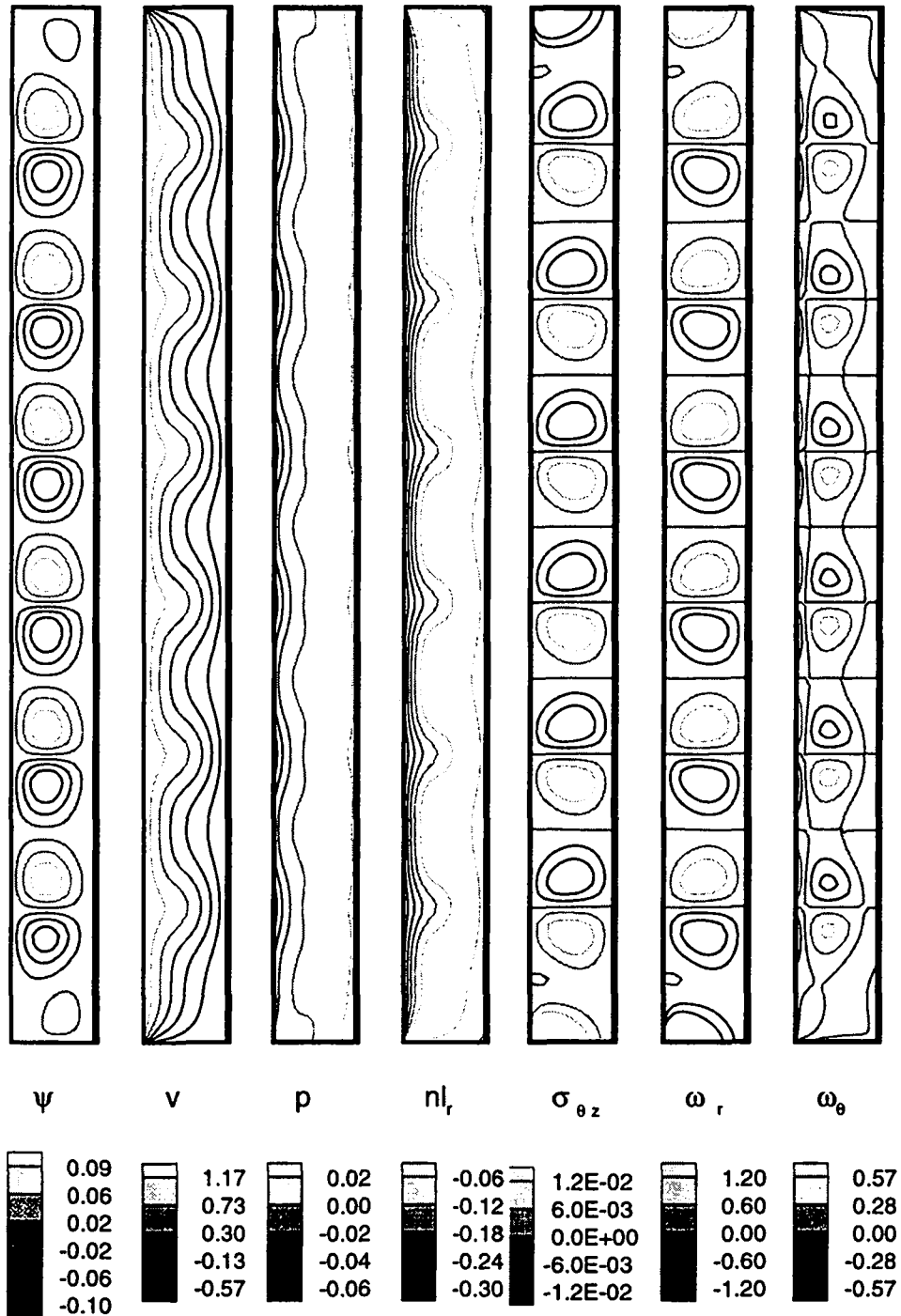


Figure 7.2: Six pairs of Taylor vortices and four weak Ekman cells.

$Re_2 = -132$

$Re_1 = 155$

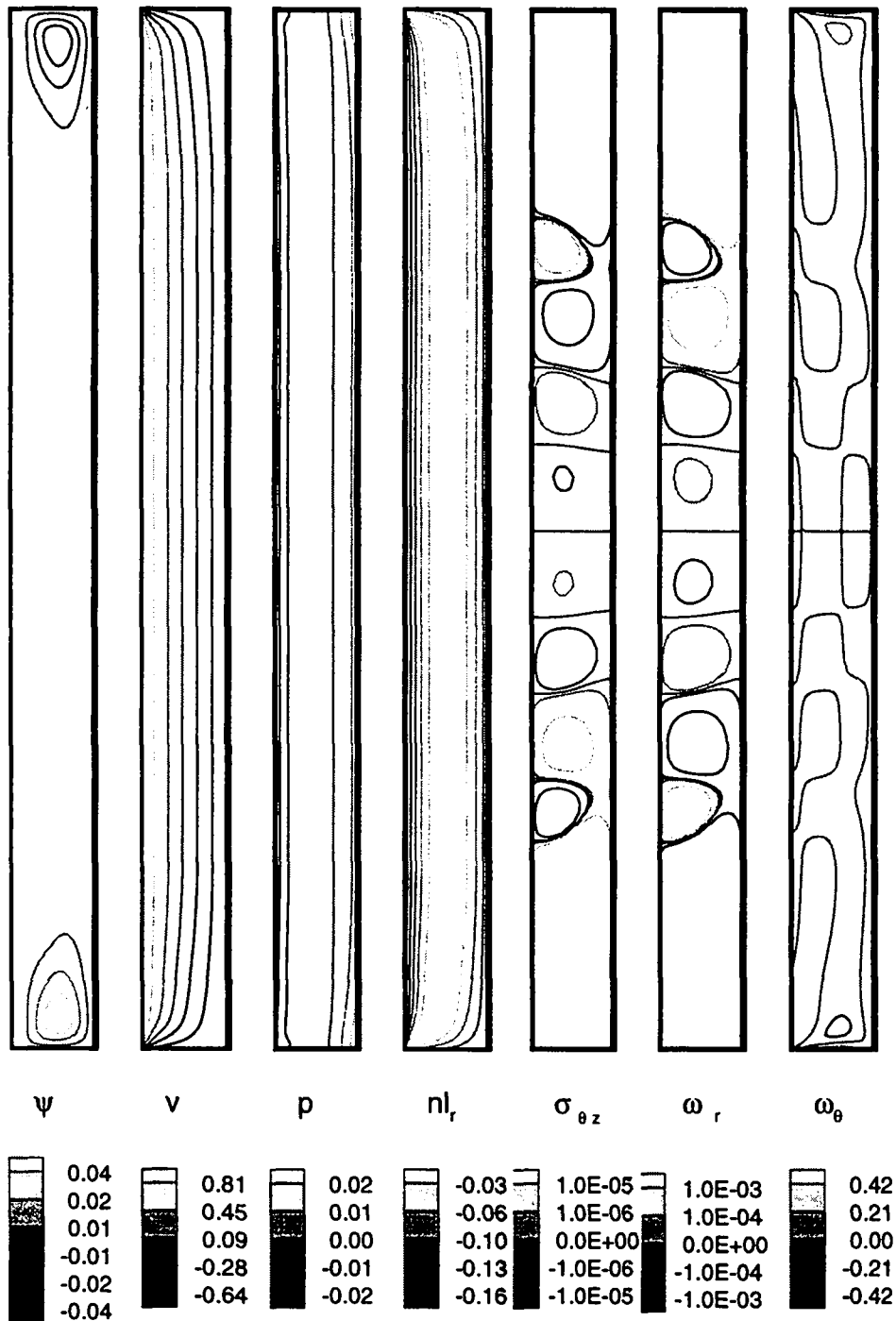


Figure 7.3: Couette flow with four Ekman cells and eight ghost cells.

$Re_2 = -132$

$Re_1 = 175$

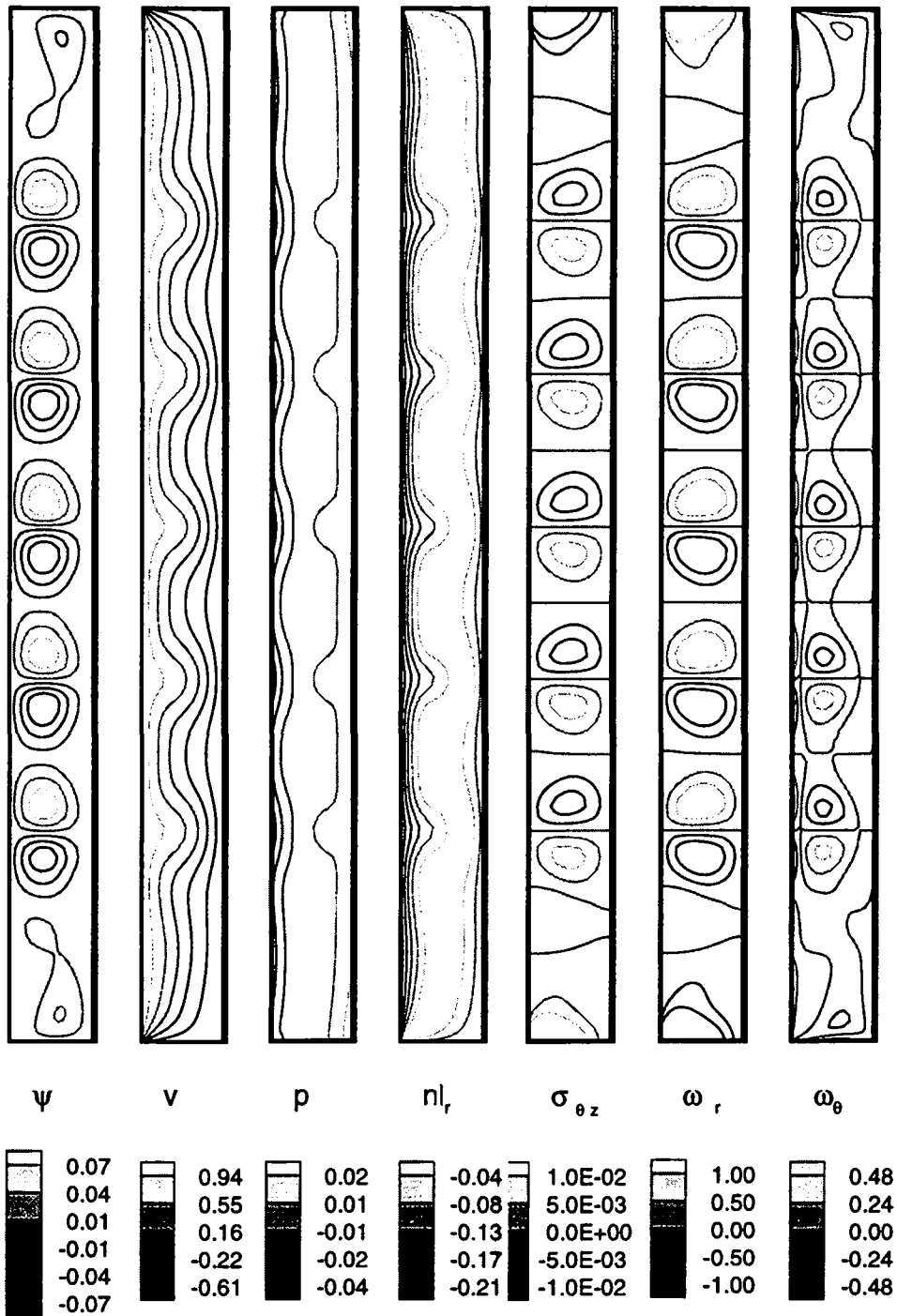


Figure 7.4: Five pairs of Taylor vortices and four weak Ekman cells.

$Re_2 = -165$

$Re_1 = 170$

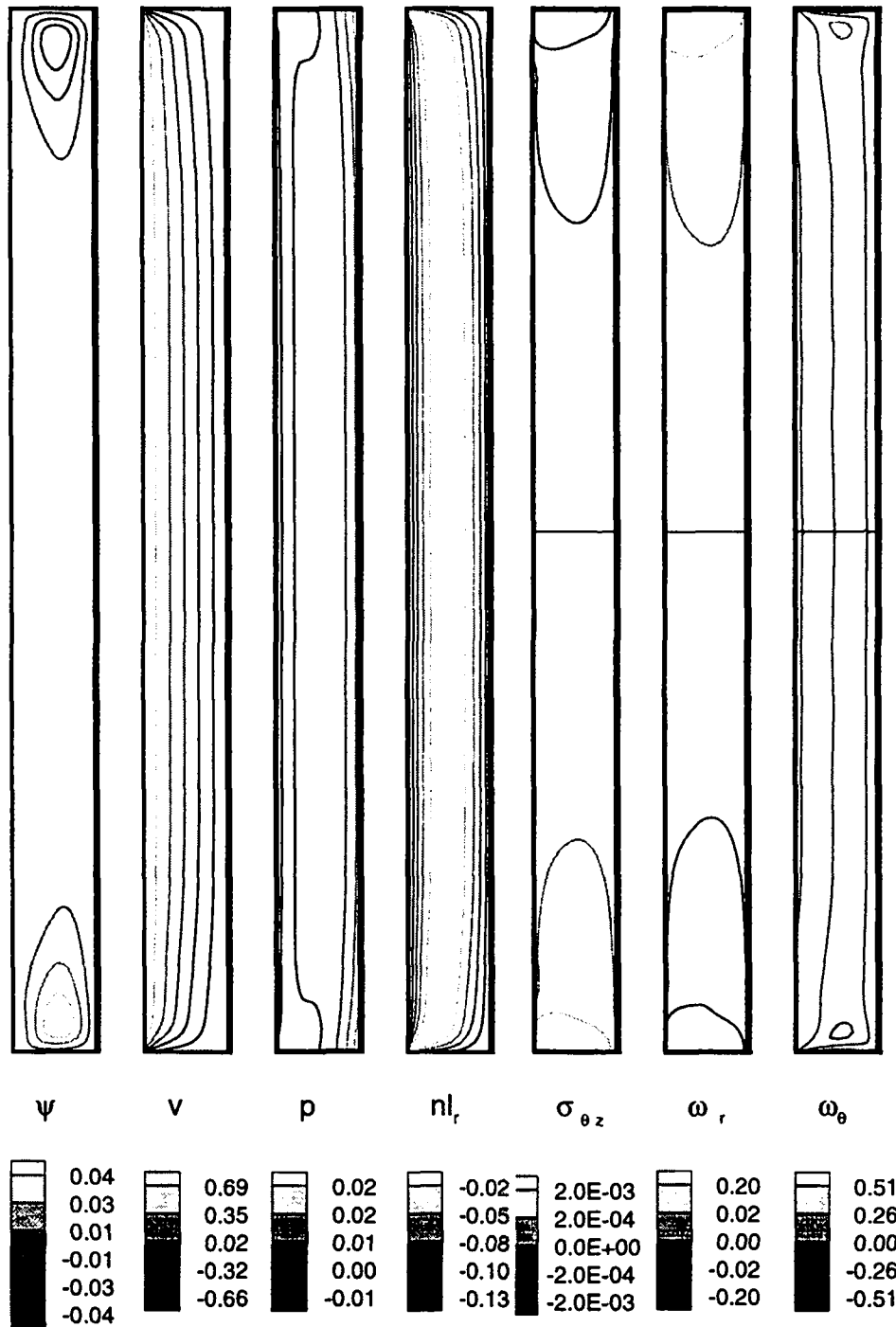


Figure 7.5: Couette flow with four weak Ekman cells.

$Re_2 = -165$

$Re_1 = 190$

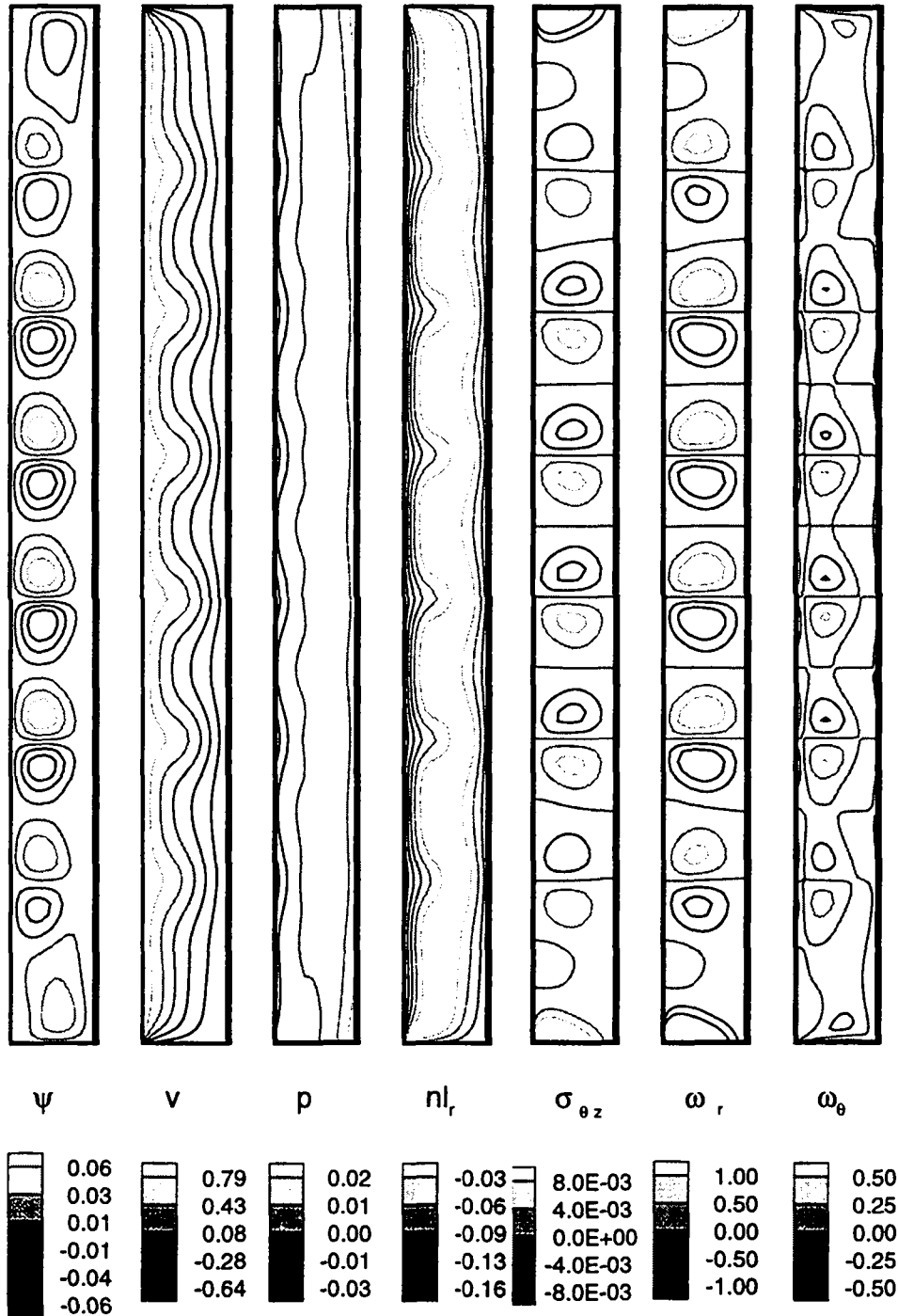


Figure 7.6: Six pairs of Taylor vortices and four Ekman cells.

$Re_2 = -200$

$Re_1 = 180$

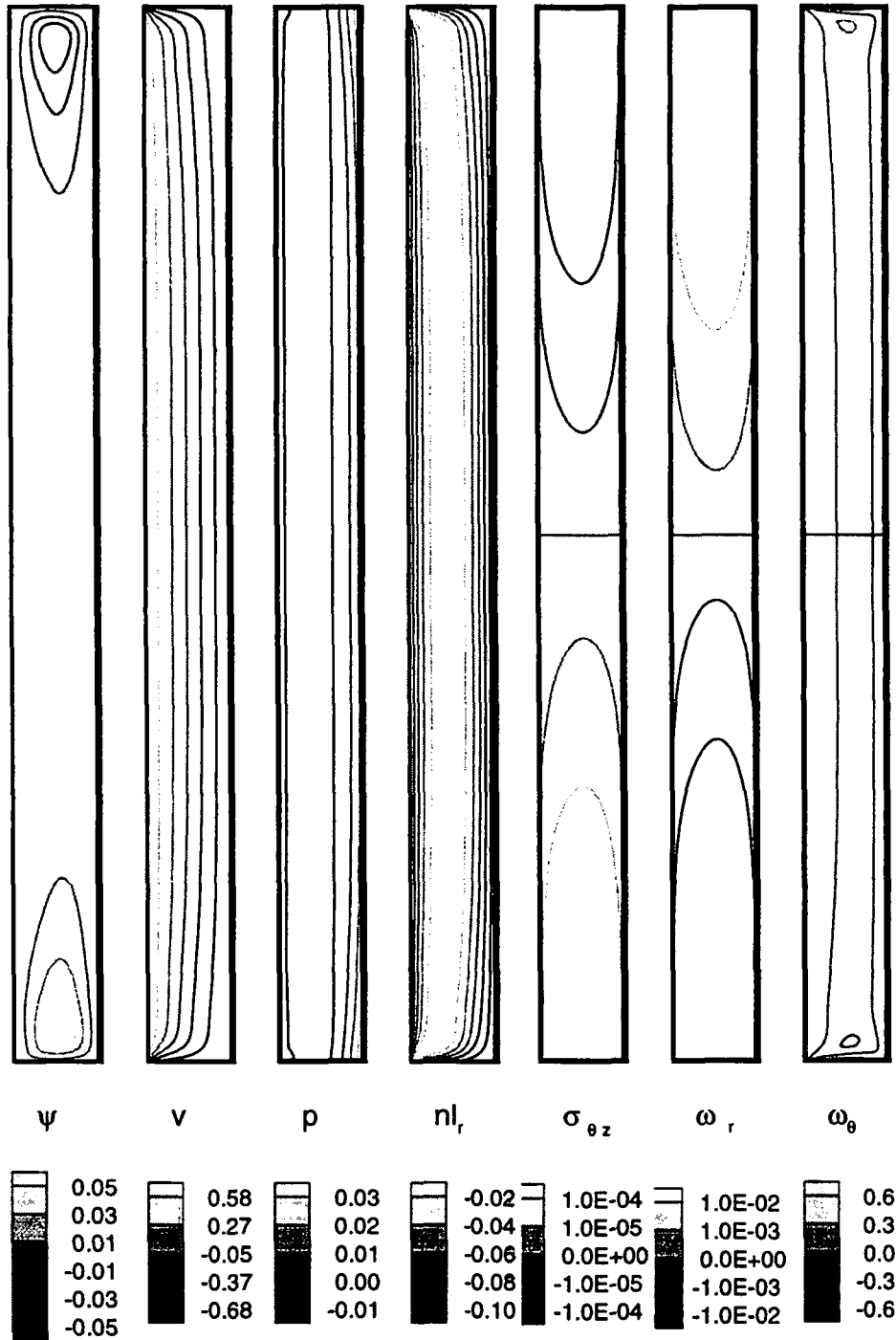


Figure 7.7: Couette flow with four weak Ekman cells.

$Re_2 = -200$

$Re_1 = 200$

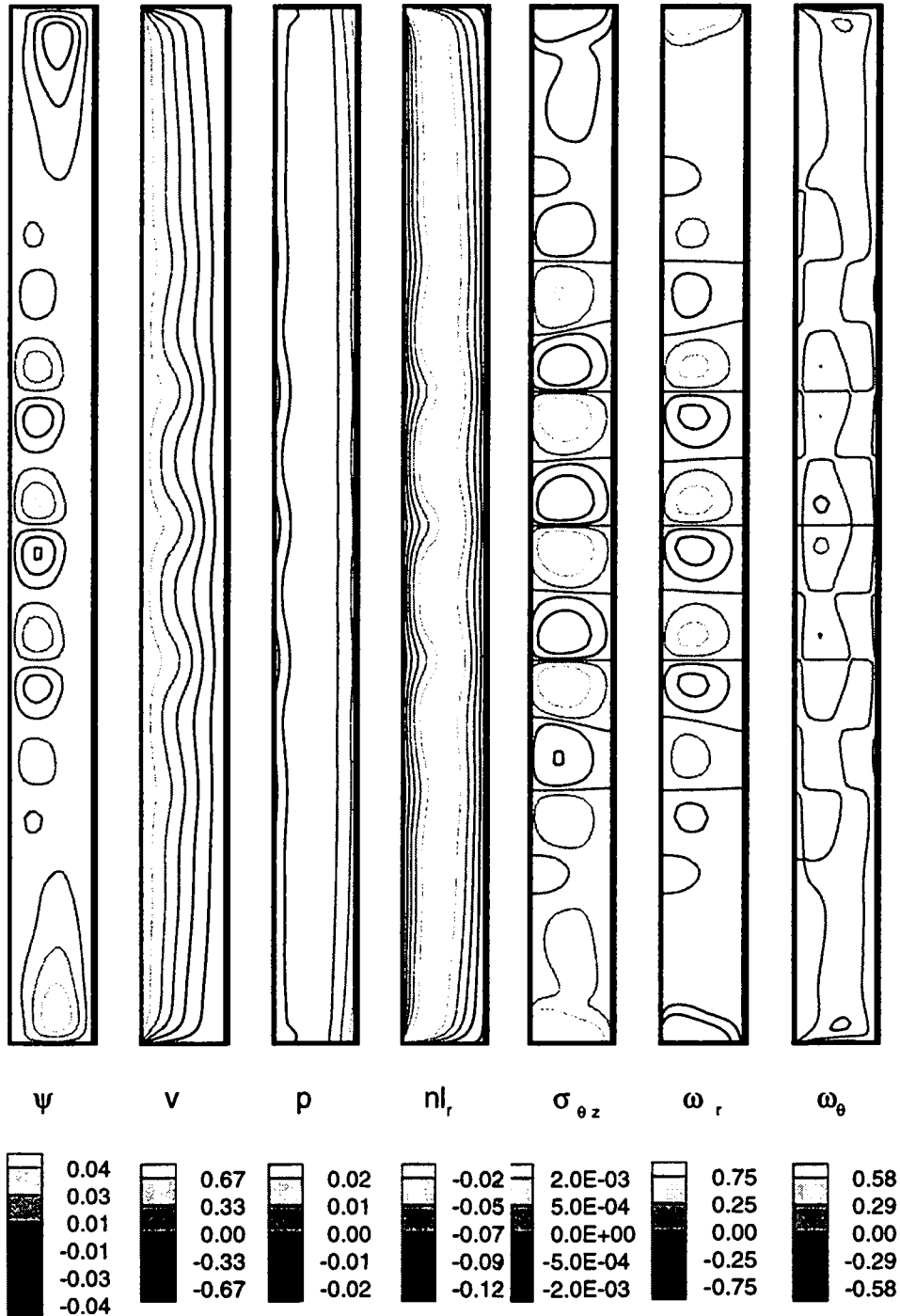


Figure 7.8: Five pairs of weakened Taylor vortices and four Ekman cells.

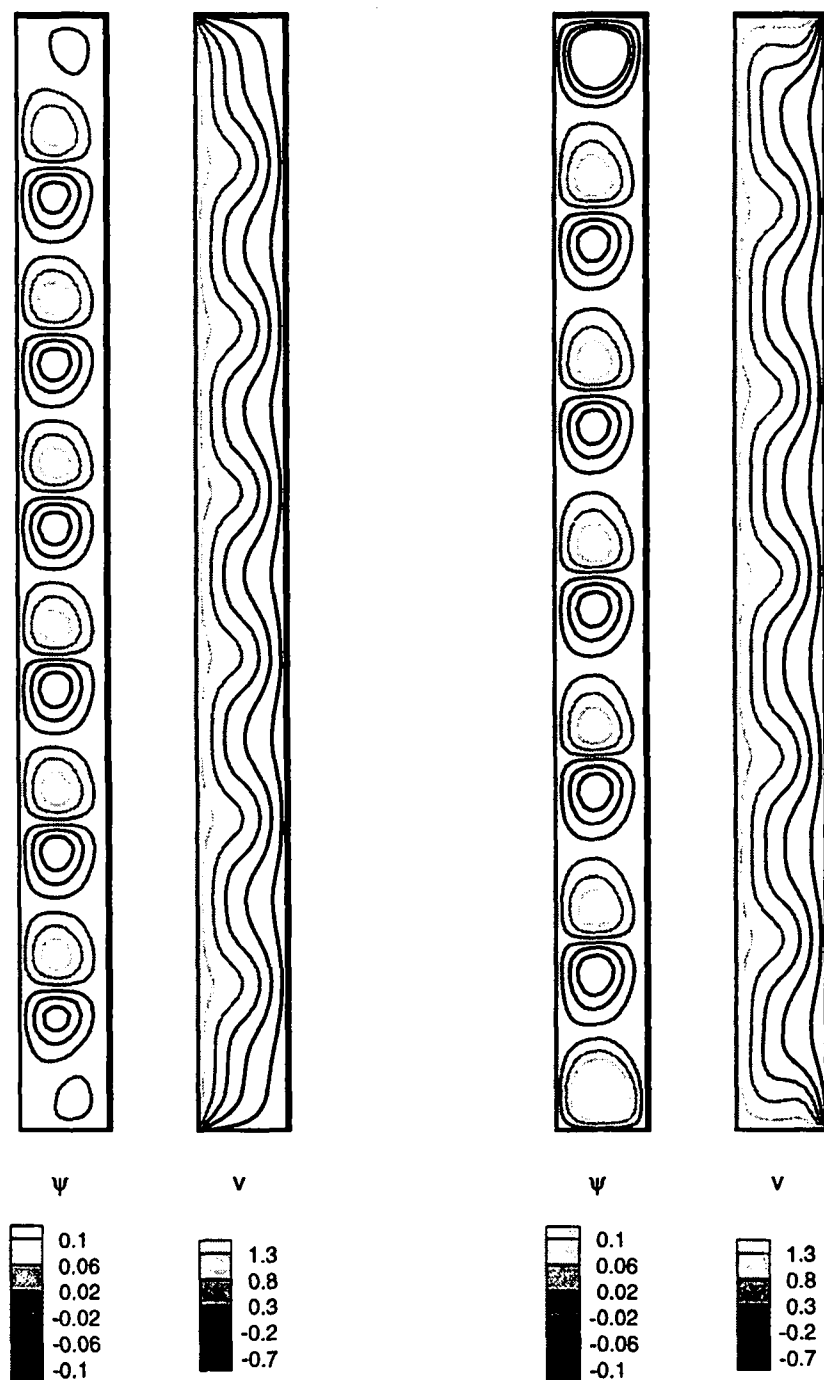


Figure 7.9: Comparison between one simulation with end plates fixed to the outer cylinder (two left pictures) and another with end plates fixed to the inner cylinder (on the right). Both simulations are performed at $Re_1 = 160$ and $Re_2 = -100$.

Re_1	160	175	190	200
Re_2	-100	-132	-165	-200
N_v	12	10	12	10
λ	1.766	1.710	1.628	1.556
e	0.71	0.65	0.63	0.58
$\frac{\lambda}{e}$	2.49	2.63	2.58	2.67
$R_n - R_1$	0.60	0.55	0.52	0.48

Table 7.1: Evolution of the number of inner vortices N_v , their wavelength λ , their radial extent e , and the distance from the inner cylinder to the nodal surface $R_n - R_1$, with Re_1 and Re_2 .

7.2 Transition to bouncing vortices

In this section, the $Re_2 = -132$ and -165 axisymmetric simulations are taken as starting points for complete 3D simulations.

We have seen in chapter 5 that the first transition is to axisymmetric flow for $Re_2 \geq -125$, and in the case of cylinders of infinite length. From the experience we gained in chapter 6, we can predict that the reduction of Γ (from ∞ to 12) will have a damping effect on non-axisymmetric modes. We can therefore expect the first transition to become non-axisymmetric for higher absolute values of the outer Reynolds number.

Expecting the axisymmetric flow at ($Re_1 = 175, Re_2 = -132$) to be unstable to non-axisymmetric perturbations of mode $k = 1$, we introduce a perturbation, $(u_p, 0, w_p)$, with just one non-zero Fourier azimuthal mode. We give here the Fourier transform of \mathbf{v}_p in the azimuthal direction:

$$\begin{cases} \hat{u}_p(r, z) &= -\epsilon \frac{1}{r} \sin^2(\pi x(r)) \frac{2\pi}{\lambda} \exp(2i\pi y(z))(1 + \epsilon \rho) \quad , \\ \hat{w}_p(r, z) &= -\epsilon \frac{i\pi}{rd} \sin(2\pi x(r)) \exp(2i\pi y(z))(1 + \epsilon \rho) \quad , \end{cases} \quad (7.1)$$

where λ is the expected axial wavelength, ρ is a random number in the interval $[-1, 1]$, ϵ (10^{-2}) is the initial level of the perturbation, and

$$\begin{cases} x(r) &= \frac{r-R_1}{d} \quad , \\ y(z) &= \frac{z}{\lambda} \quad . \end{cases} \quad (7.2)$$

The perturbation, \mathbf{v}_p , does not behave as predicted in chapter 5, but decays to zero. The axisymmetric solution presented in figure 7.4 is therefore stable.

We introduced the same perturbation in the axisymmetric solution obtained for case ($Re_1 = 190, Re_2 = -165$). This time, the mode 1 perturbation grows until a final state is reached in which the kinetic energy of each of the simulated modes remains constant. The figure 7.10 shows that the kinetic energy decreases exponentially as k increases. The perturbation we have introduced initially only contained energy in mode 1. The

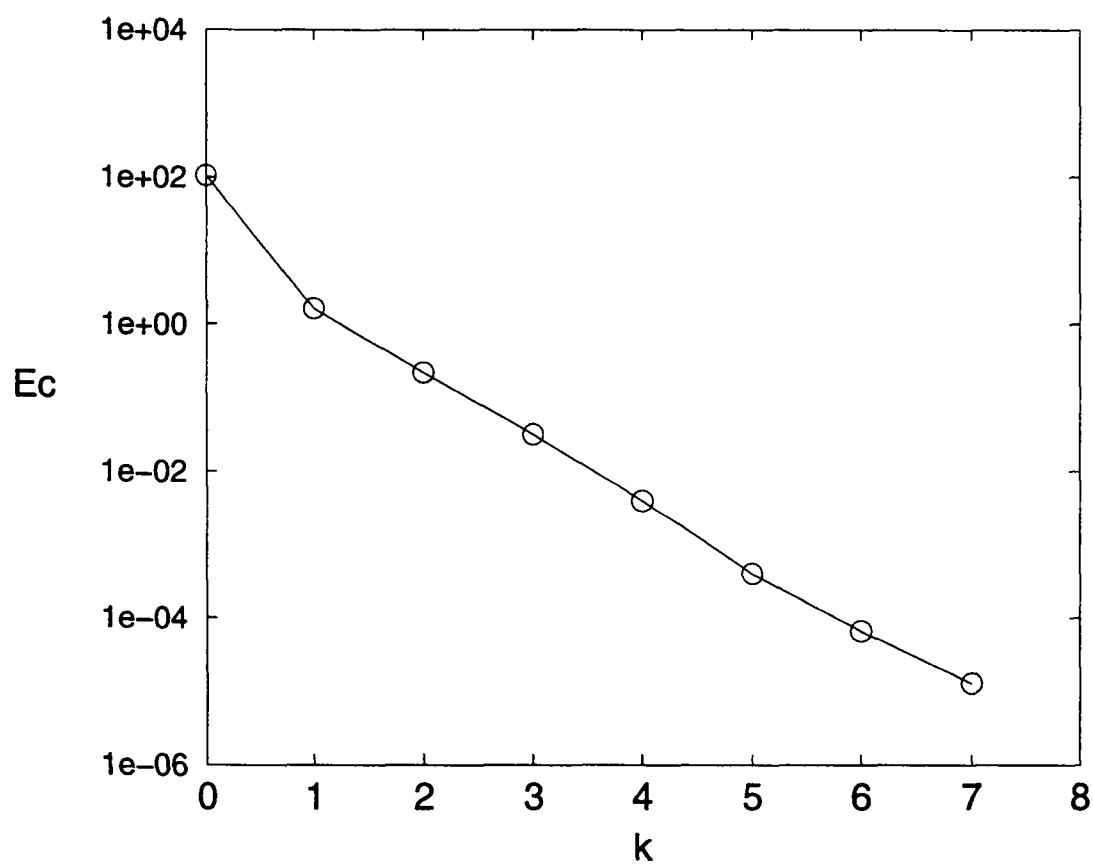


Figure 7.10: Final kinetic energy, E_c , per azimuthal Fourier mode, k .

fact that the final flow state displays energy in mode 1, and its harmonics shows, that among the non-zero modes, only this one is able to destabilize the flow. The energy in modes higher than 1 would otherwise grow at the expense of the first mode to produce a different distribution of energy.

Here, the kinetic energy per azimuthal Fourier mode remains constant with time. It is also true in the case of wavy vortex flow, as is reported in chapter 6. The whole flow pattern behaves in both cases like a solid body, when considered in the appropriate rotating reference frame.

Description and comparison of the new flow pattern, with wavy vortex flow and spirals flow

According to the results we have obtained in chapter 5 for $\Gamma \rightarrow \infty$, we would expect the super-critical flow at $Re_2 = -165$ to form spirals. But this is not what we find. The structure that we observe is neither wavy vortex flow, or spirals flow. We will see later the reason why we call these structures “bouncing vortices”.

The vortex structures we observe in figures 7.11 and 7.12 are closed azimuthally, and also display a wavy pattern, which are typical of wavy vortex flow.

But, in contrast to what is observed for wavy vortex flow, the axial movement of the vortices is the same, whether they are at mid-height or close to the end plates, as can be observed in figure 7.11. The amplitude of this axial displacement is also more important. The vortex pairs are separated by a bigger distance, about 2.5 gap widths, than for wavy vortex flow, about 2 gap widths. The strength of the vortices of each pair remains constant (except when such a pair approaches one of the end plates), which is not the case for the wavy vortex flow regime, where the clockwise and anti-clockwise vortices alternate in strength. As can be seen both in figures 7.11 and 7.12, the vortices disappear in pairs as they approach the end plates. Such a behaviour is expected for spirals in an axially-closed domain.

Another remarkable feature of this flow is the axial shearing of the vortices that propagates from top to bottom and back, as can be seen in figures 7.11 and 7.12. This deformation wave may be related to a global secondary motion of the flow. Just after the maximal deformation reaches the bottom end plate, the lower pair of vortices disappears and the global motion of the vortices is reversed.

The wave speed is deduced from the time evolution of the azimuthal vorticity presented in figure 7.12. It is $\frac{s}{\Omega_2} = 0.449$. Hence, the period of the azimuthal wave is $T = 2.23 T_2$, where T_2 is the rotation period of the outer cylinder. We also have $T = 2.93 T_1$, T_1 being the rotation period of the inner cylinder.

We call the new flow pattern observed here “bouncing vortices” because the whole pattern behaves like a column of counter-rotating vortices stacked on each other, and

moving up until the top pair of vortices nearly vanishes and down until the bottom pair also disappears and appears again.

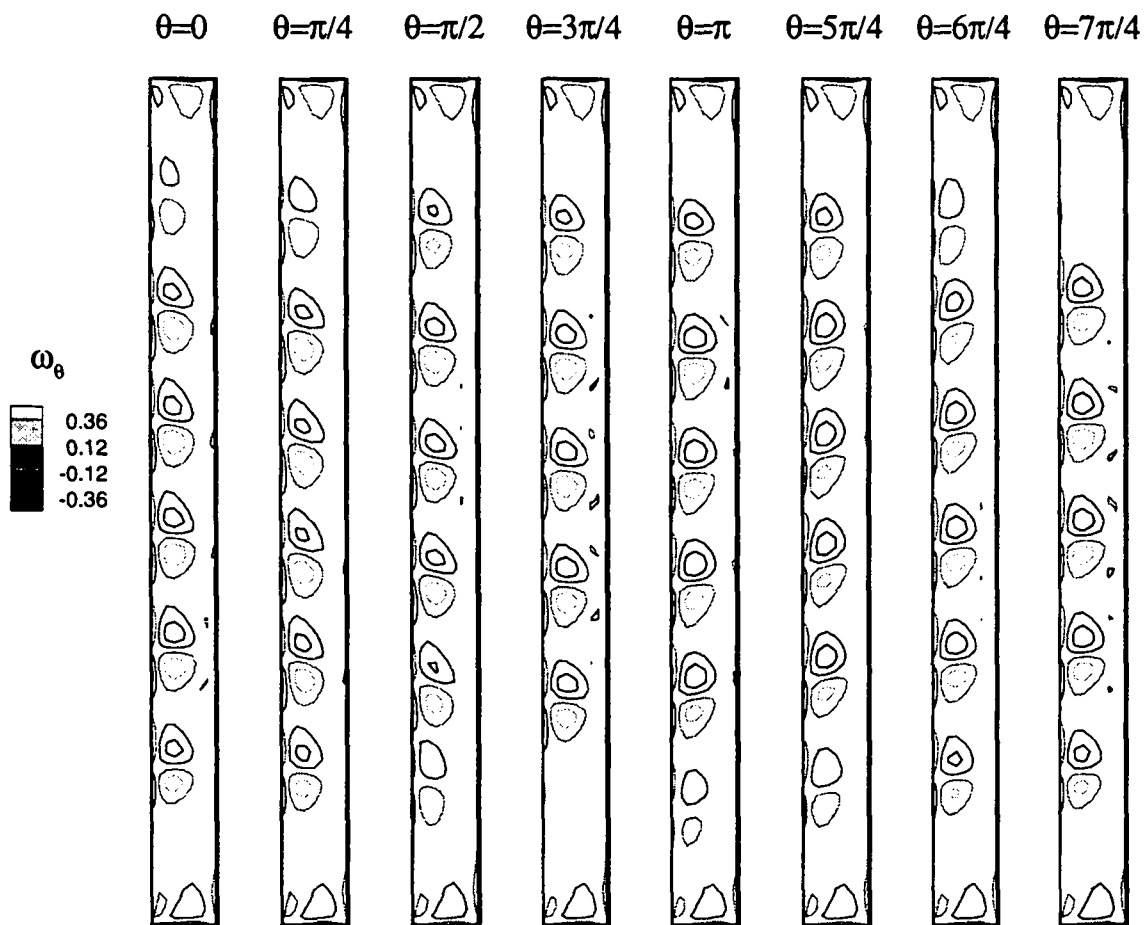


Figure 7.11: Successive meridional cross-sections showing the azimuthal vorticity contours at $(Re_1 = 190, Re_2 = -165)$.

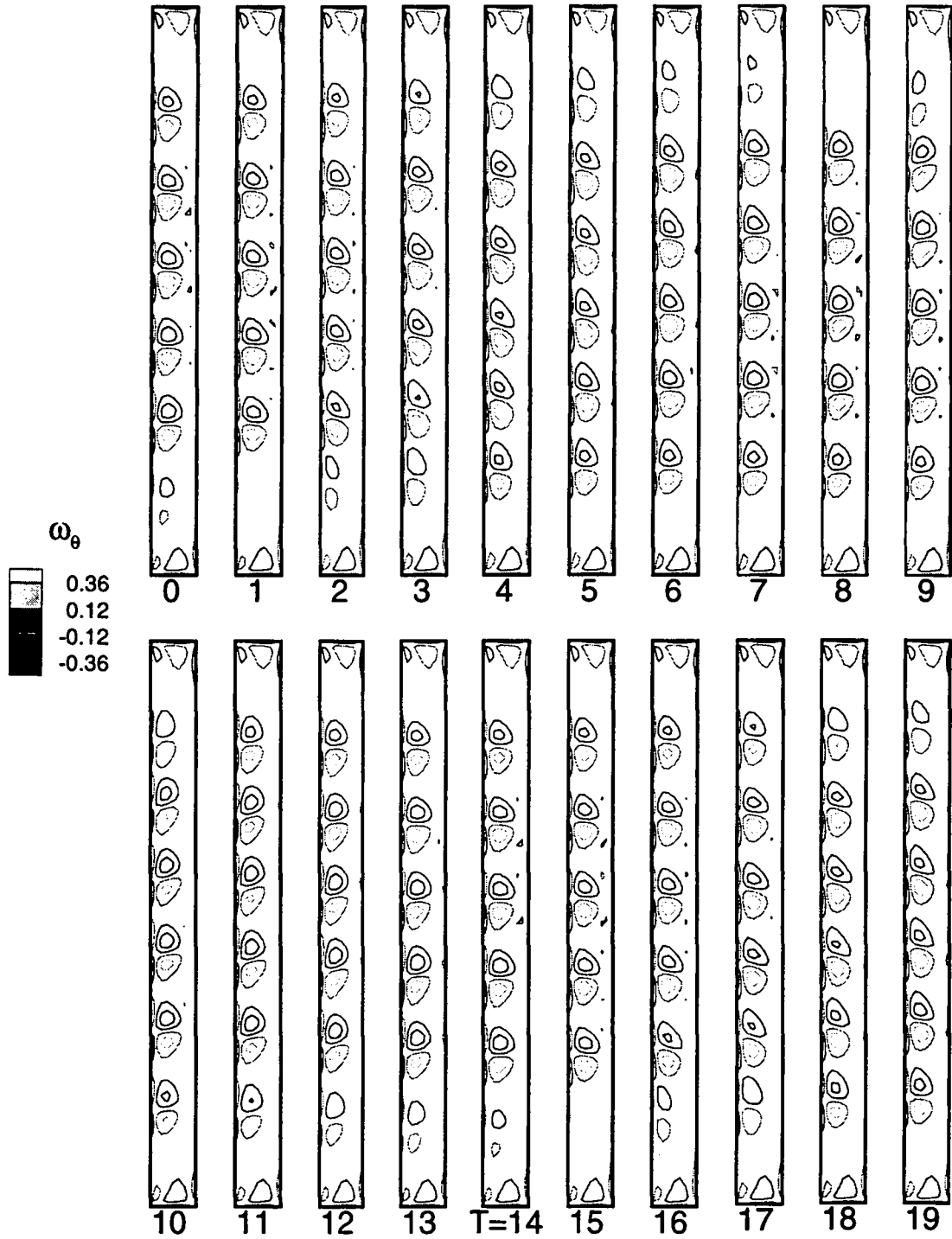


Figure 7.12: Time evolution of the azimuthal vorticity, ω_θ , during one period, at $(Re_1 = 190, Re_2 = -165)$. The period is $T = 14 \tau$, with $\tau = \frac{1}{\Omega_2}$.

Chapter 8

Conclusions and perspectives

8.1 Conclusions

Tools

The DNS code developed here has proved to be efficient. The computational speed of the code is characterized by the CPU time needed per mesh point, and per time step. Its best value is $40\mu s$ (on the Cray YMP), which corresponds to $10\mu s$ per variable node and per time step. There are two main reasons for this efficiency. The first is that it was designed specifically for one application, namely the study of transition of a Newtonian fluid enclosed between rotating coaxial cylinders and horizontal end plates. The second reason is linked to the choice of the algorithms, which were perfectly adapted to our case. Even better performances could however be achieved by improving the implementation of these algorithms in the program. We indeed only reached 40% of the peak performance of the Cray J90. The specific design of our code has another advantage, the relative simplicity of its implementation.

Though our main goal was not to create an original numerical method, some of its features are innovative. The regularization of the singular boundary conditions we apply is new. Whereas Tavener *et al.* [65] only impose one tangent in the velocity field they adopt to regularize the singularity, we impose the tangents at both ends of the small regularization interval. Furthermore, the tangents we adopt correspond to natural physical requirements.

The time discretization we have chosen is based on the well known second-order Runge-Kutta scheme. The way we incorporate the boundary conditions in this scheme is also original. The boundary conditions appearing in the pressure solver are $\nabla \cdot \mathbf{v}$, whereas the classical boundary conditions in that case would be $\nabla \cdot [\frac{1}{Re} \nabla^2 \mathbf{v} - (\mathbf{v} \cdot \nabla) \mathbf{v}]$. These two kinds of boundary conditions are in fact equivalent, but we believe that the ones we introduce in the time marching scheme are more straightforward.

In the course of our work, we have found that however efficient the DNS code was,

the time needed for some of the simulations was huge. For example, the simulation of wavy Taylor vortex flow for $\Gamma = 30$, $\eta = 0.875$, $Re_1 = 180$ and $Re_2 = 0$ took two months on the Cray J90, which corresponds to about 10 days CPU. The space discretization consisted of a polynomial degree $N_r = N_z = 12$, the number of azimuthal modes $N_\theta = 16$, and the number of elements 1×30 . The number of mesh point was therefore 75088. This number is relatively small for a DNS, but the large aspect ratio for this simulation, 30, causes very long transients. The number of time steps required for the flow to settle is $2 \cdot 10^5$.

We have therefore designed a second code, which performs only a linear stability analysis of the base Couette flow, and have undertaken parametric studies before proceeding with the direct numerical simulations for the most interesting parameter values. This code is able to compute a complete transition curve, at a given η , overnight on the Cray J90.

Both codes have been thoroughly validated, although only the validation of the DNS code is presented in the thesis. Numerical tests were performed before the physical ones. We obtained very good qualitative agreement with the numerical results of Streett and Hussaini [61]. We also found good agreement with the theoretical and experimental results of Ern [28]. The slight differences observed between our numerical results and hers are explainable: many simplifications had to be made in the theoretical approach, and the experimental measurements of the axial velocity we compare against are averaged on a small surface, whereas our measures are pointwise.

Results of

linear stability analysis code With the linear stability code, we have obtained the first transition curve for different types of perturbations in the range ($0 < Re_1 \leq 300$, $-400 \leq Re_2 \leq 0$). The most unstable perturbations, introduced initially in the base Couette flow, were first axisymmetric and then non-axisymmetric, with k azimuthal modes, k ranging from 1 to 4. From this study, we have deduced the complete transition curve, presented in figure 5.4, as well as the number of azimuthal modes that can be observed in the supercritical solutions. These results are only valid for cylinders of infinite length. This explains why we found different results with our DNS code.

DNS code We found an axisymmetric supercritical flow at $Re_2 = -132$, while we expected a non-axisymmetric flow with one azimuthal mode from the linear stability analysis. The supercritical flow we obtained at $Re_2 = -165$ is non-axisymmetric, but with only one azimuthal mode instead of the two modes predicted by the theoretical approach. The finiteness of the cylinders tends to delay the appearance of non-axisymmetric flows, and to diminish the number of azimuthal modes. These results are related to those obtained in the classical Taylor-Couette configuration (where only the inner cylinder is rotating) by Brindley and Mobbs [11]. They observed that

the second critical Reynolds number, Re_w , where the non-axisymmetric modes appear, increased drastically as the aspect ratio, Γ , was decreased. We also observed in figure 6.15 that the waviness in the wavy Taylor vortex flow pattern is damped by the end plates, i.e. influenced by the finiteness of the aspect ratio.

We have focused our investigations on two kinds of non-axisymmetric flows. The first is the wavy Taylor vortex flow, that we have simulated for the geometrical parameters $\eta = 0.875$ and $\Gamma = 30$, and for the dynamical parameters $Re_1 = 180$ and $Re_2 = 0$. We have found good qualitative agreement with the infinite-length, numerical results of Marcus [48]. The azimuthal wavenumber we found is 6 and the dimensionless wavespeed of the whole flow pattern is 0.438. We have found a close relation between the periodic strength oscillation of the counter-rotating Taylor vortices and the periodic strength and position oscillations of the vorticity. Furthermore, we have observed that the non-linear combination of vorticity and velocity is of leading order in the vorticity transport equation, and that these terms are nearly time independent. Therefore, when the velocity in one of the vortices decreases, the vorticity increases in that same vortex. This lasts for half a period and for the other half-period, the velocity grows at the expense of the vorticity.

The other non-axisymmetric flow we have focused on is the counter-rotating regime observed for $\eta = 0.875$ and $\Gamma = 12$ at $(Re_1 = 190, Re_2 = -165)$. Here, the number of the azimuthal mode is one and the wavespeed is $\frac{s}{\Omega_2} = 0.449$. When considered in a reference frame rotating with the cylinders, this flow pattern is fixed. This flow, that we call bouncing vortices flow, shares properties of both spirals flow and wavy vortex flow. According to large aspect ratios experiments, a spirals flow was expected. The aspect ratio we have chosen, 12, is small enough to counteract the “natural behaviour” of the flow, so that it exhibits a new pattern. This flow may be described as the sum of the classical Taylor vortex flow in the unstable region near the inner cylinder, and a global, periodically-alternating, axial flow confined in the stable region. The unstable region for the viscous flow is larger (about 20%) than the unstable region predicted by theory for an inviscid fluid. This finding could explain why the first azimuthally-asymmetric flow is observed for a negative value of the outer Reynolds number, the global axial movement starting when the viscous unstable region do not reach the outer cylinder anymore.

8.2 Perspectives

In parallel to this numerical study, a Taylor-Couette apparatus was designed and built at the Fluid Mechanics Laboratory. The experimentalists focused on the so-called hour-glass geometry, consisting of a straight outer cylinder and a curved inner cylinder. The radius of the inner cylinder depends on the axial position, and is symmetric with respect to the mid-height plane.

A 3D algorithm able to deal with this configuration has been proposed. This algorithm is based on the same principles as those described in chapter 3. The transfinite interpolation of Gordon and Hall is used to map the original, deformed domain onto a rectangular reference domain. Very useful simplifications can be made if the deformation of the originally square cross-section flow domain is made in one direction only, as explains Appendix C. We treat the case where the deformation we apply is limited to the radial direction, and obtain an algorithm that is of the order of ten times slower than the one designed for the straight geometry. A parallel implementation is therefore required for the calculations to stay affordable.

Appendix A

Useful formulae in cylindrical polar coordinates

A.1 Viscous shear stress tensor

$$\left\{ \begin{array}{l} \tau_{rr} = 2\mu \frac{\partial u}{\partial r} , \\ \tau_{\theta\theta} = 2\mu \left(\frac{1}{r} \frac{\partial v}{\partial \theta} + \frac{u}{r} \right) , \\ \tau_{zz} = 2\mu \frac{\partial w}{\partial z} , \\ \tau_{r\theta} = \tau_{\theta r} = \mu \left[\frac{1}{r} \frac{\partial u}{\partial \theta} + r \frac{\partial}{\partial r} \left(\frac{v}{r} \right) \right] , \\ \tau_{rz} = \tau_{zr} = \mu \left(\frac{\partial w}{\partial r} + \frac{\partial u}{\partial z} \right) , \\ \tau_{\theta z} = \tau_{z\theta} = \mu \left(\frac{\partial v}{\partial z} + \frac{1}{r} \frac{\partial w}{\partial \theta} \right) . \end{array} \right.$$

A.2 Vorticity

$$\nabla \wedge \mathbf{v} = \boldsymbol{\omega} = \begin{pmatrix} \frac{1}{r} \frac{\partial w}{\partial \theta} - \frac{\partial v}{\partial z} \\ \frac{\partial u}{\partial z} - \frac{\partial w}{\partial r} \\ \frac{1}{r} \frac{\partial(rv)}{\partial r} - \frac{1}{r} \frac{\partial u}{\partial \theta} \end{pmatrix} .$$

A.3 Stream function in the axisymmetric case

$$\left\{ \begin{array}{l} u = \frac{1}{r} \frac{\partial \psi}{\partial z} , \\ w = -\frac{1}{r} \frac{\partial \psi}{\partial r} . \end{array} \right.$$

From this formula, we derive: $\psi(r, z) = \int_{z_1}^z r u(r, z) dz = - \int_{r_1}^r r w(r, z) dr$, for $\psi|_{\partial\Omega} = 0$.

Appendix B

Spectral element method

B.1 Spectral approximation of functions

B.1.1 Singular Sturm-Liouville problem

Polynomial solutions of a singular Sturm-Liouville problem are of special numerical interest because they can be evaluated and differentiated with high efficiency. The Sturm-Liouville problem consists in finding the eigenfunction f_i (corresponding to the eigenvalue λ_i) solution of equation:

$$-\frac{d}{dx} \left(a(x) \frac{df_i}{dx}(x) \right) + b(x)f_i(x) = \lambda_i \rho(x)f_i(x) \quad \text{on }]-1, 1[.$$

The coefficient a has to belong to $C_1(]-1, 1[)$ and has to be strictly positive in $]-1, 1[$. The coefficient b , as well as the weight function ρ , have to be positive on $]-1, 1[$. This problem is said to be singular if:

$$a(-1) = a(1) = 0 .$$

Fourier series, Chebyshev and Legendre polynomials are classical solutions of singular Sturm-Liouville problems.

B.1.2 Legendre polynomials

Legendre polynomials, L_n , satisfy the following singular Sturm-Liouville problem:

$$\begin{cases} \frac{d}{dx} \left((1-x^2) \frac{dL_n}{dx}(x) \right) + n(n+1)L_n(x) = 0, \\ L_n(1) = 1. \end{cases}$$

Legendre polynomials are orthogonal with respect to weight unity scalar product:

$$\int_{-1}^1 L_m L_n = \frac{2}{2m+1} \delta_{mn} .$$

These polynomials are computed via the following recurrence relation:

$$\begin{cases} (n+1)L_{n+1}(x) &= (2n+1)xL_n(x) - nL_{n-1}(x), \\ L_1(x) &= x, \\ L_0(x) &= 1. \end{cases}$$

B.1.3 Gauss-Lobatto-Legendre weights and points

GLL weights Gauss-Lobatto-Legendre weights and points are defined so that the quadrature rule associated with them is exact for polynomials of degree less than or equal to $2N - 1$:

$$\sum_{i=0}^N P(x_i)\rho_i = \int_{-1}^1 P(x)dx .$$

From the $2N$ equations that one can derive from this assumption, one obtains the $N - 1$ relations $L'_N(x_i) = 0$ and the $N + 1$ GLL weights, ρ_i :

$$\rho_i = \frac{2}{N(N+1)[L_N(x_i)]^2} \quad \forall i = 0, \dots, N.$$

GLL points The $N + 1$ Gauss-Lobatto-Legendre points, x_i , are defined on $[-1, 1]$ by:

$$\begin{cases} x_0 &= -1, \\ L'_N(x_i) &= 0 \quad \forall i = 1, \dots, N-1, \\ x_N &= 1. \end{cases}$$

B.1.4 Lagrange-Legendre interpolants

Of degree N The Lagrange-Legendre interpolants are the Lagrange interpolants based on the $N + 1$ GLL points. They are given by the following equation:

$$h_j(x) = -\frac{(1-x^2)L'_N(x)}{N(N+1)L_N(x_j)(x-x_j)} .$$

Of degree $N-2$ These Lagrange-Legendre interpolants are the Lagrange interpolants based on the $N - 1$ inner GLL points. They are given by the following equation:

$$\tilde{h}_i(x) = \frac{L'_N(x)}{L_N''(x_i)(x-x_i)} \quad \forall x \in [-1, 1] \quad \forall i \in \{1, 2, \dots, N-1\} .$$

B.1.5 Lagrange-Legendre interpolants derivatives

The derivatives of the Lagrange-Legendre interpolants of degree N on the $N + 1$ GLL points, x_i , are given by:

$$\begin{cases} d_{ij} &= \frac{L_N(x_i)}{L_N(x_j)(x_i-x_j)} \quad \forall i \neq j, \\ d_{ii} &= 0 \quad \forall i \neq 0, N, \\ d_{00} &= -\frac{N(N+1)}{4}, \\ d_{NN} &= \frac{N(N+1)}{4}. \end{cases}$$

B.2 Tensor product

B.2.1 Definition

The tensor product of two matrices A and B of size $N \times N$ is defined as:

$$A \otimes B = \begin{pmatrix} A_{11}B & A_{12}B & \dots & A_{1N}B \\ A_{21}B & A_{22}B & \dots & A_{2N}B \\ \cdot & \cdot & \dots & \cdot \\ \cdot & \cdot & \dots & \cdot \\ A_{i1}B & A_{i2}B & \dots & A_{iN}B \\ \cdot & \cdot & \dots & \cdot \\ \cdot & \cdot & \dots & \cdot \\ \cdot & \cdot & \dots & \cdot \\ A_{N1}B & A_{N2}B & \dots & A_{NN}B \end{pmatrix}.$$

B.2.2 Properties

$$\begin{aligned} (A \otimes B)(C \otimes D) &= AC \otimes BD, \\ (A \otimes B)^{-1} &= A^{-1} \otimes B^{-1}, \\ (A \otimes B)u &= AUB^T. \end{aligned}$$

Where u is the vector array $(u_{ij})_{(i,j) \in |N \times N|}$ and U the corresponding matrix: $U_{ij} = u_{ij}$.

B.3 Operation count for a matrix vector multiplication

In axisymmetric geometry, one can perform a $2D$ matrix vector multiplication for each azimuthal Fourier mode, N_θ , instead of doing the same operation on a $3D$ vector. If the matrix is a Laplacian or a Helmholtz operator, the leading order of the operation count for a matrix vector multiplication is: $(N_r^2 I N_z J + N_z^2 J N_r I) N_\theta$. The evaluations of $A^r \otimes B^z u$ and $rB^r \otimes A^z u$ are indeed the most expensive parts of the Laplacian calculus. If we take $M = N_r = N_z = N_\theta$ and $I = J = 1$, we obtain a simpler formula for the operation count, that is: $2M^4$.

Appendix C

Navier-Stokes solver in hourglass geometry

C.1 Mapping of the hourglass geometry

We now want to simulate the Taylor-Couette flow in a slightly modified domain. We add a localized deformation of the gap at mid-height. This involves defining a transformation from the physical domain onto a rectangular reference domain. Such a transformation, called a mapping, cannot be constructed analytically in most cases. Instead one has to use the approximation of the unknown continuous mapping. We only need a 2D mapping because the hourglass geometry is axisymmetric. The methods for two-dimensional mappings are cast into three groups:

- Methods involving the solution of partial differential equation.
- Conformal mappings.
- Interpolation from the boundaries, referred to as Gordon's transfinite interpolation [33].

We have chosen the last of these options because it is the fastest computationally and is very simple to implement.

Transfinite interpolation of Gordon and Hall To create the mesh in deformed geometry, we use the transfinite interpolation of Gordon and Hall, that transforms the reference square, $\hat{\Upsilon} = [-1, 1] \times [-1, 1]$, in any quadrangular plane surface defined by its four contours. The four contours, $\Gamma_{i \in \{1,2,3,4\}}$, of the hourglass geometry are defined by:

- Γ_1 : $r_1(x, y) = r_1(x) = \frac{R_2 - R_1}{2}x + \frac{R_2 + R_1}{2}$, and $z_1(x, y) = H_1$.
- Γ_2 : $r_2(x, y) = R_2$, and $z_2(x, y) = z_2(y) = \frac{H_2 - H_1}{2}y + \frac{H_2 + H_1}{2}$.
- Γ_3 : $r_3(x, y) = r_3(x) = \frac{R_2 - R_1}{2}x + \frac{R_2 + R_1}{2}$, and $z_3(x, y) = H_2$.

- Γ_4 : $r_4(x, y) = r_4(y)$, and $z_4(x, y) = z_4(y) = \frac{H_2 - H_1}{2}y + \frac{H_2 + H_1}{2}$.

Let us introduce the so-called linear blending functions: $\Phi_1(x) = \frac{1-x}{2}$, $\Phi_2(x) = \frac{1+x}{2}$, $\Psi_1(y) = \frac{1-y}{2}$ and $\Psi_2(y) = \frac{1+y}{2}$. The approximate mapping is then expressed as:

$$r(x, y) = \Phi_1(x)r_4(y) + \Phi_2(x)r_2 + \Psi_1(y)r_1(x) + \Psi_2(y)r_3(x) \\ - \Phi_1(x)\Psi_1(y)r_1(-1) - \Phi_2(x)\Psi_1(y)r_1(1) - \Phi_2(x)\Psi_2(y)r_1(1) - \Phi_1(x)\Psi_2(y)r_1(-1).$$

Knowing that: $r_1(x) = r_3(x)$ and that: $r_1(-1) = r_4(-1)$, this expression is simplified as:

$$r(x, y) = \left(\frac{1-x}{2} \right) [r_4(y) - r_4(-1)] + r_1(x).$$

In our case the height, z , is a linear function of y : $z(y) = \frac{H_2 - H_1}{2}y + \frac{H_2 + H_1}{2}$.

C.2 Spatial discretization

We start from the dimensionless Navier-Stokes equations (3.4), and project this system of equations in Fourier space, as described in chapter 3, to obtain the set of θ -discrete (r, z, t) continuous equations (3.6).

Weak formulation of the equations in $\hat{\Upsilon}$ The integral over Υ can be expressed as:

$$\int_{\Upsilon} F(r, z) r dr dz = \int_{\hat{\Upsilon}} F(x, y) r(x, y) J(x, y) dx dy.$$

In transforming the equations from Υ to $\hat{\Upsilon}$, modifications appear in the expression of the Navier-Stokes equations. A term, $J(x, y)$, called the Jacobian of the transformation, appears in the formulation. It is defined by:

$$J(x, y) = \frac{\partial r}{\partial x} \frac{\partial z}{\partial y},$$

with:

$$\begin{cases} \frac{\partial r}{\partial x} &= -\frac{1}{2}[r_4(y) - r_4(-1)] + \frac{1}{2}[r_1(1) - r_1(-1)], \\ \frac{\partial z}{\partial y} &= \frac{1}{2}[z_4(1) - z_4(-1)]. \end{cases}$$

The Jacobian is then only a function of y . The two other partial derivatives of the mapping, defined by $(r(x, y), z(x, y))$, are $\frac{\partial r}{\partial y} = \left(\frac{1-x}{2}\right) r'_4(y)$ and $\frac{\partial z}{\partial x} = 0$, where: $r'_4(y) = \frac{dr_4}{dy}(y)$.

The following relations will also be useful:

$$\begin{cases} \frac{\partial x}{\partial r} &= J^{-1} \frac{\partial z}{\partial y}, \\ \frac{\partial x}{\partial z} &= -J^{-1} \frac{\partial r}{\partial y}, \\ \frac{\partial y}{\partial r} &= 0, \\ \frac{\partial y}{\partial z} &= J^{-1} \frac{\partial r}{\partial x}. \end{cases}$$

Decomposition into macro-elements The domain $\hat{\Upsilon}$ is further decomposed in $I \times J$ rectangular elements, $\hat{\Upsilon}^{el} =]x_0^e, x_0^e + g^e[\times]y_0^l, y_0^l + h^l[$, each of which is mapped onto its so-called “parent element”, $\hat{\Upsilon}^{\hat{el}} = [-1, 1] \times [-1, 1]$. This mapping is affine: to (x, y) in $\hat{\Upsilon}^{el}$ there corresponds (ζ, ξ) in $\hat{\Upsilon}^{\hat{el}}$, such that

$$\begin{cases} x(\zeta) = x_0^e + \frac{g^e}{2}(\zeta + 1) & , \\ y(\xi) = y_0^l + \frac{h^l}{2}(\xi + 1) & . \end{cases}$$

$$\begin{cases} x_0^e = -1 + \sum_{i=1}^{e-1} g^i & \forall e \geq 2, \\ y_0^l = -1 + \sum_{i=1}^{l-1} h^i & \forall l \geq 2. \end{cases}$$

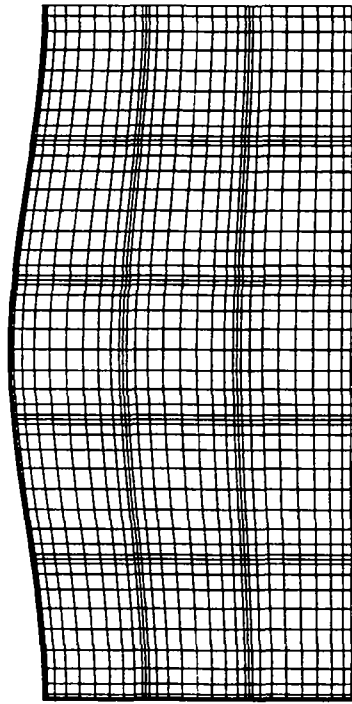


Figure C.1: *Grid of the physical domain: Υ , in deformed geometry. The polynomial degree is 10 in both directions and there are 3×5 elements. Here, $r_4(y) = R_1 - \delta[1 + \cos(\pi y)]$. And δ is a few percents of the gap width, $R_2 - R_1$.*

Ordinary differential equations In each macro-element $\hat{\Upsilon}^{\hat{el}}$, we use the expansions 3.10 and 3.11, the corresponding test functions and the quadrature 3.12 of chapter 3.

The Jacobian of the transformation is: $J(\xi) = \frac{\partial r}{\partial x}(\xi) \frac{\partial z}{\partial y}$. Let us define $a(\zeta)$, $b(\xi)$ and $c(\zeta)$ such that: $r(\zeta, \xi) = a(\zeta)b(\xi) + c(\zeta)$. We have:

$$a(\zeta) = \frac{1 - x(\zeta)}{2} ,$$

$$b(\xi) = r_4[y(\xi)] - r_4(-1) ,$$

and

$$c(\zeta) = r_1[x(\zeta)] .$$

We do not write the full development of the calculations this time but come directly to the final system of ordinary differential equations:

$$\left\{ \begin{array}{l} \mathcal{B}^r \otimes \mathcal{J}\mathcal{B}^z \frac{du_k}{dt} + \left[\widetilde{a\mathcal{G}^r} \otimes \widetilde{b\mathcal{B}^z} + \widetilde{c\mathcal{G}^r} \otimes \widetilde{\mathcal{B}^z} - \widetilde{\mathcal{B}^r} \otimes \widetilde{\mathcal{J}\mathcal{B}^z} \right] p_k = s_k^r , \\ \mathcal{B}^r \otimes \mathcal{J}\mathcal{B}^z \frac{dv_k}{dt} + ik\widetilde{\mathcal{B}^r} \otimes \widetilde{\mathcal{J}\mathcal{B}^z} p_k = s_k^\theta , \\ \mathcal{B}^r \otimes \mathcal{J}\mathcal{B}^z \frac{dw_k}{dt} + \left[a^2\widetilde{\mathcal{G}^r} \otimes \widetilde{b\mathcal{B}^z} + \widetilde{ac\mathcal{G}^r} \otimes \widetilde{b\mathcal{B}^z} + \widetilde{a\mathcal{B}^r} \otimes \widetilde{b\mathcal{G}^z} + \widetilde{c\mathcal{B}^r} \otimes \widetilde{\mathcal{G}^z} \right] p_k = s_k^z , \\ \left[-\widetilde{a\mathcal{G}^r}^T \otimes \widetilde{b\mathcal{B}^z}^T - \widetilde{c\mathcal{G}^r}^T \otimes \widetilde{\mathcal{B}^z}^T + \widetilde{\mathcal{B}^r}^T \otimes \widetilde{\mathcal{J}\mathcal{B}^z}^T \right] u_k + ik\widetilde{\mathcal{B}^r}^T \otimes \widetilde{\mathcal{J}\mathcal{B}^z}^T v_k \\ - \left[a^2\widetilde{\mathcal{G}^r}^T \otimes \widetilde{b\mathcal{B}^z}^T + \widetilde{ac\mathcal{G}^r}^T \otimes \widetilde{b\mathcal{B}^z}^T + \widetilde{a\mathcal{B}^r}^T \otimes \widetilde{b\mathcal{G}^z}^T + \widetilde{c\mathcal{B}^r}^T \otimes \widetilde{\mathcal{G}^z}^T \right] w_k = 0 . \end{array} \right.$$

With:

$$\left\{ \begin{array}{l} s_k^r = (\mathcal{L}_k u_k - \frac{\mathcal{B}^r}{r} \otimes \mathcal{J}\mathcal{B}^z u_k - 2ik\frac{\mathcal{B}^r}{r} \otimes \mathcal{J}\mathcal{B}^z v_k) - Re \mathcal{B}^r \otimes \mathcal{J}\mathcal{B}^z n l_k^r , \\ s_k^\theta = (\mathcal{L}_k v_k - \frac{\mathcal{B}^r}{r} \otimes \mathcal{J}\mathcal{B}^z v_k + 2ik\frac{\mathcal{B}^r}{r} \otimes \mathcal{J}\mathcal{B}^z u_k) - Re \mathcal{B}^r \otimes \mathcal{J}\mathcal{B}^z n l_k^\theta , \\ s_k^z = \mathcal{L}_k w_k - Re \mathcal{B}^r \otimes \mathcal{J}\mathcal{B}^z n l_k^z . \end{array} \right.$$

And:

$$\begin{aligned} \mathcal{L}_k = & a\mathcal{A}^r \otimes b\mathcal{B}^z + c\mathcal{A}^r \otimes \mathcal{B}^z - k^2 \frac{\mathcal{B}^r}{r} \otimes \mathcal{J}\mathcal{B}^z + a^3 \mathcal{A}^r \otimes b\mathcal{B}^z + a^2 c \mathcal{A}^r \otimes \mathcal{B}^z \\ & + a\mathcal{B}^r \otimes b\mathcal{A}^z + c\mathcal{B}^r \otimes \mathcal{A}^z \\ & + a^2 \mathcal{D}^r \otimes (b\mathcal{D}^z)^T + ac\mathcal{D}^r \otimes \mathcal{D}^z + (a^2 \mathcal{D}^r)^T \otimes b\mathcal{D}^z + (ac\mathcal{D}^r)^T \otimes \mathcal{D}^z . \end{aligned}$$

Direct stiffness has been performed as indicated by the use of calligraphic letters for the matrices.

Locally to each element Υ^{el} , we have:

- $B_{ij}^r = \rho_j \delta_{ij} \frac{g^e}{2}$,
- $(\frac{\mathcal{B}^r}{r})_{ij} = \frac{1}{r_j^e} \rho_j \delta_{ij} \frac{g^e}{2}$,
- $aB_{ij}^r = a_j^e \rho_j \delta_{ij} \frac{g^e}{2}$,
- $cB_{ij}^r = c_j^e \rho_j \delta_{ij} \frac{g^e}{2}$,

- $B_{ij}^z = \rho_j \delta_{ij} \frac{h^l}{2},$
- $JB_{ij}^z = J_j^l \rho_j \delta_{ij} \frac{h^l}{2},$
- $bB_{ij}^z = b_j^l \rho_j \delta_{ij} \frac{h^l}{2},$
- $bb'^2 B_{ij}^z = b_j^l \left(\frac{db^l}{d\xi}(\xi_j) \right)^2 \rho_j \delta_{ij} \frac{h^l}{2},$
- $b'^2 B_{ij}^z = \left(\frac{db^l}{d\xi}(\xi_j) \right)^2 \rho_j \delta_{ij} \frac{h^l}{2},$
- $D_{ij}^r = \frac{2}{g^e} \frac{dh_j}{d\zeta}(\zeta_i),$
- $aD_{ij}^r = a_j^e \frac{2}{g^e} \frac{dh_j}{d\zeta}(\zeta_i),$
- $cD_{ij}^r = c_j^e \frac{2}{g^e} \frac{dh_j}{d\zeta}(\zeta_i),$
- $a^2 D_{ij}^r = (a_j^e)^2 \frac{2}{g^e} \frac{dh_j}{d\zeta}(\zeta_i),$
- $acD_{ij}^r = a_j^e c_j^e \frac{2}{g^e} \frac{dh_j}{d\zeta}(\zeta_i),$
- $D_{ij}^z = \frac{2}{h^l} \frac{dh_j}{d\xi}(\xi_i),$
- $bD_{ij}^z = b_j^l \frac{2}{h^l} \frac{dh_j}{d\xi}(\xi_i),$
- $aA_{ij}^r = -\frac{2}{g^e} \sum_{k=0}^N a_k^e r_k^e \rho_k^r d_{ki}^r d_{kj}^r,$
- $cA_{ij}^r = -\frac{2}{g^e} \sum_{k=0}^N c_k^e r_k^e \rho_k^r d_{ki}^r d_{kj}^r,$
- $a^3 A_{ij}^r = -\frac{2}{g^e} \sum_{k=0}^N (a_k^e)^3 r_k^e \rho_k^r d_{ki}^r d_{kj}^r,$
- $a^2 cA_{ij}^r = -\frac{2}{g^e} \sum_{k=0}^N (a_k^e)^2 c_k^e r_k^e \rho_k^r d_{ki}^r d_{kj}^r,$
- $A_{ij}^z = -\frac{2}{h^l} \sum_{k=0}^N \rho_k^z d_{ki}^z d_{kj}^z,$
- $bA_{ij}^z = -\frac{2}{h^l} \sum_{k=0}^N b_j^l \rho_k^z d_{ki}^z d_{kj}^z,$
- $\widetilde{B}_{ij}^r = \rho_i \tilde{h}_j(\zeta_i) \frac{g^e}{2},$
- $\widetilde{aB}_{ij}^r = a_j^e \rho_i \tilde{h}_j(\zeta_i) \frac{g^e}{2},$
- $\widetilde{cB}_{ij}^r = c_j^e \rho_i \tilde{h}_j(\zeta_i) \frac{g^e}{2},$
- $\widetilde{B}_{ij}^z = \rho_i \tilde{h}_j(\xi_i) \frac{h^l}{2},$
- $\widetilde{bB}_{ij}^z = b_j^l \rho_i \tilde{h}_j(\xi_i) \frac{h^l}{2},$
- $\widetilde{JB}_{ij}^z = J_j^l \rho_i \tilde{h}_j(\xi_i) \frac{h^l}{2},$

- $\widetilde{b' B^z}_{ij} = \frac{db^l}{d\xi}(\xi_j) \rho_i \tilde{h}_j(\xi_i) \frac{h^l}{2}$,
- $\widetilde{bb' B^z}_{ij} = b^l_j \frac{db^l}{d\xi}(\xi_j) \rho_i \tilde{h}_j(\xi_i) \frac{h^l}{2}$,
- $\widetilde{a G^r} = -(a D^r)^T \widetilde{B^r} - \widetilde{B^r}$,
- $\widetilde{c G^r} = -(c D^r)^T \widetilde{B^r} - \widetilde{B^r}$,
- $\widetilde{a^2 G^r} = -(a^2 D^r)^T \widetilde{B^r} - \widetilde{B^r}$,
- $\widetilde{ac G^r} = -(ac D^r)^T \widetilde{B^r} - \widetilde{B^r}$,
- $\widetilde{G^z} = -(D^z)^T \widetilde{J B^z}$,
- $\widetilde{b G^z} = -(b D^z)^T \widetilde{J B^z}$.

C.3 Time discretization

The same RK2 scheme as in chapter 3 is chosen. Instead of the skew-symmetric form of the non-linear term we prefer its alternate form which is twice as fast.

Pressure solver The different mass matrices, $\widetilde{B^r}$, $\widetilde{a B^r}$, $\widetilde{c B^r}$, $\widetilde{b B^z}$, $\widetilde{B^z}$, $\widetilde{J B^z}$, $\widetilde{b' B^z}$, and $\widetilde{bb' B^z}$, are too numerous for the pseudo-Laplacian matrix to be expressed in a separate form. The fast diagonalization method can therefore not be used. An iterative method is needed. We propose a pre-conditioned conjugate gradient method. The best pre-conditionner is the inverse of the pseudo-Laplace operator calculated in straight geometry. Couzy [22] has obtained very good results using this technique.

Bibliography

- [1] Abramowitz M. and Stegun I. A. *Handbook of mathematical functions with formulas, graphs and mathematical tables*. Dover Publications, Inc., New-York, 1972.
- [2] Aitta A., Ahlers G. and Cannel D. S. Tricritical phenomena in rotating Couette-Taylor flow. *Phys. Rev. Lett.*, 54:673–676, 1985.
- [3] Alziary de Roquefort T. and Grillaud G. Computation of Taylor vortex flow by a transient implicit method. *Comput. Fluids*, 6:259–269, 1978.
- [4] Andereck C. D., Liu S. S. and Swinney H. L. Flow regimes in a circular Couette system with independently rotating cylinders. *J. Fluid Mech.*, 164:155–183, 1986.
- [5] Aouidef A. Instabilités hydrodynamiques dues aux effets des forces centrifuges et de rotation. *Thèse de Doctorat*, Université Paris VI, 1994.
- [6] Ashwin P. and King G. P. A study of particle paths in non-axisymmetric Taylor-Couette flows. *J. Fluid Mech.*, 338:341–362, 1997.
- [7] Atkhen K. Etude hydrodynamique d'un extracteur centrifuge utilisant les propriétés des écoulements de Couette-Taylor. *Thèse de Doctorat*, Université Paris VI, 1998.
- [8] Azaiez M., Fikri A. and Labrosse G. A unique grid spectral solver of the nd cartesian unsteady Stokes system. Illustrative numerical results. *Finite Elements in Analysis and Design*, 16:247–260, 1994.
- [9] Babuška I., Szabo B. A. and Katz I. N. The p -version of the finite element method. *SIAM J. Numer. Anal.*, 18:515–545, 1981.
- [10] Benjamin T. B. and Mullin T. Notes on the multiplicity of flows in the Taylor experiment. *J. Fluid Mech.*, 121:219–230, 1982.
- [11] Brindley J. and Mobbs F. R. An experimental investigation of transition to turbulence in Taylor-Couette flow using digital image processing. In G. Comte-Bellot and J. Mathieu, Editors, *Advances in turbulence*, pages 7–15, Berlin, 1987. Springer-Verlag.

- [12] Burkhalter J. E. and Koschmieder E. L. Steady supercritical Taylor vortices after sudden starts. *Phys. Fluids*, 17:1929–1935, 1974.
- [13] Canuto C., Hussaini M. Y., Quarteroni A. and Zang T. A. *Spectral methods in fluid dynamics*. Springer-Verlag, New-York, 1988.
- [14] Chandrasekhar S. On characteristic value problems in high order differential equations which arise in studies of hydrodynamic and hydromagnetic stability. *Amer. Math. Monthly*, 61:32–45, 1954.
- [15] Child M. S., Holton D., Keating J., May R. M., Mullin T., Read P. L. and Thompson J. M. T. *The nature of chaos*. Clarendon press, Oxford, 1993.
- [16] Chossat P. Interaction of azimuthal modes in the Couette-Taylor problem. In *Contemporary mathematics, Multiparameter bifurcation theory*, volume 56, pages 355–356. American Mathematical Society, 1986.
- [17] Chossat P. and Iooss G. *The Couette-Taylor problem*. Springer, New-York, 1994.
- [18] Ciarlet P. G. *The finite element method for elliptic problems*. North-Holland, Amsterdam, 1978.
- [19] Coles D. Transition in circular Couette flow. *J. Fluid Mech.*, 21:385–425, 1965.
- [20] Couette M. M. Etudes sur le frottement des liquides. *Ann. Chim. Phys.*, 6 (21):433–510, 1890.
- [21] Coughlin K. T. and Marcus P. S. Modulated waves in Taylor-Couette flow. part 1. analysis. part 2. numerical simulation. *J. Fluid Mech.*, 234:1–18, 19–46, 1992.
- [22] Couzy W. Spectral element discretization of the unsteady Navier-Stokes equations and its iterative solution on parallel computers. *PhD thesis*, EPF Lausanne: No 1380, 1995.
- [23] Davey A. The growth of Taylor vortices in flow between rotating cylinders. *J. Fluid Mech.*, 14:336–368, 1962.
- [24] Davey A., Di Prima R. C. and Stuart J. T. On the instability of Taylor vortices. *J. Fluid Mech.*, 31:17–52, 1968.
- [25] Drazin P. G. and Reid W. H. *Hydrodynamic stability*. Cambridge University press, Cambridge, 1995.
- [26] Edwards W. S., Beane S. R. and Varma S. Onset of wavy vortices in the finite-length Couette-Taylor problem. *Phys. Fluids A*, 3 (6):1510–1518, 1991.
- [27] Ern P. Instabilités d'écoulements périodiques en temps avec effets de courbure et de rotation. *Thèse de Doctorat*, Université Paris VI, 1997.

- [28] Ern P. and Wesfreid J. E. Experimental study of pulsed centrifugal instabilities. In *10th International Couette-Taylor workshop*, pages 65–66, Paris, 1997.
- [29] Esser A. and Grossmann S. Analytic expression for Taylor-Couette stability boundary. *Phys. Fluids*, 8 (7):1814–1819, 1996.
- [30] Fasel H. and Booz O. Numerical investigation of supercritical Taylor-vortex flow for a wide gap. *J. Fluid Mech.*, 138:21–52, 1984.
- [31] Gavrilakis S., Machiels L. and Deville M. O. A spectral element method for direct simulation of turbulent flows with two inhomogeneous directions. In J.-A. Desideri, C. Hirsch, P. Le Tallec, M. Pandolfi and J. Periaux, Editors, *Computational Fluid Dynamics '96*, pages 1080–1084, Chichester, 1996. John Wiley & Sons Ltd.
- [32] Girault V. and Raviart P. A. *Finite element methods for Navier-Stokes equations*. Springer-Verlag, New-York, 1986.
- [33] Gordon W. J. and Hall C. A. Transfinite element methods: Blending-function interpolation over arbitrary curved element domains. *Num. Math.*, 21:109–129, 1973.
- [34] Gorman M. and Swinney H. L. Visual observation of the second characteristic mode in a quasiperiodic flow. *Phys. Rev. Lett.*, 17:1871–1875, 1979.
- [35] Gorman M. and Swinney H. L. Spatial and temporal characteristics of modulated waves in the circular Couette system. *J. Fluid Mech.*, 117:123–142, 1982.
- [36] Haidvogel D. B. and Zang T. The accurate solution of Poisson's equation by expansion in Chebyshev polynomials. *J. Comp. Phys.*, 30:167–180, 1979.
- [37] Hirschberg G. S. Direkte simulation der turbulenten Taylor-Couette stromung und der ebenen kanalstromung. *PhD Thesis*, ETH Zuerich: Nr. 9912, 1992.
- [38] King G. P., Li Y., Lee W., Swinney H. L. and Marcus P. S. Wave speeds in wavy Taylor-vortex flow. *J. Fluid Mech.*, 141:365–390, 1984.
- [39] Kogelman S., Di Prima R. C. Stability of spatially periodic supercritical flows in hydrodynamics. *Phys. Fluids*, 13:1–11, 1970.
- [40] Koschmieder E. L. *Bénard cells and Taylor vortices*. Cambridge University Press, New York, 1993.
- [41] Krueger E. R., Gross A. and Di Prima R. C. On the relative importance of Taylor-vortex and non-axisymmetric modes in flow between rotating cylinders. *J. Fluid Mech.*, 24:521–538, 1966.

- [42] Litschke H. and Roesner K. G. New experimental methods for turbulent spots and turbulent spirals in the Taylor-Couette flow. *Experiments in fluids*, 24:201–209, 1998.
- [43] Lücke M., Mihelcic M., Wingerath K. and Pfister G. Flow in a small annulus between concentric cylinders. *J. Fluid Mech.*, 140:343–353, 1984.
- [44] Lynch R. E., Rice J. R. and Thomas D. H. Direct solution of partial difference equations by tensor product methods. *Num. Math.*, 6:185–199, 1964.
- [45] Maday Y. and Patera A. T. Spectral element methods for the Navier-Stokes equations. In A. K. Noor, Editor, *State-of-the-art surveys in computational mechanics*. ASME, New-York, 1988.
- [46] Magère E. Description et validation d'un code spectral Navier-Stokes. Rapport IMHEF T-97-1, EPFL, 1997.
- [47] Mallock A. Experiments on fluid viscosity. *Phil. Trans. Roy. Soc. London*, A 187:41–56, 1896.
- [48] Marcus P. S. Simulation of Taylor-Couette flow. part 1. numerical methods and comparison with experiment. part 2. numerical results for wavy-vortex flow with one travelling wave. *J. Fluid Mech.*, 146:45–64, 65–113, 1984.
- [49] Moser R. D., Moin P. and Leonard A. A spectral numerical method for the Navier-Stokes equations with applications to Taylor-Couette flow. *J. Comp. Phys.*, 52:524–544, 1983.
- [50] Mullin T. Mutations of steady cellular flows in the Taylor experiment. *J. Fluid Mech.*, 121:207–218, 1982.
- [51] Neitzel G. P. Numerical computation of time-dependent Taylor-vortex flows in finite-length geometries. *J. Fluid Mech.*, 141:51–66, 1984.
- [52] Patera A. T. A spectral element method for fluid dynamics: laminar flow in a channel expansion. *J. Comp. Phys.*, 54:468, 1984.
- [53] Pfister G. Period doubling in Couette flow. In *Lecture notes in physics*, volume 235, pages 199–210, Berlin, 1985. Springer.
- [54] Pfister G., Schmidt H., Cliffe K. A. and Mullin T. Bifurcation phenomena in Taylor-Couette flow in a very short annulus. *J. Fluid Mech.*, 191:1–18, 1988.
- [55] Rayleigh Lord. On the dynamics of revolving fluids. *Proc. R. Soc. London*, A 93:148–154, 1916.

- [56] Rayleigh Lord. On the stability of the laminar motion of an inviscid fluid. In *Scientific papers of Lord Rayleigh*, volume VI, page 197, Cambridge, 1920. Cambridge University Press.
- [57] Riecke H. and Paap H.-G. Stability and wave-vector restriction of axisymmetric Taylor vortex flow. *Phys. Rev. A*, 33 (1):547–553, 1986.
- [58] Rønquist E. M. Spectral element methods for the unsteady Navier-Stokes equations. In *Lecture Series 1991-01*. Von Karman Institute, Rhode-St-Genèse, Belgique, 1991.
- [59] Roberts P. H. The solution of the characteristic value problems. *Proc. R. Soc. London, A* 283:550–556, 1965.
- [60] Snyder H. A. Wave-number selection at finite amplitude in rotating Couette flow. *J. Fluid Mech.*, 35 (2):273–298, 1969.
- [61] Streett C. L. and Hussaini M. Y. A numerical simulation of finite-length Taylor-Couette flow. In G. de Vahl Davis and C. Fletcher, Editors, *Computational Fluid Dynamics*, pages 663–675, Amsterdam, 1988. Elsevier Science.
- [62] Streett C. L. and Hussaini M. Y. A numerical simulation of the appearance of chaos in finite-length Taylor-Couette flow. *Appl. Num. Math.*, 7:41–71, 1991.
- [63] Synge J. L. The stability of heterogeneous liquids. *Trans. Royal Society Canada*, 27:1–18, 1933.
- [64] Synge J. L. On the stability of a viscous liquid between two coaxial rotating cylinders. *Proc. R. Soc. London, A* 167:250–256, 1938.
- [65] Tavener S. J., Mullin T. and Cliffe K. A. Novel bifurcation phenomena in a rotating annulus. *J. Fluid Mech.*, 229:483–497, 1991.
- [66] Taylor G. I. Stability of a viscous liquid contained between two rotating cylinders. In G. K. Batchelor, Editor, *Scientific papers of Sir Geoffrey Ingram Taylor*, volume IV, pages 34–87, Cambridge, 1971. Cambridge University Press.
- [67] Timmermans L. J. P. Analysis of spectral element methods with application to incompressible flow. *PhD thesis*, Eindhoven University of Technology, 1994.
- [68] Wereley S. T. and Lueptow R. M. Azimuthal velocity in supercritical circular Couette flow. *Experiments in Fluids*, 18:1–9, 1994.
- [69] Zang T. A. On the rotation and skew-symmetric forms for incompressible flow simulations. *Appl. Num. Math.*, 7:27–40, 1991.
- [70] Zhang L. and Swinney H. L. Nonpropagating oscillatory modes in Couette-Taylor flow. *Phys. Rev. A*, 31:1006–1009, 1985.

Curriculum Vitae

Eric Magère
French citizen
Born on June 2, 1967 in St-Ouen, France
Married

- 1994-1999 **Swiss Federal Institute of Technology, Lausanne, Switzerland**
Ph.D.
Supervisor : Prof. M. O. Deville
Thesis title: "Numerical Study of transition in counter-rotating Taylor-Couette flow"
- 1993-1994 **Paris XI University, France**
'DEA' in "fluid dynamics and transfer"
Majors in non linear systems, instabilities and turbulence
Internship at the fluid mechanics laboratory of EPFL (Switzerland)
- 1993-1994 **KEB, La Queue-en-Brie, France**
Technical advisor in fluid mechanics related problems
- 1992-1993 **CFPA la Joliverie, Nantes, France**
Teacher of mathematics and mechanics in undergraduate classes leading to a qualified technician degree
- 1988-1991 **National High School for Mechanics and Aerotechnics (EN-SMA), Poitiers, France**
Engineer diploma, majors in energetics, thermodynamics and aerodynamics
Internships at SEW-Eurodrive, Bruchsal (Germany), Aerospatiale, Chatillon (France), SNECMA, Villaroche (France) and the fluid dynamics laboratory of Poitiers (France)
- 1985-1988 **Lycée Henri IV, Paris, France**
Preparation to a nationwide competitive examination for acceptance to the "Grandes Ecoles", graduate level engineering colleges
- 1985 **Lycée Henri IV, Paris, France**
A-level in mathematics and physics

Publications

E. Magère and P. Ern

Simulations of pulsed centrifugal instabilities in a Taylor-Couette geometry

Computational Fluid Dynamics '98

Papailiou, Tsahalis, Périaux, Hirsch and Pandolfi editors

John Wiley & Sons Ltd.

Volume 1, Part 2

Pages 1307 – 1310

1998

E. Magère, M. O. Deville, K. Atkhen and J. Fontaine

Simulation of the pressure distribution in a spent nuclear fuel reprocessing Taylor-Couette device

Computational Fluid Dynamics '98

Papailiou, Tsahalis, Périaux, Hirsch and Pandolfi editors

John Wiley & Sons Ltd.

Volume 1, Part 2

Pages 1094 – 1098

1998

E. Magère and M. O. Deville

Simulation of the Taylor-Couette flow in a finite geometry by spectral element method

Accepted in Applied Num. Math.

Elsevier Science

E. Magère

Rapport interne T-97-1: *Description et validation d'un code spectral Navier-Stokes*

LMF/IMHEF/DGM/EPFL

1997